Doctoral theses at NTNU, 2025:175

David Urban

Novel effects in light-actuated systems based on dispersed azobenzene dyes and azopolymers

Doctoral thesis

NTNU
Norwegian University of Science and Technology
Thesis for the Degree of
Philosophiae Doctor
Faculty of Information Technology and Electrical
Engineering
Department of Electronic Systems

NTNU
Norwegian University of
Science and Technology

David Urban

Novel effects in light-actuated systems based on dispersed azobenzene dyes and azopolymers

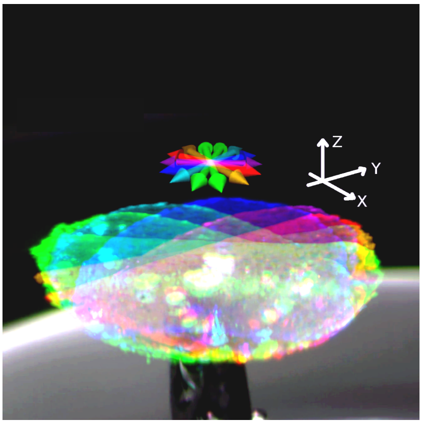

Thesis for the Degree of Philosophiae Doctor

Trondheim, May 2025

Norwegian University of Science and Technology
Faculty of Information Technology and Electrical Engineering
Department of Electronic Systems

NTNU
Norwegian University of
Science and Technology

NTNU
Norwegian University of Science and Technology

Thesis for the Degree of Philosophiae Doctor

Faculty of Information Technology and Electrical Engineering
Department of Electronic Systems

ISBN 978-82-326-8946-0 (printed ver.)
ISBN 978-82-326-8945-3 (electronic ver.)
ISSN 1503-8181 (printed ver.)
ISSN 2703-8084 (online ver.)

Doctoral theses at NTNU, 2025:175

Printed by NTNU Grafisk senter

Novel effects in light-actuated systems based on dispersed azobenzene dyes and azopolymers.

PhD Thesis

Institute of Electronic Systems (IES)
Norwegian University of Science and Technology (NTNU)

Department of Applied Science and Technology (DISAT)
Politecnico di Torino (POLITO)

Author
David Urban

Main Supervisors
Emiliano Descrovi (Politecnico di Torino)
Dag Roar Hjelme (Norwegian University of Science and Technology)

Co-supervisors
Jan Torgersen (Technische Universität München)
Carlo Liberale (King Abdullah University of Science and Technology)

Keywords:

Azopolymers, Soft robots, Opto-fluidics, Elastic Metamaterials

I. Summary

In this thesis we explore soft polymeric materials that can be steered by light – quite literally. Through illumination in suitable settings, these materials cannot only be modulated for example in terms of softness, but they can be brought to physically deform, meaning they change *shape*. The directionality and amplitude of such effects laying largely in the hands of the experimenter, a wide playground of new technological scenarios and cascading effects is explored. Acknowledging the decade-spanning efforts to elucidate the photo-deformation properties of azopolymers in fixed and quasi-static situations, we focus particularly on dynamic situations where the light-fueled system interacts, or hopefully will be capable to interact, with other components of a device or its environment. During this endeavor, we encounter a range of open-ended questions relating to the maximal size of actuating structures, the possibility of overwriting previous shape changes, and even the prospect of producing never-ending light-induced motion. The generated insights – for example on interaction effects between light-triggered azopolymer parts of a system and passive elastomer surroudings – may benefit the further understanding of azopolymer photo-deformation on a fundamental level. On the other hand, the systems derived from the pursuit of these questions naturally open for new application scenarios. For example, we introduce light-responsive elastic metamaterials which could serve to steer elastic waves, a soft robotic arm which may eventually be guided towards the manipulation of objects, and a light-controlled particle flow system where propulsion channels can freely be drawn on liquid surfaces. We hope that this approach, together with exciting recent examples from literature, may inspire further work in what could be referred to as *azopolymer system design*, aiming not only at azopolymers' photo-deformation per se, but also at their study and application as components of more complex systems and devices.

II. Preface

This thesis is submitted to the Norwegian University of Science and Technology (NTNU), for partial fulfillment of the requirements for the degree of Doctor of Philosophy, and to the Polytechnic University of Turin (Polito) for partial fulfillment of the requirements for the Ph.D. degree in the Graduate School of Polito (ScuDo).

The thesis was conducted as part of a cotutelle agreement between the Institute of Electronic Systems (IES) at the Norwegian University of Science and Technology and the Department of Applied Science and Technology (DISAT) at the Polytechnic University of Turin (Polito).

The thesis was supervised by Prof. Emiliano Descrovi (Polito) Prof. Dag Roar Hjelme (NTNU) and and co-supervised by Prof. Jan Torgersen (Technische Universität München) and Prof. Carlo Liberale (King Abdullah University of Science and Technology).

The experimental work was mainly carried out in the IES and DISAT facilities, as well as in the NTNU Nanolab cleanroom infrastructure for fabrication and characterization purposes, in the NTNU Department of Physics (IFY) for the use of confocal microscopes, as well as in the NTNU Department of Mechanical and Industrial Engineering (MTP) for 3D printing.

Visiting periods were spent and part of the work was carried out in the Complex Photonic group led by Prof. Diederik Wiersma at the European Laboratory for Non-Linear Spectroscopy (LENS) in Florence, Italy and in the Soft Matter Lab led by Prof. Giovanni Volpe at the University of Gothenburg, Sweden.

Additional funding for travels were provided by *Norges tekniske høgskoles fond* under the form of a travel grant, as well as by the department (IES). For access to the cleanroom infrastructure, The Research Council of Norway is acknowledged for the support to the Norwegian Micro- and Nano-Fabrication Facility, NorFab, project number 295864. Finally, some of the work during the PhD thesis gave rise to additional funding for the exploitation of results, under a pilot project awarded by NTNU Discovery.

III. Acknowledgements

First, I would like to thank my supervisors for the time and efforts dedicated to supporting me in the work for this thesis and for their continuous guidance. I would like to thank Prof. Dag Roar Hjelme, not only for inspiring discussions and rigorous reviewing, but also for being a great help in navigating NTNU's environment and for sharing his various professional insights extending far beyond the realm of academia. Equally, I would like to thank Prof. Emiliano Descrovi for hiring me on this fascinating topic and for providing outstanding scientific support all along the way. It was a pleasure to work this way. Your well-balanced supervision style, determined, engaged and instructional, but also empathic, non-authoritarian and somewhat easy-going is highly inspirational to me. I am also very grateful to Prof. Jan Torgersen for opening and facilitating fruitful collaborations, and for readily including me in his group activities from Day 1.

I further would like to thank all co-authors for allowing me to collaborate with them on our common articles and all colleagues that I had the pleasure to work and/or interact with during my research visits, some of them even hosting me personally. In particular, I am grateful to the people at LENS, for demonstrating the perfect balance between a highly productive and very social work environment (and I wish I could have played even more calcetto), to Dr. Niccolò Marcucci for the great fun we had in the lab and at conferences, and to Prof. Marcel Rey for the exciting, numerous and friendly scientific discussions as well as for his advice.

I am also indebted to the engineers from Nanolab and the other departments, for their valuable instructions, trouble-shooting assistance, and technical advice. Particularly I would like to thank Jens Høvik, Mathilde Barriet, Astrid Bjørkøy, Verner Håkonsen and Mark Ciappa, who have gifted me especially much of their time. I also would like to thank Dr. David Barriet for countless insightful chats around the cleanroom and his perpetual willingness to share some of his long-standing fabrication experience.

Finally, I feel fortunate to thank my family and friends who have supported me along the way, expressed interest in my research adventures, and sometimes helped me to take a step back from work. In particular, this includes old friends from Switzerland, new ones in Norway, my joyful colleagues at the institute, and some friends scattered here and there. I would like to thank my parents for their support and occasionally still needed advice,

as well as my sister Sarah, who has been my most dedicated visitor from abroad. As it happens, she does “real robotics” - whatever that is supposed to mean. I would specifically like to thank Miriam for her dedication in holding my back during the accomplishment of this thesis, April which is certainly Norway’s if not Europe’s best cheer-up, Torgny for providing most of the work clothes, and my son Markus, who peacefully slept through most of the writing in what follows.

IV. Table of Contents

I. Summary **ii**

II. Preface **iii**

III. Acknowledgements **iv**

IV. Table of Contents **vi**

1 Introduction **1**

1.1 Fundamentals of Amorphous Azopolymer Deformation *3*
- 1.1.1 Azobenzene *trans* and *cis* isomers 3
- 1.1.2 Photo-orientation and the Weigert effect 4
- 1.1.3 Amorphous Azopolymer Deformation in Milestones 8
- 1.1.4 Deformation Mechanism 9

1.2 Other Material Systems *13*
- 1.2.1 Azobenzene Containing Liquid Crystal Networks 14
- 1.2.2 Other Azobenzene *trans-cis* Systems 16

1.3 Focal point: Reversibility *19*
- 1.3.1 Emergence of the Reversibility Question 20
- 1.3.2 Definitions of Reversibility 21
- 1.3.3 Reversibility in an Application Perspective 25

1.4 Focal point: System Scales *26*
- 1.4.1 Scaling Systems – Which way? 27
- 1.4.2 Azopolymer Deformation Scales 29

1.5 Focal point: Saturation Behavior *33*
- 1.5.1 Deformation Saturation – Usual case 33
- 1.5.2 Oscillating Systems 34
- 1.5.3 Continuous Linear Motion 35

2 Summary of Articles **40**

2.1 Articles 1 & 2: Photo-tunable Elastic Metamaterials *40*

2.2 Article 3: Polarization Sensitive Soft Robots *43*

2.3 Article 4: Opto-capillary Directional Flows *45*

3 Outlook and Conclusions **48**

3.1 Outlook *48*
- 3.1.1 Reversible Degrees of Freedom 48
- 3.1.2 Scaling in the Third Dimension 52
- 3.1.3 Application Perspectives 56

3.2 Conclusion *58*

V. References **60**

VI. Index List **80**

VII. Appendix A: List of Contributions **82**

VIII. Appendix B: Included Articles **84**

IX. Appendix C: Reversibility Measure **85**

1 Introduction

Stimuli-responsive organic materials and polymers are a vast and thriving research field. Whilst in some areas, their use has become industrially relevant already decades ago, for example in display technology where electrical signals are routinely used to control the orientation and hence the optical properties of organic liquid crystal (LC) molecules[1], the concept is of a much more emerging nature in other domains. For example, mechanical actuation and deformation of so-called "soft robots" is an interesting new field of study, where besides electrical fields, various other parameters such as temperature, pH-levels, pressure, magnetic fields or even light can be used to induce physical changes in various types of actuators[2]. Ultimately, many of these materials offer the promise of inexpensive polymeric elements being able to perform versatile and complex tasks, guided either by control schemes much simpler than for example electronic circuits, or by directly exploiting natural environmental conditions, such as e.g., diurnal temperature or humidity variations[3,4] and sunlight[5,6].

In this thesis, we have employed several photo-responsive azobenzene-based polymeric systems which were able to undergo mechanical changes and, in some settings, even large directional deformations in response to light. These materials are of particular interest due to several reasons. First, light as a stimulus presents important practical advantages. In contrast to other aforementioned stimuli, (e.g., temperature, chemical changes, magnetic or electrical fields), which are often used as global parameters whose variation will influence entire samples at once, light can easily be spatially patterned, and irradiation can be readily localized in specific points of a specimen. More precisely, such patterning can be achieved without the use of control structures of similar size to the desired modulation (such as for example microelectrodes for highly resolved electric fields)[7], but rather through focusing of light using modifiable optical setups, made of macroscopic components, and often combined with regular microscopes. In addition, light is also a multiparametric stimulus and besides intensity, one may control the wavelength (color), propagation direction (incidence), orbital angular momentum (vortex beams) and polarization (vectorial property) of the illumination. As a matter of fact, the latter property was heavily employed in the main body of this work, where we used amorphous azopolymers which are able to *elongate anisotropically in the direction of the polarization of the employed illumination*. This intrinsically direction-tunable behavior is a second highly interesting property of the azobenzene-derived material class that was utilized in this thesis. Finally, it is worth noting that, whilst not quite at the intensities of unconcentrated sunlight, the effects shown in this work could all be induced at moderate intensities (from below 1 to ~10^2 W/cm^{-2}) and at visible green wavelengths, which are safer and more biocompatible compared to for example ultraviolet (UV) radiation. Not limited to dedicated setups, these illuminations may therefore also be achieved using inexpensive light-emitting diodes (LEDs) or even the built-in ~10mW laser diodes of standard confocal microscopes.

The thesis, a collection of articles comprising several new effects in azobenzene-based polymer materials is structured as follows. The first part of this chapter (section 1.1) provides an introduction to the fundamental properties of azobenzene-based amorphous azopolymers that were employed in large parts of the experimental work shown. A short subsequent chapter introduces a series of distinct, but related, azobenzene-based light-responsive material classes which are useful for the purposes of comparison (section 1.2). Thereafter, the main body of the introduction is focusing on three topical aspects*, reversibility, system size, and saturation behavior* of light-triggered actuation (sections 1.3-1.5), which provide additional context to the article collection. We highlight that the addressed issues are by no means intended as an exhaustive list of challenges that the field unanimously faces, but rather as lines of thought that have inspired the work, and where we deem that existing limitations have been shifted to a certain extent by the discoveries made. In chapter 2, the included articles are summarized, with special attention attributed to the aspects outlined before. The chapter includes two works where the author built upon the optomechanical tuning of elastic metamaterials and developed a simpler fabrication method, enabling more versatile structures. The main works then comprise two entirely new research threads, where the directional deformation of amorphous azopolymers was harnessed in versatile, polarization-sensitive soft actuators and in novel air-water interface optofluidic systems with directional flows. Finally, chapter 3 provides some outlooks linking the observed effects with remaining challenges in a more general application perspective. In its entirety, the work reflects our attempt to identify, and partially address, some of the issues standing in the way of azopolymers being used in active, dynamic devices, as opposed to their more established use in micro- and nanofabrication.

1.1 Fundamentals of Amorphous Azopolymer Deformation

A light-responsive polymeric system needs a photoactive unit permitting the optically induced effects. Throughout this work, we have used an azobenzene derivative known as Disperse Red 1 (DR1) to this aim, either in its molecular form or integrated into a linear azopolymer as side-chain building block as poly[(Disperse Red 1 methacrylate)-*co*-(methyl methacrylate)] (pDR1m-co-mma). The chemical structures relating to both cases are shown in Figure 1. As a matter of fact, illuminating these and similar materials with (polarized) light can provoke a multitude of effects across different time and length scales, from fast molecular configurational changes and reorientation to the slower generation of supramolecular deformation at the micron-scale and beyond. In this section we will briefly outline the different effects and their interconnection. For a recent, more comprehensive overview summarizing these effects in azopolymers one may refer to the corresponding volume by Xiaogong Wang[8].

1.1.1 Azobenzene *trans* and *cis* isomers

The molecular structure of the azobenzene-derived chromophore Disperse Red 1, whose name reveals its applicability as strong, deep red dye, shows the typical azobenzene structure comprised of two phenyl rings connected by a N=N double bond (Fig. 1a). However, the depicted state is only one of the two molecular ground states, called *isomers,* with distinct shapes. In fact, for azobenzene and some of its derivatives, the rod-like *trans* molecule may be converted into a bent *cis* shape via a process called *isomerization*, and vice versa (see Fig. 1b) [9]. This process, as well as the two isomers, are illustrated in

Figure 1b. It should be highlighted that, whilst the *trans* state, which usually is lower in energy, is sometimes referred to as the ground state, both states are ground states in principle. Electronic excitation obtained upon optical absorption in either ground state constitutes an intermediate state instead, which can facilitate the transition into the other ground state via several possible pathways, as discussed and studied in detail and for different azobenzene-derived compounds elsewhere[9–14]. In practice, transitions between the rod-like *trans* and the bent *cis* form may be induced either optically (with light) or via thermal transitions, with the *trans* state being the thermally more stable isomer which the molecule will eventually relax back to in the dark[15,16]. For azobenzene-type molecules, UV wavelengths needed to go from *trans* to *cis* states are well-separated from the blue visible wavelengths favoring the reverse transition[17] and thermal relaxation is slow[18]. Such systems can therefore readily be used as photo-switchable systems. The targeted switching between differently weighted isomer populations using distinct wavelengths is widely used in several of the other material systems which will be introduced in section 1.2.

1.1.2 Photo-orientation and the Weigert effect

In the case of the dye employed here, the situation is slightly different. In fact, DR1 belongs to the class of pseudostilbenes[18]. For this class, due the addition of an electron-donating and an electron-accepting group on either side of the azobenzene moiety, the spectra of the *trans* and *cis* isomers are red-shifted[19] and show an increased overlap[20–22]. Instead of photo-switching using two different wavelengths, one can then also induce efficient photo-cycling between the two isomers under continuous irradiation at a suitable single wavelength, situated around 500 nm (lime/green) for DR1 side-chain polymers (see also scheme in Fig. 1c)[23]. This will cause the following two effects: First, each time the molecule undergoes a *trans-cis-trans* cycle due to two subsequent isomerization events, the spatial orientation of the rod-shaped *trans* molecule's long axis will be altered. Secondly, the absorption of the *trans* molecule is much more efficient when the electric field of the light wave is oscillating along the molecule's long axis. For irradiation with linearly polarized light, this means that *trans* isomers with their long axis initially aligned with the incident polarization are more likely to absorb, undergo a *trans-cis-trans* cycle, and end up in a new orientation. This new orientation, if different from the polarization axis, leads to a lower absorption/reorientation probability and hence a lower probability to undergo another *trans-cis-trans* cycle. The combination of these effects thus causes a statistical reorientation of dyes into the two axes not coinciding with the linear polarization[23–26]. A two-dimensional sketch of the final molecular reorientation is shown in Figure 1d.

The polarization-induced molecule reorientation also causes optical anisotropies which are referred to as the Weigert effect, after Fritz Weigert's initial discoveries of polarization-induced optical anisotropies in suitable photographic materials or dyes[27,28]. In fact, a trivial first consequence of the reorientation of rod-like molecules out of the polarization axis - due to preferential absorption in this state - is the reduced absorption for this polarization when most molecules have been reoriented. This effect, known as dichroism, is well described and can lead to a light penetration depth that increases in time, at the characteristic timescale of average reorientation into an orientational equilibrium[29]. It should be noted that absorption reduction also occurs for circularly polarized or unpolarized light[30,31], as the molecules can always statistically reorient along the optical axis (i.e., the propagation direction of the illumination). In practical experimental settings, such as for the photo-deformable materials in this thesis, it is useful to keep this effect (which can lead to a reduction in brightfield absorption as well as reduced fluorescence in irradiation zones when using circularly/unpolarized light) in mind and not automatically attribute changes in absorption to irreversible photo-degradation of molecules[32]. The second anisotropy concerns the refractive indexes and is known as birefringence. At wavelengths longer than the absorption peak, the susceptibility is generally higher along the long axis of the rod-like *trans* molecule, giving rise to a higher refractive index along this axis[33–35]. Birefringence can rotate linear polarization and thus make light pass through a setup of two crossed polarizers on either side of a birefringent sample with appropriately oriented anisotropy. An example of this effect, which was acquired using early precursors of the composites studied in article 3, is shown in Figure 1e. The birefringence emerging from the Weigert effect, which for some polymers can be stable over several years in the dark[23], made optical storage an early application perspective for such materials[36]. In systems where the birefringence is readily overwritten on the other hand, tunable features can be designed, for example to modulate the spectral features of resonant surface modes within anisotropic cavities[37].

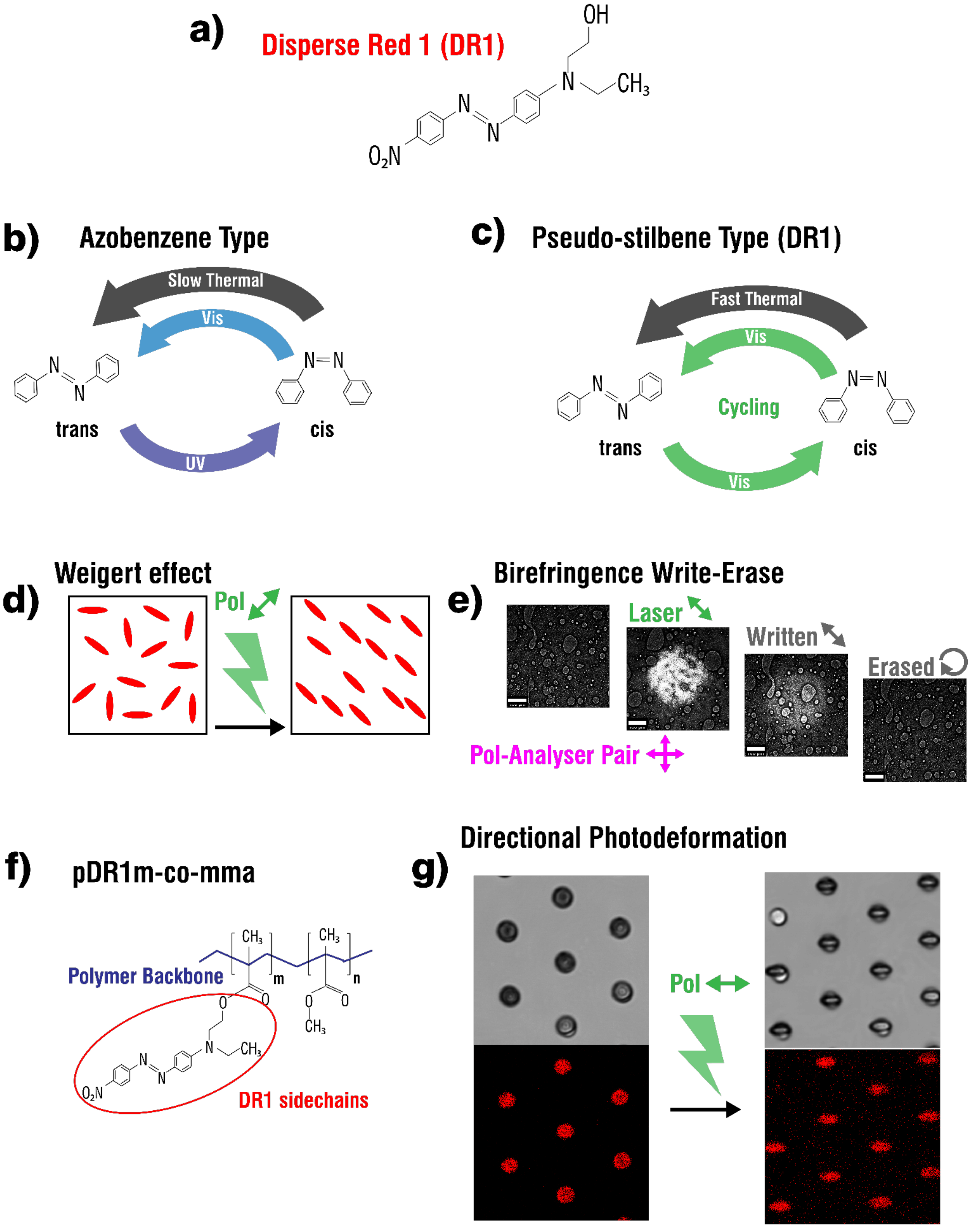

Figure 1. Azobenzene-derived materials: isomerization, reorientation, deformation. a) Chemical structure of the azobenzene-derived Disperse Red 1 (DR1) dye. b) Scheme of main optical and thermal isomerization triggers for azobenzene. Distinct wavelengths are particularly efficient for *cis-trans* and *trans-cis* isomerization respectively. c) Scheme of main optical and thermal isomerization triggers for pseudo-stilbenes (including DR1). Visible wavelengths can efficiently trigger both isomerization events, inducing photo-cycling. d) Sketch showing the statistical reorientation of dyes upon photo-cycling, referred to as the Weigert effect. e) Unpublished data acquired on azopolymer-containing composites. Between crossed polarizers, are shown from left to right: the (dark) pristine sample, the laser spot with diagonal polarization, the birefringence written after the laser spot is turned off, and the final (dark) sample, where birefringence was erased with circular polarization. f) Chemical structure of pDR1m-co-mma, a linear methacrylate azopolymer bearing DR1 and methyl sidechains. g) Directional, polarization-dependent (here linear horizontal) deformation of azopolymer nanoparticle layers dried onto PDMS pillars.

1.1.3 Amorphous Azopolymer Deformation in Milestones

Intriguingly, the molecular reorientation is not the only polarization sensitive effect that can be obtained with DR1 and similar dye molecules. Namely, when these dyes are covalently attached as sidechains to a linear polymer backbone, mass migration and deformation effects can appear on the micron-scale. In the following we will quickly recite some important experimental discoveries relevant in the context of this work. By the accounts of some of the first researchers reporting on them, light-induced deformations in azopolymers were discovered rather unexpectedly[23,38]. It was during attempts to stabilize volume holographic bulk gratings introduced above and to develop new non-linear optics polymers, that the groups of Tripathy and Kumar, as well as Nathansohn and Rochon, independently discovered a surprising effect in early 1995: namely, that interfering laser beams used to inscribe birefringence gratings would actually cause a physical surface relief grating (SRG) to form on top of the amorphous azopolymer thin films which could be shown by atomic force microscopy (AFM)[39,40]. These first experiments used interferometric recombination of two equally polarized beams (for example p-polarized), hence creating a sinusoidal intensity interference pattern, and early explanations for the phenomenon often highlighted the role of intensity modulation[41]. However, already some years later from 1998 onwards, SRGs inscribed by pure polarization interference patterns with homogeneous intensity (obtained e.g., by recombining orthogonally polarized beams) were widely demonstrated[42–44], clearly indicating a role of polarization in dictating the local mass migration/deformation effect. Note that such gratings can have half the optical period, since the spatial variation of the polarization follows a trajectory on the Poincaré sphere (see also section 3.1.1) dictated solely by a revolving polar angle. If the interfering beams are s- and p-polarized, the polarization pattern along this path is +45° linear, right-handed circular, -45° linear, left-handed circular. Hence, circular polarization, shown to coincide with local depressions in such an experiment[45,46], will appear twice per grating period (at the north and south pole of the sphere), with only its handedness inverted and with grating vector symmetric linear polarization states in between, enabling doubled frequency gratings. After these discoveries, the polarization's influence on the effect was investigated further in experiments involving the filling of pre-inscribed scratches[47] and using the polarization-dependent inscription of optical near-field features[48–50], amongst others in the vicinity of plasmonic structures[51,52].

A next relevant milestone is the deformation of prefabricated microstructures, starting from the large aspect ratio deformation in the direction of linear polarization of colloidal azopolymer particles, dried on a substrate, into ellipsoids by Li et. al. in 2005[53]. These studies were followed by the polarization-directed deformation of hemispherical cap arrays[54,55], lines[56], square posts[57], and all kinds of prefabricated pillars which can either be linearly stretched[58–61] or bent[62–64]. Alternatively, prefabricated inverse structures such as microwells[65,66], nanoholes[67] and the voids in breath figure arrays[68–70] have also been reshaped using azopolymers as the surrounding material. More recently, and eventually leading up to article nr 3 (see section 2.2), the photo-deformation of azopolymer particles was also studied when encapsulated in different types of soft matrices made of elastomers or hydrogels[71,72]. Finally, one can mention the deformation-induced oriented wrinkling of azopolymer films on a mechanically mismatched compliant[73] and even on liquid substrates (floating films)[74]. In article 4, we studied the behavior and interaction of deforming colloidal azopolymer particles on a liquid substrate, by adsorbing them to an air-water interface.

1.1.4 Deformation Mechanism

Despite the long history of experimental studies and practical uses of the polarization-sensitive directional deformation in azopolymers, the mechanism of this effect is still somewhat debated[75,76]. A comprehensive review of different models and their technical details being beyond the scope of this work, we will instead aim to provide the reader with a certain phenomenological intuition about these effects, which we employed in rather application-oriented settings in our own work. Hence, we will briefly, and in a somewhat simplified manner, introduce some of the concepts which have been proposed. Whilst in early days, a variety of models have been developed to, mainly, explain different type of surface grating formations[77], in later years most works dealing with directional azopolymer deformations have referred to two explanation types, or versions thereof. These are athermal directional photo-fluidization[78] and what was termed the photo-orientation approach[79,80], respectively.

The first approach seems to originate from a pioneering article by Karageorgiev et.al., inducing deformations in the near field of a plasmonic tip[47]. The authors explicitly showed that the employed azopolymer underwent considerable photo-softening in terms of elastic modulus (although less than in a molten state) and acquired low viscosity upon irradiation, all the while staying far below the polymers glass transition temperature (T_g) and in the absence of significant heating. They also showed that homogeneous irradiation of scratched polymer films would make material creep into the scratches only when the polarization of light was perpendicular to the channel. They hence employed the term anisotropic photo-fluidization, postulating that in this light-induced state of matter small forces are able to cause deformation. The anisotropic nature of these forces was attributed to the orientation of the azobenzene-derived sidechains, i.e., the Weigert effect (see section 1.1.2), via mechanisms including orientation-induced stresses, anisotropic molecular interactions and/or the light-induced vibrations of the anisotropically oriented molecules.

The photo-orientation approach, developed largely by the group of Saphiannikova, also takes the azobenzene molecular orientation, away from the polarization direction, as starting point. However, it specifically attributes the deformation along the polarization direction of amorphous sidechain azopolymers to a torque exerted by the oriented sidechains onto the polymer backbone. In this framework, the deformation would be driven by the polarization-parallel backbone alignment following from the sidechain perpendicular alignment. Indeed, experimental observations favoring this hypothesis have been reported. In one study, it was shown that while the elongation of the polymer is parallel to the polarization vector when the active sidechains are covalently attached, weakly coupled ionic attachment produces an opposite deformation[81]. This difference was attributed by the authors to the fact, that in the latter case, backbone reorientation may be inefficient, and the deformation perpendicular to the polarization may arise due to the side-chain reorientation only. Conceptually similar observations have been made by others, which used the same azobenzene sidechains, but covalently attached to different polymer backbones[82]. In this case, the observation was that elongation along the polarization direction could only be obtained for the more rigid backbone, whilst the soft backbone polymer again experienced a weaker effect in the opposite direction. Finally, in a very recent contribution, the deformation of a floating azopolymer film was analyzed via its wrinkling[74]. Due to the high sensitivity of this deformation measurement method, the authors were able to detect a small initial elongation perpendicular to the polarization, followed by the expected large elongation parallel to the polarization. This first deformation was then attributed to the orientation of sidechains, whilst the second, larger effect was associated with subsequent, slower backbone orientation. Interestingly, the reported timescales agreed with the well-known quick appearance of birefringence (<1s), due to reorientation of azobenzene moieties, followed by the slower polarization-parallel deformation for amorphous sidechain azopolymers (seconds to minutes)[83]. Worth to note that while covalent bonds were responsible for strong backbone attachment in the above examples, high efficiency SRGs can also be inscribed in some supramolecular azopolymers[84], where azobenzene-derived side-chains are attached via ionic[85], hydrogen[86], or halogen bonding[87]. Finally, while the directional photo-fluidization framework does not exclude such sequential orientational effects, we point out that a major difference between the explanation types lies in the photo-orientation approach having been used to predict giant photo-mechanical stresses up to 1 GPa[88]. Hence, the authors argued that the yield stress of the glassy azopolymer can be surpassed even in the absence of photo-softening effects.

Experimentally, it should be highlighted that high stresses around the order of magnitude of GigaPascal have been indirectly measured, for example via inscription of surface relief gratings in azopolymer films covered with a graphene layer used as strain gauge[89] or by grating inscriptions causing cracks within metallic coating layers[90]. Similarly, in the context of azobenzene-containing polymer brush systems grafted to substrates, surface relief grating formation was reported to induce the rupture of covalent bonds, leading to estimated stresses of same order of magnitude[91,92]. On the other hand, photo-softening in common azopolymers is a well-known effect which has been explicitly distinguished from purely thermal effects by dedicated rheological and nanoindentation studies[93–95]. Differently from heating above glass transition temperatures, significant changes in viscous behavior can occur under illumination despite only moderate changes in elastic modulus. This is reflected in fluidization-like observations when deforming azopolymers. For example, square posts deformed with circular polarization at intensities also used for directional elongation, were reported to end up in a rounded dome shape[58]. In the same work, circular polarization was also used to induce self-healing behavior, rendering the ruptured edges of a cracked polymer film completely smooth again. In another example, rounded polymer lines were transformed into rectangular cross-section lines using linearly polarized light and the soft appliance of a flat PDMS layer[96] and hierarchical structures were created by molding 100-nm features onto the photo-softened top layer of pristine micrometer structures[97]. Further examples of photo-softening effects appearing jointly with light-induced deformation are the overwriting of previous deformations in azopolymer particles embedded in an elastomeric matrix[71] and the sinking of polystyrene particles into a thin film whose surface topography is simultaneously remodeled by the light scattered from the spheres[98], although the latter example is based on an azo molecular glass compound (see below). In fact, already in the seminal study by Karageorgiev et. al., the authors noted the apparent absence of a yield stress in the illuminated azopolymer, stating that for nanoindentation "*the most impressive change upon illumination is the complete disappearance of the region with a pure elastic response – the film surface undergoes irreversible deformation by a minute force*"[47]. We note, that in recent theoretical frameworks, the incorporation of photo-softening and other illumination-induced effects into a more generalized photo-orientation model was proposed[76].

Finally, we point out that polarization-sensitive deformations like the ones described above have also been described in other azobenzene-derived systems, which do not even have to include a polymeric part. For example, azobenzene-containing molecular glasses are made from low molecular weight molecules, which despite the lack of a polymeric structure, also can undergo polarization-directed deformation of microstructures[99–101] and efficient surface relief grating formation[102–106]. Their phenomenology is to a large extent analogous, although differences in efficiency, depending on the type of illumination pattern, have been described[107] and their glass transition temperature can be readily lowered such as to e.g., produce self-collapsing gratings at room temperature[108]. To make matters more complicated, not all directional photo-deformation phenomena can be explained by simple polarization-directed elongation or compression. For example, spin or orbital momentum of light has been shown to induce features reflecting the handedness of the illumination, generally at comparingly elevated intensities. Specifically, azopolymer films can exhibit chiral features when illuminated with focused circular polarization (spin orbital momentum)[109], and similar effects have been shown for azo molecular glass micropillars[110]. Importantly, when optical vortex beams are used, large spiral patterns and other chiral reliefs can appear on azopolymer thin films, which are linked to the phase pattern of the illuminating beam and which cannot be simply explained by intensity gradients or polarization patterns[111–114].

1.2 Other Material Systems

In this section, we will briefly mention some other light-responsive polymeric systems which can incorporate azobenzene-derived molecules. Although some of them can be polarization-sensitive, they usually do not rely on the photo-orientation effect, but rather on properties stemming from the isomerization of molecules. Several of these systems will be occasionally used as comparison systems later on in the manuscript.

1.2.1 Azobenzene Containing Liquid Crystal Networks

Liquid crystal networks (LCNs) are materials where reactive mesogens, i.e. polymerizable molecules which display liquid crystalline properties in the monomer state, are cross-linked into a polymer network[115–117]. This way, the molecular orientation properties of the mesogens can be maintained in the final material, whilst the relative positions of the constituents are fixed in the solid material. For the sake of simplicity, we will not explicitly distinguish between glassy LCNs and liquid crystal elastomers, which are more flexible and less densely cross-linked materials. The literature on LCNs is abundant and specialized reviews may be consulted on this topic[118]. Here we will briefly outline a typical working mechanism of such materials, focusing on light-induced mechanical actuation, and pick some illustrative application examples. Recent reviews focusing entirely on photo-mechanical actuation of LCNs are also available[119,120].

Macroscopic actuation in LCNs can arise when the orientational order of mesogens in the polymer network is decreased. For example, rod-like mesogens in a uniform nematic state have their long axes oriented in parallel, along what is referred to as the nematic director. Decreasing the order of the mesogens will then induce anisotropic shrinking of the macroscopic material along the director axis[121], an effect that can be very large for soft elastomeric networks [122,123]. The decrease of order itself can result, for example, from a given temperature increase, which may be induced optically if absorbing components are present in the network[124–126]. Alternatively, azobenzene-derived dye molecules may be incorporated into the network, which in the rod-like *trans* state tend to align with other mesogens[127]. Besides photothermal actuation, ensuing from the absorption of the azobenzene compounds, photochemical actuation based on isomerization can then be produced in these systems (see scheme in Figure 2a)[128–130]. In this case, an order decrease can be induced by the aligned *trans* molecules being converted to the *cis* isomer form, thereby reducing the overall degree of order. Using suitable azobenzene compounds (see section 1.1.1), one may then reversibly switch between different isomer populations by employing two distinct wavelengths and hence switch between related macroscopic actuator states. We note that for some materials, and especially under *trans-cis-trans* cycling conditions, free-volume generation[131] (see section 1.2.2) and reorientation effects[132] (see section 1.1.2) can also be dominant in azobenzene containing LCNs.

A frequently used working mechanism for light-responsive LCN actuators is bending along the long axis of a strip. Such bending can for example emerge from inhomogeneous deformation due to the absorption across the film thickness (shown schematically in Figure 2b)[133]. It can also be induced without relying on absorption, for example by utilizing a bilayer system[134]. Such a system can combine an actively deforming and a passive layer[135] or two orthogonally aligned layers with directors parallel and perpendicular to the strip axis[136]. In the latter case both layers deform, but one of them will expand, while the other will shrink along the strip axis. Interestingly, bilayer systems made of two strips with an alignment mismatch of 45 degrees[137] are one of several[138–140] ways to induce curled, helicoidal deformation of LCN actuator strips. Finally, a particularly efficient way to induce regular bending is splay alignment[141–143], in which case the director anchoring is different on each side of the strip (perpendicular and planar respectively), producing an effect conceptually similar to the orthogonal bilayers.

Applications scenarios for light-controlled LCNs are very wide-ranging. They include for example gripping systems based on several assembled strips[144,145], applications in haptics[146,147], microfluidics using optically controlled valves[148] and pumping systems[149,150], bioinspired photo-controllable cilia[151,152], dynamic cell-culture substrates[153], smart textile fibers[154], or physical encryption optics[155]. Feedback-controlled “smart” systems such as self-regulated LCN irises[156], structures automatically orienting themselves towards light sources and sunlight[157,158], or grippers being able to selectively grasp objects based on their optical properties[159,160] have also been proposed. Finally, large application subfields of study are oscillating systems (see section 1.5.2) and photo-mobile ones, which have been separately reviewed[161]. The latter type, i.e. LCN-based soft robots capable of light-actuated locomotion, include directed floating[162], swimming[163,164], walking[165], crawling[166,167], as well as rolling paradigms[168–170]. In this context, we mention the recent work of Hu et al. where the deformation of floating LCN strips was used to control their capillary interactions at a liquid interface[171]. Upon actuation the strips would not only swim towards each other, but also reversibly assemble due to the liquid interface deformation profiles they create upon bending. A similar opto-capillary effect is one of the ingredients we applied to deforming azopolymer colloidal particles in article 4, to assemble particles and generate large-scale interfacial flows.

In short, the above applications benefit from the high reversibility of LCN actuation as well as its programmability via the director alignment procedures. A drawback for some applications, may be that the director alignment, once inscribed, can usually not be altered anymore. Efforts to achieve post-fabrication tunability have for example included the combination of different actuator pieces responding to separate wavelengths[151,172,173]. Similarly, reconfigurability was shown by using one wavelength to photo-chemically program and another one to photo-thermally activate versatile actuator motions[174]. Thermo-mechanical remolding of systems consisting of a thermoplastic elastomer and an LCN layer are another strategy[175]. Finally, polarization-sensitive actuation was obtained in polydomain LCNs where the domains, whose dichroic azobenzene molecules were aligned with the polarization direction, responded most to the illumination[176].

1.2.2 Other Azobenzene *trans-cis* Systems

Apart from LCNs, a wide range of other material systems can also employ the conversion between *trans* and *cis* states of azobenzene-derived molecules. We will here leave out small scale systems where such molecules are for example integrated as triggers directly into biological components (cell membranes, micelles, DNA etc.)[177], or neural channels[178], or used as surface-functionalizing monolayers, for example to modulate electrical properties of organic thin films[179]. Instead, we non-comprehensively list some macroscopic materials of interest, whose properties can be tailored using the optical *trans-cis* isomerization of azobenzene-derived molecules or *trans-cis-trans* cycling effects. These have in common that they harness other properties ensuing from isomerization than the polarization-induced reorientation of the molecules (section 1.1.2) or the related polarization-sensitive deformation (section 1.1.3).

For example, azobenzene-derived molecules can be cross-linked into or simply dispersed in amorphous polymeric networks. In the simplest scenario, a single wavelength can then be used to convert the population distribution from mostly *trans* states in thermal equilibrium to a more significant photo-stationary *cis* population. Besides heating and its material-dependent consequences, this causes both explicit mechanical effects, due to the free volume requirement of the molecular conversion[180–182], and explicit optical effects, in the form of refractive index changes (see Figure 2c for schematic summary)[183]. It is important to highlight that the latter effect is distinct from the birefringence effect introduced in section 1.1.2. In fact, whilst the birefringence effect involves a refractive index lowering only for the axis of the illumination's polarization, due to reorientation of *trans* molecules away from it, the isotropic refractive index decrease is caused by the switching of *trans* molecules into the *cis* state (with intrinsically different refractive index) as well as by the volume changes[33,34]. The three aforementioned effects, and combinations thereof, can be for example employed as a simple means of driving the isotropic volume changes in intricate two-photon printed[184,185] and other structures[186,187], to change the gas permeability of membranes[188,189] or to inscribe optical functions such as graded refractive index lenses into flat membranes[190]. Another possibility is the tuning of the Young's modulus of materials for application e.g., in elastic metamaterials[191]. This was the framework of articles 1 and 2, where DR1m was simply dispersed, post-fabrication, in 3D printed elastic waveguides. Localized illumination at a *trans-cis-trans* cycling wavelength was then used to locally change the Young's modulus of these waveguides in specific points of the sample.

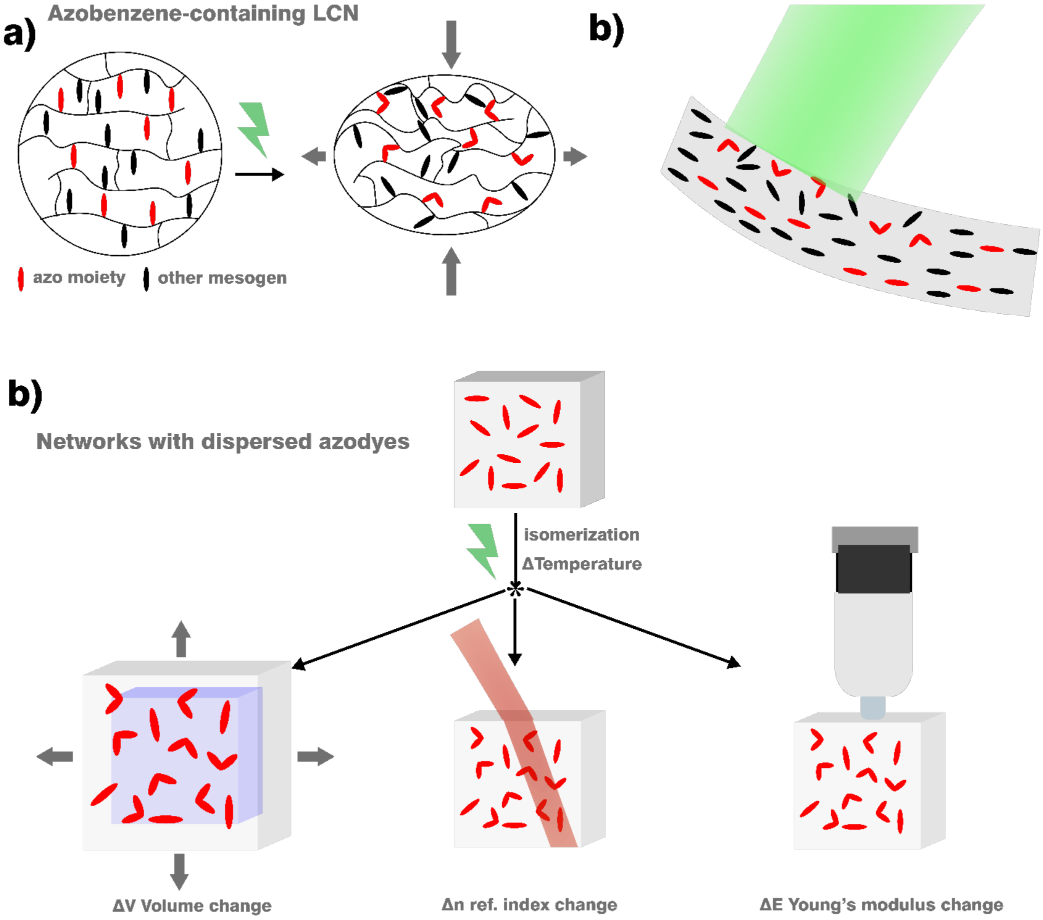

Figure 2. Scheme of other isomerization-related effects in azobenzene-containing materials. a) Scheme of a liquid crystalline polymer network (LCN) containing both azobenzene-derived dyes (red) and other mesogens (black). In real-world networks either component may be incorporated as cross-linkers (e.g., bis-acrylate) or sidechains (e.g., acrylates) and backbone compositions vary. Upon illumination the isomerization contributes to breaking the order of the LCN, leading to shrinking along the (here vertical) nematic director axis. b) Scheme showing laser beam laterally incident onto an azo-LCN strip, leading to a higher shrinking deformation on the incident side due to absorption. As a result, the shown strip is expected to bend towards the light source. c) Sketch of a generic polymeric material containing azobenzene dyes. Isomerization and photothermal heating will produce several (partly interconnected) effects, such as volume changes, refractive index changes and elastic modulus changes. Although these effects will be present in any azobenzene-containing network, they are usually dominant in networks where no strong reorientation effects are present (such as in some amorphous sidechain azopolymers) and where no pre-alignment of molecules is given (such as e.g., azo-LCNs).

A further interesting mechanism relying on *trans-cis* conversions are guest-host systems based e.g., on azobenzene molecules as guest molecules, combined with cyclodextrin (CD) hosts. These systems become switchable when the host molecule preferentially accepts the trans state of the azobenzene moiety, forming a photo-reversible bond. They can then be operated in photo-switching mode, with two wavelengths, permitting forth and back between *trans* and *cis* molecule states, and thus reversible (de)-bonding of the guest-host complex. In macroscopic systems the bond can then be used as a switchable cross-linker, permitting reversible sol-gel transitions of hydrogels[192] or actuators based on expansion-contraction behavior when the network is already cross-linked[193]. It may also be used to enable molecular recognition between gels separately incorporating the guest and the host molecules, permitting photo-switchable adhesion between them[194].

Finally, we briefly mention photo-sensitive surfactants based on azobenzene containing molecules. These exploit a difference in hydrophilicity of the two isomerization states. When e.g., brought to an interface, their isomerization can be used to reduce and increase the surface tension locally and create Marangoni flows. The systems employing such surfactants can either be operated at two wavelengths, photo-switching between different equilibrium states[195], or in continuous flow driving mode[196], and for example be used to guide particles in optically induced Marangoni traps[197,198]. An elegant way to use single-wavelength illumination to drive long-range, stationary flow phenomena based on diffusio-osmosis is detailed and used as a comparison phenomenon later (section 1.5.3).

1.3 Focal point: Reversibility

We now return to the materials employed in this work and try to outline why the question of reversibility is a matter of interest in this work. Precisely, whilst dye isomerization as well as photo-stationary changes in free-volume, refractive index or temperature are typically reversible processes, the polarization-directed deformation of amorphous azopolymers (see section 1.1.3) is not. Instead, it is a plastic deformation, where sequential deformations are cumulatively superimposed. This is apparent when considering the possibility of superimposing sinusoidal gratings created by two interfering beams, which can lead to perfect square lattices for sequential orthogonal grating superposition, beating envelope gratings for frequency mismatched constituent gratings, and blazed gratings for phase-mismatched ones[38]. In more recent years, such effects have been used to inscribe many more different gratings with varying orientations and frequencies on the same thin film, eventually enabling up to 12-fold/60-fold rotationally symmetric quasicrystal topographies for azopolymer[199]/azo molecular glass[200] thin films respectively or complex Fourier surfaces with up to 80 underlying SRGs[201]. Analogously, the deformation of pristine substrate-adhering azopolymer microstructures with distinct sequential linear polarizations has been shown to lead to complex, super-imposed, in plane expanded shapes[202,203].

1.3.1 Emergence of the Reversibility Question

Interestingly, the question of reversibility has only recently received major attention in the field of polarization sensitive photo-deformable azopolymers. We speculate that this may be linked to the deformation effect having first been evidenced on thin films and, for about a decade, mostly used to inscribe surface relief gratings (see section 1.1.3). These surface gratings can, in fact, be simply erased by heating above the glass transition temperature[39,204]. Alternatively, partial or full erasure, depending on the material employed, can be obtained by homogeneous blanket exposures with linearly (along the grating vector), circularly or unpolarized light[83,205–209]. The latter approach must have been a rather intuitive choice initially, since the same method can also be used for the erasure of optically stored local birefringence[32,210,211] and birefringent volume gratings[41,212,213] in thin films, an initial motivation for many early works. However, erasure by temperature or e.g., circular polarization will fail or be impractical in at least two situations, which were naturally concerning more recent works. First, if the azopolymer thin films are immersed in water, the films are less stable and bubble-like islands can form upon attempted wet erasure with circular polarization[214]. Whilst such an effect may be employed as optical microfabrication technique[215], it is undesirable for bioengineering applications such as topography-guided cell culture[60,216–218], which intrinsically involve aqueous immersion and where heating above the glass transition temperature would be detrimental to the biological materials. Mitigation strategies consisting for example in the encapsulation of photo-deformable azo thin films by a compliant, hydrophobic protection layer, have been only partially successful so far[219] and reconfiguration of the surface by temporarily removing the aqueous medium may be functional, but cumbersome in final applications[220]. Secondly, if the pristine structure to be deformed is a prefabricated protruding microstructure, for example a pillar, then circular polarization has been shown to lead to isotropic in plane expansion accompanied by pillar flattening[58,202]. Hence, neither temperature nor circular polarization can be used to restore such a structure's initial state, a priori making conventional erasure paradigms only applicable to initially smooth and flat films. In recent years, different strategies have therefore been proposed to remediate to this problem. They involved polymer blends[59], partially cross-linked amorphous azopolymers[62,70], tilted illumination schemes[221], or embedding of microparticles in an external elastomeric matrix[71]. The latter approach, which we may term "passive reversibility", was employed and expanded to mesoscopic soft actuators in article 3.

1.3.2 Definitions of Reversibility

Since the emergence of the question, reversibility in azopolymers has been assessed and treated in various ways. For example, in the very early days of deforming pristine microstructures, reversibility was sometimes based simply on the phenomenological aspect of roughly re-obtaining a similar shape, for example elongation of structures in the same direction after exposures with varying doses[57]. Since then, the field has evolved amongst others through the works mentioned previously. Yet, the assessment criteria and definitions still vary depending on the scope, the targeted applications and the underlying systems of different reports. Here, we will try to outline some possible criteria which may be used especially in the domain of azopolymers and aim to highlight that several of these may be appropriate depending on the context. This categorization is then be applied to characterize the works included herein in terms of extent and type of reversibility.

The simplest and strictest criterion that may be used, which we will term "perfect reversibility" would be the return to the exact initial state, or in the case of deformable structures, the return to the initial shape (Figure 3a). Whilst this is a common feature for example in LCN systems, in the context of amorphous azopolymers it may be a very stringent criterion. For example, starting from a spherical azopolymer particle, this would imply eventually returning to a spherical state. However, all the deformations induced on azopolymers by a (near) plane-wave illumination condition will lead to a compression along the optical axis (for simplicity defined as z-axis from here on), regardless of the in-plane polarization state. If the final aim is to return to a spherical state by an all-optical method without other external effects, optically induced stretching along the z-direction would be necessary, for which strategies are mentioned in outlook section 3.1.1. On the other hand, passive reversibility has been demonstrated for sparse azopolymer particles in an elastomer matrix upon exposure to unpolarized light, which the authors attributed to isotropic photo-softening[71].

In the framework of article 3, a passive reversibility system was obtained by incorporating high densities of azopolymer microparticles in an elastomeric matrix. Also in this system, previous deformations could be overwritten by subsequent illuminations, which was shown by precisely quantifying the strain in both directions tracking an imprinted array of micropillars. However, for any first deformation, a significant in plane expansion was observed, which decreased for subsequent illuminations. Eventually, the system would enter a stable switching regime, where alternating polarization states would induce transitions between different deformation states with similar in plane area. To characterize such an overwriting behavior, an alternative, weaker definition of reversibility may be induced, which we will refer to as “pre-conditioned reversibility” (Figure 3b). Conceptually, this type of reversibility would apply to all systems where reversibility can be obtained after an initial, irreversible transformation, i.e., a pre-conditioning step. Yet, depending on the application, such a system may still outperform a purely deformation superimposing one. For example, in the corresponding article a circular membrane’s bending axis could, after an initial transformation from the flat shape, be continuously rotated using the overwriting effect.

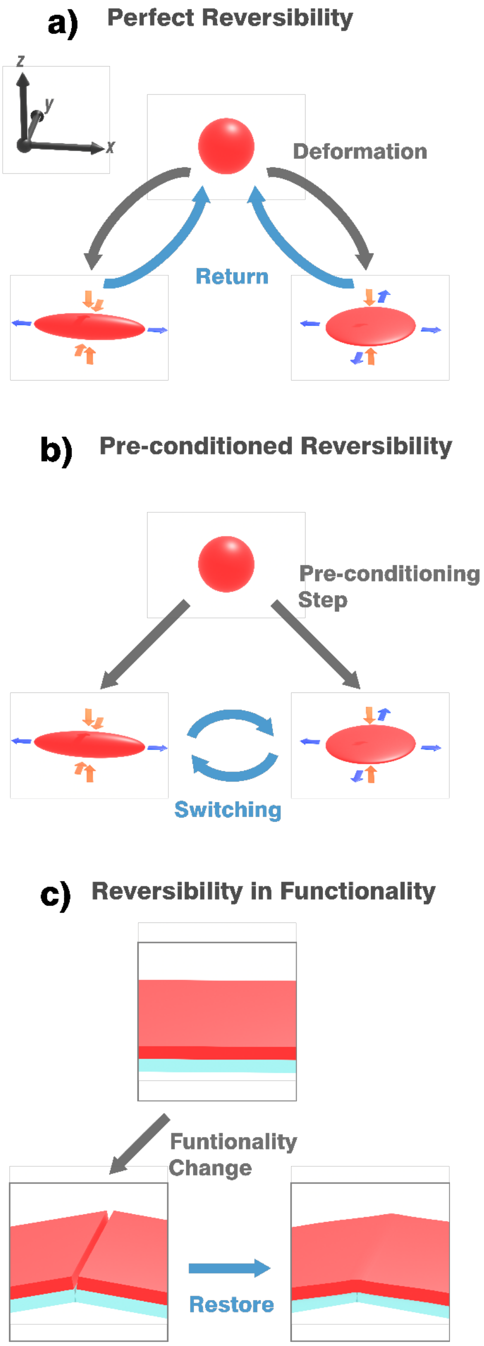

Figure 3. Proposed definitions of reversibility for azopolymers. a) Strictest reversibility criterion, implying a return to the exact initial shape. For a structure deformed by a beam incident from the *z*-axis, this implies a “de-flattening” deformation, i.e., a transformation involving stretching along the *z*-axis (see also section *3.1.1*). b) Weaker definition, allowing for an irreversible pre-conditioning step (here an initial deformation by a beam incident from the *z*-axis) after which reversible shape transitions can be achieved. c) Weakest definition which is relevant to some specific applications. While the initial shape is not restored, a higher-level functionality may be restored by illumination, which can for example be linked to an azopolymer film exhibiting a smooth continuous surface. An example of this concept was introduced by Kang et. al.[58], which developed a light-healable conductive polymer.

Still, the observed reversibility in the addressed work was not perfect, and a small in plane expansion component subsisted for each illumination. To address this partial reversibility feature, we further introduced a measure considering the degree of (pre-conditioned) reversibility. This measure was introduced for repeated illumination cycles consisting of two illumination steps with different polarization and was defined as $R = 1 - {}^{\delta A}/_{\varepsilon}$ where δA was the measured relative area expansion after two sequential illuminations (an illumination cycle) and ε was the measured relative strain along the linear polarization axis for one of the illuminations (linearly polarized illumination step). This measure has the advantage that it returns 1 for full reversibility (since $\delta A = 0$ in that case) and 0 for a purely cumulative effect, assuming an incompressible material and a small strain regime (see Appendix C, section IX). In the context of azopolymers, which tend to expand in the plane and vertically flatten under illumination, such a metric, based on the relative area expansion, may be a suitable to distinguish reversible and irreversible contributions to the overall deformation behavior. However, care should be taken that switching between states associated with orthogonal linear polarizations will produce a larger relative deformation than switching between states associated with a linear and a circular polarization, as apparent in the Appendix' small strain calculations. Hence, the same system, for a fixed amount of irreversible in plane expansion, would appear more reversible if using orthogonal linear polarizations and the exact sequence should be specified if comparing material systems.

Finally, the least stringent definition regarding the deformation of azopolymers could be "reversibility in functionality" (Figure 3c). This may account for systems where, whilst the underlying shape is not exactly restored, an ensuing property can reversibly be restored. An example for such a case is anisotropic wettability, i.e., a state where a droplet deposited on a surface will have different contact angles along different directions. Such a property can for example be induced by anisotropic deformation of a pristine array of hydrophobic azopolymer micropillars[222,223]. In such a case, isotropic wettability may be restored by rendering the underlying structures isotropic in the plane again, without necessarily reproducing their initial state exactly. Another example can be made for light-induced wrinkle erasure, demonstrated for several types of azobenzene-containing polymer films[224–226]. In these works, wrinkling was first induced by compression or expansion of a bilayer system, where there is a mechanical mismatch of a top azopolymer film with the soft, underlying substrate. The wrinkled layer was then illuminated with a suitable wavelength, which lead to modification or erasure of the wrinkles, attributed to stress release in the azopolymer film. If wrinkles of an azopolymer film were now to be induced, voluntarily or involuntarily, by a mechanical constraint and subsequently erased by illumination the film topography may still be regarded as restorable, even if the final shape of the film is compressed or stretched with respect to the initial condition. In practice, such reversibility in functionality may be the entire point of an application with azopolymers, such as e.g., in the case of self-healing wearable conductors[58]. In this work, after cracks in the conductor were induced by mechanical stresses, the aim was evidently to restore the conductivity by bridging the gap, rather than to re-obtain the initial shape.

1.3.3 Reversibility in an Application Perspective

Above, partial reversibility was mentioned. Partial reversibility can stem from irreversible phenomena and material fatigue, limiting the number of cycles over which a certain functionality can be provided. Whilst the number of actuation cycles is very high e.g., in piezo-electric actuators, where up to 10^{10} load cycles may be routinely required by engineers[227], light-responsive polymeric materials will usually show signs of fatigue earlier. In the case of LCNs, known as materials with good reversibility, high numbers of oscillating bending strip motions spanning up to 250000 cycles with little fatigue have been reported in some systems[228]. In other reports, evolution of the oscillation mode in an LCN strip, based on slight changes in the material, were reported already at much lesser numbers of about 80 cycles[229]. They were attributed to underlying irreversible effects such as dye bleaching and polymer chain friction during continuous illumination. As of today, tens of actuation cycles are also what seems feasible for systems built from amorphous polymers such as the system studied in article 3.

This comparably low number of reversible actuation cycles should hence be outweighed by some other benefits of these systems in view of concrete applications. For light-responsive polymeric systems in general, such benefits include the low cost of fabrication as well as the ease of remote control instead of building fixed circuitry. When the reversible behavior refers to polarization-sensitive actuators, the versatility of deformations that can be obtained post-fabrication is added. Such behavior may be relevant in bioengineering applications (as outlined in Outlook section 3.1.3), where the position of objects such as cells and cell spheroids on a device cannot always be controlled deterministically. Hence, being able to choose the location and type of an actuation during the use of the device may be advantageous. The obtainable number of reversible actions must then match the application objective. For example, disposable actuators grabbing, fixing and releasing objects several times can be imagined. Alternatively, this type of reversibility combined with directional deformation control may be used to reconfigure an actuator during the completion a specific task, such as wrapping objects, based on feedback loops. Finally, the creation of complex three dimensional structures via origami-inspired folding techniques[175,230] could require bending and folding of the same area several times, a task which may also benefit from intrinsic overwriting effects.

1.4 Focal point: System Scales

Next, we will focus on another factor defining the application scope of light-responsive materials: the system scale. It appears that scaling systems towards smaller or larger scales, sometimes stemming from a specific application need, other times resulting from mere curiosity, is a valuable driver of scientific discoveries in the field of photo-mechanical materials. Correspondingly, when a specific property can be transferred to a different characteristic size scale, new application scenarios can almost always be sought. Interestingly, the direction of such trends may vary between different subfields, depending on the technologies available, the scale on which initial discoveries were made, and the presence of fundamental limitations which can be hard to overcome. Here, we will first use selected examples to show how in some of the other photo-mechanical materials (see section 1.2) microscale and micro-structured systems have emerged more recently than larger bulk structures. We will then argue that in the specific case of amorphous sidechain azopolymers the inverse pathway, towards larger systems, may be a fruitful pathway at present.

1.4.1 Scaling Systems – Which way?

As introduced in section 1.2.1, Liquid Crystal Networks can be prepared by "freezing" the liquid crystalline order of reactive mesogens by polymerizing them into a cross-linked network. Widespread techniques to control the initial mesogen ordering are, amongst others, surface anchoring (for example via rubbed polymer (e.g., polyimide, polyvinyl alcohol) surfaces inducing homogeneous planar alignment of molecules in vicinity of the surface)[231,232] or mechanical stretching before the final crosslinking[233,234]. These techniques, ranging back more than three decades, can then be used in the domain of photo-mechanical actuators to fabricate strips with large-scale, well-defined alignments able to undergo significant light-induced contractions[129,235] or bending[133] as a whole. An early approach to more local control of the alignment consisted in sequential, masked photo-polymerization steps while changing the underlying global LC order[236], enabling for example films with selective regions deforming and protruding under global illumination[237]. In recent years, numerous techniques to pattern director alignments in LCNs all the way down to the microscale were then developed. These rely for example on the adaptation of polarization-guided photo-alignment approaches[238–241] to the microscale[242–245], or on microgroove topographies determining the local surface anchoring and hence the local alignment patterns[246–248], in addition to methods employing director patterning by microelectrodes[249] or by molecular self-assembly using chiral dopants[250]. The resulting LCN films with micropatterned director alignment may for example be used to induce corresponding patterns in biological cell colonies[251] and have complemented the realm of responsive LCNs with (photo-) switchable topographies that can be employed for surfaces with tunable friction and wettability, self-cleaning behavior, switchable diffractive properties or mixing control in microfluidic channels[252,253].

Another technology that has expanded photo-mechanical LCN concepts to the microscale is the increasing availability of two-photon 3D printers. Using such equipment to carve three-dimensional microstructures out of pre-aligned LCN precursors, additional application scenarios have emerged. These structures are very promising for the direct writing for photonic microstructures[254], such as tunable optical ring microresonators[255] or cavities hosting whispering gallery modes[256]. In the soft robotic domain, an intriguing example was provided by a mobile microrobot capable of directional motion by combining longitudinal expansion-contraction behavior with intricately two-photon printed anisotropic frictional feet[257]. Finally, the combination of two-photon printing with an adjustable external electric field has been recently used to precisely adjust the local LCN director alignment in 3D on the micron scale[258].

In this context, it is worth mentioning that also the photo-switchable azobenzene-cyclodextrin host-guest bond, used for switchable bulk gels (see section 1.2.2), has been increasingly used together with micropatterning techniques in recent years[259–261]. Coating prefabricated microstructures or defining micropatterned areas with switchable photo-ligands based on this interaction, cell-substrate adhesion can for example be locally and optically controlled[259,260]. A similar development was seen in photo-responsive surfactants, which instead of large scale systems only, have recently been combined with particles and structures of well-defined microporosity in several studies[262–265]. This approach allowed for the particles to become “active” flow drivers on the microscale, and hence gave control over their assembly in lattices with various spacings, clusters of defined shapes and over their expulsion from specific zones. The approach also allows for separation of particles in a microfluidic device, precisely due to differences in size, porosity and surface properties[266]. In summary, many photo-mechanical and azobenzene-derived systems have expanded their application range in recent years by the advent of new microscale fabrication techniques, allowing for the downscaling of specific functionalities, or the creation of entirely new ones.

1.4.2 Azopolymer Deformation Scales

Curiously, in amorphous sidechain azopolymers, this situation is somewhat inverted. Specifically, these deformations were directly discovered on the microscale, via use of optical interference patterns for inscription (see section 1.1.3), and have thereafter been rapidly used to develop versatile micro- and nanopatterning techniques[267]. As it turns out, scaling their ample polarization-directed deformations up to the macroscopic scale may not be straightforward. On the nano and micron scale relative elongations as high as 525 % have been produced for azopolymer particles in the range of 100-1600 nm[72]. Similarly, arrays of pre-structured micropillars of 4.5 µm with large 10 µm spacing can be fused into almost uniform lines, corresponding to at least 200% deformation[61]. On the other hand, only few reports have described (the lesser) deformation of wider structures. The exact reasons for the polarization-dependent deformation in linear azopolymers being usually restricted to the (sub-)micron scale is therefore not entirely clear to us yet and some observations are outlined below.

For example, in large azopolymer particles the achievable deformation was found to be heavily limited at particle sizes above 20 µm[203]. In particular, the largest particles in this study did not undergo homogeneous deformation anymore and the small overall deformation showed undulating features and several protrusion sites on the same particle edge. This may indicate that the distance over which the light induced stresses can smoothly propagate is limited for some of these non-crosslinked amorphous polymers. In addition, substrates can have a mechanical restraining effect, as further discussed in section 1.5.1. For example, it is evident that an azopolymer thin film deposited on a substrate cannot undergo large-scale linear stretching. On the other hand, macroscopic linear deformations for centimeter scale films floating on water surfaces have been reported in two cases[74,82]. The deformation extent in both these studies was lesser (around 40-50%), which may however be due to the polymers employed, exposure conditions, the thickness of the films and other factors. To our understanding, in none of the studies the authors have explicitly tried to maximize such deformations. Closely linked to the substrate constraints is the role of absorption throughout large structures which is discussed in more detail in the Outlook section 3.1.2 As an example, photo-deformation of 44 µm high, 17 µm wide pillar posts, used to render surfaces hydrophobic, merely produced a slightly protruding edge of the top layer (reprinted in Figure 4a)[268]. In this case, the same azopolymer is frequently used by the Lee and Park group and has often been used to inscribe large (>100%) relative deformations in microscale features[269,270]. For the large 44 µm pillars, due to absorption-induced gradients, the non-deformed part of the pillar can take the role of the constraining substrate and lead to a vertically decreasing deformation velocity profile, as highlighted by the authors. This may restrain the overall deformation and leads to downwards bending of the protruding edge. In addition, surface tension, which the authors evoke to explain the smooth top surface after deformation, may also play a role in the small (<1 µm) protruding edge eventually folding upon the pillar structure itself during prolonged exposure. We point out that in some cases, several of the mentioned effects seem to be at play, as observable in the insightful 3D SEM images shown by Jeong et. al.[271], which show the saturation of a 4.5 µm azopolymer particle deformation ending up in a spindle-like shape (Figure 4b). Here, due to the particle size and thus the considerable absorption, only the top half of the particle deforms significantly. When the wings of the deforming particle reach the substrate, an additional mechanical constraint comes into play. Finally, stress seems to build up in the particle due to the constraint, which leads to collapse into an undulating, spindle-like 3D-morphology. Similar collapse into a worm-like shape was observed by Ryabchun et. al., for particles deformed to high aspect ratios in an external matrix[71].

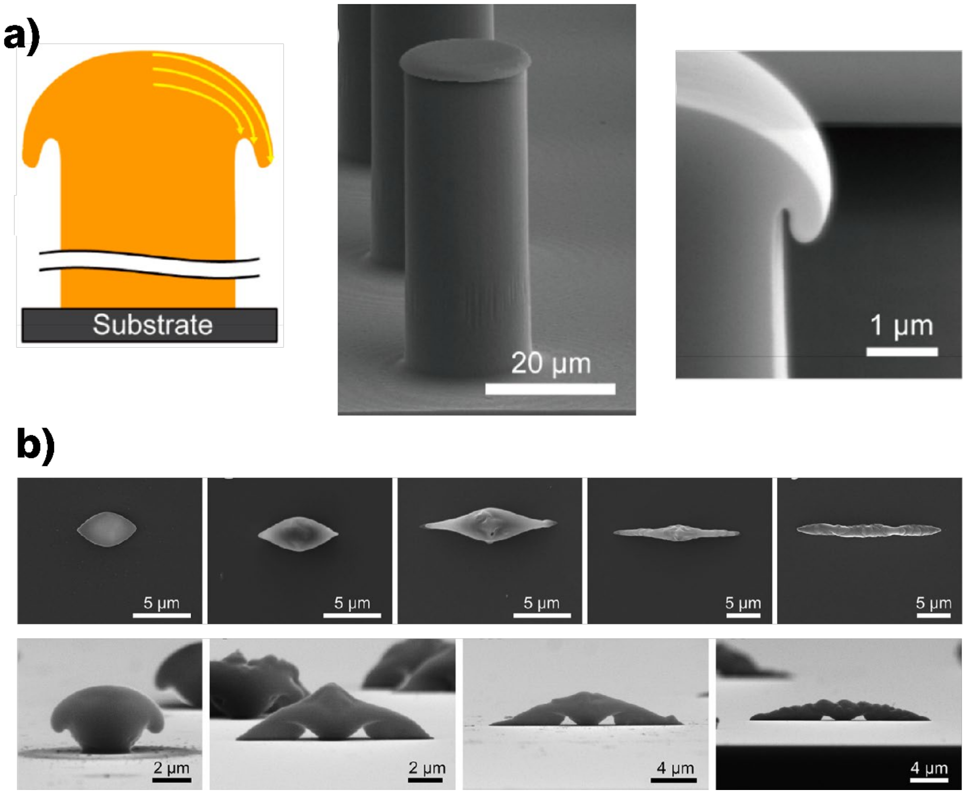

Figure 4. Literature examples showing the deformation of larger azopolymer structures. a) SEM images of 44 µm pillars deformed with circularly polarized light, generating a slightly protruding, downwards-bending edge. Adapted with permission from Choi et al.[268], Copyright © 2017, American Chemical Society. b) SEM images showing the deformation of 4.5 µm azopolymer particles on a solid substrate. Several effects limiting the overall deformation can be distinguished, notably only the top layer initially deforming (absorption), the "wings" of the structure adhering to the substrate (mechanical constraints) and the structure collapsing into a non-uniform, spindle-like shape upon prolonged exposure. Adapted from Jeong et al.[271], Copyright © 2018, with permission from Elsevier.

Furthermore, scale limitations also occur in surface relief gratings (SRGs, see section 1.1.3) on thin films. Here, the height of surface relief gratings on azopolymer films can be increased by e.g., using a larger inscription pattern period[272] and by increasing the initial film thickness, recruiting more volume for the grating generation and increasing the independence of the surface from the underlying substrate[273,274]. Yet the absolute modulations are usually limited to values below 2 µm[85,275], and the thickness-amplitude effect in these studies saturates above a certain initial film thickness value, which may again involve absorption effects. In an early study, this behavior was compared to a similar correlation of surface relief grating amplitude with dye amount, a monotonically increasing function which saturates possibly due to higher absorption at higher dye concentrations[276]. In summary, we can speculate that the expansion of amorphous linear side-chain azopolymers' directional polarization-dependent response to supra-micrometric scales is hampered in most cases by combinations of external mechanical constraints (e.g., substrates, matrices), as well as internal ones (absorption-induced gradients), surface tension, and possibly a limited propagation length for homogeneous deformation.

One option to ensure homogeneous propagation of the deformations in the polymer matrix is using a cross-linked system. In this context, it is worth to mention the work in the groups of White and Bunning, which have developed several cross-linked azo-polyimide materials[277–279] and glassy LCNs[280–283] capable of polarization-sensitive deformation when irradiated with *trans-cis-trans* cycling wavelengths. In that case, the cross-linked structure itself provides a matrix that can propagate deformations. However, the authors generally found the elongation, which they attributed to the reorientation of azo dyes, to occur perpendicular, not parallel to the polarization direction. In the context of the works mentioned in section 1.1.4, such effects would be expected to lead to smaller deformations, comparable to those induced by side-chain reorientation only in amorphous sidechain azopolymers. Indeed, in these studies the deformation was usually harnessed via the ample bending of long, thin cantilevers.

Another way of achieving polarization-sensitive deformations in larger systems may be based on using strongly deformable azopolymer microparticles, while providing a medium through which they can interact and propagate deformation over macroscopic length scales. In other words, the particles may push onto each other and create collective deformations if there is a soft material between them which allows for particle deformation, but still transmits the created forces between particles. In articles 3 and 4, two such systems are explored, which utilize an elastomeric matrix and a deformable water-air interface as propagation media respectively.

1.5 Focal point: Saturation Behavior

Closely linked to the previous focal point (system scales) is the saturation behavior of azopolymer deformations. As will be exemplified in this section, saturation of photochemically induced mechanical effects under constant illumination is a phenomenon affecting many such material systems intrinsically. Apart from temporally varying illumination schemes and systems provoking self-oscillation, systems where the illumination zone automatically gets replenished with fresh photo-chemical fuel may be designed. Conceptually, these systems may then constantly transform light into continuous directed linear motion, opening for new application scenarios.

1.5.1 Deformation Saturation – Usual case

The maximal deformations of azopolymers for differently sized pristine structures addressed in the previous focal point is usually defined upon saturation of the photo-deformation under constant illumination. In fact, on the second timescale, the polarization-dependent deformation of azopolymer microstructures usually starts with a constant deformation rate, before saturating to a maximal extent which can depend e.g., on the employed material[284,285] or particle sizes[72,286]. Mechanical constraints, which are thought to play a role in the latter case, can be nicely illustrated for example in azopolymer Janus particles (reprinted in Figure 5a)[287]. In that example, particles consisted of an azopolymer on one side and an unresponsive poly (methyl methacrylate) PMMA part on the other. Photo-deformation with polarization parallel to the separating interface was shown to be far more constrained, and to saturate to much lower aspect ratios, than deformation through orthogonally polarized illumination. Furthermore, saturation behavior also occurs for the growth of surface relief gratings using interference patterns[83,288,289] or for local protrusions created on thin films[290]. Such behavior is also intrinsically predicted by some models such as the orientation approach with an underlying finite orientation potential linked to the azobenzene moieties[80,291], while it may be attributed to external constraints (surface tension, external matrices or stamps) in some of the approaches invoking the concept of directional photo-fluidization (see section 1.1.4 for possible mechanisms)[96].

On the other hand, such saturation behavior under constant illumination is not limited to the azopolymers used in this work. It will usually also occur in azobenzene-containing LCNs (see section 1.2.1), when all effects such as e.g., photo-thermal heating, free volume generation, reorientation and the respective isomer populations have reached equilibrium (example shown in Figure 5b)[131,292,293]. If the last mechanism is the dominating one (conventional photochemical actuation), the respective *trans* and *cis* proportions will define the extent of deformation, although temporal lags in deformation and relaxation can occur in some cases due to polymer matrix effects[130]. The saturation then directly stems from a so-called photo-stationary regime where the different transition mechanisms, for example optical transition and thermal relaxation of isomers, are in equilibrium. Finally, saturation in photo-stationary regimes can also occur for Marangoni flows created by azo-surfactants adsorbed to interfaces (see section 1.2.2). When a delimited zone of the interface is illuminated in such a system, the surface tension will locally change due to the different hydrophilicity of the isomerized molecules. For thin systems and large irradiation zones, i.e., in the absence of a refueling mechanism including interface desorption and diffusive recycling via the bulk[196], transient, saturating flows have been reported also for these systems[195].

1.5.2 Oscillating Systems

One way to achieve continuous motion in saturating photo-mechanical systems, which so far has mostly been implemented in LCN systems, is the provoking of self-oscillation (example from literature shown in Figure 5c). One conceptually simple way to provoke such oscillation is the constant illumination of a uniform actuator strip from the direction of its long axis (a configuration which may be obtained after an initial bending)[139,143,294]. In this case, for a slight initial deformation one of the strip sides will be exposed to the light directly, whilst the other side gets shadowed. When the absorbing side contracts, the bending direction of the strip inverts, exposing the other side to illumination and eventually causing oscillations which have achieved frequencies up to 271 Hz[228]. Slightly modified mechanisms of self-shadowing can also drive oscillation in non-uniformly, for example splay-aligned LCNs which have a preferred bending direction[125], and chaotic oscillating systems have been proposed where the oscillation is driven by small local fluctuations in the material (temperature, photo-softening, *trans-cis* populations)[5], or by switches between different modes influenced by local material fatigue[229]. Self-shadowing oscillators can also be mechanically coupled, analogous to Huygens' synchrony observations on pendulum clocks[295], and if interfaced with an anisotropic support, have been shown to permit step-wise directional motion (reproduced in Figure 5d)[296]. Further, they do not need to have standing wave character, but may consist of propagating waves[297]. In the latter example, a slanted incidence angle onto a polymer film would hit crest-like folds in the film from one side. Inducing downwards or upwards buckling on the irradiated side, the crest could propagate away or towards the light source respectively. The created waves could even transport objects much heavier than the film uphill.

Finally, in a wider sense one may also qualify systems as oscillating, though not self-oscillating, where one of the illumination parameters is periodically modulated by the experimenter, resulting in periodic movement. Using a strip composed of two differently responding materials, the periodic modulation of the intensity of a single wavelength may then be used to induce non-reciprocal beating motions, a key for transfer of momentum at low Reynolds number and hence for the locomotion of small natural or artificial objects[298]. Along the same line, an intriguing swimming motion of LCN particles that undulate directionally under swept sinusoidal light patterns was shown[299]. Finally, in article 3 we employed a polarization sensitive membrane, illuminated from the top side, which would bend around the in-plane axis perpendicular to the polarization. By continuously rotating the polarization direction of the illumination, this bending axis and thus the membrane shape was continuously rotated.

1.5.3 Continuous Linear Motion

Apart from oscillating motion, linear directed motion may also be obtained, even from saturating photo-mechanical materials under constant illumination regimes. As we will attempt to illustrate in the following, such a mechanism relies on replacing actuated photo-chemical fuel with non-actuated one, optimally but not necessarily in a closed loop. A simple scheme to implement such a mechanism in a *trans-cis* photo-switching system is by providing illumination with different wavelengths from different incidence directions[300]. Due to shadowing, an irradiated particle will then mostly undergo *trans*-to-*cis* switching on one of its sides and *cis*-to-*trans* switching on the other. If these population switching events are for example linked to a mechanical expansion-contraction behavior (as for azo-LCNs) or to a liquefaction-crystallization behavior (as for some azobenzene crystals), a continuous directed motion can be initiated. Schematically, a piece of material will then expand/liquefy on one side upon isomerization of the molecules before rolling over to the other side where it contracts/solidifies upon inverse isomerization. When it returns to the initial position, it is thus again in an actuatable state. The process is continuous, and the constant illumination is transformed into steady linear motion. Variations of this principle may either use two wavelengths as described, or one actuating wavelength and thermal relaxation effects as its counterpart. They have thus been utilized both to induce crawling in azobenzene crystals (example scheme reproduced in Figure 5e)[300,301] and rolling of LCN strips[169,170]. Conceptually very similar is the light driven motor demonstrated by Yamada et.al. (Figure 5f), which converts light into the rotational motion of two pulleys[302]. Wrapped around the pulleys is a LCN strip that is illuminated with two different wavelengths in two different spots, driving expansion-contraction behavior locally and thus eventually linear motion of the strip around the system. Still along the same line, a swimmer based on a ring made from an initially straight LCN fiber was very recently proposed[303]. Under irradiation from one side, the pre-strained torus can undergo inversion/eversion due to one-sided photo-thermal contraction/expansion respectively, without additional costs in elastic energy. After inversion/eversion, the other side of the torus is exposed to the light, hence the previously actuated material can cool down while the initially shadowed material is heated. Further inversion/eversion will thus occur, and the torus can continuously rotate around its azimuthal long axis, propelling itself linearly in exchange with a viscous medium.

Another example for sustained motion from a refueling mechanism are the local light-driven diffusioosmotic flows discovered by Feldmann et al., which can be driven in the vicinity of a solid-liquid interface using azo-surfactant molecules[304]. For example, upon localized UV irradiation, *trans* molecules will be converted to the more hydrophilic *cis* state, initiating an osmotic outward flow along the solid surface, away from the illumination zone. As *trans* molecules diffuse from the surrounding bulk solution back into the illumination zone, fresh photo-chemical fuel is provided to drive the flow under constant illumination. In this case, a single *trans*-to-*cis* wavelength can drive the flow, as long as a sufficient number of *trans* molecules is available in the surrounding bulk solution. The authors also describe how the flow direction can be inverted. In this case, blue light, converting *cis* isomers to *trans* can drive radial inward flows, towards the illumination zone. However, since the surfactant molecules are mostly in the *trans* state in thermal equilibrium, homogeneous UV illumination is needed to ensure a sufficient *cis* isomer population in the surrounding bulk solution, which can diffuse into the illumination zone, be converted, and drive sustained flows. Doing so, the flow becomes quasi-infinite, since the same molecules that were converted from *cis* to *trans* in the illumination zone can diffuse out into the bulk, become *cis* isomers again and hence undergo closed loops. Intriguingly, diffusioosmotic flows can even be driven under completely spatially homogeneous illumination conditions, utilizing microporous particles in vicinity of the solid-liquid interface (see also section 1.4.1)[263,304]. In this case, the microporous structure can store the more hydrophobic *trans* molecules. When part of the molecules is converted to the *cis* form by blue light*,* they will be expelled from the particles and drive the outward flow along the surface. However, even if the illumination is homogeneous, the porous structure can continuously and preferentially adsorb new *trans* molecules from the bulk solution (under blue light the photo-stationary *trans* isomer population is 66%), which then are expelled again, leading to a sustained micro-pumping action. Also here, the key mechanism, is a replacement of converted molecules by non-converted ones.

Finally, in article 4, we found a similar concept to drive sustained flows from deformable azopolymer particles adsorbed to water-air interface. Although the particles themselves can only deform to a limited saturating extent, continuous directional flows emerge. As the particles propagate their respective deformation using capillary interactions, heavily deformed particles get expelled from the localized illumination zone along the deformation direction and fresh undeformed particles get pulled in along the orthogonal direction, refueling the motion under constant illumination conditions. Non saturating constant flows ensue, as long as fresh particles are available.

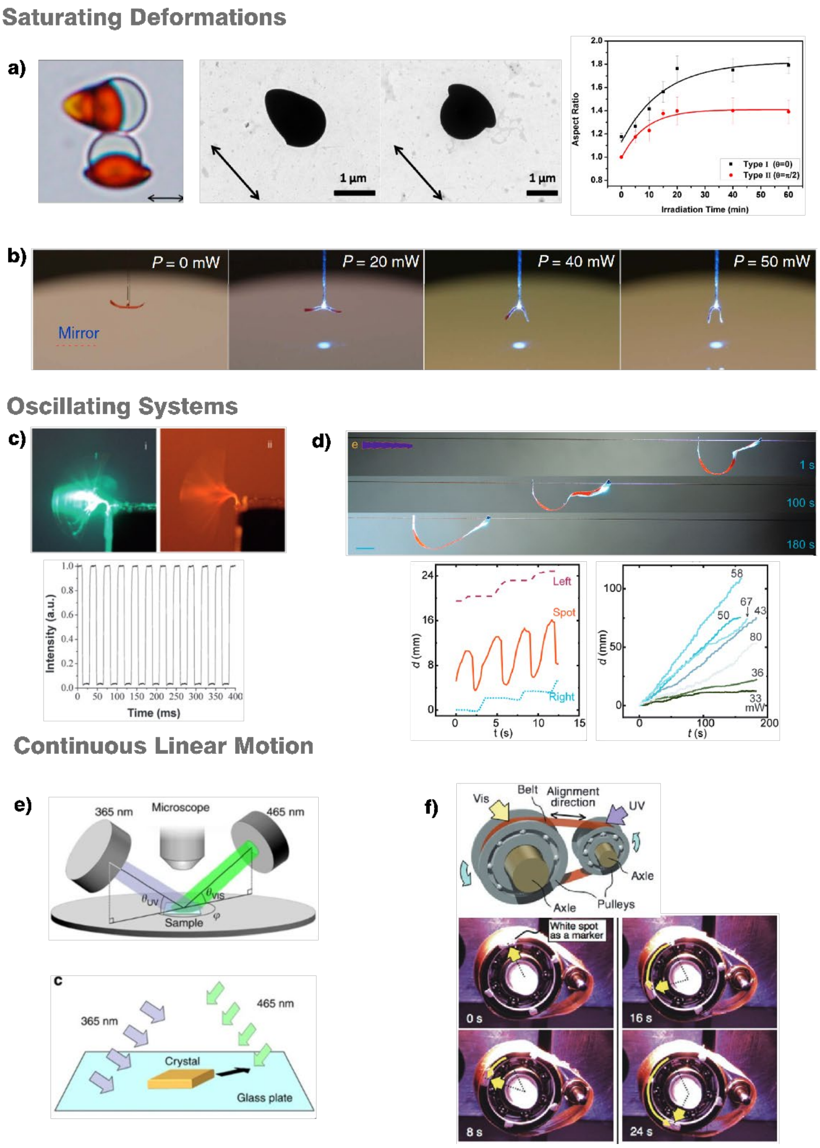

Figure 5. Examples of systems showing saturating, oscillating or linear motion under illumination. a) Janus particles containing an azopolymer hemisphere (red color) on one side. Mechanical constraints permit different degrees of deformation upon saturation, depending on the polarization with respect to the particle axis, as the authors showed in the graph reprinted to the right. Adapted with permission from Zhou et al.[287], Copyright © 2016, American Chemical Society. b) Strip bending of a grasping actuator, with equilibrium positions depending on the illumination power. Adapted from Wani et al.[159] under CC-BY 4.0, Copyright © 2017, The Authors. c) Oscillation of an azo-LCN strip under illumination from the left and optical reflection readout (bottom). Adapted from White et.al.[294], Copyright © 2008, Royal Society of Chemistry, with permission conveyed through Copyright Clearance Center, Inc. d) Stepwise motion of an azo-LCN actuator under self-shadowing conditions on a human hair. The graphs (bottom) show the displacement of the left and right feet as well as the position of the laser spot with respect to time (left) and the absolute displacement for longer time intervals (right). Adapted from Cheng et al.[296], under CC-BY 4.0, © 2021 The Authors. e) Schemes of the crawling (here by liquefaction/crystallization) of azobenzene crystals under two wavelengths incident on either side of the particle. Adapted from Uchida et al.[300], under CC-BY 4.0, Copyright © 2015, The Authors. f) Linear motor driven by an azo-LCN strip irradiated with UV and Visible light at two different positions along the strip, driving motion through continuous local contraction/expansion respectively. Reprinted with permission from Yamada et al.[302], Copyright © 2008, John Wiley and Sons.

2 Summary of Articles

Here, we briefly summarize the main results of the included articles. As outlined previously, in all of them we use materials integrating the photo-responsive properties of the azobenzene-derived molecule DR1. In the first two works, this molecule is simply dispersed in a prefabricated polymer network, whilst in the latter two we build systems from a sidechain azopolymer (pDR1-co-mma) incorporating the molecule. Hence, the first works exploit the local tuning of an isotropic photomechanical effect, whilst the latter two exploit a directional one. Special attention will be attributed to linking the works with the focal points described previously.

2.1 Articles 1 & 2: Photo-tunable Elastic Metamaterials

In these two articles, we built upon a concept previously developed in the group, which consists of including azobenzene-derived dyes in 3D-printed structures to design polymeric, tunable elastic metamaterials[191]. Upon spatially confined illumination, the elastic modulus of the illuminated part can be selectively altered resulting in targeted modifications of local resonance conditions and thus modulating the properties of the overall structure. Here, a much-simplified method for functionalizing the material was tested. Instead of dispersing the dye in the liquid monomer resin prior to printing of the structures, the dye was added *a posteriori*, through swelling of the 3D-printed structure in a solution of Disperse Red 1 methacrylate in azobenzene (see Figure 6a). Due to the underlying thermal and free volume generation effects during isomerization of the dye, also in absence of cross-linking, efficient elastic modulus changes were optically inscribed in the materials obtained by this method. Thus, the printing and the functionalization of the structures can be fully decoupled. Finally, the structures were used for two demonstration purposes.

In article 1, we tuned the discrete eigenfrequency of a tunable topological edge mode at the interface between two periodic lattices made of cylindrical high aspect ratio pillars with alternating spacing on an elastic waveguide slab. The two regions share a bandgap within which the frequency of the edge mode lies. This frequency is in principle determined by the spacing between the two neighboring regions. Instead of altering this distance, the edge mode frequency can be equivalently modulated by dynamically reducing the elastic modulus in the zone hosting the localized resonance. This is achieved via the described mechanism of local illumination of the dye-doped structure with green light. In contrast, article 2 reports on a structure whose elastic wave transmission spectrum can be locally altered. This is achieved by employing a graded pillar structure (see Figure 6b), where each pillar has different height and thus a different eigenfrequency. Each of the pillars then locally produces a bandgap centered around this frequency, contributing with a dip to the transmission spectrum. Selective illumination of a single pillar allows to tune the corresponding frequency and thus, in principle, to selectively displace the associated dip only. Although minor crosstalk occurs in the physical system, the principle allows actuation of the system in a keyboard-like manner, where the resulting frequency spectrum can be defined by the combination of individual pillars that are simultaneously irradiated, similar to pressing multiple keys on the instrument.

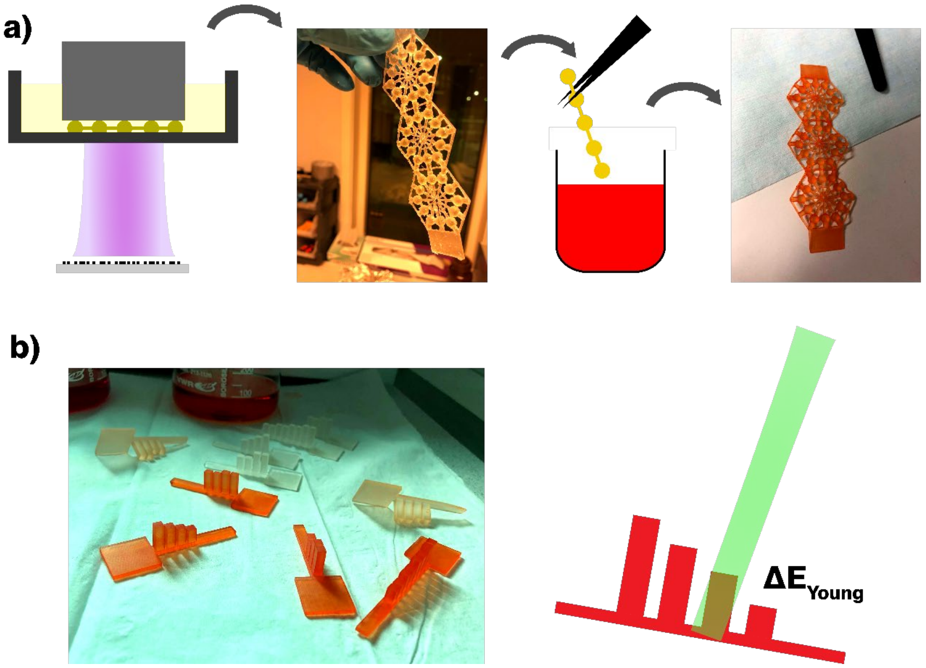

Figure 6. Fabrication method for light responsive elastic metamaterial printing. a) Scheme of elastic metamaterial production. Intricate structures can be printed using regularly optimized recipes with commercial resins on a digital light processing (DLP) printer. The printer projects a UV pattern onto the bottom of the printing vat. As the structure is raised stepwise, layer-by-layer printing is done on such a machine, the printing layer thickness being adjusted by the amounts of absorptive components in the resin and the exposure dose per layer. The transparent structure is then cleaned and immersed into an acetone bath containing DR1 dye. When homogeneously

soaked, the structure can be removed and optionally post-cured. b) Image (left) of heavily, lightly and non-functionalized graded pillar elastic waveguides. Scheme (right) of the basic working principle of such a device. As a single pillar is irradiated, the Young's modulus is locally decreased, altering the eigenfrequency of said pillar, and hence the corresponding frequency region in the transmission spectrum of the elastic waveguide.

Although simple as a concept, the method of sequential printing and functionalizing by azobenzene dyes bears several advantages. First, larger amounts of dye can be inserted into the structure. In fact, when the dye is dispersed in the liquid resin beforehand, its strong absorption competes with the photo-initiators and absorbers present in the resin. This concerns the standard UV wavelengths for digital light processing printers (DLP) as used in this work, as well as (for dyes similar to the one employed here) the fabrication by multiphoton printers (for two-photon cross-section see also section 3.1.2). Besides limiting the total amount of functional dye that may be added, the process also avoids recalibration of the printing settings for each different amount of dye. Since a DLP printer prints layer by layer, the absorption of the resin and the corresponding dose need to be tuned such as to obtain the correct polymerization layer thickness for each printing step. Finally, the a posteriori functionalization also avoids photolysis and thus destruction of the functional dyes[305], or scavenging of the free radical initiators by the latter[306]. In summary, one may use structures obtained by any previously established printing procedure with commercial resins, as long as they can non-destructively be swollen by the solvent and permit diffusion of the dye. The functional dyes can then be inserted at the wished quantity (see Figure 6).

The functional mechanism of the tunable elastic metamaterials showed good reversibility and was obtained at the macroscale. However, in contrast to the two next articles, the work did not concern any polarization-dependent deformations. Actually, the material may be regarded as belonging to the *Other Azobenzene trans-cis systems* (see section 1.2.2) and the concept may rather be a candidate for miniaturization (see section 1.4.1 *Scaling Systems – Which Way?*). Indeed, if system sizes were reduced to the (sub-) micron scale, absorption effects throughout the final structure would be less prominent, and higher dye doping as permitted by the introduced method would become possible. Miniaturized, highly responsive elastic metamaterials could then be produced without the need of altering existing fabrication recipes to incorporate the light-responsive azobenzene units.

2.2 Article 3: Polarization Sensitive Soft Robots

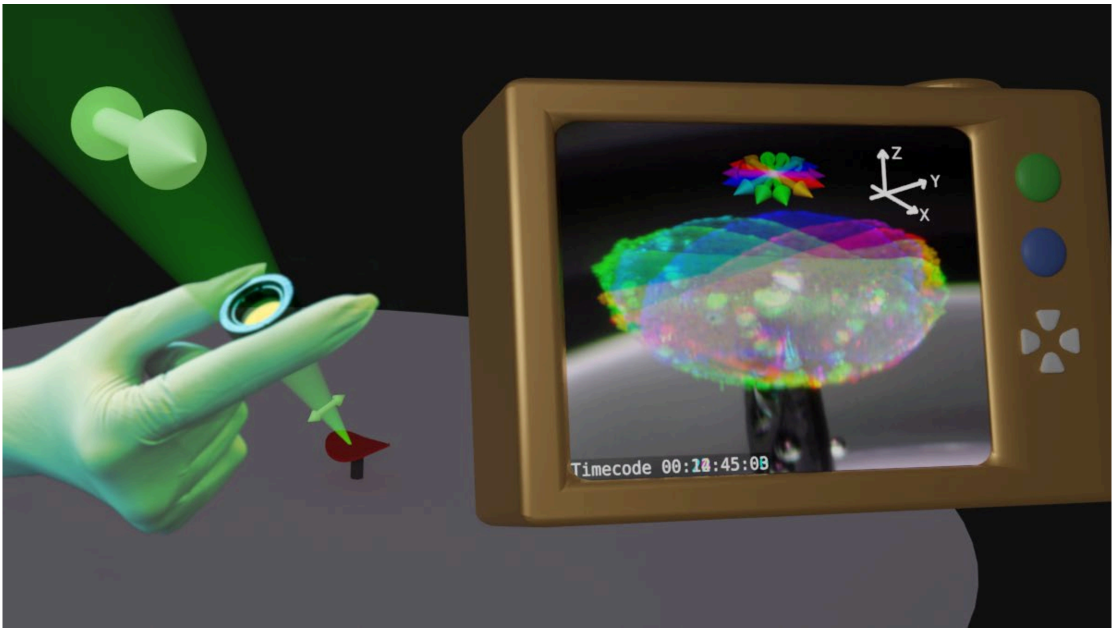

Figure 7. Polarization-controlled soft actuator (artistic representation based on article data). By rotating the polarization of the laser illumination incident from the top, a bent membrane shape can be continuously rotated. The camera display shows the superposition of colored frames along such a deformation sequence.

In article 3, we studied a photo-responsive polymer composite and employed it to develop a new type of soft, light-actuated "robotic" manipulator on the millimetric scale. The most intriguing feature of the manipulator was its ability to undergo versatile sequences of different actuation modes, which were steered by altering the polarization of the illumination used for actuation. The composite incorporated light-responsive azopolymer microparticles, which were embedded in a soft rubbery thermoplastic elastomer matrix. It was obtained by a facile method relying on the different solubility of the two components in Toluene, from which the material was cast after thorough mixing. This material was then able to harness the properties of its two constituents in interesting ways. For example, whilst the pure azopolymer is a tough, brittle material with a Young's modulus in the GigaPascal range, the composite material benefitted of the stretchability and compliance of the rubber matrix, which is four orders of magnitude softer. Yet, the overall material inherited the main functionality of the incorporated azopolymer, namely the capability of polarization-sensitive, directional deformation. Finally, the interplay between the two materials was found to be highly relevant as well. Whilst pure azopolymers will usually undergo cumulative plastic deformation (see section 1.3), a restoring effect was observed for the embedded azopolymer particles. This means that their deformations could be to a large extent, although not perfectly, overwritten, a property transferred to the overall composite and enabling the actuation sequences.

This reversibility property corresponds closely to the second definition of reversibility which was provided in section 1.3.2 (focal point: reversibility) and which was termed pre-conditioned reversibility. In fact, the deformation types that could be forced onto the composite by linearly and circularly polarized light were uniaxial stretching and isotropic in plane expansion respectively. The reversibility discovery reported in the article is that upon subsequent illumination with two different polarizations, the deformed state did not become the cumulative effect of the deformation steps, but rather resembled the one that would have been obtained by the second deformation type alone, which would also apply to further illuminations. Hence there was a switching behavior between states provoked by alternating linear-circular or orthogonal linear polarization sequences instead of deformations accumulating. For the macroscopic, free-standing actuator, this implied that deformation states could be directly overwritten, and the bending axis of a circular membrane could be for example continuously rotated.

The system is also an example of a viable strategy to scale azopolymer deformations beyond the usual (micrometric) scales (see section 1.4.2, focal point: scaling). Here, both the directional, polarization-sensitive response and the reversibility effect stemming from elastomer embedding were transferred from the individual microparticles to the overall composite. The elastomeric matrix hence provided a medium across which the individual microparticles could interact, transmit their deformation and produce macroscopic displacements. It is believed that, employing the right materials, this concept may lead to substantially more ample macroscopic, polarization-controlled deformation behavior in the future.

2.3 Article 4: Opto-capillary Directional Flows

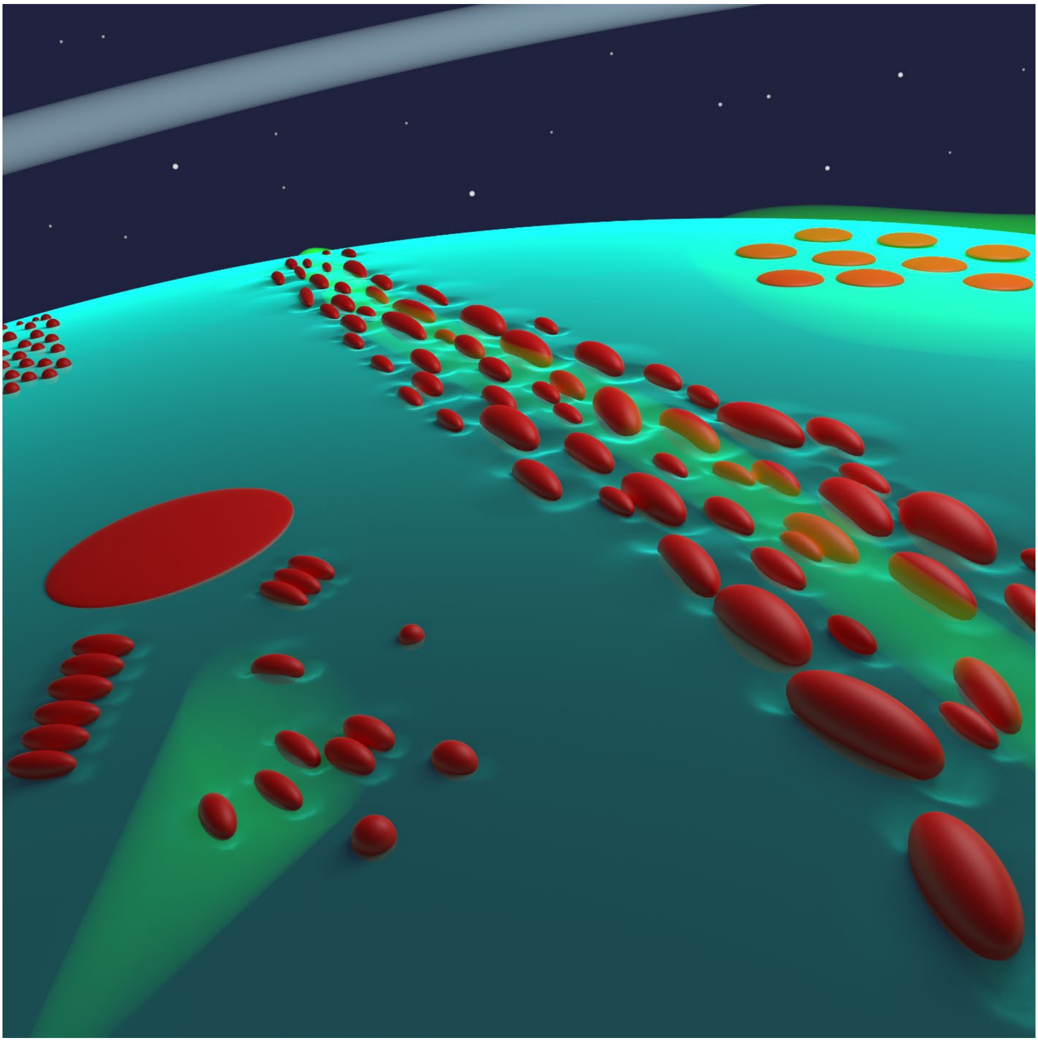

Figure 8. Light-responsive particles at air-water interfaces (artistic representation based on article concepts). Through light-induced directional deformations, particles become anisotropic and cause local interface deformations. In this new interface landscape, capillary forces arise and can be harnessed for the targeted assembly, disassembly and collective flow displacement of particles.

In article 4, we built a material system from colloidal azopolymer particles which were dispersed at an air-water interface. The particles were again fabricated using a comparably simple fabrication method, using solvent evaporation of an emulsion containing dissolved azopolymer. At the air-water interface, we discovered an intriguing effect, namely the possibility to create sustained, stationary particle flows across the interface. Interestingly, inheriting from the polarization-sensitivity of azopolymer deformation, the directionality of these flows could be precisely tuned by changing the linear polarization direction of the illumination. In fact, the flows could even be engineered such as to shift from a symmetric flow pattern to a pure shear flow, whose directionality could again be switched by flipping the linear polarization. Although the effect obviously involved the directional deformation of the particles, this was not the whole story. Another ingredient, namely capillary interaction, was necessary for this behavior to emerge. In brief, ellipsoidal particles adsorbed to liquid interfaces are known to produce anisotropic wetting, due to the combination of their shape with a constant liquid contact angle. This produces near-quadrupolar deformations in the interface around the particle. In order to minimize the overall interface deformation, and hence the total surface energy, like deformations caused by different particles should overlap. This causes strong, far-ranging capillary attraction between the particles, leading to their assembly into side-by-side or tip-to-tip structures. In the article we hence first showed the in-situ deformation of spherical particles into ellipsoidal particles by polarized light at the interface, as well as multi-particle assemblies caused by the ensuing capillary effects. Finally, sustained flows emerged when the illumination was left on, leading to the particles further deforming. As a result, the assemblies would also deform and fresh particles would be dragged into the illumination zone, being themselves inserted into the remodeling assembly. As long as fresh particles were available to integrate the assembly and push already deformed particles out of the illumination zone, the flow would go on indefinitely.

Compared to the previous article, reversibility (see section 1.3) was not the major strength of this system, due to the use of the irreversibly deforming azopolymer particles without e.g., an elastomeric matrix to mediate this property. Hence, although a stationary flow regime could be created locally by recruiting fresh particles from the surroundings of the illumination area, irreversibly deformed particles would be constantly created, and would be expected lead to the system's functionality degrading for exposures long enough to deplete the pristine, undeformed particles. Regarding the aspect of light-induced capillary assembly on the other hand, it should be mentioned that we could reverse the assembly of deformed ellipsoidal particles by subjecting them to prolonged circularly polarized illumination, creating heavily flattened shapes. In this sense, the system is reversible based on the weakest criterion provided in section 1.3.2 (focal point: reversibility), termed reversibility in functionality, albeit for one assembly-disassembly cycle only. The demonstration of this fundamental possibility may thus inspire fully reversibly assembling particle systems at interfaces, if intrinsically reversible materials (LCNs, cross-linked azopolymers, etc., see section 1.3.1) were to be used as material for the particles.

On the other hand, the system is another example of scaling polarization-sensitive deformation of azopolymers (see section 1.4.2, focal point: scaling). Differently from article 3, where an elastomeric matrix ensured the transmission of microparticle deformation into an overall deformation involving large displacements, here the interface was the transmitting medium permitting interaction. Via capillary forces, as well as the interfaces incompressible behavior, millimetric displacements of particles could be obtained from the collective deformation of many micrometric particles.

Finally, the flows are a good example of an "indefinitely photo-deforming" system (see section 1.5.3, focal point: saturation). Due to the constant recruitment of fresh particles driving the flow, the deformation saturation of the individual particles can be easily circumvented to create arbitrary overall displacements. This also ensures an ongoing conversion of light, provided by a constant stimulus, into work. Although azopolymer systems circumventing the saturation limitation are still scarce, it is believed that there are many other ways to create conceptually similar behaviors which still are to be discovered.

3 Outlook and Conclusions

3.1 Outlook

3.1.1 Reversible Degrees of Freedom

Reversibility of actuation movements becomes more interesting, the more versatile the reversible deformations are. This versatility may be measured in terms of (reversible) degrees of freedom. For the simplest type of actuator, for example a strip that can be reversibly bent along one direction, the number of reversible degrees of freedom would be one. This degree of freedom, if the actuator is light-responsive, will usually be controlled via the illumination intensity, or dose, and be reflected by the amplitude of deformation. In this thesis, the work focusing most on reversibility is article 3. There, due to the polarization-dependence, the number of reversible degrees of freedom was two. In the following, we will first try to underline this explicitly and then reflect on how a third degree of freedom may be enabled.

As described in the article summary, the composite studied in article 3 was able to reversibly switch between in plane flattened states and anisotropic states of similar overall deformation extent, induced by circularly and linearly polarized illumination respectively. The deformation extent was determined by the illumination dose, which was maintained constant for all illumination steps in an experiment. Yet, it was not only the anisotropy of the deformations that could be controlled reversibly, but also the orientation of the anisotropic deformation. This was confirmed by inducing switching behavior with orthogonal linear polarizations. In summary, for a given dose, one can then switch reversibly between distinct deformation states associated directly to a corresponding polarization state. This polarization state is controlled by two distinct waveplates (a quarter-wave plate for ellipticity and a half-wave plate for major axis orientation), which can be independently adjusted and experimentally represent the two reversible degrees of freedom. More abstractly, one can experimentally move between distinct deformation states associated to the polarization states on a Poincaré quarter-sphere, as illustrated in Figure 9a. In this example, we consider the upper hemisphere only, as no difference in deformation due the handedness of the polarization is produced. Hence, the north and south half-sphere would map the same deformation states. The same reasoning applies for linear polarizations flipped by 180 degrees with respect to each other, which produce the same deformation. Yet the deformation states, represented here as particle deformations rather than overall composite deformations, are evidently mapped onto the two-dimensional surface of the quarter-sphere, along which the system can reversibly wander.

The key to a third reversible degree of freedom is the radius of the Poincaré half-sphere mapping the deformation states. The experiments described above relied on fixing a dose, which determine this radius by fixing the extent of deformation of the attainable states, as depicted in Figure 9b. Crucially, it was not possible to return to the pristine, initial state of deformation or more generally, to a state with much lower deformation extent. Doing so would require restoring a more spherical particle shape, instead of overwriting by in plane expanded disk-like or prolate ellipsoidal shapes only. Yet, if implemented successfully, one would be able to reversibly access the full three-dimensional space spanned by all the possible quarter-spheres pictured in Fig. 9c.

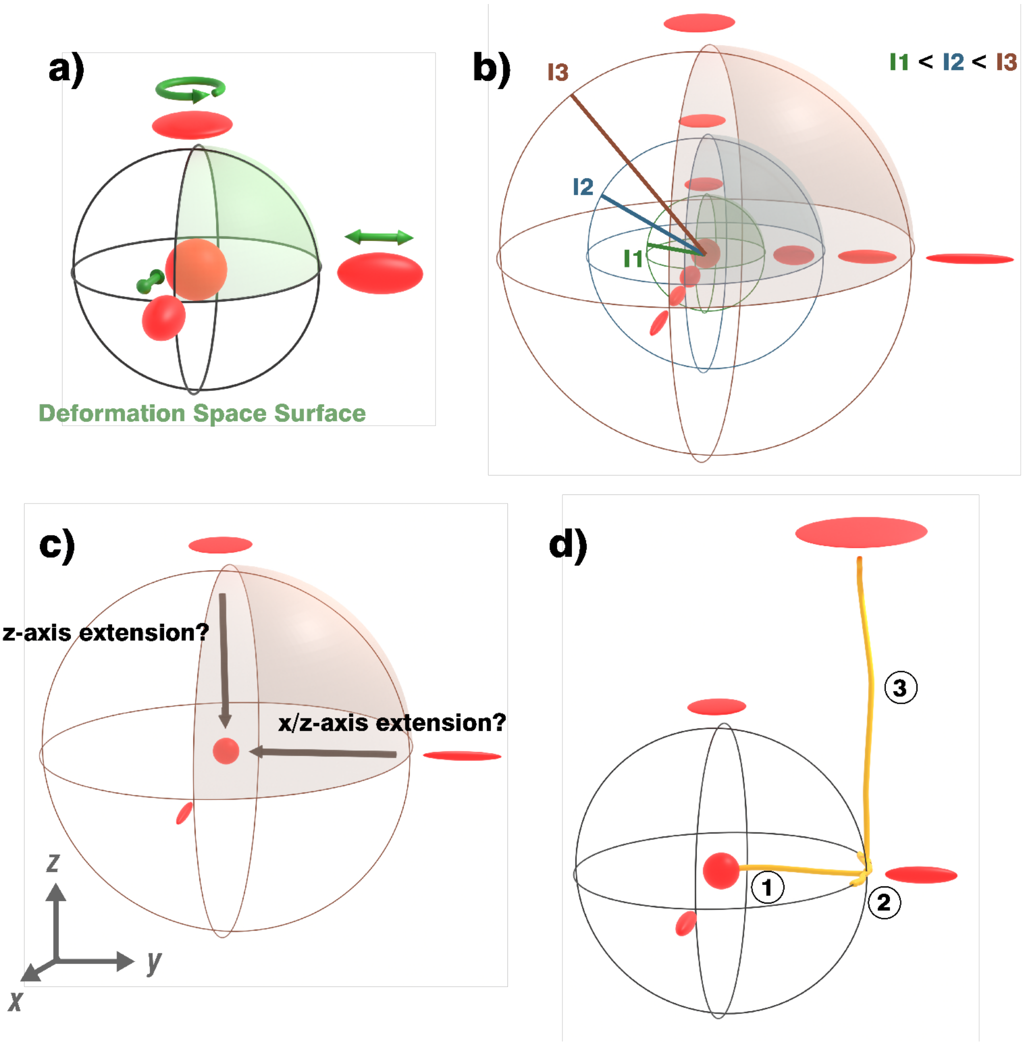

Figure 9. Deformation space mapped onto the Poincaré sphere. a) Each polarization on the quarter sphere (light green) corresponds to a deformation state of a particle. When reversibly moving between these deformed states, one is then moving on the corresponding two-dimensional deformation space surface, leading to two reversible degrees of freedom. b) For different intensities used in the deformation switching procedure, the radius of the sphere is altered, which is reflected by different extents of particle deformation. c) In order to add a third degree of freedom, i.e., to move through the entire three-dimensional deformation space given by the sum of all surfaces at fixed intensity in b, one would need a mechanism to reverse particle flattening. This implies stretching along the *z*-axis. d) Trajectory of particles in the capillary assembly part of article 4. Here the particles are first rendered anisotropic by linear polarization (step 1), which will provoke anisotropic wetting and interface-mediated particle assembly. The particle orientation is then randomly altered by diffusion and rotation during assembly (step 2), in the absence of illumination. Finally, circular polarization is used to flatten the pre-deformed particle, leading to a vertical trajectory (step 3). During this displacement, the in-plane aspect ratio is reduced, and the particles are flattened, leading to particle disassembly. However, since the flattening cannot be reversed (as discussed in c), no subsequent assembly steps are possible.

Several strategies can be imagined, to achieve the return to spherical particle states and initial composite shapes optically. A first strategy may rely on thermal effects. In fact, in a seminal work Ryabchun et. al., studied sparsely distributed particles inside an elastomeric matrix using an azopolymer with lower glass transition temperature (the temperature above which the polymer considerably softens), compared to article 3. They established that sample heating above this temperature can passively restore the initial spherical shape[71]. Elegant methods may induce this heating optically at a wavelength outside of the azopolymer absorption spectrum. Indeed, in the context of LCNs, incorporating orthogonal dyes with non-overlapping absorption spectra have been used several times and allowed for independent addressing of different functionalities[137,174]. The single-wavelength alternative to this opto-thermal approach would be direct overwriting by an azopolymer deformation that avoids compression along the z-axis. Such an inscription must necessarily result from a polarization state containing a non-zero longitudinal electrical field along z. If light is incident from this direction, a significant E_z component may be created using tight focusing by a high numerical aperture. This approach has been previously shown to for example permit inscription of vertical protrusions in azopolymer thin films[307–309]. However, since the light is focused in one spot, general actuation by this procedure would require beam scanning procedures. A different approach, using plane waves, is the use of tilted illumination. Although this concept has been explored in the context of reversible azopolymer particle deformation[221], full reversibility according to the strictest criterion of section 1.3.2 was not yet shown. A viable strategy could include a first inscription by a beam aligned with the z-axis, followed by a secondary deformation using two incoherent tilted beams. In this case, propagating electric field vectors can be used which partially point along z, since the beams come from a different incidence direction than the first illumination. The approach could also be generalized to multiple beams and may lead up to five reversible degrees of freedom if both polarization and incidence angle can be freely chosen in space. This can be visualized by considering a spherical particle that can be strained into a general ellipsoid along three principal axes. However, due to the incompressibility reported for large azopolymer deformations[72,82], the strain along the two first axes will define the strain on the third, leading only two independent strain parameters. For an arbitrary incidence angle, the resulting ellipsoid may then freely be rotated in space, leading three more angular parameters. As simple example for these additional degrees of freedom, we highlight that a prolate ellipsoid which is uniaxially stretched along the z-axis is not represented in the three-dimensional deformation space of

Figure 9a. We also note that the outlined theoretical possibility of up to five degrees of freedom comes with increased experimental complexity, and the feasibility of its implementation may depend on the system to be designed. For example, deformation of actuators in 3D can change the incidence angle of static illuminations onto the actuator surface as well as lead to shadowing effects, whose observation is mentioned in article 3 and introduced more generally in section 1.5, and which may interfere with the full control over irradiation angles.

Finally, we point out that the deformation space introduced above may also be useful in the context of the light-induced capillary assembly aspect in article 4. Here, particles were first rendered elliptical in the plane, using linearly polarized light. Rotational diffusion as well as the assembly of particles could then change the orientation of the major axis of the particle in absence of illumination. Finally, prolonged illumination with circular polarization cumulatively added a strong isotropic in-plane expansion on top of the first. The corresponding trajectory in the three-dimensional deformation space was sketched in Figure 9d. Upon reduction of the in-plane aspect ratio and further particle flattening, the capillary interactions were observed to weaken and the particles disassembled. However, subsequent cycles cannot be induced in this case, since any additional deformation will further increase the distance from the origin and particle flattening cannot be reversed, both inhibiting the return into a deformation zone suitable for capillary interactions. Particles with some built-in reversibility mechanism may achieve this, and for full reversibility paradigms restoring the initial spherical shape, any point of the deformation space would be attainable multiple times permitting full tunable (re-) assembly control.

3.1.2 Scaling in the Third Dimension

In section 1.4.2 the scaling of systems containing amorphous azopolymers towards larger length scales was discussed, especially with respect to translating polarization-dependent, light-induced directional effects in azopolymers from microstructures to the millimetric scale, and possibly beyond. The polarization-dependent actuators in article 3 and the large area interfacial flows in article 4 are examples of such a mechanical transmission, where the deformation of micron-sized particles is translated via an external medium into the overall deformation of structures which largely exceed the individual particles' size. However, in both these cases, the scaling of the material concerns mostly two dimensions, as will be briefly outlined below.

In article 3, the composite actuators hosting the deformable particles are extremely thin (10-20 µm) compared to their millimetric lateral sizes, such that the overall volume that needs to be deformed in order to actuate the structure is comparatively small and sub-millimetric (~10^{-2} mm^3). Macroscopic three-dimensional effects were displayed only by exploiting the bending of the actuator, as shown in the Figures 6 and 7 of article 3. In these experiments, by shining light onto the actuator from the top, a deformation gradient could be created across the thin side of the actuator (*z*-axis), which translated into a large movement of the strip ends along the optical *z*-axis due to the large, millimetric lateral dimension over which the bending occurred. In this way, a 2D interface deformation on the top of the actuating strip is giving rise to a large displacement along the third dimension, although the initial actuator size is micrometer-ranged along this direction. In summary, three-dimensional movement, here, is achieved through bending of a quasi-two-dimensional strip.

In the case of article 4, the system was even more evidently quasi-two-dimensional, as the particles were trapped at - and interacted via - deformation of an air-water interface, which is a flat two-dimensional surface in the undeformed state. On the interface, when deformed particles formed assemblies via capillary interactions, they were able to span structures over millimetric dimensions sideways. Similarly, collective flows were demonstrated over length scales of 100ths of microns along the interface when continuously deforming the assemblies, hence constituting mesoscopic deformation-mediated systems in the interface plane. On the other hand, even in the deformed state, the interface which mediated the forces was limited in height by the size of the largest particles, since capillary interface deformations due to anisotropic shapes are essentially a wetting phenomenon[310]. In summary, large deforming and collectively flowing assemblies could be created in an interface plane and interact in a two-dimensional mesoscopic system. The third dimension (bulk fluid) was concerned only in that high-speed flows occasionally were observed to drag liquid and out-of-focus bulk particles along, as discernible in Supplementary Movie 13 of the corresponding work.

Given these examples, one may naturally wonder if it would be possible to expand azopolymer based, micro-structured systems along all three dimensions, such as to obtain fully millimetric systems with a directional, polarization-dictated response. We will argue here that the limitation to overcome in such a case is mainly absorption from the azopolymer itself, which limits the depth over which deformations can be induced in practice. In fact, common azopolymers such as poly(Disperse Red 1)methacrylate can absorb so strongly that extinction lengths from one hundred to several hundred nanometers have been reported at the most efficient deformation inscription wavelengths of 500-530 nm[29,35,311]. One may take into account that the reorientation of dyes away from the axis of polarization (see Weigert effect in section 1.1.2) can lead to a reduction of absorptivity for the inscribing polarization and thus favors slightly deeper penetration[29]. Still, the deformation is intrinsically a surface effect when system sizes largely exceed these short extinction lengths. This is reflected by the reports on mushroom shaped structures obtained from irradiated larger structures (several microns high)[312], with sometimes just the very top sheet being deformed, as reported for example in the case of very large 14 µm diameter azo molecular glass particles[313] or even higher 44 µm azopolymer pillars[268]. Conversely, the absorption-induced deformation gradient effect has been used to selectively deform the lateral surface on only one side of either micro- or nanopillars via tilted illumination, thus easily producing bent pillars which would be difficult to obtain via conventional lithographic approaches[62–64].

One strategy for the scaling of azopolymer deformation systems along the third dimension may be to directly work with the role of linear absorption. Indeed, recent studies have focused explicitly on the role of wavelength in shaping the three-dimensional deformation profile of larger pristine azo-microstructures (Figure 10a)[314,315]. Essentially, deeper deformation profiles were systematically shown for less absorbed wavelengths in these studies, as the latter can penetrate further into and cause deformation deeper in the structure. Yet, to our knowledge, this avenue is still scarcely explored in view of finding the limiting wavelengths where one might induce deep, homogeneous deformation by high-power, weakly absorbed irradiation. If such a strategy were to be combined with the micro-structured composites developed in this thesis (article 3), large scale, bending-free three-dimensional actuation might be possible, even in millimetric bulk materials. Alternatively, the absorption of the material at conventional actuation wavelengths may be reduced by simply reducing the concentration of the absorbing dye, or in this context, of the azopolymer particles. In such a case however, the efficiency of the local photo-deformation and its transmission into the overall structure would both have to be excellent such as to obtain exploitable effects. In this context, it is worth to mention supramolecular azopolymers, where ample surface gratings (170 nm) were inscribed using a material containing a particularly low amount of 1mol% hydrogen-bonded azobenzene-derived sidechains[316].

The other possible strategy to penetrate deeper into azopolymer-based composites would be to switch over to non-linear absorption (see Figure 10b). Interestingly, the chromophore employed in this work, DR1 has a two-photon absorption cross-section as high as 110 GM[317]. Although, polarization-sensitive two-photon induced deformation of azopolymer thin films, analogous to the linear case, was demonstrated over a decade ago[318], this possibility has not been widely exploited yet. Due to the prospect of inducing deformations in very specific points along the optical axis, non-linearly induced deformations may serve the creation of more complex three-dimensional structures, for example from pristine high aspect ratio azopolymer templates. For large millimetric composites as introduced in this thesis, non-linearly induced deformation effects may be used to address regions otherwise fully shadowed by absorption. Since sufficiently strong non-linear effects are usually tightly confined in the area of the focal spot, essentially two scenarios can be thought: Either one may target deformation at precise locations deep inside the bulk material, or one may, at the cost of long exposure times, attempt homogeneous deformation of the whole material via scanning procedures. In either case, one would end up scaling the size of the largest polarization-sensitively deformable material cube along all three dimensions.

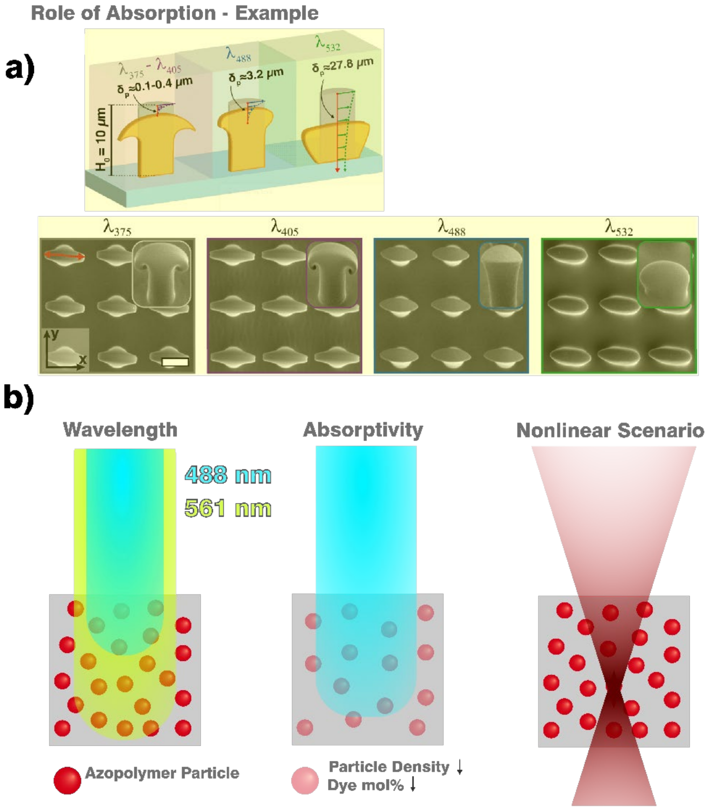

Figure 10. Scenarios to increase illumination penetration depth for azopolymer actuators. a) Scheme and SEM images from Januariyasa et al.[314], highlighting the dependence of the 3D deformation profile on the wavelength used for inscription. Adapted under CC-BY 4.0, copyright © 2023, The Authors. b) Scenarios to increase the penetration depth, for example in the case of a composite incorporating deformable azopolymer particles. From left to right: Different wavelengths (in the range suitable for DR1), absorptivity (tunable e.g., by particle density or polymeric dye content), and the possibility of inducing deformation in the tightly confined focal region using nonlinear effects.

3.1.3 Application Perspectives

In this section, we will briefly discuss the more general application perspectives of the two main findings reported in this thesis: azopolymer-driven opto-fluidics and azopolymer-based composite soft actuators. Both these systems showed high versatility since they could be steered by the polarization of the illumination. In the opto-fluidic system for example, shear flow channels were inscribed on the air-water interface by orienting the polarization diagonally with respect to the channel defined by the light intensity pattern. The resulting flows, which under appropriate conditions could even show turbulent behavior, may constitute an efficient interfacial mixing strategy. In fact, since the shear flow is driven by the diagonally oriented elongation of the particles, this flow mode intrinsically incorporates transverse components known to be crucial to efficient mixing in microfluidics[319]. It will be interesting to see if parts of the general conceptual approach can be translated to other fluidic systems, which do not rely on the experimentally and device-implementation-wise limiting use of air-water interfaces as deformation and flow propagation medium. In this regard, we highlight that light-responsive approaches in microfluidics draw strong motivation from the goal of eliminating bulky compressors used to induce flows and control pneumatic valves, which can largely exceed the size and cost of the actual microfluidic device[320]. Existing light-responsive microfluidic concepts outlined in the referenced review article encompass polymer actuators as light-controlled valves, switchable channel features or peristaltic pumps, photo-responsive surfactants for tunable flow regimes and methods to propel various types of particles and micro-vehicles, some of which were mentioned earlier in this work and some of which are reproduced in Figure 11a. On the other hand, the direct driving of fluid motion by light, such as for example in the case of the diffusioosmotic azo-surfactant flows shown in the rightmost panel (see also sections 1.4.2 and 1.5.3), seems much less explored.

Finally, also the composite soft actuators displayed intriguing polarization-guided manipulation possibilities. As briefly discussed in section 1.3, this ability to undergo complex deformations – at the cost of perfect reversibility for high numbers of cycles – may be well-suited to address challenges in bioengineering applications. In the same section, multiple studies were mentioned where cells were guided by light-controlled azopolymer topographies. While the developed material may play a role in this such endeavors due to its increased reversibility, the complex 3D deformations may open for completely different scenarios. Here, we draw inspiration from concepts such as the recently introduced “e-flower” (reprinted in Figure 11b)[321]. In this work, the authors integrated a microelectrode array on top of a humidity actuated, flower-shaped strip assembly. They demonstrated how they could then use the swelling-induced actuation of the flower to wrap the electrode array around brain spheroids and measure the latter from all sides instead of just the substrate-exposed one. Apart from the intrinsic benefit of light-actuated structures to be actuated on demand (to enable for example trap-release schemes), the polarization-guided approach can be imagined permitting additional features. As an example, objects might be displaced or rotated, using sequences of soft actuator shapes like the ones demonstrated in Article 3 (see Figure 7), potentially serving various purposes such as all-around imaging or exposure to different stimuli.

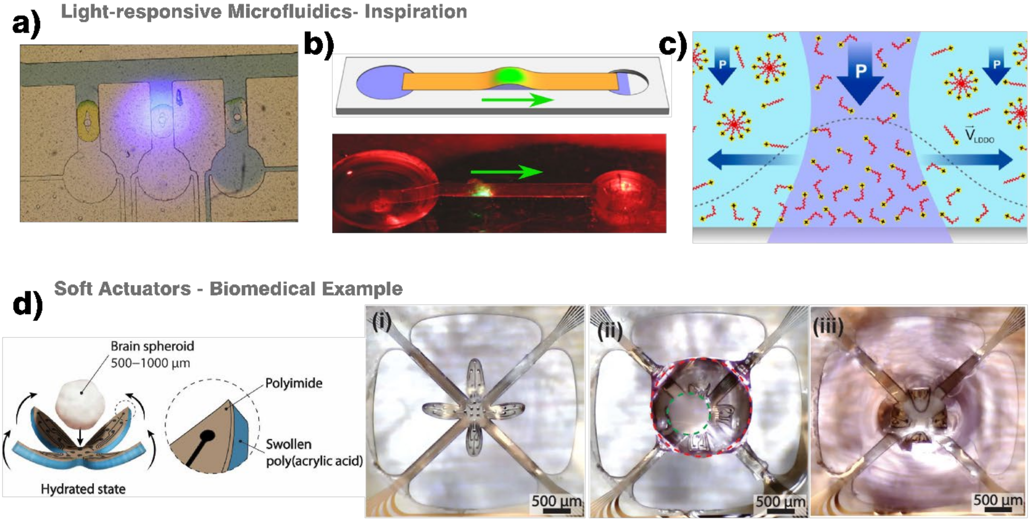

Figure 12. Inspirational Works on Light-Controlled Microfluidics and Soft Actuators. a) Light-controlled hydrogel valves in a microfluidic channel. Adapted from Sugiura et.al.[322], Copyright © 2007, with permission from Elsevier. b) Peristaltic pumping of liquids from one reservoir to another by directional displacement of a fluid-filled bump created between a solid substrate and a light-responsive azo-LCN strip. Adapted from Dradrach et.al.[150], under CC-BY 4.0, Copyright © 2023, The Author(s). c) Diffusioosmotic flows driven in the vicinity of a solid-liquid interface using azo-surfactants. Reprinted with permission from Feldmann et al.[262], Copyright © 2020, American Chemical Society. d) Schemes (left) and images in action (right) of a humidity-driven soft actuator flower integrated with a microelectrode array, wrapping and measuring a single brain spheroid. Adapted from Martinelli et. al.[321], under CC-BY-NC 4.0, Copyright © 2024 The Authors.

3.2 Conclusion

The light-responsive materials studied in this work are a fascinating phenomenon, which has not ceased to amaze the author even after four years of intense study. The possibility to simply place polymeric materials under a microscope and guide their large mechanical deformations, flows and shape-changes by – in the simplest case – just using a laser and some polarization control is a rather unique tool.

Despite its intuitive potential, and the soon 30 years since the first discoveries, the phenomenon seems not yet highly known outside its scientific field and so far, has found limited application for technological or industrial solutions. Yet, promising solutions are being developed and new application scenarios are still emerging, as highlighted by some of the exciting works referenced throughout the manuscript. In this context, the thesis followed from an attempt to extend the range of potential utility of azopolymers, inspired by the “focal point” key concepts: scaling, reversibility, and saturation. The material systems that resulted from work guided by these objectives had the following points in common: 1) They utilized facile fabrication methods, not necessitating any high-tech equipment to obtain the effect in its simplest form. 2) They led to the quantifiable emergence of new physical effects, occurring at a higher system level than the underlying deformation and molecular isomerization processes. 3) They open for the potential application of these materials, and especially the polarization-sensitive deformable amorphous azopolymers, in domains where these have not been widely used yet, such as millimetric soft actuators or free-form opto-fluidics. This underlines that, while some understanding of the general underlying phenomenology is being corroborated in the field and a large choice of materials with different optimization targets is available, the application space of these polymers is still widely untapped. We hope that some of the findings presented here will inspire further discoveries extending this application space.

V. References

(1) Kawamoto, H. The History of Liquid-Crystal Display and Its Industry. In *2012 Third IEEE HISTory of ELectro-technology CONference (HIS^{TEL}CON)*; 2012; pp 1–6. https://doi.org/10.1109/HIS^{TEL}CON.2012.6487587.

(2) Hines, L.; Petersen, K.; Lum, G. Z.; Sitti, M. Soft Actuators for Small-Scale Robotics. *Advanced Materials* **2017**, *29* (13), 1603483. https://doi.org/10.1002/adma.201603483.

(3) Pan, Y.; Yang, Z.; Li, C.; Hassan, S. U.; Shum, H. C. Plant-Inspired TransfOrigami Microfluidics. *Science Advances* **2022**, *8* (18), eabo1719. https://doi.org/10.1126/sciadv.abo1719.

(4) Wani, O. M.; Verpaalen, R.; Zeng, H.; Priimagi, A.; Schenning, A. P. H. J. An Artificial Nocturnal Flower via Humidity-Gated Photoactuation in Liquid Crystal Networks. *Advanced Materials* **2019**, *31* (2), 1805985. https://doi.org/10.1002/adma.201805985.

(5) Kumar, K.; Knie, C.; Bléger, D.; Peletier, M. A.; Friedrich, H.; Hecht, S.; Broer, D. J.; Debije, M. G.; Schenning, A. P. H. J. A Chaotic Self-Oscillating Sunlight-Driven Polymer Actuator. *Nat Commun* **2016**, *7* (1), 11975. https://doi.org/10.1038/ncomms11975.

(6) Bushuyev, O. S.; Aizawa, M.; Shishido, A.; Barrett, C. J. Shape-Shifting Azo Dye Polymers: Towards Sunlight-Driven Molecular Devices. *Macromolecular Rapid Communications* **2018**, *39* (1), 1700253. https://doi.org/10.1002/marc.201700253.

(7) Scharf, T. *Polarized Light in Liquid Crystals and Polymers*; John Wiley & Sons, 2006.

(8) Wang, X. *Azo Polymers*; Soft and Biological Matter; Springer Berlin Heidelberg: Berlin, Heidelberg, 2017. https://doi.org/10.1007/978-3-662-53424-3.

(9) Dhammika Bandara, H. M.; C. Burdette, S. Photoisomerization in Different Classes of Azobenzene. *Chemical Society Reviews* **2012**, *41* (5), 1809–1825. https://doi.org/10.1039/C1CS15179G.

(10) Bahrenburg, J.; Röttger, K.; Siewertsen, R.; Renth, F.; Temps, F. Sequential Photoisomerisation Dynamics of the Push-Pull Azobenzene Disperse Red 1. *Photochem Photobiol Sci* **2012**, *11* (7), 1210–1219. https://doi.org/10.1039/c2pp05400k.

(11) Ho, C.-H.; Yang, K.-N.; Lee, S.-N. Mechanistic Study of Trans⇆cis Isomerization of the Substituted Azobenzene Moiety Bound on a Liquid-Crystalline Polymer. *Journal of Polymer Science Part A: Polymer Chemistry* **2001**, *39* (13), 2296–2307. https://doi.org/10.1002/pola.1206.

(12) Lednev, I. K.; Ye, T.-Q.; Hester, R. E.; Moore, J. N. Femtosecond Time-Resolved UV−Visible Absorption Spectroscopy of Trans-Azobenzene in Solution. *J. Phys. Chem.* **1996**, *100* (32), 13338–13341. https://doi.org/10.1021/jp9610067.

(13) Cembran, A.; Bernardi, F.; Garavelli, M.; Gagliardi, L.; Orlandi, G. On the Mechanism of the Cis−trans Isomerization in the Lowest Electronic States of Azobenzene: S0, S1, and T1. *J. Am. Chem. Soc.* **2004**, *126* (10), 3234–3243. https://doi.org/10.1021/ja038327y.

(14) Conti, I.; Garavelli, M.; Orlandi, G. The Different Photoisomerization Efficiency of Azobenzene in the Lowest Nπ* and Ππ* Singlets: The Role of a Phantom State. *J. Am. Chem. Soc.* **2008**, *130* (15), 5216–5230. https://doi.org/10.1021/ja710275e.

(15) Paik, C. S.; Morawetz, H. Photochemical and Thermal Isomerization of Azoaromatic Residues in the Side Chains and the Backbone of Polymers in Bulk. *Macromolecules* **1972**, *5* (2), 171–177. https://doi.org/10.1021/ma60026a015.

(16) Barrett, C.; Natansohn, A.; Rochon, P. Cis-Trans Thermal Isomerization Rates of Bound and Doped Azobenzenes in a Series of Polymers. *Chem. Mater.* **1995**, *7* (5), 899–903. https://doi.org/10.1021/cm00053a014.

(17) Vetráková, Ľ.; Ladányi, V.; Al Anshori, J.; Dvořák, P.; Wirz, J.; Heger, D. The Absorption Spectrum of *Cis* -Azobenzene. *Photochem. Photobiol. Sci.* **2017**, *16* (12), 1749–1756. https://doi.org/10.1039/C7PP00314E.

(18) Mahimwalla, Z.; Yager, K. G.; Mamiya, J.; Shishido, A.; Priimagi, A.; Barrett, C. J. Azobenzene Photomechanics: Prospects and Potential Applications. *Polym. Bull.* **2012**, *69* (8), 967–1006. https://doi.org/10.1007/s00289-012-0792-0.

(19) A. Beharry, A.; Andrew Woolley, G. Azobenzene Photoswitches for Biomolecules. *Chemical Society Reviews* **2011**, *40* (8), 4422–4437. https://doi.org/10.1039/C1CS15023E.

(20) Loucif-Saibi, R.; Nakatani, K.; Delaire, J. A.; Dumont, M.; Sekkat, Z. Photoisomerization and Second Harmonic Generation in Disperse Red One-Doped and -Functionalized Poly(Methyl Methacrylate) Films. *Chem. Mater.* **1993**, *5* (2), 229–236. https://doi.org/10.1021/cm00026a014.

(21) Wildes, P. D.; Pacifici, J. G.; Irick, G.; Whitten, D. G. Solvent and Substituent Effects on Thermal Isomerization of Substituted Azobenzenes-Flash Spectroscopic Study. *Journal of the American Chemical Society* **1971**, *93* (8), 2004.

(22) Natansohn, A.; Rochon, P. Photoinduced Motions in Azo-Containing Polymers. *Chem. Rev.* **2002**, *102* (11), 4139–4176. https://doi.org/10.1021/cr970155y.

(23) Natansohn, A.; Rochon, P. 13 - Photoinduced Motions in Azobenzene-Based Polymers. In *Photoreactive Organic Thin Films*; Sekkat, Z., Knoll, W., Eds.; Academic Press: San Diego, 2002; pp 399–427. https://doi.org/10.1016/B978-012635490-4/50014-7.

(24) Todorov, T.; Nikolova, L.; Tomova, N. Polarization Holography. 1: A New High-Efficiency Organic Material with Reversible Photoinduced Birefringence. *Appl. Opt., AO* **1984**, *23* (23), 4309–4312. https://doi.org/10.1364/AO.23.004309.

(25) Anderle, K.; Birenheide, R.; Werner, M. J. A.; Wendorff, J. H. Molecular Addressing? Studies on Light-Induced Reorientation in Liquid-Crystalline Side Chain Polymers. *Liquid Crystals* **1991**, *9* (5), 691–699. https://doi.org/10.1080/02678299108030382.

(26) Sekkat, Z.; Dumont, M. Photoinduced Orientation of Azo Dyes in Polymeric Films. Characterization of Molecular Angular Mobility. *Synthetic Metals* **1993**, *54* (1–3), 373–381. https://doi.org/10.1016/0379-6779(93)91083-E.

(27) Weigert, F. Uber Einen Neuen Effekt Der Strahlung in Lichtempfindlichen Schichten. *Verh. Dtsch. Phys. Ges.* **1919**, *21*, 479–491.

(28) Weigert, F. Photodichroismus und Photoanisotropie. I: Grunderscheinungen und Definitionen. *Zeitschrift für Physikalische Chemie* **1929**, *3B* (1), 377–388. https://doi.org/10.1515/zpch-1929-0328.

(29) Rochon, P.; Bissonnette, D.; Natansohn, A.; Xie, S. Azo Polymers for Reversible Optical Storage. III. Effect of Film Thickness on Net Phase Retardation and Writing Speed. *Appl. Opt., AO* **1993**, *32* (35), 7277–7280. https://doi.org/10.1364/AO.32.007277.

(30) Wu, Y.; Ikeda, T.; Zhang, Q. Three-Dimensional Manipulation of an Azo Polymer Liquid Crystal with Unpolarized Light. *Advanced Materials* **1999**, *11* (4), 300–302. https://doi.org/10.1002/(SICI)1521-4095(199903)11:4<300::AID-ADMA300>3.0.CO;2-Y.

(31) Macdonald, R.; Schulz, R.; Schreiber, C. Investigation of Polarization-Induced Orientational Order and Surface Gratings in Liquid Crystalline AZO-Polymers. *Molecular Crystals and Liquid Crystals Science and Technology. Section A. Molecular Crystals and Liquid Crystals* **2001**, *359* (1), 1–16. https://doi.org/10.1080/10587250108035563.

(32) Rochon, P.; Gosselin, J.; Natansohn, A.; Xie, S. Optically Induced and Erased Birefringence and Dichroism in Azoaromatic Polymers. *Applied Physics Letters* **1992**, *60* (1), 4–5. https://doi.org/10.1063/1.107369.

(33) Dumont, M. L.; Hosotte, S.; Froc, G.; Sekkat, Z. Orientational Manipulation of Chromophores through Photoisomerization; Lessard, R. A., Ed.; Quebec City, Canada, 1994; p 2. https://doi.org/10.1117/12.166297.

(34) Shishido, A.; Tsutsumi, O.; Kanazawa, A.; Shiono, T.; Ikeda, T.; Tamai, N. Rapid Optical Switching by Means of Photoinduced Change in Refractive Index of Azobenzene Liquid Crystals Detected by Reflection-Mode Analysis. *J. Am. Chem. Soc.* **1997**, *119* (33), 7791–7796. https://doi.org/10.1021/ja9706312.

(35) Rodriguez, V.; Adamietz, F.; Sanguinet, L.; Buffeteau, T.; Sourisseau, C. Quantitative Determination of the Polar Order Induced under High Electric Field in Amorphous PDR1M Azobenzene Polymer Films. *J. Phys. Chem. B* **2003**, *107* (36), 9736–9743. https://doi.org/10.1021/jp035230p.

(36) Natansohn, A.; Rochon, P. Reversible Optical Storage in Azo Polymers. In *Progress in Pacific Polymer Science 3*; Ghiggino, K. P., Ed.; Springer Berlin Heidelberg: Berlin, Heidelberg, 1994; pp 295–305. https://doi.org/10.1007/978-3-642-78759-1_25.

(37) Marcucci, N.; Giordano, M. C.; Zambito, G.; Troia, A.; Mongeot, F. B. de; Descrovi, E. Spectral Tuning of Bloch Surface Wave Resonances by Light-Controlled Optical Anisotropy. *Nanophotonics* **2023**, *12* (6), 1091–1104. https://doi.org/10.1515/nanoph-2022-0609.

(38) Viswanathan, N. K.; Kim, D. Y.; Bian, S.; Williams, J.; Liu, W.; Li, L.; Samuelson, L.; Kumar, J.; Tripathy, S. K. Surface Relief Structures on Azo Polymer Films. *J. Mater. Chem.* **1999**, *9* (9), 1941–1955. https://doi.org/10.1039/a902424g.

(39) Rochon, P.; Batalla, E.; Natansohn, A. Optically Induced Surface Gratings on Azoaromatic Polymer Films. *Applied Physics Letters* **1995**, *66* (2), 136–138. https://doi.org/10.1063/1.113541.

(40) Kim, D. Y.; Tripathy, S. K.; Li, L.; Kumar, J. Laser-induced Holographic Surface Relief Gratings on Nonlinear Optical Polymer Films. *Applied Physics Letters* **1995**, *66* (10), 1166–1168. https://doi.org/10.1063/1.113845.

(41) Barrett, C. J.; Natansohn, A. L.; Rochon, P. L. Mechanism of Optically Inscribed High-Efficiency Diffraction Gratings in Azo Polymer Films. *J. Phys. Chem.* **1996**, *100* (21), 8836–8842. https://doi.org/10.1021/jp953300p.

(42) Naydenova, I.; Nikolova, L.; Todorov, T.; Holme, N. C. R.; Ramanujam, P. S.; Hvilsted, S. Diffraction from Polarization Holographic Gratings with Surface Relief in Side-Chain Azobenzene Polyesters. *J. Opt. Soc. Am. B, JOSAB* **1998**, *15* (4), 1257–1265. https://doi.org/10.1364/JOSAB.15.001257.

(43) Pedersen, T. G.; Johansen, P. M.; Holme, N. C. R.; Ramanujam, P. S.; Hvilsted, S. Mean-Field Theory of Photoinduced Formation of Surface Reliefs in Side-Chain Azobenzene Polymers. *Phys. Rev. Lett.* **1998**, *80* (1), 89–92. https://doi.org/10.1103/PhysRevLett.80.89.

(44) Labarthet, F. L.; Buffeteau, T.; Sourisseau, C. Time Dependent Analysis of the Formation of a Half-Period Surface Relief Grating on Amorphous Azopolymer Films. *Journal of Applied Physics* **2001**, *90* (7), 3149–3158. https://doi.org/10.1063/1.1399025.

(45) Yadavalli, N. S.; Santer, S. In-Situ Atomic Force Microscopy Study of the Mechanism of Surface Relief Grating Formation in Photosensitive Polymer Films. *Journal of Applied Physics* **2013**, *113* (22), 224304. https://doi.org/10.1063/1.4809640.

(46) Jelken, J.; Henkel, C.; Santer, S. Formation of Half-Period Surface Relief Gratings in Azobenzene Containing Polymer Films. *Appl. Phys. B* **2020**, *126* (9), 149. https://doi.org/10.1007/s00340-020-07500-w.

(47) Karageorgiev, P.; Neher, D.; Schulz, B.; Stiller, B.; Pietsch, U.; Giersig, M.; Brehmer, L. From Anisotropic Photo-Fluidity towards Nanomanipulation in the Optical near-Field. *Nature Mater* **2005**, *4* (9), 699–703. https://doi.org/10.1038/nmat1459.

(48) Ikawa, T.; Mitsuoka, T.; Hasegawa, M.; Tsuchimori, M.; Watanabe, O.; Kawata, Y.; Egami, C.; Sugihara, O.; Okamoto, N. Optical Near Field Induced Change in Viscoelasticity on an Azobenzene-Containing Polymer Surface. *J. Phys. Chem. B* **2000**, *104* (39), 9055–9058. https://doi.org/10.1021/jp001172l.

(49) Kawata, Y.; Murakami, M.; Egami, C.; Sugihara, O.; Okamoto, N.; Tsuchimori, M.; Watanabe, O.; Nakamura, O. Nonoptically Probing Near-Field Microscopy for the Observation of Biological Living Specimens. *Appl. Phys. Lett.* **2001**, *78* (15), 2247–2249. https://doi.org/10.1063/1.1350965.

(50) Fukuda, T.; Sumaru, K.; Kimura, T.; Matsuda, H.; Narita, Y.; Inoue, T.; Sato, F. Observation of Optical Near-Field as Photo-Induced Surface Relief Formation. *Jpn. J. Appl. Phys.* **2001**, *40* (8B), L900. https://doi.org/10.1143/JJAP.40.L900.

(51) Derouard, M.; Hazart, J.; Lérondel, G.; Bachelot, R.; Adam, P.-M.; Royer, P. Polarization-Sensitive Printing of Surface Plasmon Interferences. *Opt. Express, OE* **2007**, *15* (7), 4238–4246. https://doi.org/10.1364/OE.15.004238.

(52) Hubert, C.; Rumyantseva, A.; Lerondel, G.; Grand, J.; Kostcheev, S.; Billot, L.; Vial, A.; Bachelot, R.; Royer, P.; Chang, S.; Gray, S. K.; Wiederrecht, G. P.; Schatz, G. C. Near-Field

Photochemical Imaging of Noble Metal Nanostructures. *Nano Lett.* **2005**, *5* (4), 615–619. https://doi.org/10.1021/nl047956i.

(53) Li, Y.; He, Y.; Tong, X.; Wang, X. Photoinduced Deformation of Amphiphilic Azo Polymer Colloidal Spheres. *J. Am. Chem. Soc.* **2005**, *127* (8), 2402–2403. https://doi.org/10.1021/ja0424981.

(54) Liu, B.; He, Y.; Fan, P.; Wang, X. Azo Polymer Microspherical Cap Array: Soft-Lithographic Fabrication and Photoinduced Shape Deformation Behavior. *Langmuir* **2007**, *23* (22), 11266–11272. https://doi.org/10.1021/la7016402.

(55) Huang, J.; Wu, S.; Beckemper, S.; Gillner, A.; Zhang, Q.; Wang, K. All-Optical Fabrication of Ellipsoidal Caps on Azobenzene Functional Polymers. *Opt. Lett., OL* **2010**, *35* (16), 2711–2713. https://doi.org/10.1364/OL.35.002711.

(56) Lee, S.; Shin, J.; Lee, Y.-H.; Fan, S.; Park, J.-K. Directional Photofluidization Lithography for Nanoarchitectures with Controlled Shapes and Sizes. *Nano Lett.* **2010**, *10* (1), 296–304. https://doi.org/10.1021/nl903570c.

(57) Gritsai, Y.; Goldenberg, L. M.; Stumpe, J. Efficient Single-Beam Light Manipulation of 3D Microstructures in Azobenzene-Containing Materials. *Opt. Express, OE* **2011**, *19* (19), 18687–18695. https://doi.org/10.1364/OE.19.018687.

(58) Kang, H. S.; Kim, H.-T.; Park, J.-K.; Lee, S. Light-Powered Healing of a Wearable Electrical Conductor. *Advanced Functional Materials* **2014**, *24* (46), 7273–7283. https://doi.org/10.1002/adfm.201401666.

(59) Pirani, F.; Angelini, A.; Frascella, F.; Rizzo, R.; Ricciardi, S.; Descrovi, E. Light-Driven Reversible Shaping of Individual Azopolymeric Micro-Pillars. *Scientific Reports* **2016**, *6* (1), 31702. https://doi.org/10.1038/srep31702.

(60) Puliafito, A.; Ricciardi, S.; Pirani, F.; Čermochová, V.; Boarino, L.; De Leo, N.; Primo, L.; Descrovi, E. Driving Cells with Light-Controlled Topographies. *Adv. Sci.* **2019**, *6* (14), 1801826. https://doi.org/10.1002/advs.201801826.

(61) Salvatore, M.; Borbone, F.; Reda, F.; Maddalena, P.; Oscurato, S. L. Programmable Surface Anisotropy from Polarization-Driven Azopolymer Reconfiguration. *J. Phys. Photonics* **2021**, *3* (3), 034013. https://doi.org/10.1088/2515-7647/abf944.

(62) Yin, X.; Dong, H.; Wang, S.; Liang, Y.; Zhang, W.; Gao, N.; Liu, X.; Wang, X.; Li, G. Coupling of Photoinduced Mass Immigration with Polymer Networks to Produce Nanostructured Materials Capable of Reversibly Creating Arbitrary Deformations. *Macromolecular Chemistry and Physics* **2018**, *219* (14), 1800113. https://doi.org/10.1002/macp.201800113.

(63) Jo, W.; Choi, J.; Kang, H. S.; Kim, M.; Baik, S.; Lee, B. J.; Pang, C.; Kim, H.-T. Programmable Fabrication of Submicrometer Bent Pillar Structures Enabled by a Photoreconfigurable Azopolymer. *ACS Appl. Mater. Interfaces* **2020**, *12* (4), 5058–5064. https://doi.org/10.1021/acsami.9b19420.

(64) Ho, J.-H.; Chen, Y.-F.; Chang, M.-H.; Shih, T.-W.; Liu, C.-T.; He, H.-C.; Lin, Y.-L.; Lee, L.-R.; Tseng, Y.-H.; Sugiyama, T.; Chen, J.-T. Stretching and Bending of Azopolymer Nanorod Arrays via Laser-Induced Photo-Fluidization. *ACS Applied Polymer Materials* **2022**. https://doi.org/10.1021/acsapm.2c00553.

(65) Kang, H. S.; Lee, S.; Choi, J.; Lee, H.; Park, J.-K.; Kim, H.-T. Light-Induced Surface Patterning of Silica. *ACS Nano* **2015**, *9* (10), 9837–9848. https://doi.org/10.1021/acsnano.5b03946.

(66) Pirani, F.; Angelini, A.; Frascella, F.; Descrovi, E. Reversible Shaping of Microwells by Polarized Light Irradiation. *International Journal of Polymer Science* **2017**, *2017*, e6812619. https://doi.org/10.1155/2017/6812619.

(67) Wang, S.; Dong, H.; Sun, F.; Zhang, W.; Liang, Y.; Tian, L.; Wang, P.; Yin, X.; Li, G. Large-Area Fabrication of Highly Tunable Hybrid Plasmonic–Photonic Structures Based on Colloidal Lithography and a Photoreconfigurable Polymer. *Advanced Optical Materials* **2019**, *7* (19), 1900483. https://doi.org/10.1002/adom.201900483.

(68) Wang, W.; Du, C.; Wang, X.; He, X.; Lin, J.; Li, L.; Lin, S. Directional Photomanipulation of Breath Figure Arrays. *Angew. Chem.* **2014**, *126* (45), 12312–12315. https://doi.org/10.1002/ange.201407230.

(69) Wang, W.; Yao, Y.; Luo, T.; Chen, L.; Lin, J.; Li, L.; Lin, S. Deterministic Reshaping of Breath Figure Arrays by Directional Photomanipulation. *ACS Appl. Mater. Interfaces* **2017**, *9* (4), 4223–4230. https://doi.org/10.1021/acsami.6b14024.

(70) Wang, W.; Shen, D.; Li, X.; Yao, Y.; Lin, J.; Wang, A.; Yu, J.; Wang, Z. L.; Hong, S. W.; Lin, Z.; Lin, S. Light-Driven Shape-Memory Porous Films with Precisely Controlled Dimensions. *Angewandte Chemie* **2018**, *130* (8), 2161–2165. https://doi.org/10.1002/ange.201712100.

(71) Ryabchun, A.; Bobrovsky, A. Photocontrollable Deformations of Polymer Particles in Elastic Matrix. *Advanced Optical Materials* **2019**, *7* (24), 1901486. https://doi.org/10.1002/adom.201901486.

(72) Loebner, S.; Lomadze, N.; Kopyshev, A.; Koch, M.; Guskova, O.; Saphiannikova, M.; Santer, S. Light-Induced Deformation of Azobenzene-Containing Colloidal Spheres: Calculation and Measurement of Opto-Mechanical Stresses. *J. Phys. Chem. B* **2018**, *122* (6), 2001–2009. https://doi.org/10.1021/acs.jpcb.7b11644.

(73) Liu, E.; Li, L.; Wang, J.; Han, X.; Li, X.; Xu, F.; Cao, Y.; Lu, C. Light-Induced In Situ Dynamic Ordered Wrinkling with Arbitrarily Tailorable Wrinkling Orientation for Photoresponsive Soft Photonics. *Advanced Functional Materials* **2023**, *33* (24), 2300182. https://doi.org/10.1002/adfm.202300182.

(74) Liu, E.; Zhang, X.; Ji, H.; Li, Q.; Li, L.; Wang, J.; Han, X.; Yu, S.; Xu, F.; Cao, Y.; Lu, C. Polarization-Dependent Ultrasensitive Dynamic Wrinkling on Floating Films Induced by Photo-Orientation of Azopolymer. *Angewandte Chemie International Edition* **2022**, *61* (31), e202203715. https://doi.org/10.1002/anie.202203715.

(75) Sekhar Yadavalli, N.; Loebner, S.; Papke, T.; Sava, E.; Hurduc, N.; Santer, S. A Comparative Study of Photoinduced Deformation in Azobenzene Containing Polymer Films. *Soft Matter* **2016**, *12* (9), 2593–2603. https://doi.org/10.1039/C6SM00029K.

(76) Saphiannikova, M.; Toshchevikov, V.; Tverdokhleb, N. Optical Deformations of Azobenzene Polymers: Orientation Approach vs. Other Concepts. *Soft Matter* **2024**, *20* (12), 2688–2710. https://doi.org/10.1039/D4SM00104D.

(77) Yager, K. G.; Barrett, C. J. All-Optical Patterning of Azo Polymer Films. *Current Opinion in Solid State and Materials Science* **2001**, *5* (6), 487–494. https://doi.org/10.1016/S1359-0286(02)00020-7.

(78) Lee, S.; Kang, H. S.; Park, J.-K. Directional Photofluidization Lithography: Micro/Nanostructural Evolution by Photofluidic Motions of Azobenzene Materials. *Advanced Materials* **2012**, *24* (16), 2069–2103. https://doi.org/10.1002/adma.201104826.

(79) Toshchevikov, V.; Saphiannikova, M.; Heinrich, G. Microscopic Theory of Light-Induced Deformation in Amorphous Side-Chain Azobenzene Polymers. *J. Phys. Chem. B* **2009**, *113* (15), 5032–5045. https://doi.org/10.1021/jp8078265.

(80) Yadav, B.; Domurath, J.; Kim, K.; Lee, S.; Saphiannikova, M. Orientation Approach to Directional Photodeformations in Glassy Side-Chain Azopolymers. *J. Phys. Chem. B* **2019**, *123* (15), 3337–3347. https://doi.org/10.1021/acs.jpcb.9b00614.

(81) Yadavalli, N. S.; König, T.; Santer, S. Selective Mass Transport of Azobenzene-Containing Photosensitive Films towards or Away from the Light Intensity. *Journal of the Society for Information Display* **2015**, *23* (4), 154–162. https://doi.org/10.1002/jsid.306.

(82) Bublitz, D.; Helgert, M.; Fleck, B.; Wenke, L.; Hvilsted, S.; Ramanujam, P. S. Photoinduced Deformation of Azobenzene Polyester Films. *Appl Phys B* **2000**, *70* (6), 863–865. https://doi.org/10.1007/PL00021146.

(83) Jelken, J.; Santer, S. Light Induced Reversible Structuring of Photosensitive Polymer Films. *RSC Adv.* **2019**, *9* (35), 20295–20305. https://doi.org/10.1039/C9RA02571E.

(84) Vapaavuori, J.; Geraldine Bazuin, C.; Priimagi, A. Supramolecular Design Principles for Efficient Photoresponsive Polymer–Azobenzene Complexes. *Journal of Materials Chemistry C* **2018**, *6* (9), 2168–2188. https://doi.org/10.1039/C7TC05005D.

(85) Kulikovska, O.; Goldenberg, L. M.; Stumpe, J. Supramolecular Azobenzene-Based Materials for Optical Generation of Microstructures. *Chem. Mater.* **2007**, *19* (13), 3343–3348. https://doi.org/10.1021/cm070512d.

(86) Gao, J.; He, Y.; Liu, F.; Zhang, X.; Wang, Z.; Wang, X. Azobenzene-Containing Supramolecular Side-Chain Polymer Films for Laser-Induced Surface Relief Gratings. *Chem. Mater.* **2007**, *19* (16), 3877–3881. https://doi.org/10.1021/cm0707197.

(87) Priimagi, A.; Cavallo, G.; Forni, A.; Gorynsztejn–Leben, M.; Kaivola, M.; Metrangolo, P.; Milani, R.; Shishido, A.; Pilati, T.; Resnati, G.; Terraneo, G. Halogen Bonding versus Hydrogen Bonding in Driving Self-Assembly and Performance of Light-Responsive Supramolecular Polymers. *Advanced Functional Materials* **2012**, *22* (12), 2572–2579. https://doi.org/10.1002/adfm.201200135.

(88) Toshchevikov, V.; Ilnytskyi, J.; Saphiannikova, M. Photoisomerization Kinetics and Mechanical Stress in Azobenzene-Containing Materials. *J. Phys. Chem. Lett.* **2017**, *8* (5), 1094–1098. https://doi.org/10.1021/acs.jpclett.7b00173.

(89) Di Florio, G.; Bründermann, E.; Yadavalli, N. S.; Santer, S.; Havenith, M. Graphene Multilayer as Nanosized Optical Strain Gauge for Polymer Surface Relief Gratings. *Nano Lett.* **2014**, *14* (10), 5754–5760. https://doi.org/10.1021/nl502631s.

(90) Yadavalli, N. S.; Linde, F.; Kopyshev, A.; Santer, S. Soft Matter Beats Hard Matter: Rupturing of Thin Metallic Films Induced by Mass Transport in Photosensitive Polymer Films. *ACS Appl. Mater. Interfaces* **2013**, *5* (16), 7743–7747. https://doi.org/10.1021/am400682w.

(91) Schuh, C.; Lomadze, N.; Rühe, J.; Kopyshev, A.; Santer, S. Photomechanical Degrafting of Azo-Functionalized Poly(Methacrylic Acid) (PMAA) Brushes. *J. Phys. Chem. B* **2011**, *115* (35), 10431–10438. https://doi.org/10.1021/jp2041229.

(92) Kopyshev, A.; Galvin, C. J.; Genzer, J.; Lomadze, N.; Santer, S. Opto-Mechanical Scission of Polymer Chains in Photosensitive Diblock-Copolymer Brushes. *Langmuir* **2013**, *29* (45), 13967–13974. https://doi.org/10.1021/la403241t.

(93) Vapaavuori, J.; Mahimwalla, Z.; Chromik, R. R.; Kaivola, M.; Priimagi, A.; Barrett, C. J. Nanoindentation Study of Light-Induced Softening of Supramolecular and Covalently Functionalized Azo Polymers. *J. Mater. Chem. C* **2013**, *1* (16), 2806–2810. https://doi.org/10.1039/C3TC30246F.

(94) M. Harrison, J.; Goldbaum, D.; Christopher Corkery, T.; J. Barrett, C.; R. Chromik, R. Nanoindentation Studies to Separate Thermal and Optical Effects in Photo-Softening of Azo Polymers. *Journal of Materials Chemistry C* **2015**, *3* (5), 995–1003. https://doi.org/10.1039/C4TC02336F.

(95) Hurduc, N.; Donose, B. C.; Rocha, L.; Ibanescu, C.; Scutaru, D. Azo-Polymers Photofluidisation – a Transient State of Matter Emulated by Molecular Motors. *RSC Adv.* **2016**, *6* (32), 27087–27093. https://doi.org/10.1039/C6RA03842E.

(96) Choi, J.; Kang, H. S.; Jo, W.; Kim, S.-H.; Jung, Y. S.; Kim, H.-T. Photo-Reconfigurable Azopolymer Etch Mask: Photofluidization-Driven Reconfiguration and Edge Rectangularization. *Small* **2018**, *14* (11), 1703250. https://doi.org/10.1002/smll.201703250.

(97) Choi, J.; Cho, W.; Jung, Y. S.; Kang, H. S.; Kim, H.-T. Direct Fabrication of Micro/Nano-Patterned Surfaces by Vertical-Directional Photofluidization of Azobenzene Materials. *ACS Nano* **2017**, *11* (2), 1320–1327. https://doi.org/10.1021/acsnano.6b05934.

(98) Wang, Z.; Huang, H.; Wang, X. Self-Organized Patterning on Azo Molecular Glass Film via Optical near-Field Effect. *Commun Mater* **2023**, *4* (1), 1–12. https://doi.org/10.1038/s43246-023-00361-8.

(99) Ichikawa, R.; Nakano, H. Photoinduced Change in the Shape of Azobenzene-Based Molecular Glass Particles Fixed in Agar Gel. *RSC Adv.* **2016**, *6* (43), 36761–36765. https://doi.org/10.1039/C6RA05792F.

(100) Hsu, C.; Xu, Z.; Wang, X. Holographic Recording and Hierarchical Surface Patterning on Periodic Submicrometer Pillar Arrays of Azo Molecular Glass via Polarized Light Irradiation. *Advanced Functional Materials* **2018**, *28* (34), 1802506. https://doi.org/10.1002/adfm.201802506.

(101) Hsu, C.; Xu, Z.; Wang, X. Symmetry-Breaking Response of Azo Molecular Glass Microspheres to Interfering Circularly Polarized Light: From Shape Manipulation to 3D Patterning. *Advanced Functional Materials* **2019**, *29* (3), 1806703. https://doi.org/10.1002/adfm.201806703.

(102) Fuhrmann, T.; Tsutsui, T. Synthesis and Properties of a Hole-Conducting, Photopatternable Molecular Glass. *Chem. Mater.* **1999**, *11* (8), 2226–2232. https://doi.org/10.1021/cm9901820.

(103) Nakano, H.; Takahashi, T.; Kadota, T.; Shirota, Y. Formation of a Surface Relief Grating Using a Novel Azobenzene-Based Photochromic Amorphous Molecular Material. *Advanced Materials* **2002**, *14* (16), 1157–1160. https://doi.org/10.1002/1521-4095(20020816)14:16<1157::AID-ADMA1157>3.0.CO;2-Z.

(104) Yadavalli, N. S.; Saphiannikova, M.; Lomadze, N.; Goldenberg, L. M.; Santer, S. Structuring of Photosensitive Material below Diffraction Limit Using Far Field Irradiation. *Appl. Phys. A* **2013**, *113* (2), 263–272. https://doi.org/10.1007/s00339-013-7945-3.

(105) Laventure, A.; Bourotte, J.; Vapaavuori, J.; Karperien, L.; Sabat, R. G.; Lebel, O.; Pellerin, C. Photoactive/Passive Molecular Glass Blends: An Efficient Strategy to Optimize Azomaterials for Surface Relief Grating Inscription. *ACS Appl. Mater. Interfaces* **2017**, *9* (1), 798–808. https://doi.org/10.1021/acsami.6b11849.

(106) Ristola, M.; Fedele, C.; Hagman, S.; Sukki, L.; Kapucu, F. E.; Mzezewa, R.; Hyvärinen, T.; Kallio, P.; Priimagi, A.; Narkilahti, S. Directional Growth of Human Neuronal Axons in a Microfluidic Device with Nanotopography on Azobenzene-Based Material. *Advanced Materials Interfaces* **2021**, *8* (11), 2100048. https://doi.org/10.1002/admi.202100048.

(107) Yadavalli, N. S.; Saphiannikova, M.; Santer, S. Photosensitive Response of Azobenzene Containing Films towards Pure Intensity or Polarization Interference Patterns. *Applied Physics Letters* **2014**, *105* (5), 051601. https://doi.org/10.1063/1.4891615.

(108) Diggins, A.; Dawson, E.; Kamaliardakani, M.; Pellerin, C.; Sabat, R. G.; Lebel, O. Azobenzene Molecular Glasses with Tuned Glass Transition Temperatures: From Optimal Light-Induced Motion to Self-Erasable Gratings. *J. Mater. Chem. C* **2020**, *8* (18), 6203–6213. https://doi.org/10.1039/D0TC00393J.

(109) Masuda, K.; Nakano, S.; Barada, D.; Kumakura, M.; Miyamoto, K.; Omatsu, T. Azo-Polymer Film Twisted to Form a Helical Surface Relief by Illumination with a Circularly Polarized Gaussian Beam. *Opt. Express, OE* **2017**, *25* (11), 12499–12507. https://doi.org/10.1364/OE.25.012499.

(110) Wang, Z.; Huang, H.; Hsu, C.; Wang, X. Azo Molecular Glass Patterning from Chiral Submicron Pillar Array to Self-Organized Topographic Transition via Irradiation with Circularly Polarized Light. *Advanced Optical Materials* **2021**, *9* (21), 2100922. https://doi.org/10.1002/adom.202100922.

(111) Ambrosio, A.; Marrucci, L.; Borbone, F.; Roviello, A.; Maddalena, P. Light-Induced Spiral Mass Transport in Azo-Polymer Films under Vortex-Beam Illumination. *Nat Commun* **2012**, *3* (1), 989. https://doi.org/10.1038/ncomms1996.

(112) Ambrosio, A.; Maddalena, P.; Marrucci, L. Molecular Model for Light-Driven Spiral Mass Transport in Azopolymer Films. *Phys. Rev. Lett.* **2013**, *110* (14), 146102. https://doi.org/10.1103/PhysRevLett.110.146102.

(113) Watabe, M.; Juman, G.; Miyamoto, K.; Omatsu, T. Light Induced Conch-Shaped Relief in an Azo-Polymer Film. *Sci Rep* **2014**, *4* (1), 4281. https://doi.org/10.1038/srep04281.

(114) Masuda, K.; Shinozaki, R.; Kinezuka, Y.; Lee, J.; Ohno, S.; Hashiyada, S.; Okamoto, H.; Sakai, D.; Harada, K.; Miyamoto, K.; Omatsu, T. Nanoscale Chiral Surface Relief of Azo-Polymers with Nearfield OAM Light. *Opt. Express, OE* **2018**, *26* (17), 22197–22207. https://doi.org/10.1364/OE.26.022197.

(115) Broer, D. J.; Boven, J.; Mol, G. N.; Challa, G. In-Situ Photopolymerization of Oriented Liquid-Crystalline Acrylates, 3. Oriented Polymer Networks from a Mesogenic Diacrylate. *Die*

Makromolekulare Chemie **1989**, *190* (9), 2255–2268. https://doi.org/10.1002/macp.1989.021900926.

(116) Broer, D. J.; Heynderickx, I. Three-Dimensionally Ordered Polymer Networks with a Helicoidal Structure. *Macromolecules* **1990**, *23* (9), 2474–2477. https://doi.org/10.1021/ma00211a012.

(117) Finkelmann, H.; Kock, H.-J.; Rehage, G. Investigations on Liquid Crystalline Polysiloxanes 3. Liquid Crystalline Elastomers — a New Type of Liquid Crystalline Material. *Die Makromolekulare Chemie, Rapid Communications* **1981**, *2* (4), 317–322. https://doi.org/10.1002/marc.1981.030020413.

(118) White, T. J.; Broer, D. J. Programmable and Adaptive Mechanics with Liquid Crystal Polymer Networks and Elastomers. *Nature Mater* **2015**, *14* (11), 1087–1098. https://doi.org/10.1038/nmat4433.

(119) Jiang, Z.-C.; Xiao, Y.-Y.; Zhao, Y. Shining Light on Liquid Crystal Polymer Networks: Preparing, Reconfiguring, and Driving Soft Actuators. *Advanced Optical Materials* **2019**, *7* (16), 1900262. https://doi.org/10.1002/adom.201900262.

(120) Mehta, K.; Peeketi, A. R.; Liu, L.; Broer, D.; Onck, P.; Annabattula, R. K. Design and Applications of Light Responsive Liquid Crystal Polymer Thin Films. *Applied Physics Reviews* **2020**, *7* (4), 041306. https://doi.org/10.1063/5.0014619.

(121) Broer, D. J.; Mol, G. N. Anisotropic Thermal Expansion of Densely Cross-Linked Oriented Polymer Networks. *Polymer Engineering & Science* **1991**, *31* (9), 625–631. https://doi.org/10.1002/pen.760310902.

(122) Wermter, H.; Finkelmann, H. Liquid Crystalline Elastomers as Artificial Muscles. *e-Polymers* **2001**, *1* (1). https://doi.org/10.1515/epoly.2001.1.1.111.

(123) Tajbakhsh, A. R.; Terentjev, E. M. Spontaneous Thermal Expansion of Nematic Elastomers. *Eur. Phys. J. E* **2001**, *6* (2), 181–188. https://doi.org/10.1007/s101890170020.

(124) Yang, L.; Setyowati, K.; Li, A.; Gong, S.; Chen, J. Reversible Infrared Actuation of Carbon Nanotube–Liquid Crystalline Elastomer Nanocomposites. *Advanced Materials* **2008**, *20* (12), 2271–2275. https://doi.org/10.1002/adma.200702953.

(125) Gelebart, A. H.; Vantomme, G.; Meijer, E. W.; Broer, D. J. Mastering the Photothermal Effect in Liquid Crystal Networks: A General Approach for Self-Sustained Mechanical Oscillators. *Advanced Materials* **2017**, *29* (18), 1606712. https://doi.org/10.1002/adma.201606712.

(126) Kuenstler, A. S.; Chen, Y.; Bui, P.; Kim, H.; DeSimone, A.; Jin, L.; Hayward, R. C. Blueprinting Photothermal Shape-Morphing of Liquid Crystal Elastomers. *Advanced Materials* **2020**, *32* (17), 2000609. https://doi.org/10.1002/adma.202000609.

(127) Ikeda, T.; Tsutsumi, O. Optical Switching and Image Storage by Means of Azobenzene Liquid-Crystal Films. *Science* **1995**, *268* (5219), 1873–1875.

(128) Ikeda, T.; Mamiya, J.; Yu, Y. Photomechanics of Liquid-Crystalline Elastomers and Other Polymers. *Angewandte Chemie International Edition* **2007**, *46* (4), 506–528. https://doi.org/10.1002/anie.200602372.

(129) Finkelmann, H.; Nishikawa, E.; Pereira, G. G.; Warner, M. A New Opto-Mechanical Effect in Solids. *Phys. Rev. Lett.* **2001**, *87* (1), 015501. https://doi.org/10.1103/PhysRevLett.87.015501.

(130) Iamsaard, S.; Anger, E.; Aßhoff, S. J.; Depauw, A.; Fletcher, S. P.; Katsonis, N. Fluorinated Azobenzenes for Shape-Persistent Liquid Crystal Polymer Networks. *Angewandte Chemie* **2016**, *128* (34), 10062–10066. https://doi.org/10.1002/ange.201603579.

(131) Liu, D.; Broer, D. J. New Insights into Photoactivated Volume Generation Boost Surface Morphing in Liquid Crystal Coatings. *Nat Commun* **2015**, *6* (1), 8334. https://doi.org/10.1038/ncomms9334.

(132) Lee, K. M.; White, T. J. Photochemical Mechanism and Photothermal Considerations in the Mechanical Response of Monodomain, Azobenzene-Functionalized Liquid Crystal Polymer Networks. *Macromolecules* **2012**, *45* (17), 7163–7170. https://doi.org/10.1021/ma301337e.

(133) Ikeda, T.; Nakano, M.; Yu, Y.; Tsutsumi, O.; Kanazawa, A. Anisotropic Bending and Unbending Behavior of Azobenzene Liquid-Crystalline Gels by Light Exposure. *Advanced Materials* **2003**, *15* (3), 201–205. https://doi.org/10.1002/adma.200390045.

(134) Chen, Y.; Yang, J.; Zhang, X.; Feng, Y.; Zeng, H.; Wang, L.; Feng, W. Light-Driven Bimorph Soft Actuators: Design, Fabrication, and Properties. *Mater. Horiz.* **2021**, *8* (3), 728–757. https://doi.org/10.1039/D0MH01406K.

(135) M. Boothby, J.; H. Ware, T. Dual-Responsive, Shape-Switching Bilayers Enabled by Liquid Crystal Elastomers. *Soft Matter* **2017**, *13* (24), 4349–4356. https://doi.org/10.1039/C7SM00541E.

(136) Kotikian, A.; McMahan, C.; Davidson, E. C.; Muhammad, J. M.; Weeks, R. D.; Daraio, C.; Lewis, J. A. Untethered Soft Robotic Matter with Passive Control of Shape Morphing and Propulsion. *Science Robotics* **2019**, *4* (33), eaax7044. https://doi.org/10.1126/scirobotics.aax7044.

(137) Wang, M.; Lin, B.-P.; Yang, H. A Plant Tendril Mimic Soft Actuator with Phototunable Bending and Chiral Twisting Motion Modes. *Nat Commun* **2016**, *7* (1), 13981. https://doi.org/10.1038/ncomms13981.

(138) Iamsaard, S.; Aßhoff, S. J.; Matt, B.; Kudernac, T.; Cornelissen, J. J. L. M.; Fletcher, S. P.; Katsonis, N. Conversion of Light into Macroscopic Helical Motion. *Nature Chem* **2014**, *6* (3), 229–235. https://doi.org/10.1038/nchem.1859.

(139) Lee, K. M.; Smith, M. L.; Koerner, H.; Tabiryan, N.; Vaia, R. A.; Bunning, T. J.; White, T. J. Photodriven, Flexural–Torsional Oscillation of Glassy Azobenzene Liquid Crystal Polymer Networks. *Advanced Functional Materials* **2011**, *21* (15), 2913–2918. https://doi.org/10.1002/adfm.201100333.

(140) Lee, K. M.; Bunning, T. J.; White, T. J. Autonomous, Hands-Free Shape Memory in Glassy, Liquid Crystalline Polymer Networks. *Advanced Materials* **2012**, *24* (21), 2839–2843. https://doi.org/10.1002/adma.201200374.

(141) Mol, G. N.; Harris, K. D.; Bastiaansen, C. W. M.; Broer, D. J. Thermo-Mechanical Responses of Liquid-Crystal Networks with a Splayed Molecular Organization. *Advanced Functional Materials* **2005**, *15* (7), 1155–1159. https://doi.org/10.1002/adfm.200400503.

(142) van Oosten, C. L.; Harris, K. D.; Bastiaansen, C. W. M.; Broer, D. J. Glassy Photomechanical Liquid-Crystal Network Actuators for Microscale Devices. *Eur. Phys. J. E* **2007**, *23* (3), 329–336. https://doi.org/10.1140/epje/i2007-10196-1.

(143) Li, Y.; Liu, Y.; Luo, D. Polarization Dependent Light-Driven Liquid Crystal Elastomer Actuators Based on Photothermal Effect. *Adv. Optical Mater.* **2020**, 2001861. https://doi.org/10.1002/adom.202001861.

(144) Cheng, F.; Yin, R.; Zhang, Y.; Yen, C.-C.; Yu, Y. Fully Plastic Microrobots Which Manipulate Objects Using Only Visible Light. *Soft Matter* **2010**, *6* (15), 3447–3449. https://doi.org/10.1039/C0SM00012D.

(145) Zmyślony, M.; Dradrach, K.; Haberko, J.; Nałęcz-Jawecki, P.; Rogóż, M.; Wasylczyk, P. Optical Pliers: Micrometer-Scale, Light-Driven Tools Grown on Optical Fibers. *Advanced Materials* **2020**, *32* (33), 2002779. https://doi.org/10.1002/adma.202002779.

(146) Camargo, C. J.; Campanella, H.; Marshall, J. E.; Torras, N.; Zinoviev, K.; Terentjev, E. M.; Esteve, J. Batch Fabrication of Optical Actuators Using Nanotube–Elastomer Composites towards Refreshable Braille Displays. *J. Micromech. Microeng.* **2012**, *22* (7), 075009. https://doi.org/10.1088/0960-1317/22/7/075009.

(147) Kurylo, I.; van der Tol, J.; Colonnese, N.; Broer, D. J.; Liu, D. Photo-Responsive Liquid Crystal Network-Based Material with Adaptive Modulus for Haptic Application. *Sci Rep* **2022**, *12* (1), 19512. https://doi.org/10.1038/s41598-022-24106-8.

(148) Chen, M.; Huang, H.; Zhu, Y.; Liu, Z.; Xing, X.; Cheng, F.; Yu, Y. Photodeformable CLCP Material: Study on Photo-Activated Microvalve Applications. *Appl. Phys. A* **2011**, *102* (3), 667–672. https://doi.org/10.1007/s00339-010-6103-4.

(149) Lv, J.; Liu, Y.; Wei, J.; Chen, E.; Qin, L.; Yu, Y. Photocontrol of Fluid Slugs in Liquid Crystal Polymer Microactuators. *Nature* **2016**, *537* (7619), 179–184. https://doi.org/10.1038/nature19344.

(150) Dradrach, K.; Zmyślony, M.; Deng, Z.; Priimagi, A.; Biggins, J.; Wasylczyk, P. Light-Driven Peristaltic Pumping by an Actuating Splay-Bend Strip. *Nat Commun* **2023**, *14* (1), 1877. https://doi.org/10.1038/s41467-023-37445-5.

(151) van Oosten, C. L.; Bastiaansen, C. W. M.; Broer, D. J. Printed Artificial Cilia from Liquid-Crystal Network Actuators Modularly Driven by Light. *Nature Mater* **2009**, *8* (8), 677–682. https://doi.org/10.1038/nmat2487.

(152) Gelebart, A. H.; Mc Bride, M.; Schenning, A. P. H. J.; Bowman, C. N.; Broer, D. J. Photoresponsive Fiber Array: Toward Mimicking the Collective Motion of Cilia for Transport Applications. *Advanced Functional Materials* **2016**, *26* (29), 5322–5327. https://doi.org/10.1002/adfm.201601221.

(153) Koçer, G.; ter Schiphorst, J.; Hendrikx, M.; Kassa, H. G.; Leclère, P.; Schenning, A. P. H. J.; Jonkheijm, P. Light-Responsive Hierarchically Structured Liquid Crystal Polymer Networks for Harnessing Cell Adhesion and Migration. *Advanced Materials* **2017**, *29* (27), 1606407. https://doi.org/10.1002/adma.201606407.

(154) Silva, P. E. S.; Lin, X.; Vaara, M.; Mohan, M.; Vapaavuori, J.; Terentjev, E. M. Active Textile Fabrics from Weaving Liquid Crystalline Elastomer Filaments. *Advanced Materials* **2023**, *35* (14), 2210689. https://doi.org/10.1002/adma.202210689.

(155) Nocentini, S.; Rührmair, U.; Barni, M.; Wiersma, D. S.; Riboli, F. All-Optical Multilevel Physical Unclonable Functions. *Nat. Mater.* **2024**, *23* (3), 369–376. https://doi.org/10.1038/s41563-023-01734-7.

(156) Zeng, H.; Wani, O. M.; Wasylczyk, P.; Kaczmarek, R.; Priimagi, A. Self-Regulating Iris Based on Light-Actuated Liquid Crystal Elastomer. *Advanced Materials* **2017**, *29* (30), 1701814. https://doi.org/10.1002/adma.201701814.

(157) Li, C.; Liu, Y.; Huang, X.; Jiang, H. Direct Sun-Driven Artificial Heliotropism for Solar Energy Harvesting Based on a Photo-Thermomechanical Liquid-Crystal Elastomer Nanocomposite. *Advanced Functional Materials* **2012**, *22* (24), 5166–5174. https://doi.org/10.1002/adfm.201202038.

(158) Yao, Y.; Waters, J. T.; Shneidman, A. V.; Cui, J.; Wang, X.; Mandsberg, N. K.; Li, S.; Balazs, A. C.; Aizenberg, J. Multiresponsive Polymeric Microstructures with Encoded Predetermined and Self-Regulated Deformability. *PNAS* **2018**, *115* (51), 12950–12955. https://doi.org/10.1073/pnas.1811823115.

(159) Wani, O. M.; Zeng, H.; Priimagi, A. A Light-Driven Artificial Flytrap. *Nat Commun* **2017**, *8* (1), 15546. https://doi.org/10.1038/ncomms15546.

(160) Martella, D.; Nocentini, S.; Nuzhdin, D.; Parmeggiani, C.; Wiersma, D. S. Photonic Microhand with Autonomous Action. *Advanced Materials* **2017**, *29* (42), 1704047. https://doi.org/10.1002/adma.201704047.

(161) Zeng, H.; Wasylczyk, P.; Wiersma, D. S.; Priimagi, A. Light Robots: Bridging the Gap between Microrobotics and Photomechanics in Soft Materials. *Advanced Materials* **2018**, *30* (24), 1703554. https://doi.org/10.1002/adma.201703554.

(162) Camacho-Lopez, M.; Finkelmann, H.; Palffy-Muhoray, P.; Shelley, M. Fast Liquid-Crystal Elastomer Swims into the Dark. *Nature Mater* **2004**, *3* (5), 307–310. https://doi.org/10.1038/nmat1118.

(163) Huang, C.; Lv, J.; Tian, X.; Wang, Y.; Yu, Y.; Liu, J. Miniaturized Swimming Soft Robot with Complex Movement Actuated and Controlled by Remote Light Signals. *Sci Rep* **2015**, *5* (1), 17414. https://doi.org/10.1038/srep17414.

(164) Sartori, P.; Yadav, R. S.; del Barrio, J.; DeSimone, A.; Sánchez-Somolinos, C. Photochemically Induced Propulsion of a 4D Printed Liquid Crystal Elastomer Biomimetic Swimmer. *Advanced Science* **2024**, *11* (25), 2308561. https://doi.org/10.1002/advs.202308561.

(165) Pilz da Cunha, M.; Ambergen, S.; Debije, M. G.; Homburg, E. F. G. A.; den Toonder, J. M. J.; Schenning, A. P. H. J. A Soft Transporter Robot Fueled by Light. *Adv. Sci.* **2020**, *7* (5), 1902842. https://doi.org/10.1002/advs.201902842.

(166) Yamada, M.; Kondo, M.; Miyasato, R.; Naka, Y.; Mamiya, J.; Kinoshita, M.; Shishido, A.; Yu, Y.; Barrett, C. J.; Ikeda, T. Photomobile Polymer Materials—Various Three-Dimensional Movements. *J. Mater. Chem.* **2008**, *19* (1), 60–62. https://doi.org/10.1039/B815289F.

(167) Babaei, M.; Clement, J. A.; Dayal, K.; Shankar, M. R. Steering with Light: Indexable Photomotility in Liquid Crystalline Polymers. *RSC Adv.* **2017**, *7* (83), 52510–52516. https://doi.org/10.1039/C7RA10619J.

(168) Pilz da Cunha, M.; Peeketi, A. R.; Mehta, K.; Broer, D. J.; Annabattula, R. K.; Schenning, A. P. H. J.; Debije, M. G. A Self-Sustained Soft Actuator Able to Rock and Roll. *Chem. Commun.* **2019**, *55* (74), 11029–11032. https://doi.org/10.1039/C9CC05329H.

(169) Lu, X.; Guo, S.; Tong, X.; Xia, H.; Zhao, Y. Tunable Photocontrolled Motions Using Stored Strain Energy in Malleable Azobenzene Liquid Crystalline Polymer Actuators. *Advanced Materials* **2017**, *29* (28), 1606467. https://doi.org/10.1002/adma.201606467.

(170) Wie, J. J.; Shankar, M. R.; White, T. J. Photomotility of Polymers. *Nat Commun* **2016**, *7* (1), 13260. https://doi.org/10.1038/ncomms13260.

(171) Hu, Z.; Fang, W.; Li, Q.; Feng, X.-Q.; Lv, J. Optocapillarity-Driven Assembly and Reconfiguration of Liquid Crystal Polymer Actuators. *Nat Commun* **2020**, *11* (1), 5780. https://doi.org/10.1038/s41467-020-19522-1.

(172) Lu, X.; Zhang, H.; Fei, G.; Yu, B.; Tong, X.; Xia, H.; Zhao, Y. Liquid-Crystalline Dynamic Networks Doped with Gold Nanorods Showing Enhanced Photocontrol of Actuation. *Advanced Materials* **2018**, *30* (14), 1706597. https://doi.org/10.1002/adma.201706597.

(173) Zuo, B.; Wang, M.; Lin, B.-P.; Yang, H. Visible and Infrared Three-Wavelength Modulated Multi-Directional Actuators. *Nature Communications* **2019**, *10* (1), 4539. https://doi.org/10.1038/s41467-019-12583-x.

(174) Lahikainen, M.; Zeng, H.; Priimagi, A. Reconfigurable Photoactuator through Synergistic Use of Photochemical and Photothermal Effects. *Nat Commun* **2018**, *9* (1), 4148. https://doi.org/10.1038/s41467-018-06647-7.

(175) Verpaalen, R. C. P.; Cunha, M. P. da; Engels, T. A. P.; Debije, M. G.; Schenning, A. P. H. J. Liquid Crystal Networks on Thermoplastics: Reprogrammable Photo-Responsive Actuators. *Angewandte Chemie International Edition* **2020**, *59* (11), 4532–4536. https://doi.org/10.1002/anie.201915147.

(176) Yu, Y.; Nakano, M.; Ikeda, T. Directed Bending of a Polymer Film by Light. *Nature* **2003**, *425* (6954), 145–145. https://doi.org/10.1038/425145a.

(177) Goulet-Hanssens, A.; Barrett, C. J. Photo-Control of Biological Systems with Azobenzene Polymers. *J. Polym. Sci. Part A: Polym. Chem.* **2013**, *51* (14), 3058–3070. https://doi.org/10.1002/pola.26735.

(178) Izquierdo-Serra, M.; Gascón-Moya, M.; Hirtz, J. J.; Pittolo, S.; Poskanzer, K. E.; Ferrer, È.; Alibés, R.; Busqué, F.; Yuste, R.; Hernando, J.; Gorostiza, P. Two-Photon Neuronal and Astrocytic Stimulation with Azobenzene-Based Photoswitches. *J. Am. Chem. Soc.* **2014**, *136* (24), 8693–8701. https://doi.org/10.1021/ja5026326.

(179) Corrado, F.; Bruno, U.; Prato, M.; Carella, A.; Criscuolo, V.; Massaro, A.; Pavone, M.; Muñoz-García, A. B.; Forti, S.; Coletti, C.; Bettucci, O.; Santoro, F. Azobenzene-Based Optoelectronic Transistors for Neurohybrid Building Blocks. *Nat Commun* **2023**, *14* (1), 6760. https://doi.org/10.1038/s41467-023-41083-2.

(180) Sekkat, Z.; Kleideiter, G.; Knoll, W. Optical Orientation of Azo Dye in Polymer Films at High Pressure. *J. Opt. Soc. Am. B* **2001**, *18* (12), 1854. https://doi.org/10.1364/JOSAB.18.001854.

(181) Yager, K. G.; Tanchak, O. M.; Godbout, C.; Fritzsche, H.; Barrett, C. J. Photomechanical Effects in Azo-Polymers Studied by Neutron Reflectometry. *Macromolecules* **2006**, *39* (26), 9311–9319. https://doi.org/10.1021/ma0617320.

(182) Vapaavuori, J.; Laventure, A.; Bazuin, C. G.; Lebel, O.; Pellerin, C. Submolecular Plasticization Induced by Photons in Azobenzene Materials. *J. Am. Chem. Soc.* **2015**, *137* (42), 13510–13517. https://doi.org/10.1021/jacs.5b06611.

(183) Tanchak, O. M.; Barrett, C. J. Light-Induced Reversible Volume Changes in Thin Films of Azo Polymers: The Photomechanical Effect. *Macromolecules* **2005**, *38* (25), 10566–10570. https://doi.org/10.1021/ma051564w.

(184) Pennacchio, F. A.; Fedele, C.; De Martino, S.; Cavalli, S.; Vecchione, R.; Netti, P. A. Three-Dimensional Microstructured Azobenzene-Containing Gelatin as a Photoactuable Cell Confining System. *ACS Appl. Mater. Interfaces* **2018**, *10* (1), 91–97. https://doi.org/10.1021/acsami.7b13176.

(185) Descrovi, E.; Pirani, F.; P. Rajamanickam, V.; Licheri, S.; Liberale, C. Photo-Responsive Suspended Micro-Membranes. *J. Mater. Chem. C* **2018**, *6* (39), 10428–10434. https://doi.org/10.1039/C8TC03877E.

(186) Wen, H.; Zhang, W.; Weng, Y.; Hu, Z. Photomechanical Bending of Linear Azobenzene Polymer. *RSC Adv.* **2014**, *4* (23), 11776–11781. https://doi.org/10.1039/C3RA48035F.

(187) Wang, J.; Song, T.; Zhang, Y.; Liu, J.; Yu, M.; Yu, H. Light-Driven Autonomous Self-Oscillation of a Liquid-Crystalline Polymer Bimorph Actuator. *Journal of Materials Chemistry C* **2021**, *9* (37), 12573–12580. https://doi.org/10.1039/D1TC02891J.

(188) Kameda, M.; Sumaru, K.; Kanamori, T.; Shinbo, T. Photoresponse Gas Permeability of Azobenzene-Functionalized Glassy Polymer Films. *Journal of Applied Polymer Science* **2003**, *88* (8), 2068–2072. https://doi.org/10.1002/app.11980.

(189) Roppolo, I.; Chiappone, A.; Angelini, A.; Stassi, S.; Frascella, F.; Pirri, C. F.; Ricciardi, C.; Descrovi, E. 3D Printable Light-Responsive Polymers. *Mater. Horiz.* **2017**, *4* (3), 396–401. https://doi.org/10.1039/C7MH00072C.

(190) Angelini, A.; Pirani, F.; Frascella, F.; Descrovi, E. Reconfigurable Elastomeric Graded-Index Optical Elements Controlled by Light. *Light Sci Appl* **2018**, *7* (1), 7. https://doi.org/10.1038/s41377-018-0005-1.

(191) Gliozzi, A. S.; Miniaci, M.; Chiappone, A.; Bergamini, A.; Morin, B.; Descrovi, E. Tunable Photo-Responsive Elastic Metamaterials. *Nature Communications* **2020**, *11* (1), 2576. https://doi.org/10.1038/s41467-020-16272-y.

(192) Tamesue, S.; Takashima, Y.; Yamaguchi, H.; Shinkai, S.; Harada, A. Photoswitchable Supramolecular Hydrogels Formed by Cyclodextrins and Azobenzene Polymers. *Angewandte Chemie International Edition* **2010**, *49* (41), 7461–7464. https://doi.org/10.1002/anie.201003567.

(193) Takashima, Y.; Hatanaka, S.; Otsubo, M.; Nakahata, M.; Kakuta, T.; Hashidzume, A.; Yamaguchi, H.; Harada, A. Expansion–Contraction of Photoresponsive Artificial Muscle Regulated by Host–Guest Interactions. *Nat Commun* **2012**, *3* (1), 1270. https://doi.org/10.1038/ncomms2280.

(194) Yamaguchi, H.; Kobayashi, Y.; Kobayashi, R.; Takashima, Y.; Hashidzume, A.; Harada, A. Photoswitchable Gel Assembly Based on Molecular Recognition. *Nat Commun* **2012**, *3* (1), 603. https://doi.org/10.1038/ncomms1617.

(195) Kavokine, N.; Anyfantakis, M.; Morel, M.; Rudiuk, S.; Bickel, T.; Baigl, D. Light-Driven Transport of a Liquid Marble with and against Surface Flows. *Angewandte Chemie International Edition* **2016**, *55* (37), 11183–11187. https://doi.org/10.1002/anie.201603639.

(196) Chevallier, E.; Mamane, A.; Stone, H. A.; Tribet, C.; Lequeux, F.; Monteux, C. Pumping-out Photo-Surfactants from an Air–Water Interface Using Light. *Soft Matter* **2011**, *7* (17), 7866–7874. https://doi.org/10.1039/C1SM05378G.

(197) Varanakkottu, S. N.; George, S. D.; Baier, T.; Hardt, S.; Ewald, M.; Biesalski, M. Particle Manipulation Based on Optically Controlled Free Surface Hydrodynamics. *Angewandte Chemie International Edition* **2013**, *52* (28), 7291–7295. https://doi.org/10.1002/anie.201302111.

(198) Lv, C.; Varanakkottu, S. N.; Baier, T.; Hardt, S. Controlling the Trajectories of Nano/Micro Particles Using Light-Actuated Marangoni Flow. *Nano Lett.* **2018**, *18* (11), 6924–6930. https://doi.org/10.1021/acs.nanolett.8b02814.

(199) Salvatore, M.; Borbone, F.; Oscurato, S. L. Deterministic Realization of Quasicrystal Surface Relief Gratings on Thin Azopolymer Films. *Advanced Materials Interfaces* **2020**, *7* (11), 1902118. https://doi.org/10.1002/admi.201902118.

(200) Guo, M.; Xu, Z.; Wang, X. Photofabrication of Two-Dimensional Quasi-Crystal Patterns on UV-Curable Molecular Azo Glass Films. *Langmuir* **2008**, *24* (6), 2740–2745. https://doi.org/10.1021/la703091x.

(201) Berdin, A.; Rekola, H. T.; Priimagi, A. Complex Fourier Surfaces by Superposition of Multiple Gratings on Azobenzene Thin Films. *Advanced Optical Materials* **2024**, *12* (4), 2301597. https://doi.org/10.1002/adom.202301597.

(202) Kong, X.; Wang, X.; Luo, T.; Yao, Y.; Li, L.; Lin, S. Photomanipulated Architecture and Patterning of Azopolymer Array. *ACS Appl. Mater. Interfaces* **2017**, *9* (22), 19345–19353. https://doi.org/10.1021/acsami.7b04273.

(203) Li, J.; Chen, L.; Xu, J.; Wang, K.; Wang, X.; He, X.; Dong, H.; Lin, S.; Zhu, J. Photoguided Shape Deformation of Azobenzene-Containing Polymer Microparticles. *Langmuir* **2015**, *31* (48), 13094–13100. https://doi.org/10.1021/acs.langmuir.5b03610.

(204) Pietsch, U.; Rochon, P.; Natansohn, A. Formation of a Buried Lateral Density Grating in Azobenzene Polymer Films. *Advanced Materials* **2000**, *12* (15), 1129–1132. https://doi.org/10.1002/1521-4095(200008)12:15<1129::AID-ADMA1129>3.0.CO;2-A.

(205) Jiang, X. L.; Li, L.; Kumar, J.; Kim, D. Y.; Tripathy, S. K. Unusual Polarization Dependent Optical Erasure of Surface Relief Gratings on Azobenzene Polymer Films. *Applied Physics Letters* **1998**, *72* (20), 2502–2504. https://doi.org/10.1063/1.121400.

(206) Lagugné-Labarthet, F.; Buffeteau, T.; Sourisseau, C. Optical Erasures and Unusual Surface Reliefs of Holographic Gratings Inscribed on Thin Films of an Azobenzene Functionalized Polymer. *Physical Chemistry Chemical Physics* **2002**, *4* (16), 4020–4029. https://doi.org/10.1039/B200810F.

(207) Ubukata, T.; Isoshima, T.; Hara, M. Wavelength-Programmable Organic Distributed-Feedback Laser Based on a Photoassisted Polymer-Migration System. *Advanced Materials* **2005**, *17* (13), 1630–1633. https://doi.org/10.1002/adma.200402080.

(208) Barillé, R.; Janik, R.; Kucharski, S.; Eyer, J.; Letournel, F. Photo-Responsive Polymer with Erasable and Reconfigurable Micro- and Nano-Patterns: An in Vitro Study for Neuron Guidance. *Colloids and Surfaces B: Biointerfaces* **2011**, *88* (1), 63–71. https://doi.org/10.1016/j.colsurfb.2011.06.005.

(209) Vapaavuori, J.; A. Ras, R. H.; Kaivola, M.; Geraldine Bazuin, C.; Priimagi, A. From Partial to Complete Optical Erasure of Azobenzene–Polymer Gratings: Effect of Molecular Weight. *Journal of Materials Chemistry C* **2015**, *3* (42), 11011–11016. https://doi.org/10.1039/C5TC01776A.

(210) Natansohn, A.; Rochon, P.; Gosselin, J.; Xie, S. Azo Polymers for Reversible Optical Storage. 1. Poly[4’-[[2-(Acryloyloxy)Ethyl]Ethylamino]-4-Nitroazobenzene]. *Macromolecules* **1992**, *25* (8), 2268–2273. https://doi.org/10.1021/ma00034a031.

(211) Natansohn, A.; Rochon, P.; Pezolet, M.; Audet, P.; Brown, D.; To, S. Azo Polymers for Reversible Optical Storage. 4. Cooperative Motion of Rigid Groups in Semicrystalline Polymers. *Macromolecules* **1994**, *27* (9), 2580–2585. https://doi.org/10.1021/ma00087a029.

(212) Kerekes, A.; Sajti, S.; Loerincz, E.; Hvilsted, S.; Ramanujam, P. S. Rewritable Azobenzene Polyester for Polarization Holographic Data Storage. In *Holography 2000*; SPIE, 2000; Vol. 4149, pp 324–331. https://doi.org/10.1117/12.402497.

(213) Sánchez, C.; Alcalá, R.; Hvilsted, S.; Ramanujam, P. S. Biphotonic Holographic Gratings in Azobenzene Polyesters: Surface Relief Phenomena and Polarization Effects. *Applied Physics Letters* **2000**, *77* (10), 1440–1442. https://doi.org/10.1063/1.1290604.

(214) Rianna, C.; Calabuig, A.; Ventre, M.; Cavalli, S.; Pagliarulo, V.; Grilli, S.; Ferraro, P.; Netti, P. A. Reversible Holographic Patterns on Azopolymers for Guiding Cell Adhesion and Orientation. *ACS Appl. Mater. Interfaces* **2015**, *7* (31), 16984–16991. https://doi.org/10.1021/acsami.5b02080.

(215) Audia, B.; Fedele, C.; Tone, C. M.; Cipparrone, G.; Priimagi, A. Surface Stability of Azobenzene-Based Thin Films in Aqueous Environment: Light-Controllable Underwater Blistering. *Advanced Materials Interfaces* **2022**, *9* (9), 2102125. https://doi.org/10.1002/admi.202102125.

(216) Rianna, C.; Ventre, M.; Cavalli, S.; Radmacher, M.; Netti, P. A. Micropatterned Azopolymer Surfaces Modulate Cell Mechanics and Cytoskeleton Structure. *ACS Appl. Mater. Interfaces* **2015**, *7* (38), 21503–21510. https://doi.org/10.1021/acsami.5b06693.

(217) De Martino, S.; Zhang, W.; Klausen, L.; Lou, H.-Y.; Li, X.; Alfonso, F. S.; Cavalli, S.; Netti, P. A.; Santoro, F.; Cui, B. Dynamic Manipulation of Cell Membrane Curvature by Light-Driven Reshaping of Azopolymer. *Nano Lett.* **2020**, *20* (1), 577–584. https://doi.org/10.1021/acs.nanolett.9b04307.

(218) Rocha, L.; Păiuş, C.-M.; Luca-Raicu, A.; Resmerita, E.; Rusu, A.; Moleavin, I.-A.; Hamel, M.; Branza-Nichita, N.; Hurduc, N. Azobenzene Based Polymers as Photoactive Supports and Micellar Structures for Applications in Biology. *Journal of Photochemistry and Photobiology A: Chemistry* **2014**, *291*, 16–25. https://doi.org/10.1016/j.jphotochem.2014.06.018.

(219) Isomäki, M.; Fedele, C.; Kääriäinen, L.; Mäntylä, E.; Nymark, S.; Ihalainen, T. O.; Priimagi, A. Light-Responsive Bilayer Cell Culture Platform for Reversible Cell Guidance. *Small Science* **2022**, *2* (3), 2100099. https://doi.org/10.1002/smsc.202100099.

(220) Rianna, C.; Rossano, L.; Kollarigowda, R. H.; Formiggini, F.; Cavalli, S.; Ventre, M.; Netti, P. A. Spatio-Temporal Control of Dynamic Topographic Patterns on Azopolymers for Cell Culture Applications. *Advanced Functional Materials* **2016**, *26* (42), 7572–7580. https://doi.org/10.1002/adfm.201602577.

(221) Ohdaira, Y.; Ikeda, Y.; Oka, H.; Shinbo, K. Optically Reversible Deformation of Azobenzene Particles Prepared by a Colloidal Method. *Journal of Applied Physics* **2019**, *125* (10), 103104. https://doi.org/10.1063/1.5086954.

(222) Pirani, F.; Angelini, A.; Ricciardi, S.; Frascella, F.; Descrovi, E. Laser-Induced Anisotropic Wettability on Azopolymeric Micro-Structures. *Applied Physics Letters* **2017**, *110* (10), 101603. https://doi.org/10.1063/1.4978260.

(223) Oscurato, S. L.; Borbone, F.; Maddalena, P.; Ambrosio, A. Light-Driven Wettability Tailoring of Azopolymer Surfaces with Reconfigured Three-Dimensional Posts. *ACS Appl. Mater. Interfaces* **2017**, *9* (35), 30133–30142. https://doi.org/10.1021/acsami.7b08025.

(224) Zong, C.; Zhao, Y.; Ji, H.; Han, X.; Xie, J.; Wang, J.; Cao, Y.; Jiang, S.; Lu, C. Tuning and Erasing Surface Wrinkles by Reversible Visible-Light-Induced Photoisomerization. *Angewandte Chemie International Edition* **2016**, *55* (12), 3931–3935. https://doi.org/10.1002/anie.201510796.

(225) Takeshima, T.; Liao, W.; Nagashima, Y.; Beppu, K.; Hara, M.; Nagano, S.; Seki, T. Photoresponsive Surface Wrinkle Morphologies in Liquid Crystalline Polymer Films. *Macromolecules* **2015**, *48* (18), 6378–6384. https://doi.org/10.1021/acs.macromol.5b01577.

(226) Vapaavuori, J.; Stimpson, T. C.; Moran-Mirabal, J. M. Dynamically Evolving Surface Patterns through Light-Triggered Wrinkling Erasure. *Langmuir* **2019**, *35* (4), 875–881. https://doi.org/10.1021/acs.langmuir.8b03542.

(227) Lange, S.; Ricoeur, A. High Cycle Fatigue Damage and Life Time Prediction for Tetragonal Ferroelectrics under Electromechanical Loading. *International Journal of Solids and Structures* **2016**, *80*, 181–192. https://doi.org/10.1016/j.ijsolstr.2015.11.003.

(228) Serak, S.; Tabiryan, N.; Vergara, R.; J. White, T.; A. Vaia, R.; J. Bunning, T. Liquid Crystalline Polymer Cantilever Oscillators Fueled by Light. *Soft Matter* **2010**, *6* (4), 779–783. https://doi.org/10.1039/B916831A.

(229) Zeng, H.; Lahikainen, M.; Liu, L.; Ahmed, Z.; Wani, O. M.; Wang, M.; Yang, H.; Priimagi, A. Light-Fuelled Freestyle Self-Oscillators. *Nat Commun* **2019**, *10* (1), 5057. https://doi.org/10.1038/s41467-019-13077-6.

(230) Fuchi, K.; H. Ware, T.; R. Buskohl, P.; W. Reich, G.; A. Vaia, R.; J. White, T.; J. Joo, J. Topology Optimization for the Design of Folding Liquid Crystal Elastomer Actuators. *Soft Matter* **2015**, *11* (37), 7288–7295. https://doi.org/10.1039/C5SM01671A.

(231) Broer, D. J.; Hikmet, R. A. M.; Challa, G. In-Situ Photopolymerization of Oriented Liquid-Crystalline Acrylates, 4. Influence of a Lateral Methyl Substituent on Monomer and Oriented Polymer Network Properties of a Mesogenic Diacrylate. *Die Makromolekulare Chemie* **1989**, *190* (12), 3201–3215. https://doi.org/10.1002/macp.1989.021901218.

(232) Thomsen, D. L.; Keller, P.; Naciri, J.; Pink, R.; Jeon, H.; Shenoy, D.; Ratna, B. R. Liquid Crystal Elastomers with Mechanical Properties of a Muscle. *Macromolecules* **2001**, *34* (17), 5868–5875. https://doi.org/10.1021/ma001639q.

(233) Küpfer, J.; Finkelmann, H. Nematic Liquid Single Crystal Elastomers. *Die Makromolekulare Chemie, Rapid Communications* **1991**, *12* (12), 717–726. https://doi.org/10.1002/marc.1991.030121211.

(234) Yang, R.; Zhao, Y. Non-Uniform Optical Inscription of Actuation Domains in a Liquid Crystal Polymer of Uniaxial Orientation: An Approach to Complex and Programmable Shape Changes. *Angewandte Chemie* **2017**, *129* (45), 14390–14394. https://doi.org/10.1002/ange.201709528.

(235) Li, M.-H.; Keller, P.; Li, B.; Wang, X.; Brunet, M. Light-Driven Side-On Nematic Elastomer Actuators. *Advanced Materials* **2003**, *15* (7–8), 569–572. https://doi.org/10.1002/adma.200304552.

(236) Broer, D. J. Creation of Supramolecular Thin Film Architectures with Liquid-Crystalline Networks. *Molecular Crystals and Liquid Crystals Science and Technology. Section A. Molecular Crystals and Liquid Crystals* **1995**, *261* (1), 513–523. https://doi.org/10.1080/10587259508033494.

(237) Sousa, M. E.; Broer, D. J.; Bastiaansen, C. W. M.; Freund, L. B.; Crawford, G. P. Isotropic “Islands” in a Cholesteric “Sea”: Patterned Thermal Expansion for Responsive Surface Topologies. *Advanced Materials* **2006**, *18* (14), 1842–1845. https://doi.org/10.1002/adma.200502733.

(238) Shannon, P. J.; Gibbons, W. M.; Sun, S. T. Patterned Optical Properties in Photopolymerized Surface-Aligned Liquid-Crystal Films. *Nature* **1994**, *368* (6471), 532–533. https://doi.org/10.1038/368532a0.

(239) McConney, M. E.; Martinez, A.; Tondiglia, V. P.; Lee, K. M.; Langley, D.; Smalyukh, I. I.; White, T. J. Topography from Topology: Photoinduced Surface Features Generated in Liquid Crystal Polymer Networks. *Advanced Materials* **2013**, *25* (41), 5880–5885. https://doi.org/10.1002/adma.201301891.

(240) de Haan, L. T.; Sánchez-Somolinos, C.; Bastiaansen, C. M. W.; Schenning, A. P. H. J.; Broer, D. J. Engineering of Complex Order and the Macroscopic Deformation of Liquid Crystal Polymer Networks. *Angewandte Chemie International Edition* **2012**, *51* (50), 12469–12472. https://doi.org/10.1002/anie.201205964.

(241) de Haan, L. T.; Gimenez-Pinto, V.; Konya, A.; Nguyen, T.-S.; Verjans, J. M. N.; Sánchez-Somolinos, C.; Selinger, J. V.; Selinger, R. L. B.; Broer, D. J.; Schenning, A. P. H. J. Accordion-like Actuators of Multiple 3D Patterned Liquid Crystal Polymer Films. *Advanced Functional Materials* **2014**, *24* (9), 1251–1258. https://doi.org/10.1002/adfm.201302568.

(242) Ware, T. H.; McConney, M. E.; Wie, J. J.; Tondiglia, V. P.; White, T. J. Voxelated Liquid Crystal Elastomers. *Science* **2015**, *347* (6225), 982–984. https://doi.org/10.1126/science.1261019.

(243) Babakhanova, G.; Turiv, T.; Guo, Y.; Hendrikx, M.; Wei, Q.-H.; Schenning, A. P. H. J.; Broer, D. J.; Lavrentovich, O. D. Liquid Crystal Elastomer Coatings with Programmed Response of Surface Profile. *Nat Commun* **2018**, *9* (1), 456. https://doi.org/10.1038/s41467-018-02895-9.

(244) Wani, O. M.; Zeng, H.; Wasylczyk, P.; Priimagi, A. Programming Photoresponse in Liquid Crystal Polymer Actuators with Laser Projector. *Advanced Optical Materials* **2018**, *6* (1), 1700949. https://doi.org/10.1002/adom.201700949.

(245) Tabiryan, N. V.; Serak, S. V.; Nersisyan, S. R.; Roberts, D. E.; Zeldovich, B. Y.; Steeves, D. M.; Kimball, B. R. Broadband Waveplate Lenses. *Opt. Express, OE* **2016**, *24* (7), 7091–7102. https://doi.org/10.1364/OE.24.007091.

(246) Zeng, H.; Wasylczyk, P.; Cerretti, G.; Martella, D.; Parmeggiani, C.; Wiersma, D. S. Alignment Engineering in Liquid Crystalline Elastomers: Free-Form Microstructures with Multiple Functionalities. *Appl. Phys. Lett.* **2015**, *106* (11), 111902. https://doi.org/10.1063/1.4915268.

(247) Xia, Y.; Cedillo-Servin, G.; Kamien, R. D.; Yang, S. Guided Folding of Nematic Liquid Crystal Elastomer Sheets into 3D via Patterned 1D Microchannels. *Advanced Materials* **2016**, *28* (43), 9637–9643. https://doi.org/10.1002/adma.201603751.

(248) Guo, Y.; Shahsavan, H.; Sitti, M. 3D Microstructures of Liquid Crystal Networks with Programmed Voxelated Director Fields. *Advanced Materials* **2020**, *32* (38), 2002753. https://doi.org/10.1002/adma.202002753.

(249) Liu, D.; Bastiaansen, C. W. M.; den Toonder, J. M. J.; Broer, D. J. Photo-Switchable Surface Topologies in Chiral Nematic Coatings. *Angewandte Chemie International Edition* **2012**, *51* (4), 892–896. https://doi.org/10.1002/anie.201105101.

(250) Liu, D.; Broer, D. J. Self-Assembled Dynamic 3D Fingerprints in Liquid-Crystal Coatings Towards Controllable Friction and Adhesion. *Angewandte Chemie International Edition* **2014**, *53* (18), 4542–4546. https://doi.org/10.1002/anie.201400370.

(251) Turiv, T.; Krieger, J.; Babakhanova, G.; Yu, H.; Shiyanovskii, S. V.; Wei, Q.-H.; Kim, M.-H.; Lavrentovich, O. D. Topology Control of Human Fibroblast Cells Monolayer by Liquid Crystal Elastomer. *Science Advances* **2020**, *6* (20), eaaz6485. https://doi.org/10.1126/sciadv.aaz6485.

(252) Liu, D.; Broer, D. J. Liquid Crystal Polymer Networks: Preparation, Properties, and Applications of Films with Patterned Molecular Alignment. *Langmuir* **2014**, *30* (45), 13499–13509. https://doi.org/10.1021/la500454d.

(253) Feng, W.; Liu, D.; Broer, D. J. Functional Liquid Crystal Polymer Surfaces with Switchable Topographies. *Small Structures* **2021**, *2* (1), 2000107. https://doi.org/10.1002/sstr.202000107.

(254) Nocentini, S.; Martella, D.; Parmeggiani, C.; Wiersma, D. S. 3D Printed Photoresponsive Materials for Photonics. *Adv. Optical Mater.* **2019**, *7* (16), 1900156. https://doi.org/10.1002/adom.201900156.

(255) Nocentini, S.; Riboli, F.; Burresi, M.; Martella, D.; Parmeggiani, C.; Wiersma, D. S. Three-Dimensional Photonic Circuits in Rigid and Soft Polymers Tunable by Light. *ACS Photonics* **2018**, *5* (8), 3222–3230. https://doi.org/10.1021/acsphotonics.8b00461.

(256) Woska, S.; Münchinger, A.; Beutel, D.; Blasco, E.; Hessenauer, J.; Karayel, O.; Rietz, P.; Pfleging, S.; Oberle, R.; Rockstuhl, C.; Wegener, M.; Kalt, H. Tunable Photonic Devices by 3D Laser Printing of Liquid Crystal Elastomers. *Opt. Mater. Express* **2020**, *10* (11), 2928. https://doi.org/10.1364/OME.402855.

(257) Zeng, H.; Wasylczyk, P.; Parmeggiani, C.; Martella, D.; Burresi, M.; Wiersma, D. S. Light-Fueled Microscopic Walkers. *Advanced Materials* **2015**, *27* (26), 3883–3887. https://doi.org/10.1002/adma.201501446.

(258) Münchinger, A.; Hahn, V.; Beutel, D.; Woska, S.; Monti, J.; Rockstuhl, C.; Blasco, E.; Wegener, M. Multi-Photon 4D Printing of Complex Liquid Crystalline Microstructures by In Situ Alignment Using Electric Fields. *Advanced Materials Technologies* **2022**, *7* (1), 2100944. https://doi.org/10.1002/admt.202100944.

(259) Gong, Y.-H.; Yang, J.; Cao, F.-Y.; Zhang, J.; Cheng, H.; Zhuo, R.-X.; Zhang, X.-Z. Photoresponsive Smart Template for Reversible Cell Micropatterning. *J. Mater. Chem. B* **2013**, *1* (15), 2013. https://doi.org/10.1039/c3tb20073f.

(260) Bian, Q.; Wang, W.; Wang, S.; Wang, G. Light-Triggered Specific Cancer Cell Release from Cyclodextrin/Azobenzene and Aptamer-Modified Substrate. *ACS Appl. Mater. Interfaces* **2016**, *8* (40), 27360–27367. https://doi.org/10.1021/acsami.6b09734.

(261) Wang, D.; Schellenberger, F.; T. Pham, J.; Butt, H.-J.; Wu, S. Orthogonal Photo-Switching of Supramolecular Patterned Surfaces. *Chemical Communications* **2018**, *54* (27), 3403–3406. https://doi.org/10.1039/C8CC00770E.

(262) Feldmann, D.; Arya, P.; Molotilin, T. Y.; Lomadze, N.; Kopyshev, A.; Vinogradova, O. I.; Santer, S. A. Extremely Long-Range Light-Driven Repulsion of Porous Microparticles. *Langmuir* **2020**, *36* (25), 6994–7004. https://doi.org/10.1021/acs.langmuir.9b03270.

(263) Sharma, A.; Bekir, M.; Lomadze, N.; Jung, S.-H.; Pich, A.; Santer, S. Generation of Local Diffusioosmotic Flow by Light Responsive Microgels. *Langmuir* **2022**, *38* (20), 6343–6351. https://doi.org/10.1021/acs.langmuir.2c00259.

(264) Arya, P.; Jelken, J.; Feldmann, D.; Lomadze, N.; Santer, S. Light Driven Diffusioosmotic Repulsion and Attraction of Colloidal Particles. *The Journal of Chemical Physics* **2020**, *152* (19), 194703. https://doi.org/10.1063/5.0007556.

(265) Arya, P.; Umlandt, M.; Jelken, J.; Feldmann, D.; Lomadze, N.; Asmolov, E. S.; Vinogradova, O. I.; Santer, S. Light-Induced Manipulation of Passive and Active Microparticles. *Eur. Phys. J. E* **2021**, *44* (4), 50. https://doi.org/10.1140/epje/s10189-021-00032-x.

(266) Bekir, M.; Sperling, M.; Muñoz, D. V.; Braksch, C.; Böker, A.; Lomadze, N.; Popescu, M. N.; Santer, S. Versatile Microfluidics Separation of Colloids by Combining External Flow with Light-Induced Chemical Activity. *Advanced Materials* **2023**, *35* (25), 2300358. https://doi.org/10.1002/adma.202300358.

(267) Priimagi, A.; Shevchenko, A. Azopolymer-Based Micro- and Nanopatterning for Photonic Applications. *Journal of Polymer Science Part B: Polymer Physics* **2014**, *52* (3), 163–182. https://doi.org/10.1002/polb.23390.

(268) Choi, J.; Jo, W.; Lee, S. Y.; Jung, Y. S.; Kim, S.-H.; Kim, H.-T. Flexible and Robust Superomniphobic Surfaces Created by Localized Photofluidization of Azopolymer Pillars. *ACS Nano* **2017**, *11* (8), 7821–7828. https://doi.org/10.1021/acsnano.7b01783.

(269) Lee, S.; Kang, H. S.; Park, J.-K. High-Resolution Patterning of Various Large-Area, Highly Ordered Structural Motifs by Directional Photofluidization Lithography: Sub-30-Nm Line, Ellipsoid, Rectangle, and Circle Arrays. *Advanced Functional Materials* **2011**, *21* (10), 1770–1778. https://doi.org/10.1002/adfm.201001927.

(270) Kang, H. S.; Lee, S.; Park, J.-K. Monolithic, Hierarchical Surface Reliefs by Holographic Photofluidization of Azopolymer Arrays: Direct Visualization of Polymeric Flows. *Advanced Functional Materials* **2011**, *21* (23), 4412–4422. https://doi.org/10.1002/adfm.201101203.

(271) Jeong, Y. J.; Park, K. J.; Kim, K.; Lee, S.; Yoo, P. J. Uniaxial Alignment of ZnO Nanowires via Light-Induced Directional Migration of Azopolymeric Microspheres. *Polymer* **2018**, *138*, 180–187. https://doi.org/10.1016/j.polymer.2018.01.068.

(272) Nedelchev, L.; Ivanov, D.; Berberova, N.; Strijkova, V.; Nazarova, D. Polarization Holographic Gratings with High Diffraction Efficiency Recorded in Azopolymer PAZO. *Opt Quant Electron* **2018**, *50* (5), 212. https://doi.org/10.1007/s11082-018-1479-z.

(273) Yager, K. G.; Barrett, C. J. Confinement of Surface Patterning in Azo-Polymer Thin Films. *The Journal of Chemical Physics* **2007**, *126* (9), 094908. https://doi.org/10.1063/1.2538787.

(274) Kulikovska, O.; Gharagozloo-Hubmann, K.; Stumpe, J.; Huey, B. D.; Bliznyuk, V. N. Formation of Surface Relief Grating in Polymers with Pendant Azobenzene Chromophores as Studied by AFM/UFM. *Nanotechnology* **2012**, *23* (48), 485309. https://doi.org/10.1088/0957-4484/23/48/485309.

(275) Kozanecka-Szmigiel, A.; Hernik, A.; Rutkowska, K.; Konieczkowska, J.; Schab-Balcerzak, E.; Szmigiel, D. Surface Relief Modulated Grating in Azo Polymer—From the Tailoring of Diffraction Order to Reshaping of a Laser Beam. *Materials* **2022**, *15* (22), 8088. https://doi.org/10.3390/ma15228088.

(276) Fukuda, T.; Matsuda, H.; Shiraga, T.; Kimura, T.; Kato, M.; Viswanathan, N. K.; Kumar, J.; Tripathy, S. K. Photofabrication of Surface Relief Grating on Films of Azobenzene Polymer with Different Dye Functionalization. *Macromolecules* **2000**, *33* (11), 4220–4225. https://doi.org/10.1021/ma991803d.

(277) Wang, D. H.; Lee, K. M.; Yu, Z.; Koerner, H.; Vaia, R. A.; White, T. J.; Tan, L.-S. Photomechanical Response of Glassy Azobenzene Polyimide Networks. *Macromolecules* **2011**, *44* (10), 3840–3846. https://doi.org/10.1021/ma200427q.

(278) Wang, D. H.; Lee, K. M.; Koerner, H.; Yu, Z.; Vaia, R. A.; White, T. J.; Tan, L.-S. Flexural-Torsional Photomechanical Responses in Azobenzene-Containing Crosslinked Polyimides. *Macromolecular Materials and Engineering* **2012**, *297* (12), 1167–1174. https://doi.org/10.1002/mame.201200240.

(279) Wie, J. J.; Wang, D. H.; Lee, K. M.; Tan, L.-S.; White, T. J. Molecular Engineering of Azobenzene-Functionalized Polyimides To Enhance Both Photomechanical Work and Motion. *Chem. Mater.* **2014**, *26* (18), 5223–5230. https://doi.org/10.1021/cm5018757.

(280) Tabiryan, N.; Serak, S.; Dai, X.-M.; Bunning, T. Polymer Film with Optically Controlled Form and Actuation. *Opt. Express, OE* **2005**, *13* (19), 7442–7448. https://doi.org/10.1364/OPEX.13.007442.

(281) Hrozhyk, U.; Serak, S.; Tabiryan, N.; White, T. J.; Bunning, T. J. Bidirectional Photoresponse of Surface Pretreated Azobenzene Liquid Crystal Polymer Networks. *Opt. Express, OE* **2009**, *17* (2), 716–722. https://doi.org/10.1364/OE.17.000716.

(282) White, T. J.; Serak, S. V.; Tabiryan, N. V.; Vaia, R. A.; Bunning, T. J. Polarization-Controlled, Photodriven Bending in Monodomain Liquid Crystal Elastomer Cantilevers. *J. Mater. Chem.* **2009**, *19* (8), 1080–1085. https://doi.org/10.1039/B818457G.

(283) Serak, S. V.; Tabiryan, N. V.; White, T. J.; Bunning, T. J. Azobenzene Liquid Crystal Polymer-Based Membrane and Cantilever Optical Systems. *Opt. Express, OE* **2009**, *17* (18), 15736–15746. https://doi.org/10.1364/OE.17.015736.

(284) Liu, J.; He, Y.; Wang, X. Influence of Chromophoric Electron-Withdrawing Groups on Photoinduced Deformation of Azo Polymer Colloids. *Polymer* **2010**, *51* (13), 2879–2886. https://doi.org/10.1016/j.polymer.2010.04.048.

(285) Zhou, Y.; Liu, B.; Wang, X. Microspheres of Polyurethanes Functionalized with *Push-Pull* Type Azo Chromophores and Their Photoinduced Deformation Behavior. *Polymer* **2017**, *111*, 229–238. https://doi.org/10.1016/j.polymer.2017.01.050.

(286) Liu, J.; He, Y.; Wang, X. Size-Dependent Light-Driven Effect Observed for Azo Polymer Colloidal Spheres with Different Average Diameters. *Langmuir* **2009**, *25* (10), 5974–5979. https://doi.org/10.1021/la8042395.

(287) Zhou, X.; Du, Y.; Wang, X. Azo Polymer Janus Particles and Their Photoinduced, Symmetry-Breaking Deformation. *ACS Macro Lett.* **2016**, *5* (2), 234–237. https://doi.org/10.1021/acsmacrolett.5b00932.

(288) Fabbri, F. Kinetics of Photoinduced Matter Transport Driven by Intensity and Polarization in Thin Films Containing Azobenzene. *Phys. Rev. B* **2012**, *86* (11). https://doi.org/10.1103/PhysRevB.86.115440.

(289) Kamaliardakani, M.; Vapaavuori, J.; Wang, X.; Sabat, R. G.; Bazuin, C. G.; Pellerin, C. Molecular-Level Photo-Orientation Insights into Macroscopic Photo-Induced Motion in Azobenzene-Containing Polymer Complexes. *J. Phys. Chem. B* **2021**, *125* (28), 7871–7885. https://doi.org/10.1021/acs.jpcb.1c01988.

(290) Ishitobi, H.; Tanabe, M.; Sekkat, Z.; Kawata, S. The Anisotropic Nanomovement of Azo-Polymers. *Opt. Express, OE* **2007**, *15* (2), 652–659. https://doi.org/10.1364/OE.15.000652.

(291) Loebner, S.; Yadav, B.; Lomadze, N.; Tverdokhleb, N.; Donner, H.; Saphiannikova, M.; Santer, S. Local Direction of Optomechanical Stress in Azobenzene Containing Polymers During Surface Relief Grating Formation. *Macromolecular Materials and Engineering* **2022**, *307* (8), 2100990. https://doi.org/10.1002/mame.202100990.

(292) Min Lee, K.; Lynch, B. M.; Luchette, P.; White, T. J. Photomechanical Effects in Liquid Crystal Polymer Networks Prepared with M-Fluoroazobenzene. *Journal of Polymer Science Part A: Polymer Chemistry* **2014**, *52* (6), 876–882. https://doi.org/10.1002/pola.27072.

(293) Donovan, B. R.; Matavulj, V. M.; Ahn, S.; Guin, T.; White, T. J. All-Optical Control of Shape. *Advanced Materials* **2019**, *31* (2), 1805750. https://doi.org/10.1002/adma.201805750.

(294) J. White, T.; V. Tabiryan, N.; V. Serak, S.; A. Hrozhyk, U.; P. Tondiglia, V.; Koerner, H.; A. Vaia, R.; J. Bunning, T. A High Frequency Photodriven Polymer Oscillator. *Soft Matter* **2008**, *4* (9), 1796–1798. https://doi.org/10.1039/B805434G.

(295) Vantomme, G.; Elands, L. C. M.; Gelebart, A. H.; Meijer, E. W.; Pogromsky, A. Y.; Nijmeijer, H.; Broer, D. J. Coupled Liquid Crystalline Oscillators in Huygens' Synchrony. *Nature Materials* **2021**, 1–5. https://doi.org/10.1038/s41563-021-00931-6.

(296) Cheng, M.; Zeng, H.; Li, Y.; Liu, J.; Luo, D.; Priimagi, A.; Liu, Y. J. Light-Fueled Polymer Film Capable of Directional Crawling, Friction-Controlled Climbing, and Self-Sustained Motion on a Human Hair. *Advanced Science* **2022**, *9* (1), 2103090. https://doi.org/10.1002/advs.202103090.

(297) Gelebart, A. H.; Jan Mulder, D.; Varga, M.; Konya, A.; Vantomme, G.; Meijer, E. W.; Selinger, R. L. B.; Broer, D. J. Making Waves in a Photoactive Polymer Film. *Nature* **2017**, *546* (7660), 632–636. https://doi.org/10.1038/nature22987.

(298) Lahikainen, M.; Zeng, H.; Priimagi, A. Design Principles for Non-Reciprocal Photomechanical Actuation. *Soft Matter* **2020**, *16* (25), 5951–5958. https://doi.org/10.1039/D0SM00624F.

(299) Palagi, S.; Mark, A. G.; Reigh, S. Y.; Melde, K.; Qiu, T.; Zeng, H.; Parmeggiani, C.; Martella, D.; Sanchez-Castillo, A.; Kapernaum, N.; Giesselmann, F.; Wiersma, D. S.; Lauga, E.; Fischer, P. Structured Light Enables Biomimetic Swimming and Versatile Locomotion of Photoresponsive Soft Microrobots. *Nature Mater* **2016**, *15* (6), 647–653. https://doi.org/10.1038/nmat4569.

(300) Uchida, E.; Azumi, R.; Norikane, Y. Light-Induced Crawling of Crystals on a Glass Surface. *Nat Commun* **2015**, *6* (1), 7310. https://doi.org/10.1038/ncomms8310.

(301) Saito, K.; Ichiyanagi, K.; Nozawa, S.; Haruki, R.; Fan, D.; Kanazawa, T.; Norikane, Y. Transportation of Nano/Microparticles via Photoinduced Crawling of Azobenzene Crystals. *Advanced Materials Interfaces* **2023**, *10* (13), 2202525. https://doi.org/10.1002/admi.202202525.

(302) Yamada, M.; Kondo, M.; Mamiya, J.; Yu, Y.; Kinoshita, M.; Barrett, C. J.; Ikeda, T. Photomobile Polymer Materials: Towards Light-Driven Plastic Motors. *Angewandte Chemie International Edition* **2008**, *47* (27), 4986–4988. https://doi.org/10.1002/anie.200800760.

(303) Deng, Z.; Li, K.; Priimagi, A.; Zeng, H. Light-Steerable Locomotion Using Zero-Elastic-Energy Modes. *Nat. Mater.* **2024**, 1–8. https://doi.org/10.1038/s41563-024-02026-4.

(304) Feldmann, D.; Maduar, S. R.; Santer, M.; Lomadze, N.; Vinogradova, O. I.; Santer, S. Manipulation of Small Particles at Solid Liquid Interface: Light Driven Diffusioosmosis. *Scientific Reports* **2016**, *6* (1), 36443. https://doi.org/10.1038/srep36443.

(305) Singleton, T. A.; Burgess, I. B.; Nerger, B. A.; Goulet-Hanssens, A.; Koay, N.; Barrett, C. J.; Aizenberg, J. Photo-Tuning of Highly Selective Wetting in Inverse Opals. *Soft Matter* **2014**, *10* (9), 1325–1328. https://doi.org/10.1039/C3SM52684D.

(306) Li, G.; Park, S.; Rittmann, B. E. Degradation of Reactive Dyes in a Photocatalytic Circulating-Bed Biofilm Reactor. *Biotechnology and Bioengineering* **2012**, *109* (4), 884–893. https://doi.org/10.1002/bit.24366.

(307) Gilbert, Y.; Bachelot, R.; Royer, P.; Bouhelier, A.; Wiederrecht, G. P.; Novotny, L. Longitudinal Anisotropy of the Photoinduced Molecular Migration in Azobenzene Polymer Films. *Opt. Lett., OL* **2006**, *31* (5), 613–615. https://doi.org/10.1364/OL.31.000613.

(308) Grosjean, T.; Courjon, D. Photopolymers as Vectorial Sensors of the Electric Field. *Opt. Express, OE* **2006**, *14* (6), 2203–2210. https://doi.org/10.1364/OE.14.002203.

(309) Ishitobi, H.; Nakamura, I.; Kobayashi, T.; Hayazawa, N.; Sekkat, Z.; Kawata, S.; Inouye, Y. Nanomovement of Azo Polymers Induced by Longitudinal Fields. *ACS Photonics* **2014**, *1* (3), 190–197. https://doi.org/10.1021/ph400052b.

(310) Botto, L.; P. Lewandowski, E.; Cavallaro, M.; J. Stebe, K. Capillary Interactions between Anisotropic Particles. *Soft Matter* **2012**, *8* (39), 9957–9971. https://doi.org/10.1039/C2SM25929J.

(311) Ho, M.-S.; Natansohn, A.; Barrett, C.; Rochon, P. Azo Polymers for Reversible Optical Storage. 8. The Effect of Polarity of the Azobenzene Groups. *Can. J. Chem.* **1995**, *73* (11), 1773–1778. https://doi.org/10.1139/v95-218.

(312) Lee, S.; Kang, H. S.; Ambrosio, A.; Park, J.-K.; Marrucci, L. Directional Superficial Photofluidization for Deterministic Shaping of Complex 3D Architectures. *ACS Appl. Mater. Interfaces* **2015**, *7* (15), 8209–8217. https://doi.org/10.1021/acsami.5b01108.

(313) Huang, H.; Wang, Z.; Li, X.; Yang, F.; Su, Y.; Xu, J.; Wang, X. Directional Mass Transfer of Azo Molecular Glass Microsphere Induced by Polarized Light in Aqueous Immersion Media. *RSC Advances* **2021**, *11* (25), 15387–15399. https://doi.org/10.1039/D1RA01904J.

(314) Januariyasa, I. K.; Borbone, F.; Salvatore, M.; Oscurato, S. L. Wavelength-Dependent Shaping of Azopolymer Micropillars for Three-Dimensional Structure Control. *ACS Appl. Mater. Interfaces* **2023**, *15* (36), 43183–43192. https://doi.org/10.1021/acsami.3c09264.

(315) Huang, H.; Su, Y.; Xu, J.; Wang, X. Asymmetric Morphology Transformation of Azo Molecular Glass Microspheres Induced by Polarized Light. *Langmuir* **2019**, *35* (47), 15295–15305. https://doi.org/10.1021/acs.langmuir.9b02882.

(316) Koskela, J. E.; Vapaavuori, J.; Ras, R. H. A.; Priimagi, A. Light-Driven Surface Patterning of Supramolecular Polymers with Extremely Low Concentration of Photoactive Molecules. *ACS Macro Lett.* **2014**, *3* (11), 1196–1200. https://doi.org/10.1021/mz500616q.

(317) De Boni, L.; Misoguti, L.; Zílio, S. C.; Mendonça, C. R. Degenerate Two-Photon Absorption Spectra in Azoaromatic Compounds. *ChemPhysChem* **2005**, *6* (6), 1121–1125. https://doi.org/10.1002/cphc.200400391.

(318) Ishitobi, H.; Shoji, S.; Hiramatsu, T.; Sun, H.-B.; Sekkat, Z.; Kawata, S. Two-Photon Induced Polymer Nanomovement. *Opt. Express* **2008**, *16* (18), 14106. https://doi.org/10.1364/OE.16.014106.

(319) Battat, S.; Weitz, D. A.; Whitesides, G. M. Nonlinear Phenomena in Microfluidics. *Chem. Rev.* **2022**, *122* (7), 6921–6937. https://doi.org/10.1021/acs.chemrev.1c00985.

(320) Schiphorst, J. ter; Saez, J.; Diamond, D.; Benito-Lopez, F.; J. Schenning, A. P. H. Light-Responsive Polymers for Microfluidic Applications. *Lab on a Chip* **2018**, *18* (5), 699–709. https://doi.org/10.1039/C7LC01297G.

(321) Martinelli, E.; Akouissi, O.; Liebi, L.; Furfaro, I.; Maulà, D.; Savoia, N.; Remy, A.; Nikles, L.; Roux, A.; Stoppini, L.; Lacour, S. P. The E-Flower: A Hydrogel-Actuated 3D MEA for Brain Spheroid Electrophysiology. *Science Advances* **2024**, *10* (42), eadp8054. https://doi.org/10.1126/sciadv.adp8054.

(322) Sugiura, S.; Sumaru, K.; Ohi, K.; Hiroki, K.; Takagi, T.; Kanamori, T. Photoresponsive Polymer Gel Microvalves Controlled by Local Light Irradiation. *Sensors and Actuators A: Physical* **2007**, *140* (2), 176–184. https://doi.org/10.1016/j.sna.2007.06.024.

VI. Index List

absorption-induced gradients 30, 32, 34, 54
actuation cycles 25, 26
actuator 15, 16, 26, 34, 44, 48, 52, 53, 58
amorphous sidechain azopolymers 10, 27, 29, 32
azo molecular glass 12, 13, 20, 54
azo thin films 8, 13, 20, 51, 55
azobenzene moiety 4, 18
azobenzene sidechains 11
azobenzene-derived chromophore 3
azobenzene-derived molecules 13, 16, 17
azobenzene-type 4
azopolymer particles 9, 12, 22, 29, 38, 44, 46, 55
backbone 10
backbone reorientation 11
bending 15, 16, 25, 26, 27, 30, 32, 34, 35, 44, 53, 55
bioengineering applications 20, 26, 57
birefringence 5, 8, 11, 17, 20
birefringent volume grating 20
capillary interactions 16, 38, 52, 53
chiral features 13
circular polarization 8, 12, 13, 20, 24, 52
colloidal azopolymer particles 9, 45
deformation space 51, 52
deformation superposition 19, 20, 22
degrees of freedom 48, 51
dichroism 5
diffusioosmosis 19, 37
directional deformation 3, 9, 26, 44, 46, 48
director 14, 15, 16, 27, 28
director alignment 16, 27, 28
Disperse Red 1 .... 3, 40, 54
DR1 .... 3, 4, 8, 40, 55
edge mode 40
elastic metamaterials 2, 17, 40, 42
elastic modulus 10, 12, 40, 41
elastic waveguide 40
elastomeric matrices 9, 21, 22, 43
embedding of microparticles 21
erasure 20, 25
extinction length 54
flattening 24
free-volume 15, 19
glass transition temperature 10, 13, 20, 50
glassy azopolymer 11
grating period 8
grating superposition 19
guest-host systems 18
holographic bulk gratings 8
in plane expansion 21, 22, 24, 44, 52
interference pattern 8
isomerization 3, 4, 13, 14, 17, 19, 36, 40, 59
isomers 3, 4, 34
LCN 15, 16, 25, 27, 28, 34, 35, 36
liquid crystal elastomers 14
Liquid crystal networks 14
liquid substrates 9
longitudinal electrical field 51
Marangoni flows 19, 34
mass migration 8
Mechanical constraints 33
mesogens 14, 27
micro- and nanopatterning 29
microstructures 9, 13, 20, 21, 28, 33, 52, 55
microwells 9
molecular glasses 13
molecule reorientation 5
nanoindentation 12
near field 10
nematic director 14
optical anisotropies 5
optical axis/z-axis 5, 22
optical near-field 9
optical storage 6
opto-fluidics 56, 59
opto-thermal 51
orientation approach 10, 33
orthogonal linear polarizations 24, 48
oscillating systems 15, 25, 33, 34, 35
overwriting behavior 22
particle flows 46
passive reversibility 21, 22
pDR1-co-mma 40
pDR1m-co-mma 3
photochemical actuation 14, 34

photo-cycling 4
photo-deformation 5, 9, 13, 20, 30, 33, 55
photo-degradation 5, 25
photo-fluidization 10, 11, 33
photo-mechanical 11, 14, 26, 27, 28, 34, 35
photo-mobile 15, 28
photo-orientation 10, 12, 13
photo-sensitive surfactants 19
photo-softening 10, 11, 12, 22, 35
photo-stationary 17, 19, 34, 37
photo-switchable 4, 19, 28
photothermal actuation 14
pillars 9, 30, 40, 54
plastic deformation 19, 44
Poincaré sphere 8, 48
polarization-dependent 9, 29, 32, 33, 42, 52
polarization-directed 9, 13, 19, 29
polarization-induced 5, 17
polarization-sensitive 3, 9, 13, 16, 17, 26, 32, 44, 46, 47, 55, 59
polymer backbone 8, 10
polymer brush systems 12
pseudostilbenes 4
refractive index 5, 17, 19
relative area expansion 24, 85
reorientation 3, 5, 8, 11, 15, 17, 32, 34, 54
reversibility 2, 16, 19, 20, 21, 22, 24, 25, 26, 42, 44, 46, 48, 51, 52, 57, 59
reversibility measure 24
self-healing behavior 12
sidechains 8, 10, 55
sol-gel transitions 19
spin or orbital momentum 13
spindle-like morphologies 30
spiral patterns 13
SRG 8
stationary flow 19
statistical reorientation of dyes 5
supramolecular azopolymers 11, 55
surface relief grating 8, 11, 12, 13, 20, 31, 33
surface tension 19, 30, 32, 33, 34
switching regime 22
thermal relaxation 4, 34, 36
thermoplastic elastomer 16, 43
timescales 11
topography 20
trans-cis-trans 4, 15, 17, 32
trans-cis-trans cycle 4
two-photon absorption **55**
two-photon printed 17, 28
two-photon printing 28, 42
water-air interface 3, 9, 32, 38, 45, 53, 56
Weigert effect 4, 5, 10, 54
wrinkling 9, 11, 25
Young's modulus 17, 43

VII. Appendix A: List of Contributions

Article Contributions:

Article 1. Chaplain, G. J.; Gliozzi, A. S.; Davies, B.; Urban, D.; Descrovi, E.; Bosia, F.; Craster, R. V. Tunable Topological Edge Modes in Su–Schrieffer–Heeger Arrays. Published in *Applied Physics Letters* 2023, 122 (22), 221703. https://doi.org/10.1063/5.0152172.

Thesis Author Contribution: I developed the method/protocol for fabrication and functionalization of the light-responsive elastic metamaterial samples, then produced the physical samples to be tested, wrote the corresponding part in the manuscript, and participated in the reviewing process.

Article 2. Dal Poggetto V. F., Urban D., Nistri F., Beoletto P. H., Descrovi E., Miniaci M., Pugno N. M., Bosia F. and Gliozzi A. S. Selective dynamic band gap tuning in metamaterials using graded photoresponsive resonator arrays. Published in *Philosophical Transactions of the Royal Society A: Mathematical, Physical and Engineering Sciences.* 2024, 382:20240150. https://doi.org/10.1098/rsta.2024.0150.

Thesis Author Contribution: I used the method that I developed in Article 1 to produce the physical samples, wrote the corresponding part in the manuscript, and participated in the reviewing process.

Article 3. Urban, D.; Marcucci, N.; Wölfle, C. H.; Torgersen, J.; Hjelme, D. R.; Descrovi, E. Polarization-Driven Reversible Actuation in a Photo-Responsive Polymer Composite. Published in *Nature Communications* 2023, 14 (1), 6843. https://doi.org/10.1038/s41467-023-42590-y.

Thesis Author Contribution: I contributed to the conception and planning of the work, developed the method for sample fabrication and performed a substantial part of the experiments. Furthermore, I wrote the Fourier-based algorithm used for data analysis (deformation tracking), supported the mechanical modelling of the composites which was led by our collaborators at TUM, conceived the figures and illustrations and wrote the initial draft, as well as participating in and performing experiments at the review stage.

Article 4. Urban, D.; Rey, M.; Ciarlo A.; Descrovi E. & Volpe G. Directional capillary flows induced by photo-deformable colloidal particles. *Article Submitted.*

Thesis Author Contribution: I participated in the conception and planning of the work amongst others by substantially contributing to the initial idea and by initiating the research collaboration. I developed the method for sample fabrication and performed all the experiments, with support from the collaborating authors. In addition, I wrote the crosscorrelation-based algorithm used for quantification of the light-induced flows, conceived the figures and illustrations, and wrote the initial draft.

Conference Contributions:

School of Plasmonics and Nano-Optics and Plasmonica Workshop, June 2022, Turin, Italy. *Poster Presentation*.

European Optical Society Annual Meeting (EOSAM), September 2022, Porto, Portugal. *Oral Presentation.*

European Material Research Society Spring meeting (EMRS), May 2023, Strasbourg, France. *Oral Presentation.*

Conference on Lasers and Electro-Optics/Europe (CLEO®/Europe-EQEC), June 2023, München Germany. *Oral Presentation.*

Norwegian NanoSymposium, Trondheim, November 2023, Norway. *Oral Presentation.*

4th International Conference on Photoalignment and Photopatterning of Soft Matter (Phosm), December 2023, Tampa, Fl, USA. *Oral Presentation.*

Norwegian Electro-Optics Meeting, May 2024, Oskarsborg, Norway. *Oral Presentation.*

Norwegian Nanouser Meeting (NNUM), June 2024, Oslo, Norway. *Poster Presentation.*

VIII. Appendix B: Included Articles

Article 1

Tunable Topological Edge Modes in Su–Schrieffer–Heeger Arrays

Appendix B (Articles): **Pages 1-8**

Article 2

Selective dynamic band gap tuning in metamaterials using graded photoresponsive resonator arrays

Appendix B (Articles): **Pages 9-20**

Article 3

Polarization-Driven Reversible Actuation in a Photo-Responsive Polymer Composite

Appendix B (Articles): **Pages 21-32**

Article 3 – Supplementary Materials

Polarization-Driven Reversible Actuation in a Photo-Responsive Polymer Composite

Appendix B (Articles): **Pages 33-47**

Article 4

Directional capillary flows induced by photo-deformable colloidal particles

Appendix B (Articles): **Pages 48-73**

Article 4 – Supplementary Materials

Directional capillary flows induced by photo-deformable colloidal particles

Appendix B (Articles): **Pages 74-89**

Tunable topological edge modes in Su-Schrieffer-Heeger arrays

G. J. Chaplain,[1] A. S. Gliozzi,[2] B. Davies,[3] D. Urban,[4] E. Descrovi,[2] F. Bosia*,[2] and R. V. Craster*[3]
[1] *Centre for Metamaterial Research and Innovation, Department of Physics and Astronomy, University of Exeter, Exeter EX4 4QL, United Kingdom*
[2] *Department of Applied Science and Technology, Politecnico di Torino, 10129 Torino, Italy*
[3] *Department of Mathematics, Imperial College London, London SW7 2AZ, UK*
[4] *Department of Electronic Systems, Norwegian University of Science and Technology, 7491 Trondheim, Norway*

(*Authors to whom correspondence should be addressed: F. Bosia, federico.bosia@polito.it; R. V. Craster, r.craster@imperial.ac.uk)

A potential weakness of topological waveguides is that they act on a fixed narrow band of frequencies. However, by 3D printing samples from a photo-responsive polymer, we can obtain a device whose operating frequency can be fine-tuned dynamically using laser excitation. This greatly enhances existing static tunability strategies, typically based on modifying the geometry. We use a version of the classical Su-Schrieffer-Heeger (SSH) model to demonstrate our approach.

Topological edge modes perform robust wave localisation at specific frequencies. This makes them an appealing starting point for designing wave control devices. A topological edge mode is formed when symmetries are broken in a periodic system that has a topologically non-trivial band gap, creating an interface along which waves of specific frequencies travel. Due to the underlying band gap material, the waves are unable to propagate away from the interface into the bulk, giving a strong waveguide. The original "topological insulators" were developed in quantum mechanics[1–3], but the principle has since spread across classical wave physics, including electromagnetism, acoustics, elasticity and mechanics[4–7].

An important feature of topological waveguides is that they are frequency specific. This is either a strength or a weakness (depending on perspective) but it means that it is important that the operating frequency can be tuned to suit the application. There are a variety of tunability strategies in the literature, which often rely on geometric manipulation, achieved for example by manufacturing new samples[8,9] or physically moving meta-atoms[10]. Tunability can also be achieved by modulating active elements[11]. Building on these ideas, we have developed a simple approach for tuning the eigenfrequency of the topological edge mode dynamically and remotely by using a laser to locally alter the material mechanical parameters.

We will study a one-dimensional topological system, based on the well-known Su-Schrieffer-Heeger (SSH) model[12], realized with periodically spaced rods on an elastic beam (Fig 1). The SSH model is often regarded as the simplest configuration supporting a topologically non-trivial band gap. One-dimensional topological models are not only convenient toy models but also have important applications, for example in energy harvesting[13] and lasing[14]. The basic principle of the SSH model is arranging elements in pairs with alternating 'strong' and 'weak' coupling strengths (in many classical wave settings, this is realised by alternating 'short' and 'long' separation distances). In this one-dimensional case, the relevant topological index is the Zak phase[15] and edge modes can be created by making a perturbation that creates an interface with different associated Zak phases on either side.

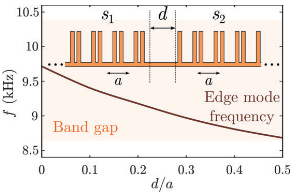

FIG. 1. Tuneable edge mode by dislocation: Frequency domain FEM simulations showing change in edge mode frequency with dislocation length d between two SSH chains s_1, s_2, with unit cell width a. We supplement this with dynamic tunability through the use of a photo-responsive material.

Our approach to tunability has two steps. The first step is to select a geometry that yields an edge mode with the desired eigenfrequency. In the context of the SSH model, this can be done straightforwardly by altering the separation length at the interface, as depicted in Fig 1. Tunable topological edge modes based on this principle have been studied theoretically in both one-dimensional[16] and three-dimensional[17] models. It was shown that varying the separation length causes the eigenfrequency of the topological edge mode to move across the band gap (Fig 1). This idea was motivated by related notions of spectral flow that have been studied in elastic[18] and quantum[19] systems.

The dynamic part of our tunability strategy relies on using photo-responsive polymers for fabrication[20]. Azobenzene-containing dyes are very common molecular photo-switches capable of undergoing a conformational change between two isomeric states upon light absorption[21]. When the two isomer absorption bands have some overlaps, as in this case, photo-isomerization can be cyclic and continuously triggered by single wavelength radiation[22]. In such a disordered arrangement of azo-dyes, the photo-thermal effect is then enhanced by photo-isomerization, leading to fast light-induced changes in the polymer mechanical properties[23]. As detailed below, our samples are 3D printed from a commercial elastic

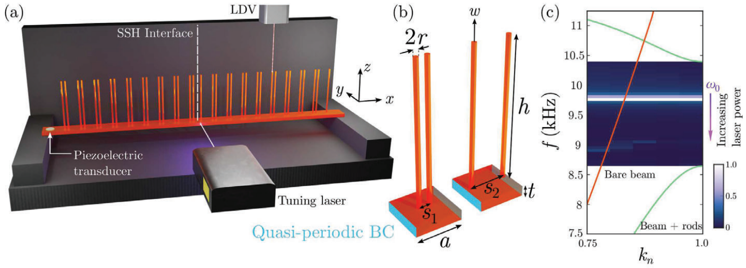

FIG. 2. (a) Schematic of experimental setup. (b) Unit cell geometries. (c) Dispersion curves for bare elastic beam (orange) and for the unit cells shown in (b) (green), plotted against normalised wavevector such that $k_n = 1 \equiv k = \pi/a$. Floquet-Bloch quasi-periodic conditions are employed in the FE eigenfrequency model, shown by the blue surfaces in (b). The out-of-plane displacement (w) in the z-direction (measured in experiments) is also shown. The colourscale in (c) shows normalised Fourier spectra, obtained via time-domain FE simulation (supplementary material), and shows the expected edge mode of frequency ω_0 within bandgap. This frequency ω_0 can be shifted down by increasing the power of the exciting laser.

resin that is impregnated with a dispersed azo-dye, producing significant variations of the Young's modulus upon laser illumination. This presents a mechanism for altering the eigenfrequency of topological edge modes. This is valuable, firstly, for correcting some of the effects of any manufacturing imperfections that may undermine our geometric tunability strategy. However, the photo-responsivity is stronger than this as it augments our tunability strategy by adding the possibility for the eigenfrequency to be tuned dynamically.

We first briefly outline the design of the SSH interface in an elastic wave system consisting of periodically spaced rods on an elastic beam. Such systems have been theoretically shown to support edge modes, with applications in elastic energy harvesting[13]. A schematic of the full structure, and experimental setup, is shown in Fig. 2(a) with the SSH interface marked by a vertical white dashed line. The structure comprises a horizontal elastic beam of thickness $t = 1.5$ mm and width $a = 7$ mm. A periodic array of elastic rods is formed, comprising of a unit cell of width a, with two rods of height $h = 20$ mm and radius $r = 0.5$ mm, separated by a distance s_i about the cell centre that mediate the 'strong' and 'weak' couplings (Fig. 2(b)). The total length of the support beam is then dictated by the number of unit cells included in the array. We denote the rod separation distance, from the centre of each unit cell, s_i where $i = 1,2$ to distinguish between the two sides of the interface. Due to the non-uniqueness of the unit cell, a periodic array with chosen $s_1 = a/3.9$ reproduces the same array as one with a separation $s_2 = a - s_1$, as shown in Fig. 2(b). The unit cells are related by a mere translation of $a/2$; they have identical dispersion curves and share a common bandgap. The dispersion relations of each cell are shown in Fig. 2(c) (evaluated by an eigenfrequency simulation employing the Finite Element Method (FEM), using COMSOL Multiphysics[24] - see supplementary material). We form an interface between two arrays (comprising 9 cells) of each configuration, that is, one with central separation s_1 and the other with s_2. We are guaranteed that this interface supports a topologically protected interface mode by virtue of each configuration sharing a common bandgap in addition to the distinct Zak phase associated with the bands of each geometry[25,26]. Leveraging the notation of quantum mechanics, the Zak phase for each dispersion curve, φ, is defined as

$$\varphi = i \int_{BZ} \langle u_{\boldsymbol{k}} | \partial_{\boldsymbol{k}} | u_{\boldsymbol{k}} \rangle d\boldsymbol{k}, \tag{1}$$

where $|u_{\boldsymbol{k}}\rangle$ is the wavefunction (eigensolution) of the elastic field at a wavevector $\boldsymbol{k}$ within the first Brillouin Zone (BZ). Several efficient schemes exist to calculate such invariants[27]. We numerically confirm the existence of this edge mode via a time domain simulation of the experimental setup, shown by the Fourier spectra in Fig. 2(c) where the edge mode is labelled ω_0. The introduction of a local defect by altering the material parameter at the interface can fine-tune the frequency of the edge mode. This is achieved by decreasing the Young's modulus, locally, at the interface position on the supporting beam by increasing the control (blue) laser power.

A more precise estimation of the effect of laser illumination on the edge mode properties can be derived from frequency domain FEM simulations, again performed using COMSOL Multiphysics. A detailed description of the numerical methods is provided in the supplementary material. The sample geometry illustrated in Fig. 2(a) is considered, with an overall beam length of 196 mm, corresponding to 28 unit cells of lattice parameter a. A harmonic boundary load is applied on the underside of the fourth unit cell from the edge, corresponding to the location of the piezoelectric transducer in Fig. 2(a) - shown in Fig. 3(c). The corresponding transmission loss (calculated as the ratio between transmitted and input power for out-of-plane vibrations) is then evaluated at various points along the sample, on top of the rods, in the 5 to 13 kHz range. Adopted material properties are Young's modulus E = 1 GPa, Poisson's ratio $\nu = 0.4$, density $\rho = 1100$ kg/m^3. Damping is accounted for by introducing an isotropic loss factor of η = 0.02. The resulting spectra are shown in Fig. 3(a). Despite being in a band gap (shaded in orange), the localized mode is detected (occurring at approximately 9.5 kHz), and visualized as an isolated peak. We are able numerically (and experimentally) to detect the edge mode with this excitation configuration due to the finite length of the sample coupled with the length of the decay of the mode within the band gap; the decay lengths of frequencies within the gap (which can be predicted through High Frequency Homogenisation[16,28]) reach the interface and ignite the edge mode. In contrast, in Fig. 1(c) we excite in the time domain (as in the experiment) at the interface position (supplementary material). In Fig. 3(a) curves of different colours, representing measurements at different spatial locations, indicate an exponential amplitude decay of the mode when moving from the central defect region ("Pos. 0") to the edge of the sample ("Pos. 3"), as illustrated in Fig. 3(c). The effect of laser illumination on the transmission loss spectrum is shown in Fig. 3(b): a Young's modulus reduction of up to 0.3 GPa ("100%") occurs in the central region of the photo-responsive sample for maximum laser power, and this leads to a frequency downshift of the localized mode of approximately 600 Hz, demonstrating that the tunablility of the edge mode can, theoretically, occur over a significant fraction of the width of the band gap (approx. 35%).

Experimental samples were fabricated using a commercial 3D digital light processing printer (Solflex SF650, W2P Engineering GmbH) with a Solflex Tech polymeric resin (material properties given above). Polymerization was induced with a 385 nm wavelength UV-LED with a power density of 8±0.5 mW/cm^2. The nominal lateral resolution is 50 μm and printing was performed in layers of 50 μm, each exposed for 1.5 s, leading to a dose of 12 mJ/cm^2 per layer. After printing, the sample was washed with Isopropyl Alcohol (IPA), sonicated in IPA, and dried thoroughly. It was then soaked for 10 minutes in an acetone bath containing 0.25 mg/mL photo-responsive azo-dye Disperse Red 1 methacrylate (DR1m), swelling the pre-cured structure, and thus permitting homogeneous dye dispersion. Finally the swollen structure was dried for 1 hour until the pristine shape was recovered before being UV-post-cured for 1 hour under all-around illumination in the wavelength range 320–450 nm.

The experimental setup is shown in Fig. 2(a): a 20 mm diameter piezoelectric transducer was glued to the sample at one end and a frequency sweep between 5 kHz and 13 kHz (with a duration of 1 s) was injected into the sample using an Agilent 33500 function generator, amplified by a linear amplifier (FLC Electronics, A400DI). The transducer was glued to the underside of the sample, but is shown on the top side of Fig. 2(a) for clarity. The out-of-plane (z-direction in Fig. 2) vibration velocity amplitude was measured at various points along the sample, on top of the rods, using a Polytec OFV-505 laser vibrometer. Using an additional 405 nm-wavelength laser beam impinging laterally on the central region of the sample (see Fig. 2(a)), the material's Young's modulus can be reduced locally by light stimulation. The laser has a maximum power output of 250 mW and can be focused on an approximately 30 mm^2 area.

The Fast Fourier Transform (FFT) of the acquired signals is plotted in Fig. 3(d), clearly showing the band gap region and an isolated peak corresponding to the localized mode near 9 kHz. As the signal detection point moves from the central position 0 to the lateral position 3 (Fig. 3(f)), the FFT peak amplitude drops exponentially, as predicted theoretically and in simulations, while other spectral features remain relatively unchanged. The experimental peak widths appear larger than those in simulations, due to an oversimplified viscoelastic model which neglects significant damping. Illumination of the central defect region with the laser, for increasing values of output power, is shown in Fig. 3(e), demonstrating that the peak relative to the localized mode shifts to lower frequencies, approaching the band edge while reaching a maximum variation of approximately 300 Hz for 250 mW, compared to the original frequency. The variation is qualitatively similar to the predictions by theory and simulation, but less drastic due to the fact that the adopted laser power is not sufficient to generate a full photo-isomerization of the azo-units in the polymeric material. The peak shift is fully reversible when removing illumination or decreasing illumination power in any number of cycles. Similar results were obtained on a second specimen with different geometric parameters (see Supplementary Material).

In summary, we have demonstrated experimentally the possibility of dynamically fine tuning the frequency of topological edge modes in SSH arrays consisting of appropriately spaced rods on a beam, realized in a 3D-printed photo-responsive polymer. The frequency shift due to local illumination of the sample is linearly dependent on laser power and can reach the band gap edge, and is fully reversible when illumination is removed. Measurements have been performed on two different sample geometries and provide similar results, demonstrating flexibility in design possibilities.

This work shows the potential to use photo-responsive materials to create topological edge modes with dynamic tunability. This builds on existing strategies for tunability through geometric manipulation. This principle could be developed to multi-dimensional topological systems, to add dynamic tunability to topological waveguides and energy splitters. By providing a means to dynamically alter the operating frequency, this would greatly increase the the versatility of these devices.

SUPPLEMENTARY MATERIAL

Details of the FE modelling, along with an additional sample geometry, are presented in the supplementary material.

ACKNOWLEDGMENTS

A.S.G., F.B. and R.V.C. are supported by the European Commission H2020 FET Open "Boheme" grant no. 863179. B.D. is supported by the Engineering and Physical Sciences

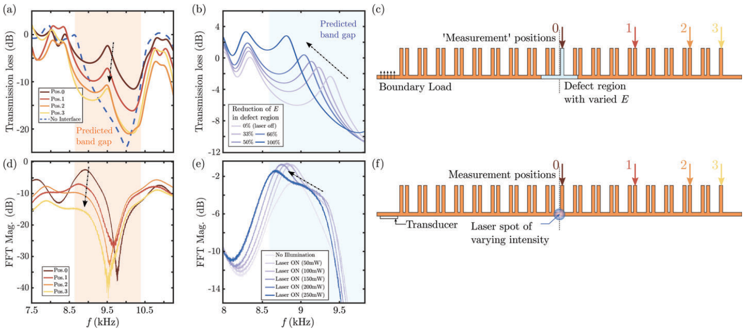

FIG. 3. Frequency domain FEM simulations and Experimental results: existence and tunablility of protected edge mode. (a) Numerical confirmation of edge mode shown by the transmission loss as a function of frequency, evaluated at different positions along the sample. Exponential decay with position of the edge mode amplitude is observed away from the interface, as expected. (b) Tuning the frequency of the edge mode by introducing a defect (altered Young's modulus, E). (c) Schematic with 'measurement' positions (pos. 1-3), defect region shown in blue, and boundary load excitation. (d) Experimental confirmation of edge mode shown by the magnitude of the Fourier spectrum, measured at different positions along the sample. Exponential decay with position of the edge mode amplitude is observed, as expected. (e) Tuning the frequency of the edge mode by introducing a defect with increasing laser power (altering the Young's modulus, E). (f) Schematic with measurement positions (pos. 1-3), defect region shown by laser spot blue, and transducer position shown.

Research Council through a Research Fellowship with grant number EP/X027422/1. G.J.C. gratefully acknowledges financial support from the Royal Commission for the Exhibition of 1851 in the form of a Research Fellowship.

DATA AVAILABILITY STATEMENT

The data that support the findings of this study are available from the corresponding author upon reasonable request.

[1] J. E. Moore, "The birth of topological insulators," Nature **464**, 194–198 (2010).
[2] M. Z. Hasan and C. L. Kane, "Colloquium: topological insulators," Rev. Mod. Phys. **82**, 3045 (2010).
[3] T. Ozawa, H. M. Price, A. Amo, N. Goldman, M. Hafezi, L. Lu, M. C. Rechtsman, D. Schuster, J. Simon, O. Zilberberg, *et al.*, "Topological photonics," Reviews of Modern Physics **91**, 015006 (2019).
[4] Z. Yang, F. Gao, X. Shi, X. Lin, Z. Gao, Y. Chong, and B. Zhang, "Topological acoustics," Phys. Rev. Lett. **114**, 114301 (2015).
[5] M. C. Rechtsman, J. M. Zeuner, Y. Plotnik, Y. Lumer, D. Podolsky, F. Dreisow, S. Nolte, M. Segev, and A. Szameit, "Photonic Floquet topological insulators," Nature **496**, 196–200 (2013).
[6] A. B. Khanikaev, S. H. Mousavi, W.-K. Tse, M. Kargarian, A. H. MacDonald, and G. Shvets, "Photonic topological insulators," Nat. Mater. **12**, 233–239 (2013).
[7] A. O. Krushynska, D. Torrent, A. M. Aragón, R. Ardito, O. R. Bilal, B. Bonello, F. Bosia, Y. Chen, J. Christensen, A. Colombi, S. A. Cummer, B. Djafari-Rouhani, F. Fraternali, P. I. Galich, P. D Garcia, J. P. Groby, S. Guenneau, M. R. Haberman, M. I. Hussein, S. Janbaz, N. Jiménez, A. Khelif, V. Laude, M. J. Mirzaali, P. Packo, A. Palermo, Y. Pennec, R. Picó, M. R. López, S. Rudykh, M. Serra-Garcia, C. M. Sotomayor Torres, T. A. Starkey, V. Tournat, O. B. Wright, "Emerging topics in nanophononics and elastic, acoustic, and mechanical metamaterials: an overview," Nanophotonics, **12**, 659–686 (2023).
[8] Z.-G. Chen and Y. Wu, "Tunable topological phononic crystals," Phys. Rev. Appl. **5**, 054021 (2016).
[9] S. Qu and P. Sheng, "Minimizing indoor sound energy with tunable metamaterial surfaces," Phys. Rev. Appl. **14**, 034060 (2020).
[10] H. J. Putley, S. Guenneau, R. Porter, and R. V. Craster, "A tunable electromagnetic metagrating," Proc. R. Soc. A **478**, 20220454 (2022).
[11] A. D. Boardman, V. V. Grimalsky, Y. S. Kivshar, S. V. Koshevaya, M. Lapine, N. M. Litchinitser, V. N. Malnev, M. Noginov, Y. G. Rapoport, and V. M. Shalaev, "Active and tunable metamaterials," Laser Photonics Rev. **5**, 287–307 (2011).
[12] W. P. Su, J. R. Schrieffer, and A. J. Heeger, "Solitons in polyacetylene," Phys. Rev. Lett. **42**, 1698–1701 (1979).
[13] G. J. Chaplain, J. M. De Ponti, G. Aguzzi, A. Colombi, and R. V. Craster, "Topological rainbow trapping for elastic energy harvesting in graded Su-Schrieffer-Heeger systems," Phys. Rev. Appl. **14**, 054035 (2020).
[14] M. Parto, S. Wittek, H. Hodaei, G. Harari, M. A. Bandres, J. Ren, M. C. Rechtsman, M. Segev, D. N. Christodoulides, and M. Khajavikhan, "Edge-mode lasing in 1D topological active arrays," Phys. Rev. Lett. **120**, 113901 (2018).
[15] J. Zak, "Berry's phase for energy bands in solids," Phys. Rev. Lett. **62**, 2747 (1989).
[16] R. V. Craster and B. Davies, "Asymptotic characterisation of localised defect modes: Su-Schrieffer-Heeger and related models," Multiscale Model. Simul. **in press** (2023).
[17] H. Ammari, B. Davies, and E. O. Hiltunen, "Robust edge modes in dislocated systems of subwavelength resonators," J. Lond. Math. Soc. **106**, 2075–2135 (2022).
[18] M. Miniaci, F. Allein, and R. K. Pal, "Spectral flow of a localized mode in elastic media," arXiv preprint arXiv:2111.09021 (2021).
[19] A. Drouot, C. L. Fefferman, and M. I. Weinstein, "Defect modes for dislocated periodic media," Commun. Math. Phys. **377**, 1637–1680 (2020).
[20] A. S. Gliozzi, M. Miniaci, A. Chiappone, A. Bergamini, B. Morin, and E. Descrovi, "Tunable photo-responsive elastic metamaterials," Nat. Commun. **11**, 2576 (2020).
[21] J. Vapaavuori, C. G. Bazuin, and A. Priimagi, "Supramolecular design principles for efficient photoresponsive polymer–azobenzene complexes," J. Mater. Chem. C **6**, 2168–2188 (2018).

[22] M. Poutanen, O. Ikkala, and A. Priimagi, "Structurally controlled dynamics in azobenzene-based supramolecular self-assemblies in solid state," Macromolecules **49**, 4095–4101 (2016).

[23] E. Descrovi, F. Pirani, V. P. Rajamanickam, S. Licheri, and C. Liberale, "Photo-responsive suspended micro-membranes," J. Mater. Chem. C **6**, 10428–10434 (2018).

[24] COMSOL, *Solid Mechanics Module User's Guide* (Stockholm, Sweden, 2021).

[25] M. Atala, M. Aidelsburger, J. T. Barreiro, D. Abanin, T. Kitagawa, E. Demler, and I. Bloch, "Direct measurement of the Zak phase in topological Bloch bands," Nat. Phys. **9**, 795–800 (2013).

[26] M. Xiao, Z. Zhang, and C. Chan, "Surface impedance and bulk band geometric phases in one-dimensional systems," Phys. Rev. X. **4** (2014).

[27] A. A. Soluyanov and D. Vanderbilt, "Computing topological invariants without inversion symmetry," Phys. Rev. B **83**, 235401 (2011).

[28] R. V. Craster, J. Kaplunov, and A. V. Pichugin, "High-frequency homogenization for periodic media," Proceedings of the Royal Society A: Mathematical, Physical and Engineering Sciences **466**, 2341–2362 (2010).

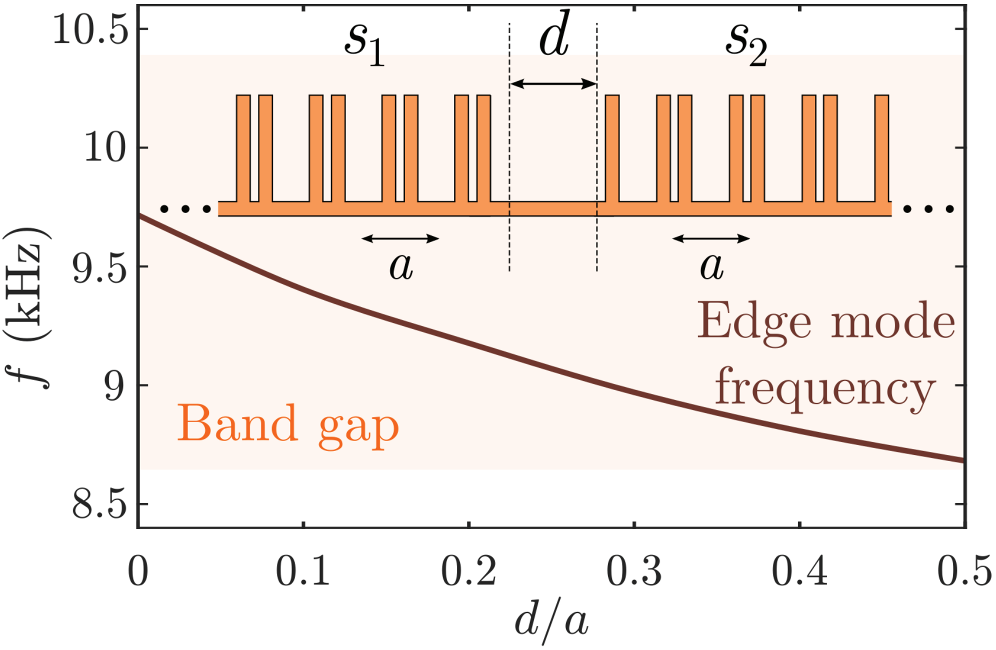
s_1
d
s_2
a
a
Edge mode frequency
Band gap
f (kHz)
10.5
10
9.5
9
8.5
0
0.1
0.2
0.3
0.4
0.5
d/a

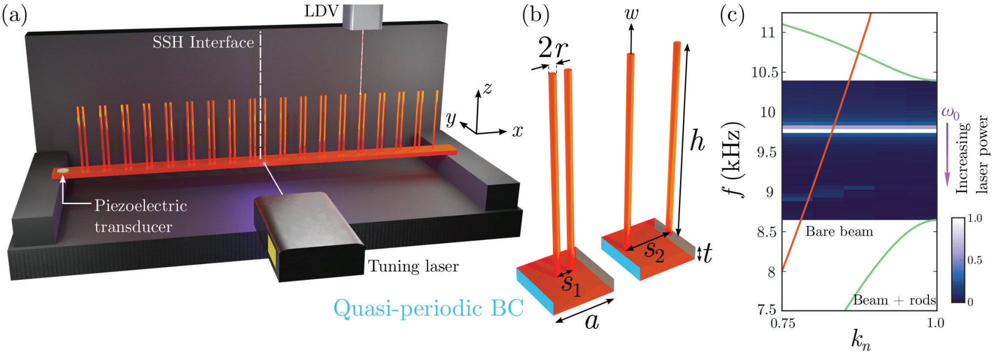
(a)
LDV
SSH Interface
z
y
x
Piezoelectric transducer
Tuning laser
(b)
$2r$
w
h
s_1
s_2
t
a
Quasi-periodic BC
(c)
f (kHz)
11
10.5
10
9.5
9
8.5
8
7.5
0.75
1.0
k_n
ω_0
Increasing laser power
Bare beam
Beam + rods
1.0
0.5
0

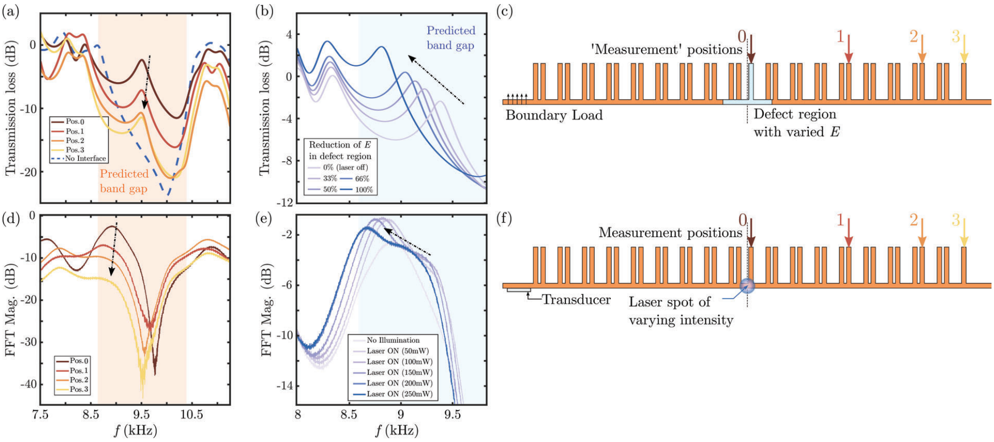
(a)
Transmission loss (dB)
0
-10
-20
Pos.0
Pos.1
Pos.2
Pos.3
No Interface
Predicted
band gap
(b)
Transmission loss (dB)
4
0
-4
-8
-12
Predicted
band gap
Reduction of E
in defect region
0% (laser off)
33%
66%
50%
100%
(c)
'Measurement' positions
0
1
2
3
Boundary Load
Defect region
with varied E
(d)
FFT Mag. (dB)
0
-10
-20
-30
-40
Pos.0
Pos.1
Pos.2
Pos.3
7.5
8.5
9.5
10.5
f (kHz)
(e)
FFT Mag. (dB)
-2
-6
-10
-14
No Illumination
Laser ON (50mW)
Laser ON (100mW)
Laser ON (150mW)
Laser ON (200mW)
Laser ON (250mW)
8
8.5
9
9.5
f (kHz)
(f)
Measurement positions
0
1
2
3
Transducer
Laser spot of
varying intensity

Selective dynamic band gap tuning in metamaterials using graded photoresponsive resonator arrays

Research

Cite this article: Dal Poggetto VF, Urban D, Nistri F, Beoletto PH, Descrovi E, Miniaci M, Pugno NM, Bosia F, Gliozzi AS. 2024 Selective dynamic band gap tuning in metamaterials using graded photoresponsive resonator arrays. *Phil. Trans. R. Soc. A* 382: 20240150. https://doi.org/10.1098/rsta.2024.0150

Subject Areas:

wave motion, mechanics, acoustics, materials science

Keywords:

metamaterials, tunability, graded resonators, photoresponsive materials, band gaps

Author for correspondence:

Antonio S. Gliozzi

e-mail: antonio.gliozzi@polito.it

V. F. Dal Poggetto[1,2], D. Urban[3,4], F. Nistri[4], P. H. Beoletto[4], E. Descrovi[4], M. Miniaci[1], N. M. Pugno[2,5], F. Bosia[4] and A. S. Gliozzi[4]

[1] Univ. Lille, CNRS, Centrale Lille, Junia, Univ. Polytechnique Hauts-de-France, UMR 8520 Lille, France
[2]Department of Electronic Systems, Norwegian University of Science and Technology, 7491 Trondheim, Norway
[3]DISAT, Politecnico di Torino, 10129 Torino, Italy
[4]Laboratory for Bioinspired, Bionic, Nano, Meta Materials & Mechanics, Department of Civil, Environmental and Mechanical Engineering, University of Trento, Trento, 38123 Italy
[5]School of Engineering and Materials Science, Queen Mary University of London, UK

The introduction of metamaterials has provided new possibilities to manipulate the propagation of waves in different fields of physics, ranging from electromagnetism to acoustics. However, despite the variety of configurations proposed so far, most solutions lack dynamic tunability, i.e., their functionality cannot be altered post-fabrication. Our work overcomes this limit by employing a photo-responsive polymer to fabricate a simple metamaterial structure and enable tuning of its elastic properties using visible light. The structure of the metamaterial consists of graded resonators in the form of an array of pillars, each giving rise to different resonances and transmission band gaps. Selective laser illumination can then tune the resonances and their frequencies individually or collectively, thus yielding many degrees of freedom in the tunability of the filtered or transmitted wave frequencies, similar to playing a keyboard, where illuminating each pillar corresponds to playing a different note. This concept can be used to realize low-power active devices for elastic wave control, including beam-splitters, switches, and filters.

1 Introduction

Elastic and acoustic metamaterials derive unconventional dynamic properties from the combined behavior of artificial structural elements [1–3]. Generally speaking, metamaterial functionality depends mainly on unit cell design, but material properties play a role in determining the frequencies at which these effects take place. To date, elastic and acoustic metamaterials exploit three main distinct mechanisms for the control of wave propagation: (i) Bragg scattering, (ii) local resonances, and/or (iii) inertial amplification [4, 5]. The wave manipulation effects that can be achieved with these mechanisms include elastic wave scattering [6], acoustic wave absorption [7], negative refraction [8], cloaking [9], focusing [10], one-way [11] or scatter-free propagation [12], and topological protection [13]. These effects can be exploited for numerous applications across scales, from isolation of large scale vibrations [14–16] to energy harvesting [17], from noise abatement [18, 19] to speech recognition [20].

Despite their scientific interest and their numerous applications, most elastic and acoustic metamaterials lack dynamic tunability, i.e., their functionality is fixed once the structure has been fabricated. To address this limitation, the coupling of metamaterials with different external fields, such as piezoelectric [21–25], thermal [26–28], mechanical (prestress/prestrain) [29–32], and electromagnetic [33–38] ones, has been explored. Alternative approaches include the use of soft magnetoactive composites exploiting instabilities [39, 40], strain-tunable dielectric elastomers [41] or magnetorheological metamaterials exploiting nonlinear effects [42], leading to the concept of “soft, smart matter” [43].

However, practical implementations often involve considerable complexity, both in specimen fabrication and in the implementation of the control mechanism. In contrast, here we propose an approach that exploits light responsiveness into a 3D printable polymeric material, enabling simple, non-contact and low-power tunability [44].

In previous work, we have demonstrated the controlled decrease of the Young’s modulus of polymers containing azobenzene dye by means of laser illumination and the corresponding modification of the transmission properties of a metamaterial structure fabricated with this material and consisting in an array of pillars on a waveguide. Selective local illumination affects the vibration eigenmodes of individual resonant pillars, significantly affecting the waveguide transmission spectrum [45, 46]. These effects occur on a time scale of less than a minute and are fully reversible. In this work, we present a continuation of previous investigations, extending the analysis to graded structures, thus allowing to increase the possible degrees of freedom in tunability of the system, and conceptually introducing the possibility of "playing" a metamaterial keyboard.

2 Specimen design and numerical analysis

In a system consisting of multiple photoresponsive pillars of identical heights on a waveguide (see Fig.1a), each pillar exhibits a similar dynamic behavior, eigenfrequencies (schematically shown in Fig.1b) and eigenmodes. When excited at their resonant frequencies, they collectively generate a band gap with a specific centre frequency and width. If one of these pillars is selectively illuminated, its resonance frequency decreases (since the material undergoes softening), causing the band gap to move to lower frequencies (Fig.1c) [46]. On the contrary, in a scenario where each pillar has a different height (Fig.1d), the resonant frequencies also differ, resulting in individual pillars attenuating the propagation of waves around different centre frequencies (Fig.1e). This system is reminiscent of the so-called "resonant metawedge", which has been extensively discussed in various contexts of elastic wave manipulation [14, 17]. In our case, when one of the photo-responsive pillars is illuminated, the corresponding band gap width remains approximately the same but shifts towards lower frequencies (Fig.1f). This behavior, together with the selective illumination of one or more graded pillars, enables the tunability of the transmission properties of the entire structure.

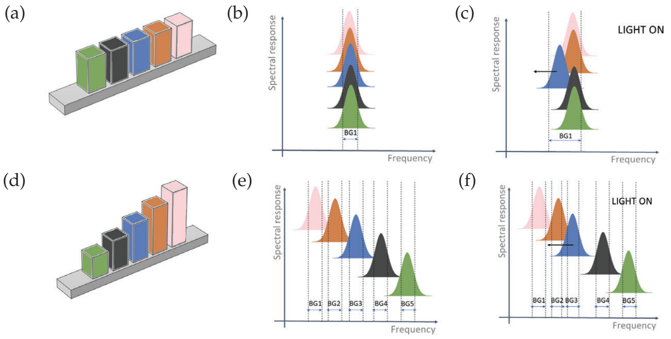

Figure 1: Schematic representation of the proposed concept: a) pillar array acting as a metamaterial filter; b) the local resonance properties of all pillars coincide and lead to a single band gap (BG1) at a characteristic frequency; c) laser illumination of a single photorespoinsive pillar leads to a downward shift of its resonance, and an overall widening of the bandgap. d) In this work, we consider an array of pillars of variable height, whose spectral response is given by e) the superposition of resonances at different frequencies, i.e. various potentially overlapping bandgaps; f) illumination of a single pillar allows manipulation of the filtering properties in a specific frequency range.

To guide the design of the resonator arrays, a first numerical investigation on the modal properties of the individual pillars is performed. The system can be considered as an array of subwavelength responators that can trap and spatially segregate certain frequencies, when the traveling waves in the beam efficiently couple with the pillar resonances, i.e., an impedance matching condition occurs. To determine this condition, we calculate the dispersion spectra of the individual pillars and their resonance frequencies as a function of their height. We design the array so that there is no overlap between the lowest bandgaps of the different pillars, identifying four distinct pillar heights that satisfy this condition.

The dispersion spectrum of the resonator array, whose unit cell is shown in Fig.2(a) with its characteristic dimensions (a hosting base of width a and height h_b, supporting a pillar of width b and height h_p), is computed using Finite Element (FE) analysis. The models are meshed using quadratic hexahedral solid elements (nodal displacements u_x, u_y, and u_z) with a characteristic length of approximately $0.5\,\mathrm{mm}$. Material properties are considered homogeneous and isotropic, with a Young's modulus value $2.75\,\mathrm{GPa}$, Poisson's ratio 0.3, and specific mass density $1120\,\mathrm{kg}\cdot\mathrm{m}^{-3}$. Bloch-Floquet periodic conditions are enforced at the edges of the one-dimensional unit cell in the x-direction [47], resulting in an eigenproblem in the form $\boldsymbol{K}(k)\boldsymbol{u}=\omega^2\boldsymbol{M}\boldsymbol{u}$, where $\boldsymbol{K}(k)$ is a wavenumber-dependent stiffness matrix, $\boldsymbol{M}$ is a mass matrix, ω^2 are the eigenvalues which correspond to propagating frequencies, and $\boldsymbol{u}$ are the eigenvectors which represent the nodal three-dimensional displacements. This eigenproblem is solved by considering the wavenumber k within the corresponding irreducible Brillouin zone [48], spanning the values between the points $\Gamma(k=0)$ and X $(k=\pi/a)$, since we are considering 1D propagation along a waveguide. Additionally, an out-of-plane polarization metric [49] expressed by $p(\mathbf{u})=(\int_V |u_z|^2\,dV)/(\int_V |u_x|^2+|u_y|^2+|u_z|^2\,dV)$, with $p\in[0,1]$, is computed for the subset of displacement vectors $\boldsymbol{u}$ considering the volume of the hosting beam (region marked in blue in Fig.2(a)), which we consider as indicative of the flexural behavior of the beam in the experimental setup. For the considered values of $a=5\,\mathrm{mm}$, $h_b=2\,\mathrm{mm}$, and $b=3.75\,\mathrm{mm}$, the dispersion relations are computed for the heights h_p of (i) $7\,\mathrm{mm}$, (ii) $9\,\mathrm{mm}$, (iii) $11\,\mathrm{mm}$, and (iv) $13\,\mathrm{mm}$, and shown in Fig.2(b) along with the computed polarization values (p) for the propagating frequencies of a branch that presents significant coupling between the in- and out-of-plane motion of the hosting beam. This behavior is illustrated for $h_p = 7$ mm by the wave modes computed at Γ_1, P_1 ($k = \pi/2a$), and X_1, which display, respectively, the propagating frequencies of 45.1, 50.6, and 71.3 kHz. The polarization values of these points are 0.70, 0.54, and 0.10, indicating a predominantly out-of-plane behavior for the hosting beam at Γ_1 and in-plane at X_1. On the other hand, the wave mode at P_1 presents a high degree of coupling between the in- and out-of-plane behavior of the hosting beam, which is also observed on the combined motion of the supported pillar (see wave mode in Fig.2(b)). The out-of-plane behavior of the hosting beam at Γ_1 suggests that corresponding peaks will arise in the transmission of a finite structure formed by these unit cells for an out-of-plane excitation. The polarization values decrease monotonically in this branch, thus suggesting that for a continuous frequency range, a coupled behavior between in- and out-of-plane motion is expected, which in turn, may yield a reduction in the transmission of out-of-plane excitation due to coupling with the pillar motion. A similar behavior is observed for each case of the pillar height, as shown in the dispersion spectra in Fig.2(b). The propagating frequencies of the corresponding branches at Γ for the pillar heights of 9, 11, and 13 mm are respectively 33.6, 25.9, and 20.5 kHz, thus indicating a trend of decrease in the propagating frequencies as the pillar height increases. We also expect these points to be associated with peaks in the transmission of out-of-plane excitation in a finite system. Interestingly, a shift in the computed frequencies can be achieved through the variation of the pillar height while maintaining a fixed lattice length, therefore indicating the prevalently locally resonant nature of the wave modes. The corresponding polarization values for these pillar heights are computed, respectively, as 0.57, 0.45, and 0.35, thus suggesting that an effective coupling between in- and out-of-plane motion can be expected for narrower frequency ranges as the pillar height increases. Upon illumination, the softening of the material of the pillars (whose Young's modulus changes to approximately 2.0 GPa for maximum illumination power) leads to a lowering of the propagating frequencies at Γ to the new values of (i) 38.5, (ii) 28.7, (iii) 22.1, and (iv) 17.5 kHz, thus corresponding to an approximate decrease of 15% from the initial values of these frequencies.

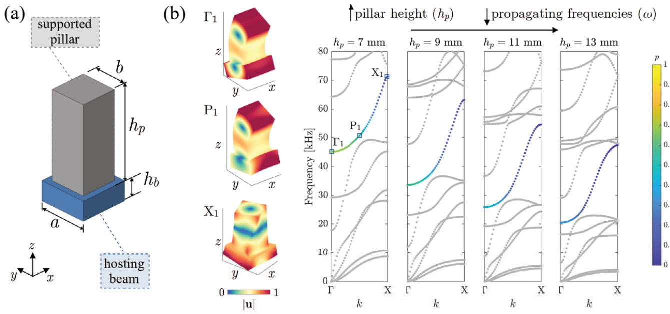

Figure 2: Dispersion properties of the photo-responsive pillars. (a) The characteristic dimensions of the unit cell are described by a hosting beam with base width a and height h_b, supporting a pillar with width b and height h_p. (b) Dispersion relations computed for the values $h_p = \{7, 9, 11, 13\}$ mm. The polarization metric (p), computed considering the hosting beam volume, is used to indicate the behavior of a branch supporting flexural waves whose behavior shifts between the wave modes shown at the lower (Γ_1) and upper (X_1) points, indicating a highly coupled in- and out-of-plane behavior for intermediate values, and hence reduced transmission. Vibration modes at the points Γ_1, P_1 and X_1 are also shown on the left of the subfigure.

We now numerically model the finite structure considered experimentally (Fig.3a), constituted by the described pillars arranged in a one-dimensional array on a thin beam (40 mm in length, 2 mm in thickness) acting as a waveguide, located between a 40x40 mm slab used to excite input signals and a 40x4.5 mm beam where output signals are detected. To reinforce the locally resonant effect of each pillar, each height is repeated twice, leading to an 8-pillar structure, whose collective transmission properties are approximately expected to be the superposition of those of the four individual pillar types. This is based on the assumption of limited coupling between vibration modes of the various pillars in the considered frequency range.

To verify this hypothesis and determine the structure's overall transmission properties, we perform FEM frequency-domain numerical analysis using the COMSOL Multiphysics software. The finite structure geometry is reproduced and meshed using tetrahedral elements, as shown in (Fig.3b). MEchanical properties are those indicate above. A harmonic boundary load is applied on one side of the waveguide (corresponding to the location of the piezoelectric transducer in experiments), as shown in (Fig.3b), and the corresponding transmission loss (calculated as the ratio between transmitted and input power for out-of-plane vibrations) is then evaluated at the beam location opposite to the pillar array (also indicated in (Fig.3b)), in the 10 to 70 kHz range. Pillar illumination is simulated by locally reducing the Young's modulus to 2 GPa.

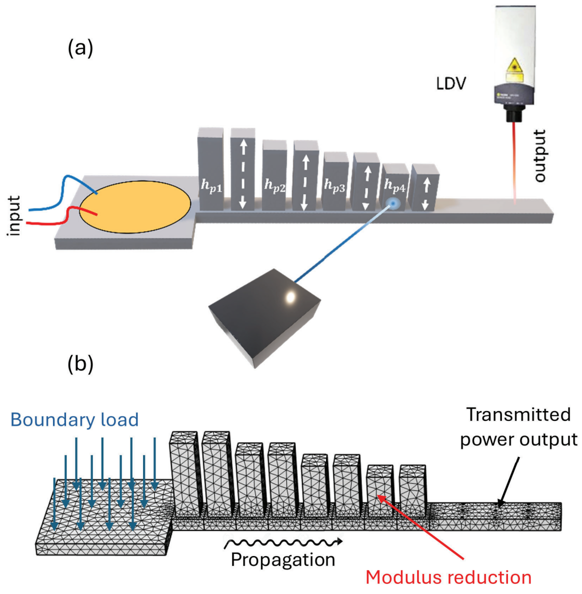

Figure 3: a) Experimental sample and measurement set-up. The heigths of the pillars are $h_{p1} = 13$ mm, $h_{p2} = 11$ mm, $h_{p3} = 9$ mm, and $h_{p4} = 7$ mm. b) FEM mesh used in frequency-domain simulations; boundary conditions are also illustrated.

The computed spectrum (blue continuous line in Fig.4(a)) clearly shows the presence of four band gaps, appearing approximately in the frequency ranges predicted in the dispersion spectra (see Fig.2). Some variation in the band gap width is observed, mainly due to coupling effects between pillars. The effect of laser illumination at selected locations of the sample is then evaluated. As an example, we consider the case when the 1st (4(a)) and 6th (4(b)) pillars are illuminated. In the first case, the pillar resonance frequency is related to the lowest band gap (I), at about 25 kHz. Figure 4(a) illustrates the variation in the transmission spectrum (red dashed line) upon softening of the first pillar, with the lowest band gap widening to lower frequencies (highlighted by red shading in the figure). In the second case, the sixth pillar is associated to the third band gap (III) at about 42 kHz, which undergoes widening and a shift to lower frequencies when the pillar undergoes softening (Fig.4(b)).

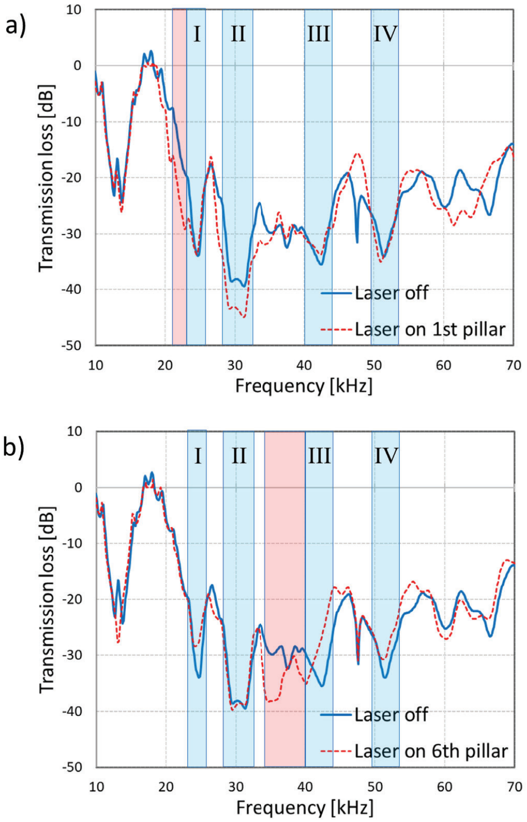

Figure 4: Numerically computed transmission spectrum of the considered 8-pillar structure. a) without ("Laser off") and with laser illumination on the first pillar ("Laser on 1st pillar"). Four band gaps (shaded in light blue and labelled from I to IV) appear in the spectrum; laser illumination on the tallest pillar results in a widening of the lowest bandgap to lower frequencies (red shading). b) without ("Laser off") and with laser illumination on the sixth pillar ("Laser on 6th pillar"). This results in a widening and lowering of the third band gap to lower frequencies (red shading).

3 Experimental realization

We now verify the numerical results through experimental tests. For the fabrication of the light-responsive specimen we follow a protocol described in [46]. The samples are first fabricated with a Digital Light Processing (DLP) 3D printer, using a commercial polymeric resin. Light-mediated tunability is then achieved by diffusing the responsive azo-dye Disperse Red 1 methacrylate (DR1m) into the as-fabricated samples prior to UV post-curing. Process parameters are selected so as to maximize homogeneous dye dispersion while preserving the integrity of the structure. The modulus of the material can thus be locally altered through illumination with visible light, producing continuous photo-isomerization cycles of the dye.

The experimental setup shown in Fig.3(a) is designed to detect the collective dynamics of the graded pillar structure. One side of the thin slab is designed to accommodate a thin piezoelectric transducer, whose mass is considered negligible. The transducer serves as the mechanical excitation source, generating elastic waves that propagate along the beam waveguide, crossing the array of pillars with varying heights, starting from the highest. The collective response of the structure is monitored by measuring the spectral response at the opposite end of the waveguide using a Laser Doppler Vibrometer (LDV). An additional laser, operating at a wavelength of $\lambda = 405\,\mathrm{nm}$, is positioned orthogonally to the structure on a motorized linear stage. This allows to selectively illuminate individual pillars (see Fig.3(a)).

To explore the frequency response of the structure, we perform a frequency sweep ranging from 10 kHz to 70 kHz, capturing the system's response using the LDV to monitor the output of the structure and performing Fast Fourier Transform Analysis to determine the transmitted spectrum. The results reveal, as expected, the emergence of four distinct bandgaps, each characterized by an increasing width for increasing frequencies. These bandgaps correspond to the lower bandgaps of each pillar pair (as illustrated in Fig.4(a), solid blue line). The central frequencies of these bandgaps align well with the positions predicted from the modal analysis of individual pillars and with those calculated in frequency domain simulations. As the frequency increases, there is a slight deviation between the experimental data and the predictions, due to the mentioned excitation of in-plane modes and coupling effects between pillars.

The subsequent phase of the experiments involves the selective illumination of the structure at selected locations. Fig.4(a) shows results when illuminating the first (tallest) pillar, responsible for the formation of the lowest frequency bandgap. The illumination induces a reduction of the elastic modulus in the illuminated pillar, resulting in a resonance frequency shift and a corresponding broadening of the first bandgap towards lower frequencies, as predicted numerically. In this case, only one of the two identical adjacent pillars undergoes a modification in its elastic behavior. At the edge of the first bandgap, this translates into a substantial difference in signal transmission of approximately 20dB at approximately 23 kHz before and after illumination. This illustrates the significant potential of the photo-induced modulation of material properties in modifying the structural response at specific frequencies, providing clear evidence of the tunable nature of the considered graded pillar metamaterial structure. Illumination of the first pillar also produces noticeable effects at other frequencies in the spectral response, due to the effect on the modification of higher modes (Fig.4(a), red line). The temporal evolution of the entire structure's elastic response is visually represented in the color map presented in Fig.4(b), with time depicted on the vertical axis. The illumination of the pillar begins after 700 seconds (lower horizontal white line), reaching a steady state approximately 150 seconds later. Subsequently, the structure returns to its initial state in roughly the same time interval after the laser is switched off (upper horizontal line in the map), demonstrating full reversibility of the process.

Similar effects are observed for the other case considered in simulations, i.e., when illuminating the sixth pillar in the array, which is responsible for opening the third bandgap. In this instance, the softening of the structure appears to have more pronounced effects, partly because the illuminated area covers a larger percentage of the pillar volume (Fig.4(c)). As a result, the second and third bandgaps combine, while the response at other frequencies remains relatively unchanged (Fig.4(d)). This dynamic response further emphasizes the versatility of the graded pillar structure in achieving tunable and selective control over specific frequency ranges, illustrating its potential for targeted reversible modulation in applications requiring tailored dynamic behavior.

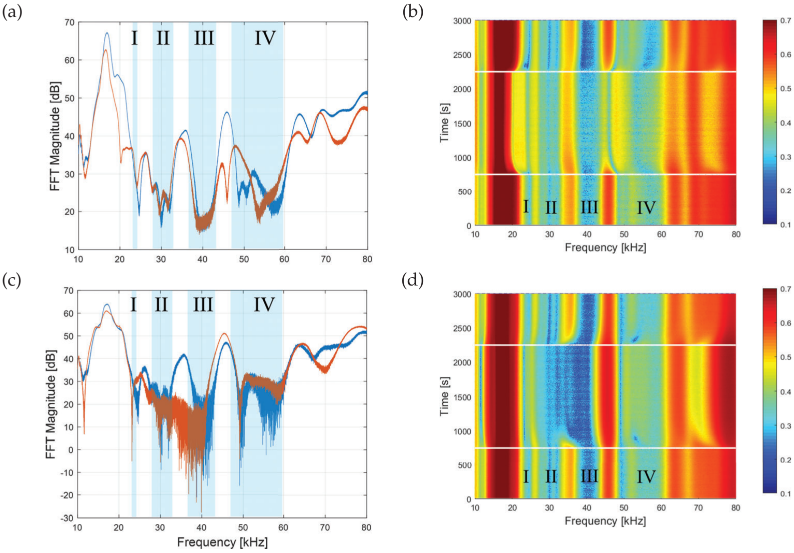

Figure 5: Transmission spectrum of the finite structure considered experimentally. a) Measured spectra before (blue) and after (red) illumination of pillar 1. Band gaps are highlighted in light blue and numbered from I to IV; b) Corresponding colour map representing transmission vs. frequency and time (vertical axis) when switching laser illumination on (t = 700 s) and off (t = 2300 s); c) same as a), with illumination of pillar 6; d) same as b), with illumination on pillar 6.

In addition to the experiments involving illumination of individual photoresponsive pillars, we explored the possibility of simultaneously illuminating multiple or all pillars in the system. We illustrate here the latter case. For this experiment, a laser was mounted on a linear stage, allowing the light beam to traverse back and forth across the array of pillars. Due to the inherent time delay in photoresponsive material property modification (a finite time is required to activate/deactivate the photo-isomerization), the continuous movement of the laser is effectively equivalent to quasi-simultaneous illumination of all pillars. As expected, the collective effect of simultaneously illuminating all pillars results in the cumulative effect of individual illuminations, in this case manifesting itself as a rigid spectral shift toward lower frequencies across the entire spectrum, as shown in Fig.6. The possibility to manipulate the optical response of multiple elements simultaneously highlights the versatility of our system.

Finally, we explore a practical application. Specifically, we inject a composite signal comprising two frequencies, $f_1 = 21.5\,\mathrm{kHz}$ and $f_2 = 71.5\,\mathrm{kHz}$ changing the selective laser illumination of the sample in time to observe the change in spectral response, as illustrated in Fig.7. During the first phase (from $t_0 = 0$ to $t_1 = 50s$), none of the pillars are illuminated, resulting in both frequencies exhibiting comparable spectral weights. Subsequently, at t_1, we selectively illuminate the fourth pillar. This action induces a local softening of the structure, effectively suppressing f_2 and causing a slight increase in f_1. Subsequently, the laser is switched off (from $t_2 = 100s$ to

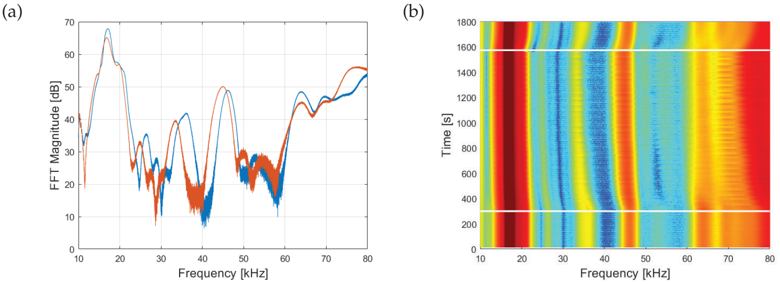

Figure 6: Transmission spectrum of the finite structure considered experimentally. a) Measured spectra before (blue) and after (red) illumination of all pillars simultaneously. A rigid down-shift of the whole spectrum is observed; b) Corresponding colour map representing transmission vs. frequency and time (vertical axis) when switching laser illumination on (t = 300 s) and off (t = 1600 s).

$t_3 = 150s$), so that the system returns to its initial state. Finally, in the last phase (from t_3 onwards), we illuminate the first pillar. This leads to a selective softening of the this pillar, resulting in a significant amplitude reduction of f_1 in favour of f_2. The relative spectral weights of the two frequencies thus become fully modifiable, offering a dynamic and reversible means of controlling signal components within the structure. This provides an example of how the tunable graded pillar structures can be used to actively modulate the spectral characteristics of injected signals.

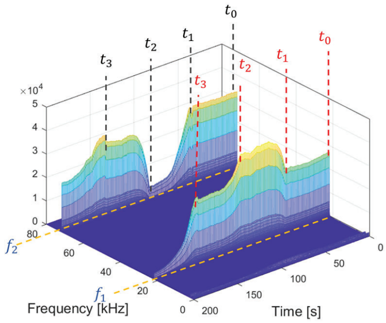

Figure 7: Dynamic modulation of signal frequencies ($f_1 = 21.5\,\text{kHz}$, $f_2 = 71.5\,\text{kHz}$) in a graded pillar structure. The different temporal intervals depict tunable suppression and enhancement of specific frequencies through selective pillar illumination.

4 Conclusion

In conclusion, we have shown how it is possible to exploit graded locally resonant structures in conjunction with light-responsive polymers to obtain metamaterials with multiple degrees of freedom of dynamic tunability. The selective modulation of the elastic properties of a photosensitive polymer by means of laser illumination provides a controlled and reversible means to manipulate the elastic characteristics of the waveguide. The spatial arrangement of pillars, each acting as a different resonator, provides a rich platform to explore the interplay between static and dynamic gradings. In this sense, we can compare this system to a piano keyboard, where the activation of different key combinations produces various note sequences, or melodies, in output. In our case, the analogy is between pillars and piano keys, and between laser illumination and finger pressure on the keys. As in the case of a piano keyboard, key combinations can be used to obtain combinations of output frequencies, or tones. Preliminary experiments on even a relatively simple structure (8 pillars of 4 different heights) indicate that due to the complex resonant behaviour of the pillars and their coupling, there is rarely a one to one relation between illumination of a single pillar and shift of a single band gap. Thus, to use such a "metamaterial keyboard" in applications, an accurate "map" of the frequency output needs to be determined, either numerically or experimentally. This will be the subject of future investigations.

Our work adds to other advances in metamaterial research that address the challenge of dynamic tunability, which allows to go beyond traditional metamaterials. Our approach introduces one possible avenue for achieving this dynamic control over elastic wave manipulation. The ability to selectively tune and suppress specific frequencies over time opens possibilities for innovative applications, particularly in dynamic signal processing, where tailored frequency responses are crucial. This is of particular relevance in active devices for elastic wave control, such as beam-splitters, switches, and filters.

Acknowledgements. V.F.D.P., F.N., P.H.B., M.M., N.M.P., F.B and A.S.G. are supported by the European Commission H2020 FET Open “Boheme” grant no. 863179. F.N. is grateful to the Cassa di Risparmio di Torino foundation for support

References

1. P. A. Deymier, Acoustic Metamaterials and Phononic Crystals, *Springer Berlin, Heidelberg* (2013).
2. R. V. Craster, S. Guenneau, Acoustic Metamaterials: Negative Refraction, Imaging, Lensing and Cloaking, *Springer Science+Business Media Dordrecht* (2013).
3. A. O. Krushynska, D. Torrent, A. M. Aragón, R. Ardito, O. R. Bilal, B. Bonello, F. Bosia, Y. Chen, J. Christensen, A. Colombi, S. A. Cummer, B. Djafari-Rouhani, F. Fraternali, P. I. Galich, P. D. Garcia, J. P. Groby, S. Guenneau, M. R. Haberman, M. I. Hussein, S. Janbaz, N. Jiménez, A. Khelif, V. Laude, M. J. Mirzaali, P. Packo, A. Palermo, Y. Pennec, R. Picó, M. R. López, S. Rudykh, M. Serra-Garcia, C. M. S. Torres, T. A. Starkey, V. Tournat, O. B. Wright, Emerging topics in nanophononics and elastic, acoustic, and mechanical metamaterials: an overview, *Nanophotonics*, 12 (4), pp. 659-686 (2023).
4. M.J. Hussein, M.J. Leamy, & M. Ruzzene, Dynamics of Phononic Materials and Structures: Historical Origins, Recent Progress, and Future Outlook. *Applied Mechanics Reviews*, 66, 040802 (2014).
5. M. Mazzotti, A. Foehr, O.R. Bilal, A. Bergamini, F. Bosia, C. Daraio, N.M. Pugno & M. Miniaci, Bio-inspired non self-similar hierarchical elastic metamaterials, *International Journal of Mechanical Sciences*, 41, pp. 107915 (2023).
6. Z. Liu, X. Zhang, Y. Mao, Y. Zhu, Z. Yang, C. Chan, P. Sheng, Locally resonant sonic materials., *Science*. 289, 1734-1736 (2000)
7. V. Romero-García, G. Theocharis, O. Richoux, A. Merkel, V. Tournat, V. Pagneux, Perfect and broadband acoustic absorption by critically coupled sub-wavelength resonators. *Scientific Reports*. **6**, 19519 (2016)
8. N. Kaina, F. Lemoult, M. Fink, G. Lerosey, Negative refractive index and acoustic superlens from multiple scattering in single negative metamaterials. *Nature*. **525**, 77-81 (2015)
9. L. Zigoneanu, B. Popa, S. Cummer, Three-dimensional broadband omnidirectional acoustic ground cloak. *Nature Materials*. **13**, 352-355 (2014)
10. J. Pendry, Negative refraction makes a perfect lens. *Physical Review Letters*. **85**, 3966 (2000)
11. A. Gliozzi, M. Miniaci, A. Krushynska, B. Morvan, M. Scalerandi, N. Pugno, F. Bosia, Proof of concept of a frequency-preserving and time-invariant metamaterial-based nonlinear acoustic diode. *Scientific Reports*. **9**, 9560 (2019)

12. Zhang, X., Xiao, M., Cheng, Y., Lu, M. & Christensen, J. Topological sound. *Communications Physics*. **1**, 97 (2018)
13. S. Mousavi, A. Khanikaev, Z. Wang, Topologically protected elastic waves in phononic metamaterials. *Nature Communications*. **6**, 8682 (2015)
14. A. Colombi, D. Colquitt, P. Roux, S. Guenneau, R. Craster, A seismic metamaterial: The resonant metawedge. *Scientific Reports*. **6**, 27717 (2016)
15. A. Palermo, S. Krödel, A. Marzani, C. Daraio, Engineered metabarrier as shield from seismic surface waves. *Scientific Reports*. **6**, 1-10 (2016)
16. M. Miniaci, A. Krushynska, F. Bosia, N. Pugno, Large scale mechanical metamaterials as seismic shields. *New Journal Of Physics*. **18**, 083041 (2016)
17. J. De Ponti, A. Colombi, R. Ardito, F. Braghin, A. Corigliano, R. Craster, Graded elastic metasurface for enhanced energy harvesting. *New Journal Of Physics*. **22**, 013013 (2020)
18. N. Jiménez, V. Romero-García, V. Pagneux, J. Groby, Rainbow-trapping absorbers: Broadband, perfect and asymmetric sound absorption by subwavelength panels for transmission problems. *Scientific Reports*. **7**, 13595 (2017)
19. N. Gao, Z. Zhang, J. Deng, X. Guo, B. Cheng, H. Hou, Acoustic metamaterials for noise reduction: a review. *Advanced Materials Technologies*. **7**, 2100698 (2022)
20. T. Dubček, D. Moreno-Garcia, T. Haag, P. Omidvar, H. Thomsen, T. Becker, L. Gebraad, C. Bärlocher, F. Andersson, S. Huber,Others In-Sensor Passive Speech Classification with Phononic Metamaterials. *Advanced Functional Materials*. pp. 2311877 (2024)
21. F. Casadei, M. Ruzzene, L. Dozio, K. A. Cunefare, Broadband vibration control through periodic arrays of resonant shunts: experimental investigation on plates, *Smart Mat. and Struct.*, 19 (1), 015002 (2010).
22. A. Bergamini, T. Delpero, L. D. Simoni, L. D. Lillo, M. Ruzzene, P. Ermanni, Phononic crystal with adaptive connectivity, *Adv. Mat.*, 26 (9), 1343–1347 (2014).
23. N. Kherraz, L. Haumesser, F. Levassort, P. Benard, B. Morvan, Controlling Bragg gaps induced by electric boundary conditions in phononic piezoelectric plates, *Appl. Phys. Lett.*, 108 (9), 093503 (2016).
24. L. Airoldi, M. Ruzzene, Design of tunable acoustic metamaterials through periodic arrays of resonant shunted piezos, *New J. Phys.*, 13 (11) 113010 (2011).
25. X. Guo, P. Wei, Dispersion relations of elastic waves in one-dimensional piezoelectric/piezomagnetic phononic crystal with initial stresses, *Ultrasonics*, 66, 72–85 (2016).
26. K. L. Jim, C. W. Leung, S. T. Lau, S. H. Choy, H. L. W. Chan, Thermal tuning of phononic bandstructure in ferroelectric ceramic/epoxy phononic crystal, *Appl. Phys. Lett.*, 94, 193501 (2009).
27. Y. Cheng, X. J. Liu, D. J. Wu, Temperature effects on the band gaps of Lamb waves in a one-dimensional phononic-crystal plate (L), *J. Acoust. Soc. Am.*, 129 (3), 1157–1160 (2011).
28. W. Lewandowski, M. Fruhnert, Mieczkowski, C. Rockstuhl, E. Górecka, Dynamically self-assembled silver nanoparticles as a thermally tunable metamaterial, *Nat. Commun.*, 6, 6590 (2015).
29. C. Goffaux, J. Vigneron, Theoretical study of a tunable phononic band gap system, *Phys. Rev. B*, 64 (7), 075118 (2001).
30. B. Florijn, C. Coulais, M. van Hecke, Programmable mechanical metamaterials, *Phys. Rev. Lett.*, 113 (17), 175503 (2014).
31. M. Miniaci, M. Mazzotti, A. Amendola, F. Fraternali, Effect of prestress on phononic band gaps induced by inertial amplification. *International Journal Of Solids And Structures*. **216** pp. 156-166 (2021)
32. M. Morvaridi, F. Bosia, M. Brun, V. Dal Poggetto, A. Gliozzi, M. Miniaci, C. Croënne, N. Pugno, G. Carta, Tunable topologically protected waveguiding in auxetic nonlinear metamaterials. *Physical Review Applied*. **21**, 034024 (2024)
33. J.-F. Robillard, O. Bou Matar, J. Vasseur, P. A. Deymier, M. Stippinger, A.-C. Hladky-Hennion, Y. Pennec, B. Djafari-Rouhani, Tunable magnetoelastic phononic crystals, *Appl. Phys. Lett.*, 95 (12), 124104 (2009).
34. Z. Xu, F. Wu, Z. Guo, Shear-wave band gaps tuned in two-dimensional phononic crystals with magnetorheological material, *Solid State Commun.*, 154, 43–45 (2013).
35. Y. G. S. Zhang, Y. Shi, Tunability of band structures in a two-dimensional magnetostrictive phononic crystal plate with stress and magnetic loadings, *Phys. Lett. A*, 381 (12), 1055 – 1066 (2017).

36. B.-I. Popa, L. Zigoneanu, S. A. Cummer, Tunable active acoustic metamaterials, *Phys. Rev. B*, 88 (2), 024303 (2013).
37. E. Walker, D. Reyes, M. M. Rojas, A. Krokhin, Z. Wang, A. Neogi, Tunable ultrasonic phononic crystal controlled by infrared radiation, *Appl. Phys. Lett.*, 105 (14), 143503 (2014).
38. E. L. Walker, Z. Wang, A. Neogi, Radio-frequency actuated polymer-based phononic metamaterials for control of ultrasonic waves, *NPG Asia Mater.* 9 (2), e350 (2017).
39. A. Goshkoderia, V. Chen, J.Li, A. Juhl, P. Buskohl, S.Rudykh, Instability-Induced Pattern Formations in Soft Magnetoactive Composites, *Physical Review Letters*, **124**, 158002 (2020)
40. N. Arora, V. Chen, A. Cherkasov, Y. Xiang, A. Juhl, P. Buskohl, S. Rudykh, Magnetically-Programmed Instability-Driven Pattern Transformations in Soft Materials, *Advanced Functional Materials*, 2401077 (2024)
41. M. R. O'Neill, D. Sessions, N. Arora, V. W. Chen, A. Juhl, G. H. Huff, S. Rudykh, R. F. Shepherd, P. R. Buskohl, Dielectric Elastomer Architectures with Strain-Tunable Permittivity. *Adv. Mater. Technol.*, **7**, 2200296 (2022)
42. Y. Xue, J. Li, Y. Wang, Z. Song, A. O. Krushynska, Widely tunable magnetorheological metamaterials with nonlinear amplification mechanism, *International Journal of Mechanical Sciences*, **264**, 108830 (2024)
43. M. Pishvar and R. L. Harne, Foundations for Soft, Smart Matter by Active Mechanical Metamaterials, *Advanced Science*, **7**, 200138 (2020)
44. A. S. Gliozzi , M. Miniaci , A. Chiappone , A. Bergamini , B. Morin , and E. Descrovi, Tunable photo-responsive elastic metamaterials, *Nat. Commun.* 11, 2576 (2020).
45. I. Roppolo, A. Chiappone, A. Angelini, S. Stassi, F. Frascella, C.F. Pirri, C. Ricciardi, C., E. Descrovi, 3D printable light-responsive polymers. *Mater. Horiz.* 4, 396–401 (2017).
46. G. J. Chaplain, A. S. Gliozzi, B. Davies, D. Urban, E. Descrovi, F. Bosia, R. V. Craster, Tunable topological edge modes in Su–Schrieffer–Heeger arrays, *Appl. Phys. Lett.* 122, 221703 (2023)
47. B. R. Mace, E. Manconi, “Modelling wave propagation in two-dimensional structures using finite element analysis,” *Journal of Sound and Vibration*, vol. 318(4-5), pp. 884-902, 2008.
48. L. Brillouin, “Wave propagation in periodic structures; electric filters and crystal lattices,” *K Courier Dover Publications* 1946.
49. Miniaci, M., Gliozzi, A., Morvan, B., Krushynska, A., Bosia, F., Scalerandi, M. & Pugno, N. Proof of concept for an ultrasensitive technique to detect and localize sources of elastic nonlinearity using phononic crystals. *Physical Review Letters*. **118**, 214301 (2017)

nature communications

Article

https://doi.org/10.1038/s41467-023-42590-y

Polarization-driven reversible actuation in a photo-responsive polymer composite

Received: 26 April 2023

Accepted: 16 October 2023

David Urban[1,2], Niccolò Marcucci[2], Christoph Hubertus Wölfle[3], Jan Torgersen[3], Dag Roar Hjelme[1] & Emiliano Descrovi[2]

Light-responsive polymers and especially amorphous azopolymers with intrinsic anisotropic and polarization-dependent deformation photo-response hold great promises for remotely controlled, tunable devices. However, dynamic control requires reversibility characteristics far beyond what is currently obtainable via plastic deformation of such polymers. Here, we embed azopolymer microparticles in a rubbery elastic matrix at high density. In the resulting composite, cumulative deformations are replaced by reversible shape switching – with two reversible degrees of freedom defined uniquely by the writing beam polarization. We quantify the locally induced strains, including small creeping losses, directly by means of a deformation tracking algorithm acting on microscope images of planar substrates. Further, we introduce free-standing 3D actuators able to smoothly undergo multiple configurational changes, including twisting, roll-in, grabbing-like actuation, and even continuous, pivot-less shape rotation, all dictated by a single wavelength laser beam with controlled polarization.

In the fast-growing domain of stimuli-responsive materials, photo-responsive polymers hold a prominent position thanks to several advantageous features, such as their intrinsically contactless control and the large variety of light sources and compounds available to tailor material responses[1]. Amorphous sidechain azopolymers are an intriguing sub-class of light-responsive polymers since many of them can undergo directional, anisotropic deformations when irradiated with linearly polarized visible light. This effect occurs below the glass transition temperature, with the polarization direction generally determining the axis of elongation[2]. Although this phenomenon is known to be linked to the Weigert effect[3] (statistical reorientation of azobenzene moieties perpendicular to the polarization), different mechanisms are still under debate to explain it[4,5]. In the meantime, polarization-dependent deformations in side-chain azopolymers have been widely used for the thin film inscription of surface relief gratings (SRGs) by pure polarization interference patterns[6,7], polarization-dependent patterning through surface plasmon interference[8], as well as directional reshaping of both nanoparticles[9,10] and pre-fabricated micro-/nanopillar structures[11–15]. Whilst these approaches are very appealing to the realm of advanced micro- and nanofabrication techniques[16], or self-healing devices[17], deformations are usually plastic and tend to apply to the materials in a cumulative manner. Achieving deformation reversibility has therefore been a major goal in recent works, where approaches included the use of azopolymer cross-linked networks[18,19], erasure of SRGs by complementary interference patterns or circular polarization irradiation[20], and embedding of azopolymer microparticles in elastomeric materials[21]. Furthermore, in concrete applications such as photo-switchable topographies guiding cells, obtaining intrinsic reversibility has been identified as a key challenge[15,22,23].

Controlling the deformation direction and reversibility is also of paramount importance in light-responsive soft actuators. In this context, working schemes have involved linear actuators based on asymmetric volume expansion in various materials such as hydrogels or

---

[1]Department of Electronic Systems, Norwegian University of Science and Technology, O.S. Bragstads plass 2b, 7034 Trondheim, Norway. [2]Dipartimento di Scienza Applicata e Tecnologia, Politecnico di Torino, Corso Duca degli Abruzzi 24, 10129 Torino, Italy. [3]Institute of Materials Science, Department of Materials Engineering, TUM School of Engineering and Design, Technical University of Munich, Boltzmannstraße 15, 85748 Garching, Germany.
e-mail: emiliano.descrovi@polito.it

azopolymer-coated substrates[24,25], bidirectionally actuatable cross-linked azo-polyimides[26], and photo-responsive liquid crystal elastomers/networks (LCNs)[27]. The latter is maybe the most well-known type of light-responsive soft actuators[28] and can benefit from excellent reversibility and actuation speeds, due to their cross-linked nature, which permits the design of light-responsive oscillating[29–32], wave-propagating[33], and even mobile actuators[33–36]. However, LCNs usually require a molecular alignment procedure to be performed during fabrication, which, at least locally, fully predetermines the directionality of their response. In addition, inscribing the sophisticated alignment patterns needed for complex actuation shapes is still far from being trivial[37,38]. To overcome these limitations, several post-fabrication tunability strategies have been proposed. Examples include multi-wavelength schemes with several dyes[39–41], the use of constituents exhibiting an enhanced polarization-sensitivity in absorption[42], or reconfigurability based on a combination of photochemical and photothermal effects[43]. Polarization-driven actuation in polycrystalline LCN has also been proposed as an interesting option[44,45]. However, performing reversible complex actuations at room temperature via polarization-driven control remains a relevant challenge.

Here we introduce an isotropic composite based on amorphous azopolymer nano-/microparticles embedded at high density within a soft rubbery Styrene-Ethylene-Butylene-Styrene (SEBS) matrix, the latter having been previously used in electrically driven soft actuators[46]. The azopolymer employed is poly [(methyl methacrylate)-co-(Disperse Red 1 methacrylate)] (pDR1m-co-mma, characterization details provided in Supplementary Fig. 1), and the composite will simply be referred to as azo-SEBS in the following. Upon irradiation with linear polarization, the azopolymer particles transmit their anisotropic strain along the polarization direction to the overall matrix, thus producing a controlled deformation. During consecutive irradiation steps, cumulative deformations that would be expected from the uncross-linked amorphous azopolymer are replaced by a more reversible behaviour, which emerges from the interaction of the particles with the surrounding elastomeric matrix. A similar effect has recently been observed for sparsely distributed, single azopolymer microparticles[21].

In the following, a detailed analysis of the local in-plane deformation of thin composite layers of azo-SEBS deposited on polydimethylsiloxane (PDMS) slabs is presented, providing a benchmark of the overall degree of reversibility upon several illumination cycles. Thereafter, from an application perspective, soft actuators based on free-standing membranes are proposed. We showcase that ample, reversible, and continuous complex actuation can be performed by merely controlling the polarization state of an illuminating laser beam. In Fig. 1, the fundamental actuation scheme for both thin coating layers and free-standing actuator membranes is illustrated.

Results

Deformation of planar substrates

To characterize the stretching of the azo-SEBS composite quantitatively, the thin coating layers (thickness 3-20 µm) were decorated with a periodic pattern of micro-pillar markers for precise deformation tracking (Fig. 2a). Since all light-induced deformations were observed to persist with switched-off illumination, the fast-scanning focused laser beam of a confocal microscope was used to illuminate tens of microns wide rectangular areas precisely and homogeneously. A movie of the repeated anisotropic deformations induced by a sequence of illumination steps with alternating linear and circular polarization of the scanning beam (wavelength $\lambda = 561$ nm, intensity $I = 5.02\,\mathrm{W{\cdot}cm^{-2}}$, step time $t = 15$ s) is provided in Supplementary Movie 1. Whilst polarization along the x-axis induces stretching along said direction, circular polarization seems to induce a return to the previous state. The associated material displacements can also be observed to extend beyond the directly illuminated zone shown in the movie, to accommodate the deformation of the latter. This is displayed in Supplementary Fig. 2, where a differential image of a wider area was used to compare the initial state and the stretched state after a single illumination step with x-oriented polarization.

Deformations within the area of irradiation were then analyzed in Fourier space (Fig. 2b), where reciprocal lattice peaks of the hexagonal pattern of cylindrical markers are detected and tracked at each illumination step. This approach of focusing only on the light-induced changes in the spatial harmonics of the lattice was found to provide greater independence from small lateral and out-of-plane sample drifts, as well as tiny contrast changes produced in the collected images over many repeated illumination steps. The photo-responsive layer's adhesion to the underlying PDMS substrate also mitigates effects such as gradual out-of-plane bulging and wrinkling, which we observed in similar experiments on suspended azo-composite layers (Supplementary Movie 2, Supplementary Fig. 3) and which have recently been reported for floating azopolymer thin films[47]. In the Methods section, more details on how polarization-induced deformations affect the film topography in both direct and reciprocal (Fourier) space are provided. Red arrows in Fig. 2c depict the vectorial shifts $\boldsymbol{\Delta k}$ of the lattice peaks after an illumination step with linear x-axis polarization, taking the configuration before illumination as a

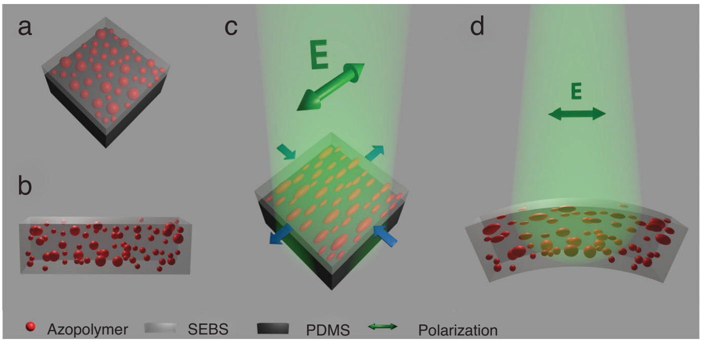

Fig. 1 | Sketch of light-induced deformation mechanisms. a azo-SEBS film deposited on a PDMS layer, (**b**) self-standing azo-SEBS membrane; (**c**) illustrative deformation of azopolymer microdomains upon linearly polarized laser irradiation, leading to overall stretching of the azo-SEBS layer on PDMS along the polarization direction; (**d**) inhomogeneous stretching of the free-standing azo-SEBS membrane and corresponding bending caused by the gradient of absorbed light through the membrane. Both SEBS and PDMS are translucent/transparent materials in the real world.

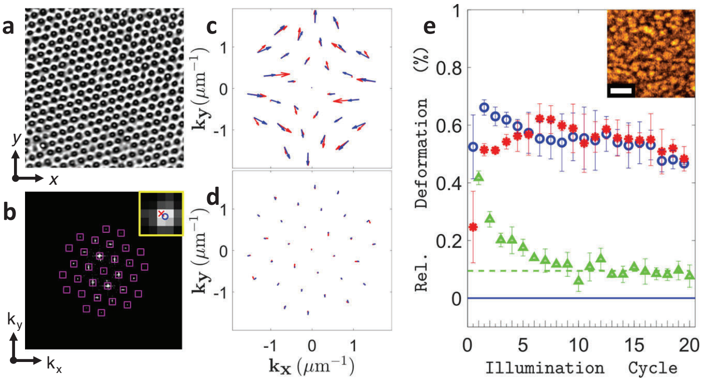

Fig. 2 | Analysis of 2D deformations. a Confocal microscope transmission image of the 33.8 × 33.8 μm² area decorated with 1 μm spaced, 1 μm wide pillars, before illumination. **b** Fourier transforms the image of a, with detected peak locations (pink squares). Inset: 2D Gaussian fitting of exact peak position. Shift of peaks in Fourier space after irradiation with (**c**) linear polarization and after irradiation with (**d**) linear and subsequent circular polarization (illumination cycle). Red arrows: data, blue arrows: fit. Arrow magnification: x45. **e** Extracted fit parameters for 20 illumination cycles: relative horizontal elongation strain ε_1 per X-POL step (blue circles), absolute value of relative vertical compression strain $|\varepsilon_2| = -\varepsilon_2$ per X-POL step (red asterisks), relative area expansion δA_{cycle} per full illumination cycle (X-POL + CIRC-POL) (green triangles). Dashed green line: asymptotic behaviour. Solid blue line: zero deformation limit. Short/tall x-axis ticks: X-pol step/two-step illumination cycle. Error bars: Sample standard deviation (s.d.) of 3 acquisitions on distinct areas. Inset: Confocal image of the sample's fine structure (bulk) showing the size of the azopolymer domains. Inset scale bar: 3 μm.

reference. In agreement with the x-axis elongation observed in direct space, peaks shift inwards along said axis in reciprocal space, whilst direct space compression behaviour leads to arrows pointing outwards in the orthogonal direction. Figure 2d shows a similar arrow plot, wherein the reference configuration is compared to the result after two irradiation steps, with a linear x-polarization (X-POL) step followed by a circular polarization (CIRC-POL) step (equal power and dose). This two-step procedure is referred to as the full illumination cycle hereafter. For the full illumination cycle, arrows are much smaller and point inwards everywhere, thereby indicating slight isotropic in-plane expansion, as opposed to complete reversal. In-plane expansion of azopolymers upon irradiation with circular polarization has been previously reported in microparticles dispersed in external matrices[21,48], microstructures anchored on flat substrates[12,17], wall thickening of breath-figure arrays[18,49] and in floating thin films[47]. It is often described to compete with a photo-softening effect of the azopolymer, also attributed to the circularly polarized irradiation[21,47]. To get more insights on the effects of repeated exposures with linearly and circularly polarized light, we quantified the stretching behaviour over 20 consecutive illumination cycles on a previously unexposed area.

In particular, when considering the i^th illumination cycle, new experimental lattice peak positions were fitted with $\mathbf{k_i}$ defined upon applying the transformation in Eq. (1) to the previous peak vectors $\mathbf{k_{i-1}}$. The transformation represents pure stretching along two principal axes in Fourier space, with associated direct space engineering strain parameters (ε_1, ε_2) and a principal stretching axis angle (θ) ranging between ±45 degrees with respect to the x-axis.

$$\mathbf{k_i} = \begin{pmatrix} \cos(\theta) & -\sin(\theta) \\ \sin(\theta) & \cos(\theta) \end{pmatrix} \cdot \begin{pmatrix} (1+\varepsilon_1)^{-1} & 0 \\ 0 & (1+\varepsilon_2)^{-1} \end{pmatrix} \cdot \begin{pmatrix} \cos(\theta) & \sin(\theta) \\ -\sin(\theta) & \cos(\theta) \end{pmatrix} \cdot \mathbf{k_{i-1}} \tag{1}$$

Furthermore, the stretching due to the illumination with linear polarization only was evaluated by applying the procedure described above to the peak positions obtained after the X-POL step alone (half illumination cycle), using the same reference positions $\mathbf{k_{i-1}}$.

Typical *R2*-values of the fits (see Methods section) were 0.71 ± 0.03 for X-POL steps and 0.49 ± 0.11 for illumination cycles respectively. The angle θ was distributed as −4.3 ± 1.4 degrees for the X-POL steps, making ε_1 close to horizontal, as expected from linear x-polarization inducing stretching along said axis. For full illumination cycles, it was found more useful to estimate the relative area expansion (per cycle) of the substrate, which can be expressed as $\delta A_{cycle} = \varepsilon_1 + \varepsilon_2$ (first-order approximation). Therefore, in the following ε_1 and ε_2 will refer to the X-POL steps, while δA_{cycle} refers to the illumination cycles (X-POL + CIRC-POL). The typical time evolution of ε_1, $|\varepsilon_2|$ and δA_{cycle} for 20 consecutive full illumination cycles at laser intensity $I = 1.30\ \mathrm{W{\cdot}cm^{-2}}$ and step time $t = 15$ s, is shown in Fig. 2e.

Interestingly, one can observe an initial transient behaviour, where the horizontal elongation strain ε_1 upon linear x-polarized irradiation is much larger than the absolute value of the associated vertical compression strain $|\varepsilon_2| = -\varepsilon_2$, approximately by a factor 2. However, after a few cycles, the absolute values of the two strains converge to a very similar and nearly constant value. The asymptotic values for both strains will be referred to as $\varepsilon_{1,\infty}$ and $\varepsilon_{2,\infty}$ hereafter and are calculated as the respective mean values of ε_1 and ε_2 over the last 10 X-POL steps. Furthermore, similar transient behaviour can also be observed for the relative area expansion δA_{cycle} at each illumination cycle. Starting at a high initial value, δA_{cycle} decreases rapidly and stabilizes to a small and constant value $\delta A_{cycle,\infty}$, indicating much less in-plane area expansion and thus significantly better relative reversibility after a few cycles.

To explain this behaviour, we note that in a small strain regime, a factor $-\varepsilon_2/\varepsilon_1 = 0.5$ is associated with volume conservation for uniaxial stretching, whilst $-\varepsilon_2/\varepsilon_1 = 1$ conserves the area of observation. In the following, we presume that the observed macroscopic engineering strains are proportional to the deformations of the embedded azopolymer microdomains. This assumption is discussed with the help of a finite element (FE) model in the next section. In Eq. (2), we write down isochoric (volume-preserving) small strain deformation gradient tensors corresponding to x-axis stretching ($\mathbf{F^1}$) and in-plane expansion ($\mathbf{F^2}$) respectively. Both tensors are constrained to induce the same z-axis compression and δ is a scalar parameter.

$$\mathbf{F^1} = \begin{pmatrix} 1+\delta & 0 & 0 \\ 0 & 1-\frac{1}{2}\delta & 0 \\ 0 & 0 & 1-\frac{1}{2}\delta \end{pmatrix}, \mathbf{F^2} = \begin{pmatrix} 1+\frac{1}{4}\delta & 0 & 0 \\ 0 & 1+\frac{1}{4}\delta & 0 \\ 0 & 0 & 1-\frac{1}{2}\delta \end{pmatrix} \tag{2}$$

Assuming axial symmetry about the x-axis for the very first (X-POL) illumination step[50], the observed deformation seems to be associated with an isochoric stretching of the azo-microparticles along the x-axis. Indeed, a deformation described by $\mathbf{F^1}$ results in an engineering strain ratio $-\varepsilon_2/\varepsilon_1 \approx 0.5 = -(-1/2\delta/\delta)$. This agrees well with observations reported for free azopolymer nano-/micro-particles wherein irradiation with linear polarization isochorically transforms spherical particles into ellipsoids elongated along the polarization direction[10]. After completing the first illumination cycle with circular polarization, however, substantial in-plane expansion $\delta A_{\mathrm{cycle}}$ subsists. Thus, in opposition to previous reports on single particles of a different side-chain azopolymer embedded in SEBS[21], circular polarization does not reverse the initial deformation here. In some cases, spherical azo-particles irradiated with circularly polarized light were reported to expand in the plane into disk shapes, as evidenced in previous works on azobenzene-based molecular glass particles in hydrogels[48]. The transformation corresponding to this deformation can be described by $\mathbf{F^2}$. Interestingly, however, after multiple illumination cycles, $\delta A_{\mathrm{cycle}}$ is reaching a very low asymptotic value meaning that the in-plane area is almost fully conserved through each cycle. Still, within those cycles, the X-POL illumination steps cause relatively high, constant asymptotic stretching amplitudes $\varepsilon_{1,\infty}$ and $\varepsilon_{2,\infty}$, therefore indicating a reversible, stationary deformation behavior. This evidence suggests that deformations induced by alternating illumination with linear and circular polarizations cannot be simply described by sequential applications of $\mathbf{F^1}$ and $\mathbf{F^2}$, which would produce a constant and substantial in-plane expansion during every cycle. As a possible explanation, we propose a reversible switching regime occurring asymptotically, between two distinct shapes of the azo-microparticles, resembling the ellipsoids elongated along the x-axis and the in-plane expanded disk-like shapes introduced above. These shapes are found experimentally to have a similar in-plane area ($-\varepsilon_{2,\infty}/\varepsilon_{1,\infty} \approx 1$) and similar compression along the z-axis, assuming incompressibility (see Methods section). We may therefore represent the switching from disk-like to x-axis stretched ellipsoid by a third transformation $\mathbf{F^3}$, defined as

$$\mathbf{F^3} = \mathbf{F^1}\cdot(\mathbf{F^2})^{-1} = \begin{pmatrix} \frac{1+\delta}{1+\frac{1}{4}\delta} & 0 & 0 \\ 0 & \frac{1-\frac{1}{2}\delta}{1+\frac{1}{4}\delta} & 0 \\ 0 & 0 & \frac{1-\frac{1}{2}\delta}{1-\frac{1}{2}\delta} \end{pmatrix} \approx \begin{pmatrix} 1+\frac{3}{4}\delta & 0 & 0 \\ 0 & 1-\frac{3}{4}\delta & 0 \\ 0 & 0 & 1 \end{pmatrix} \quad (3)$$

where the final expression is based on a first-order approximation (see Supplementary Note 1), and $\mathbf{F^3}$ is consistent with the area conservation during X-POL steps observed at later cycles. Also, the small overshoot of ε_1 during the first illuminations may be explained by the x-axis strain being larger for a transformation from a spherical to the x-axis stretched ellipsoid shape ($\mathbf{F^1}$), than from a disk-like to the same ellipsoid shape in the switching regime ($\mathbf{F^3}$). Similar reasoning holds for the y-axis strains and the initial undershoot of $|\varepsilon_2|$.

Obtaining a reversible switching regime is remarkable since the plastic deformations of sidechain azopolymers are typically cumulative. For example, SRGs with square/tetragonal geometries have been demonstrated by simply adding a second interference pattern on top of an already inscribed one[7,22,51] and multi-SRG superposition can additively create up to 12-fold rotationally symmetric structures[52]. Cumulative deformation sequences have also been used to create complex 3D shapes from pristine hemispherical microstructures[12]. For example, applying a linear polarization to pre-deformed pillars made of similar side-chain azopolymer poly(Disperse Red 1 methacrylate) (pDR1m)[15] does not erase the first inscribed shape, but simply adds another deformation, flattening the individual pillars further (Supplementary Fig. 4). On a macroscopic level, applying the methodology of this work to a pure pDR1m-co-mma film on PDMS, weaker, however, fully cumulative deformations were observed (Supplementary Movie 3, Supplementary Fig. 5). In that case, the relative area expansion remained high for all cycles and the $-\varepsilon_2/\varepsilon_1$ relationship for X-POL steps stayed close to 0.5 (as in $\mathbf{F^1}$), indicating no switching behaviour. During later frames, degradation of the pillar lattice could be observed also here (Supplementary Fig. 5b). Finally, it should be noted that the reversibility of the switching process reported for azo-SEBS, while being far from a purely cumulative effect, is not complete, since $\delta A_{\mathrm{cycle}}$ approaches a non-zero value indicating that a (much smaller) irreversible in-plane expansion persists during later cycles also in the case of the composite.

Finite element modeling of the deformation mechanism

In the previous section, the observed macroscopic engineering strains of the composite were assumed proportional to the deformations of the azopolymer microdomains embedded within. To verify the validity of this assumption, as well as to better understand the microstructural strain field causing the composite's macroscopic deformations, a 2D continuum model of a representative section of azo-SEBS composite with randomly placed, non-intersecting domains of pDR1m-co-mma (azo-domains) was set up using the FE software Abaqus/Standard. A detailed description of the model is provided in the Methods section, whilst further comments on the accuracy of the 2D modelling approximation are provided in Supplementary Note 2. In brief, both phases (azo-domains and SEBS) were considered incompressible and the constitutive model of the rubbery matrix was parametrized with mechanical data from tensile tests for SEBS of the same hardness grade and manufacturer performed by others[53]. As is common for rubbery materials, the stress-strain curve was shown to be non-linear at high strains in the cited study (see Supplementary Fig. 6a for more details). We note, however, that this non-linearity becomes dominant in such experiments at strains roughly above 20%, which is far above the macroscopic average strains measured in this work. To estimate the internal matrix strains associated with the composite's deformation, the effect of illumination was modelled via deformations imposed directly onto the embedded azo-domains. Linear x-polarization and circular polarization were modelled by the deformation gradient tensors $\mathbf{F^{lin}}$ and $\mathbf{F^{circ}}$, respectively, which are defined in the Methods section, and which correspond to $\mathbf{F^1}$ and $\mathbf{F^2}$ of Eq. (2) for small strains (first order approximation, see Supplementary Note 1).

Figure 3a shows the resulting logarithmic (Hencky) normal strain in x-direction, denoted by $\varepsilon^{\mathrm{H}}_{xx}$, over the whole simulation domain. As one can observe, the highest strain values are the uniform ones imposed on the azo-domains, while the surrounding matrix accommodates the inclusions' deformation via lower local strains. Phenomenologically, compressive strains arise in x-direction between azo-domains lying close to each other horizontally, since the elongation of the inclusions in this direction compresses the material in between. Figure 3b shows the local relative area change (to the first order) $\varepsilon^{\mathrm{H}}_{xx} + \varepsilon^{\mathrm{H}}_{yy} \cong \varepsilon_{xx} + \varepsilon_{yy}$ also indicating a net in-plane compression between horizontally neighboring azo-domains. The opposite holds for vertically neighboring azo-domains, where in-plane expansion is observed, due to azo-domain compression along the y-axis. Both those observations illustrate how the deformation of individual domains drives the overall material's response. To expand on this, the coefficients of transmission between azo-domain deformations and the overall composite deformations will be discussed below along with their dependency on the magnitude of the imposed azo-domain strain.

After denoting the engineering strains imposed onto the azo-domains by $\boldsymbol{\varepsilon}^{\mathbf{az}}$ and the average macroscopic engineering strains by $\boldsymbol{\varepsilon}^{\mathbf{m}}$, we define the scalar transmission ratio of normal strains along any of the principal axes (i = *x,y*) generically as $T^{\mathrm{type}}_{\mathrm{ii}} := \varepsilon^{\mathrm{m}}_{\mathrm{ii}}/\varepsilon^{\mathrm{az}}_{\mathrm{ii}}$ (type = {lin, circ} when applying $\{\mathbf{F^{lin}}, \mathbf{F^{circ}}\}$ to pristine spherical azo-domains respectively). Figure 3c shows $T^{\mathrm{type}}_{\mathrm{ii}}$ as a function of $\varepsilon^{\mathrm{az}}_{\mathrm{ii}}$ for both

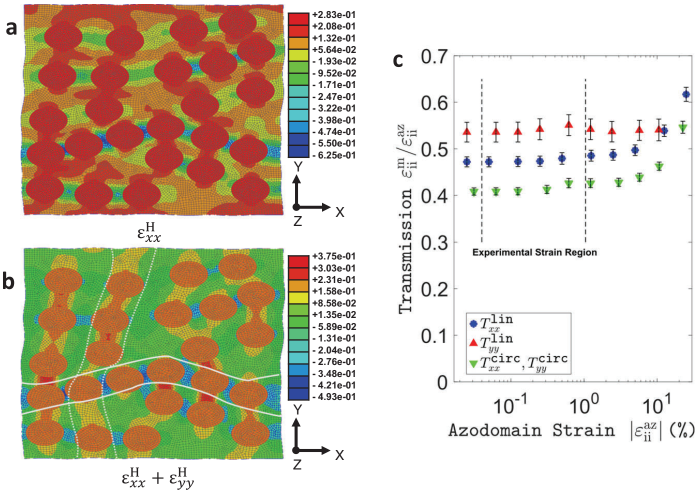

Fig. 3 | Finite element model. Logarithmic normal strain in x-direction $\varepsilon^{\mathrm{H}}_{xx}$ (**a**) and first-order in-plane expansion $\varepsilon^{\mathrm{H}}_{xx} + \varepsilon^{\mathrm{H}}_{yy}$ (**b**) around the azo-domains stretched along the x-axis using $\mathbf{F}^{\mathrm{lin}}$ to model the illumination-induced eigenstrain of the azo-domains associated to linear x-polarization. Solid and dashed white lines provide a guide to the eye for identifying compression/expansion zones, respectively. The shear component and logarithmic normal strain in y-direction are shown in Supplementary Fig. 6b, c. **c** Normal strain transmission factor $T^{\mathrm{type}}_{\mathrm{ii}}$ as a function of imposed azo-domain strain $\varepsilon^{\mathrm{az}}_{\mathrm{ii}}$ for each type of deformation (type = {lin, circ}) and principal axis (i = {x,y}). Error bars: sample standard deviation from 9 simulations with different randomly generated azo-domain arrangements. For simplicity of representation T^{circ}_{xx} and T^{circ}_{yy} are plotted with the same marker type due to their substantial overlap.

deformations studied and along either y- or x-axis, leading to four distinct data series. Since $\mathbf{F}^{\mathrm{circ}}$ has axial symmetry about the z-axis, the resulting values of T^{circ}_{xx} and T^{circ}_{yy} coincide. Further, one can observe that the transmission values do not depend on the amplitude of $\varepsilon^{\mathrm{az}}_{\mathrm{ii}}$ in the range of experimentally observed strains. Finally, all transmission factors are rather similar, which was further verified for a sequential application of $\mathbf{F}^{\mathrm{lin}}$ and $\mathbf{F}^{\mathrm{circ}}$ deformations. Although slight offsets between the different data series, which are likely due to the 2D nature of the simulation (see Supplementary Note 2) can be appreciated, the results from the FE model support the qualitative assumption made in the previous section about linear transmission between the azopolymer microparticles' and the overall material's deformation.

Varying illumination conditions and sample fine-structure

The above FE model also predicted the transmission into macroscopic strains to be independent of microparticle deformation amplitudes. Therefore, we attempted to vary the latter by altering the illumination parameters. The result of varying laser powers and illumination step time is displayed in Fig. 4 for the asymptotic values $\varepsilon_{1,\infty}$ and $\varepsilon_{2,\infty}$. Both values are found to be dependent on the illumination step dose, rather than irradiation intensity, and follow the same sublinear trend. This sublinear behaviour agrees with reports on the deformation of single microparticles in a SEBS matrix as a function of irradiation time[21]. A similar trend is also observed for $\delta A_{\mathrm{cycle},\infty}$, (see Supplementary Fig. 7) whose relative amplitude with respect to the stretching parameters is unaffected by the illumination parameters. Instead, this ratio can be sensitive to different fine structures of the azo-SEBS composite, as will be detailed below.

Note that all measurements up to this point have been carried out on what will be referred to as sample 1 hereafter. As described in the Methods section, it was possible to cast pDR1m-co-mma:SEBS blends at different degrees of dilution. In this way, samples with increasing thickness containing (larger) azopolymer aggregates could be obtained for decreasing amounts of solvent (Table 1).

Figure 5a shows the measurement of 20 actuation cycles conducted with the same illumination parameters which were used

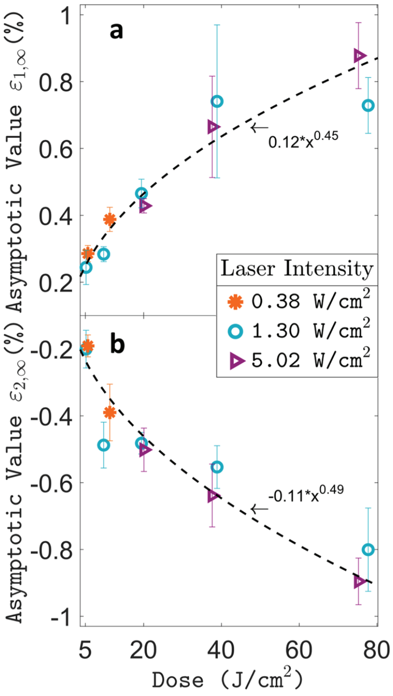

Fig. 4 | Influence of illumination conditions on macroscopic strain. Plot of asymptotic strain parameters $\varepsilon_{1,\infty}$ (**a**) and $\varepsilon_{2,\infty}$ (**b**) respectively as a function of applied dose (intensity times the exposure time) per illumination step. The asymptotic values are based on acquisitions whose graphs are shown in Supplementary Fig. 8. Error bars are three times the standard error of the mean (s.e.m.), as detailed in the Methods section.

Table 1 | Summary of geometrical features and the asymptotic strain values obtained for different samples, made from different solid content during the casting process

Name:	Solute @ casting (wt%)	Estimated aggregate size (μm)	Estimated thickness (μm)	$\varepsilon_{1,\infty}$ (%)	$\varepsilon_{2,\infty}$ (%)	$\delta A_{cycle,\infty}$ (%)	R_{irr}
Sample 1	0.7	1	3.1 ± 0.5	0.52 ± 0.03	-0.54 ± 0.03	0.095 ± 0.004	0.18 ± 0.02
Sample 2	5	2	5.4 ± 0.8	0.64 ± 0.07	-0.45 ± 0.05	0.26 ± 0.02	0.41 ± 0.07
Sample 3	10	15	12.9 ± 1.0	0.49 ± 0.06	-0.40 ± 0.01	0.19 ± 0.03	0.40 ± 0.10
Sample 4*	15	75	14.4 ± 2.0	-	-	-	-
*on top of aggregates	-	-	-	0.10 ± 0.01	-0.05 ± 0.01	0.080 ± 0.003	0.80 ± 0.09
*between aggregates	-	-	-	0.34 ± 0.07	-0.33 ± 0.08	0.06 ± 001	0.18 ± 0.07

Uncertainties are based on the s.d. of three measurements for thickness, the s.e.m. of three independent acquisitions for $\varepsilon_{1,\infty}$, $\varepsilon_{2,\infty}$, $\delta A_{cycle,\infty}$ and on the error propagation for R_{irr}.

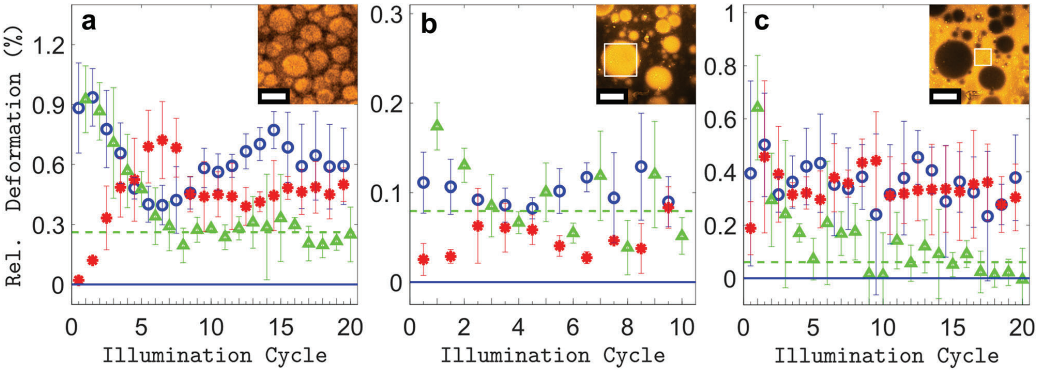

Fig. 5 | Influence of sample fine structure. Plot of fitted parameters for multiple actuation cycles for Sample 2 (**a**) and Sample 4 on top of large aggregates (**b**) and in between aggregates (**c**). Relative horizontal elongation strain ε_1 per X-POL step (blue circles), absolute value of relative vertical compression strain $|\varepsilon_2| = -\varepsilon_2$ per X-POL step (red asterisks), relative area expansion δA_{cycle} per full illumination cycle (X-POL + CIRC-POL) (green triangles). Dashed green line: asymptotic behaviour. Solid blue line: zero deformation limit. Short/tall x-axis ticks: X-pol step/Two-step illumination cycle. Error bars: s.d. of 3 acquisitions on distinct areas. Insets: confocal images of samples' structures and aggregate sizes. Inset scale bars: (**a**) 3 μm, (**b**, **c**) 75 μm. White frames on insets in (b,c) show a typical illumination area.

previously (see e.g., Fig. 2e), yet carried out on sample 2, which has a slightly thicker azo-SEBS layer, with larger (<2 μm) azopolymer aggregates (see inset of Fig. 5a and Supplementary Fig. 9b). The most striking difference in this case is that the in-plane expansion per illumination cycle (δA_{cycle}) has an asymptotic value of 0.26 ± 0.02%, which is much higher than in the case of smaller azo-aggregates (sample 1). However, the anisotropic stretching values ($\varepsilon_{1,\infty}$, $\varepsilon_{2,\infty}$) remain similar. We therefore quantify the reversibility by defining an irreversibility factor $R_{irr} \equiv \delta A_{cycle,\infty}/\varepsilon_{1,\infty}$, a measure that will result in 0% for full reversibility in the switching regime and 100% for purely irreversible (cumulative) deformations. For sample 2, we obtained $R_{irr} = 41 \pm 7\%$ which, compared to $R_{irr} = 18 \pm 2\%$ for sample 1, highlights the higher irreversibility of this sample. In addition, $\varepsilon_{1,\infty}$ lies slightly above $\varepsilon_{2,\infty}$ for sample 2, confirming that more significant incompressible plastic deformation is occurring in the asymptotic regime, which for the case of uniaxial stretching along the x-axis indeed implies ε_1 higher than $|\varepsilon_2|$ (see $\mathbf{F}^1$ in Eq. (2)). To evaluate whether higher irreversibility is correlated to large azo-aggregates, sample 4, cast from even less solvent was considered. The largest aggregates were wide enough (<70 μm) to perform measurements in areas lying completely above a single aggregate. Results for 10 illumination cycles are displayed in Fig. 5b. In this case, deformations were much smaller, approaching the limit of the detection technique used. Nevertheless, the previously observed trend continued, with the irreversibility parameter reaching $R_{irr} = 80 \pm 9\%$, and the ratio $-\varepsilon_{1,\infty}/\varepsilon_{2,\infty}$ equaling 1.9, indicating almost fully plastic cumulative deformations at every illumination step (note the similarity to the graph obtained using a pure azopolymer film in Supplementary Fig. 5a mentioned above). Measurements performed on the same sample, but on areas lying in between the large azopolymer aggregates (Fig. 5c) revealed an opposite behaviour with an irreversibility ratio as low as $R_{irr} = 17 \pm 7\%$, most likely due to the absence of big azopolymer aggregates in those interstitial areas (Supplementary Fig. 10). This suggests that not only the presence of larger aggregates but also their density could play a role in determining the average irreversibility of the overall material. In particular, interstitial volumes containing only smaller aggregates may continue to behave in a more reversible way. In fact, sample 3, which contains larger aggregates than sample 2, displays a similar average reversibility likely owing to this effect (Supplementary Fig. 11). The above findings are summarized in Table 1.

In conclusion, the preceding section shows that larger azopolymer aggregates should be avoided whenever possible, as they lose the shape-switching property and undergo the cumulative deformations of pure azopolymer instead. Furthermore, the analysis of illumination conditions shows that emerging shape-switching behaviour does not depend on a particular laser intensity or illumination dose within the investigated range. The dose however defines the amplitude of the induced deformations, meaning that intensity can be traded against illumination time, allowing for application-dependent adjustments.

3D actuation of free membranes

A potential application for the polymer composite presented herein is soft actuators able to perform complex movements in 3D[21]. To this aim, free-standing membranes were cut out and detached from PDMS,

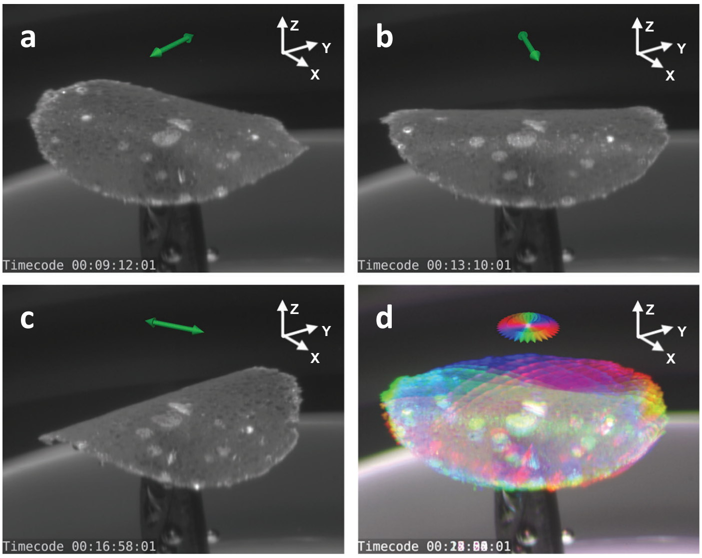

Fig. 6 | Continuous rotation of bending axis on a circular membrane patch. **a**–**c** Snapshots from Supplementary Movie 4 showing different bent states in response to illumination with linear polarization in different directions (green arrow). **d** Rainbow-coloured chronological superposition of 18 movie frames, illustrating the continuous rotation behaviour. Illumination is provided from the top, along the z-axis.

in view of exploiting bending motion due to deformation gradients (Fig. 1b, d). Supplementary Movie 4 shows a circular membrane patch (diameter: 3.4 mm, thickness: ~20 μm) on the tip of a needle, experiencing downward bending along the continuously rotating axis of linear polarization of an incoming laser beam (top illumination). Selected frames from Supplementary Movie 4 are displayed in Fig. 6a–c and a superposition of 18 rainbow-coloured frames is shown in Fig. 6d. During the photo-actuation of the free membrane, deformations are observed to occur in a basically non-cumulative way as well. When the polarization orientation is altered, the induced expansion/compression of the membrane is found to simultaneously erase (most of) the previous deformation state, thus permitting a continuous shape rotation. Worth to mention in this context that the reversible switching behaviour on patterned planar films, introduced previously by analyzing (X-POL/CIRC-POL) illumination cycles, can also be observed in the case of alternating linear polarizations along the x-and y-axis (see Supplementary Fig. 12).

It should be noted that this continuous rotation was performed with the membrane immersed in water. In fact, as shown in Supplementary Movie 5, when applying the same illumination sequence with alternating perpendicular polarizations to a circular membrane in water and in air, a drastic difference in behaviour is observed. Whilst the membrane in water reversibly bends along the orthogonal polarization directions, without visible fatigue (7 steps), the first deformation shape in air seems irreversibly inscribed and subsequent illuminations lead to much smaller deviations from said shape. Furthermore, re-immersing the same membrane in water, the reversible behavior is not fully restored. Possible reasons for this behaviour are elaborated in the Discussion section.

Finally, the circular membrane was seen to mainly experience uniaxial, elongation-associated downwards-bending, away from the light source and in the direction of the illuminating polarization. Although not systematically investigated in this article, a tendency for smaller and thinner membranes to display more simultaneous upward bending in the direction orthogonal to the polarization (where compression was measured on planar substrates) can be reported. The resulting saddle-shape, together with a single linear boundary condition, is exploited in the actuator experiment shown in Fig. 7. Here, a slightly trapezoidal strip of smaller dimensions (lateral: 1–1.2 mm × 1.6 mm, thickness ~10 μm) is glued to a glass slide, which forms a rigid boundary condition on the smaller side of the trapezoid (Fig. 7a). A colouring post-process is used to enhance the visibility of the actuator deformations (Fig. 7b). When linearly polarized light hits the sample from the top, elongation of the top surface in direction of the polarization causes downward bending, whilst the orthogonal direction shows compression-associated upwards-bending, leading to combined shapes. Merging the latter with a rigid boundary condition will produce both deformation and movement of the strip surface. For example, as shown in Fig. 7c, d, polarization at a 45-degree angle with respect to the constrained boundary causes one corner to bend upwards and one corner to bend downwards with respect to the boundary constraint, effectively producing a twist. Such photo-actuated polymer film twists have also been reported in the context of polydomain LCNs[45], cross-linked azo-polyimide cantilevers[54], and monodomain LCN strips with liquid crystal directors oriented diagonal to the cantilever[32,55]. In Ref. 55, repeated helicoidal (de-)curling of rectangular strips along a predefined direction was demonstrated. In the example presented herein, ample twisting motions to either side can be forced onto the soft strip by simply changing the polarization of the incoming light, permitting effective placement and reorientation of the actuator surface in 3D. Another interesting interplay between the two orthogonal bending directions and the boundary constraint is observed when the polarization is oriented parallel/perpendicular to the latter (Fig. 7e, f). Specifically, in Fig. 7e, the actuator front edge moves upwards whilst the two adjacent corners bend downwards simultaneously, resembling a grabbing motion. Switching the polarization by 90 degrees, the bending directions are reversed, and the tip now moves downwards, with the two adjacent corners bending upwards. It is worth noting that, in practice, the balance between the two orthogonal bending directions depends on a multitude of parameters, such as the geometry of the actuator, but also the amplitude of deformation. For example, strong deflections for downward-bending

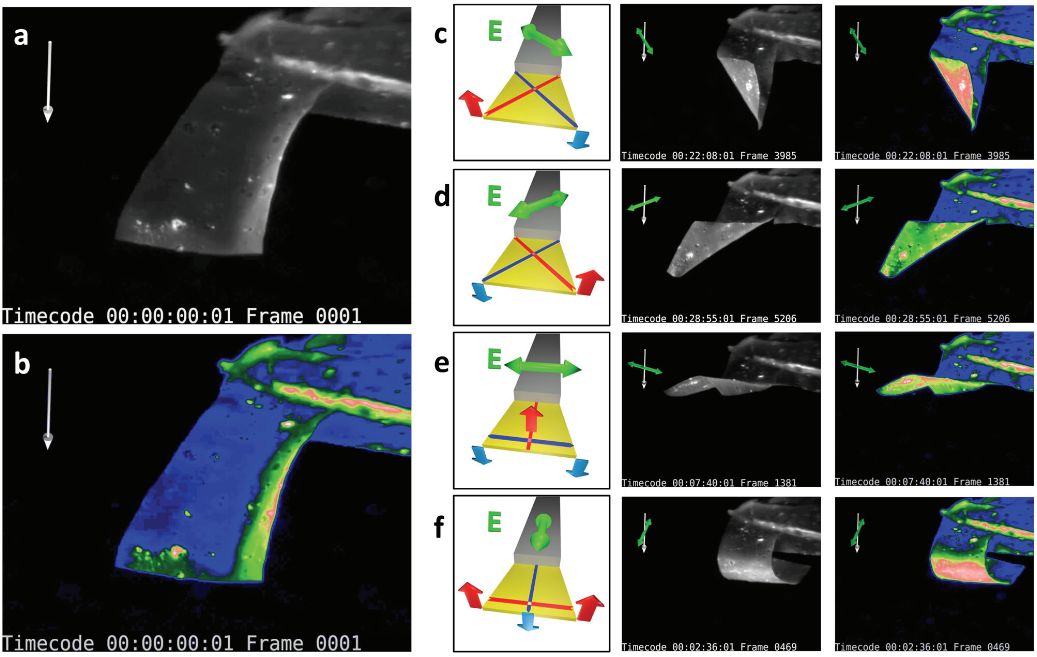

Fig. 7 | **Trapezoidal actuator.** **a** Snapshot of undeformed actuator. **b** False-coloured version of (**a**), highlighting contrast differences. **c**–**f** Image groups showing selected movie frames displaying twist to the right (**c**), twist to the left (**d**), upwards movement with transverse downward bending (**e**) and downwards movement with transverse upwards bending (**f**). Each image group consists of a schematic drawing of the deformation mechanism (left), one B/W image of the strongly deformed actuator (middle) and its false-coloured version (right). Green/white arrows: Polarization orientation/beam incidence direction.

were able to cause full roll-in of the strip, with weaker orthogonal bending (Fig. 7f). More generally, Supplementary Movie 6 allows a better understanding of all the specific features occurring during the full deformation sequence. In case circular polarization is employed, a general in-plane expansion of the illuminated side is observed (see Supplementary Fig. 13). A dependency of the strip movement on the previous deformations is observed at large actuation amplitudes, which can be attributed to the change of incidence angle of the laser beam onto the sample in motion. This may cause different projections of the polarization direction onto the sample surface, as well as shadowing effects and even the bottom surface of the sample being directly illuminated. Such effects have already been exploited to drive uniaxial oscillation of LCN strips with steady light stimuli[29,30,42,56]. To summarize, whilst the detailed actuation behaviour is more complex than one might expect at first glance, the overall nature of the deformation only depends on the polarization state. Moreover, fine-tuned experimental paradigms may lead to exploiting the more intricate details of the deformation pathways deliberately, for example, to design non-reciprocal movement sequences with single wavelength, homogeneous illumination[56].

Discussion

The emergence of a reversible shape-switching behaviour upon embedding an amorphous azopolymer into an external rubbery matrix has been shown and quantified experimentally. Since both materials are commercially available, and no polymerization and/or molecule alignment techniques are needed, we believe this type of material will open new possibilities for wider use of polarization-sensitive light-responsive materials. As to why the switching behaviour emerges, several possibilities could be imagined: in the framework of the photo-orientation model, describing optically induced ordering of main chains parallel to the polarization as deformation driving force[47,50,57], one could assume that the deformation states saturate for the microparticles, i.e., that the azo-domains' z-axis compression stops, when all main chains are oriented into the plane. However, the timescale for this (<1 min in all experiments) would be rather short, compared to other works[10,21]. In addition, longer illumination was shown to induce larger deformations at all stages, speaking against a saturation effect and rather for a continuous strain build-up[10], which however must be influenced by the previous state of deformation. One may therefore conclude that the switching behaviour is due to interaction effects between the azo-domains and the elastic SEBS matrix (e.g., surface tension, elastic restoring forces). Note that although the glass transition temperature ($T_g = 108\,°C$) is not reached during laser irradiation (Supplementary Fig. 14), photo-softening effects may be present.

On the other hand, a small irreversible component of plastic deformation was measured also in the switching regime and shown to locally depend on the size of embedded azopolymer aggregates. A possible explanation lies in larger aggregates inducing higher local heating, relaxing the elastic constraints in the surrounding matrix. Indeed, SEBS is a thermoplastic elastomer, which is physically, not chemically, cross-linked, and whose thermoplastic creeping behaviour is expected to increase with rising temperature, up to the point where it permits injection molding of the material at temperatures above 150 °C. Another observation of the negative effect of heating on reversible actuation is the drastic improvement of reversibility reported for 3D actuators immersed in water acting as a coolant, well known to play a crucial role for example in photo-thermal LCN actuators[35,58]. In this case, however, the increase of temperature is also due to a larger membrane thickness (see Supplementary Fig. 14), as compared to the patterned thin films which showed the best reversibility. Finally, irreversibility stemming from other sources, such as aggregates interacting differently with the external matrix due to e.g., absorption gradients or larger volume/interface ratios, cannot be excluded. Future development of this type of material in view of beating the reversibility benchmarks set up in this work will likely include further reduction of large azopolymer aggregates.

We would like to point out that reversibility, as it was defined here, only refers to the continuous transition between in-plane expanded states and linearly stretched states along arbitrary directions, while the pristine state of the composite cannot be restored. Nevertheless, this leads to two reversible degrees of freedom, linked to the direction and the ellipticity of the polarization. In order to recover the very initial microdomain state, mechanisms based on heating the azopolymer above the glass transition temperature have been proposed and experimentally validated[21].

Regarding biological applications, the possibility of tuning both strain magnitude and direction locally may open for interesting experimental paradigms combined with deformations propagating readily outside of the directly irradiated area. Worth mentioning here is that a similar approach has been utilized previously in our group to modify topographic features around cells without directly exposing them to light, which could potentially affect their viability. In this case, however, cells had to migrate before retrieving the topographic cues[15].

Finally, the proposed 3D soft actuators showed ample bending deformations based solely on the absorption and thus strain gradient throughout the membranes' thickness, without a bilayer system to amplify bending[25,59]. Nevertheless, such an approach could become interesting in view of miniaturizing the system, which could lead to several application prospects. For example, the possibility of controlling smooth, continuous membrane deformations, generally not possible in polycrystalline photo-chemical LCN actuation where UV-inscribed shapes first need to be erased by visible light[44,60], may constitute an efficient tool to transfer rotation from a polarizer to the shape of microscopic membranes. In addition, the use of saddle-shapes, which although observed in monodomain LCNs[34], are usually not reported for polydomain LCN membranes[44,61], combined with boundary constraints, was shown to permit the precise inscription of complex membrane shapes. Such shapes may be particularly adapted to manipulating small objects, an application attracting increasing interest[58,62,63].

Methods

Photo-responsive layer preparation

Poly[(methyl methacrylate)-co-(Disperse Red 1 methacrylate)] (Sigma-Aldrich) was dissolved in toluene at 0.2 wt% whilst stirring for 1 h at 60 °C on a regular hotplate. Subsequently, block copolymer poly(-styrene-ethylene-butylene-styrene) (SEBS, Mediprene 500120 M, Hexpol A/B) was added at 0.4 wt% and stirring at 60 °C was continued for at least 2 h. The solution was then cast on a micro hole-patterned polydimethylsiloxane (PDMS, Sylgard 184, DOW Corning) mold, either directly or after further evaporation of the solvent in an open beaker. The PDMS mold was obtained by soft lithography from an etched silicon master mold and treated with trichloro(1H, 1H, 2H, 2H-perfluorooctyl) silane (Sigma Aldrich) in a vacuum desiccator to avoid excessive sticking. Densified solutions (>1 wt% solid content) were directly sandwiched between the mold and an oxygen plasma treated (100% O2, 3 min, Diener Electronics Femto) flat PDMS receptive layer, then dried at room temperature, whilst the most dilute solution was transferred from the mold onto the receptive PDMS layer after drying (firm pressing, then bonding at 90 °C for 1.5 h). Free-standing membranes for 3D actuation were prepared via the same preparation protocol, but using two stiffer, fluorosilane-treated, flat PDMS (Sylgard 182, Dow) layers instead of a mold and a receptive layer. 3D actuators were then cut by means of a razor blade (trapezoidal membranes) or with a sharpened copper straw (round membranes). After they had been cut on the supporting PDMS, the membranes were carefully peeled off. To favour the peeling process and prevent self-wrapping caused by electrostatic forces, a few drops of deionized water mixed with salt (NaCl) and soap were poured on the surface of the membrane prior to peeling. Peeled membranes were laid onto a piece of oil-treated paper and spread out to remove all wrinkles, with the help of additional water droplets if required, before drying with optical grade cloth and/or low-temperature heat. The trapezoid membrane was glued to the edge of a glass slide with common fingernail varnish.

Planar substrate actuation

The planar samples were imaged and actuated under a confocal microscope (Zeiss 800 Airyscan, Objective: Plan-Achromat 63x oil, NA = 1.4) using the 561 nm laser line for continuous scanning illumination (writing mode, default: linear horizontal polarization) and the 640 nm line for transmission or scattered laser beam imaging (reading mode) of the sample. For actuation with circular polarization, a λ/4 plate was inserted in the optical path via the beam-blocker slit and circular polarization of the laser beam was verified in polarized optical microscopy (POM) mode. The waveplate was removed for all image acquisitions. Irradiation powers for planar substrates were defined as laser power divided by the total rectangular scanning/illumination area ($33.8 \times 33.8 - 101.4 \times 101.4\ \mu m^2$) and in writing mode the scanning speed was set to its maximal value (pixel dwell time 0.59–0.91 μs, frame time 233–360 ms). Time-delay between the end of a writing illumination step and onset of the next writing interval was approximately 45 s.

Planar substrates data analysis

In Supplementary Figure 15a, b, a schematic illustration of the deformations produced on a hexagonal pattern illuminated by a linearly polarized radiation is presented. For sake of generality, the incident linear polarization is oriented at an angle θ with respect to the x-axis. Two engineering strains ε_1 and ε_2 along two orthogonal axes are associated to light-induced stretching and compression, respectively. Such a deformation can be also described in the Fourier space as a set of transformations applied to the (reciprocal) hexagonal cell. As shown in Supplementary Fig. 15c–f, the initial lattice cell undergoes a first rotation by an angle − θ, then a stretching/compression along vertical and horizontal directions respectively, and finally a second rotation by an angle θ. Worth recalling that stretching in the direct space corresponds to compression in the reciprocal space and vice versa. Such transformations in the Fourier space are embodied in the matrix relationship of Eq. (1) used for fitting experimental data.

Data Analysis on collected images was conducted in MATLAB 2021®. After a 2D fast Fourier transform, peaks with a prominence above a peak prominence threshold were identified using the findpeaks function and further selected based on having the largest prominence in a neighborhood sized slightly below the expected pillar marker reciprocal lattice constant. The position was further adjusted using a two-dimensional Gaussian fitting procedure on the 25 pixels surrounding the detected peak. Finally, peak shifts between images were found by comparing the respective peak sets and forming pairs of peaks if their distance is below a limiting distance. They were displayed using MATLAB's quiver plot feature and fitted with a least squares approach using Eq. (1), to extract the engineering strain parameters (ε_1, ε_2) and the angle θ between the axis of ε_1 and the x-axis. The code is fully automatized and made available.

The *R2* value of the reciprocal space fitting results was defined in analogy with the linear case as

$$R2 := 1 - \frac{\sum_i ||\mathbf{a}_{f,i} - \mathbf{a}_{d,i}||_2}{\sum_i ||\mathbf{a}_{d,i}||_2} \tag{4}$$

where $\mathbf{a}_{f,i}$ and $\mathbf{a}_{d,i}$ denote the fitted and the data arrows respectively (Fig. 2c, d). Where parameters are given as a single value for a whole actuation cycle set (*R2, θ*), their value and spread are provided as mean and sample standard deviation (s.d.) for the whole actuation set. The s.d. was also used to compute error bars on Fig. 3c, based on 9 randomly initialized simulations, and to plot error bars for ε_1, ε_2, and δA_{cycle} based on 3 acquisitions in different areas for the illumination sequences displayed in Fig. 2e and Fig. 5. The asymptotic values $\varepsilon_{1,\infty}$, $\varepsilon_{2,\infty}$, $\delta A_{\text{cycle},\infty}$ (Table 1) were defined as the mean of the last 10 values of the respective parameters in such averaged illumination sequences, 8 values in the case of Fig. 5b. Their uncertainties were computed as the standard error of the mean (s.e.m.) over the 3 individual 10-point means. The spread (s.d.) of those individual 10-point means was found on average over all measurement series to be ~3 times larger than the spread expected by computing the s.e.m. over the last 10 points for individual acquisitions, indicating that new acquisitions in different areas contribute in a non-negligible manner to the spread of the mean. Therefore, for the dose plot in Fig. 4, who relies on single acquisitions, measurements were carried out in closely neighboring areas and error bars estimating the spread were computed as the s.e.m. of the last 10 points corrected by a multiplicative factor 3.

Planar substrate further characterization

The thickness of the active membranes was estimated by cross-section imaging with a tabletop scanning electron microscope (SEM) after sputter-coating of 10 nm of Pt-Pd. Example SEM images are shown in Supplementary Fig. 9a. Thicknesses and uncertainties provided in Table 1 are based on mean and s.d. of three measurements. Sample fine structure, as displayed in the insets of Fig. 2e and Fig. 5, was imaged with the same confocal microscope used for actuation, but in Airyscan mode. Microparticles and aggregates can be detected due to the weak fluorescence of the azopolymer upon green light irradiation. The largest aggregates' size was estimated based on binary images obtained through local mean filtering (~5% of image size), after smoothening with a median filter accompanied by multiple erode/dilate operations in ImageJ. Example images from areas of comparable size to the actuation zones, together with the obtained particle outlines and histograms are displayed in Supplementary Fig. 9b.

3D actuation

Recordings of the actuation were taken by means of a CMOS camera (iDS UI-1540LE-M-GL) whose upper edge was rotated slightly towards the sample (side-top-view). The membranes were placed parallel to the measurement table and irradiated with normal laser beam incidence from the top ($\lambda = 532$ nm, $I = 1$ W·cm^{-2}). The Polarization state of the laser was controlled by means of a linear polarizer followed by a half-wave plate adjusting the polarization direction and, when required, by an additional quarter-wave plate to obtain circular polarization. The half-wave plate was inserted into a motorized rotating stage (Thorlabs K10CR1/M). The image collection path further contained a 40 mm achromatic lens, a 550 nm long pass filter blocking the laser beam, and an iris placed in the focal plane of the lens to increase the depth of field of the imaging system.

Finite element model

A two-dimensional finite element model of a representative unit cell of composite with unit edge length was set up under plane-stress conditions for a mechanical analysis in the commercial software Abaqus/Standard. Periodic displacement boundary conditions were enforced on opposing edges of the simulation domain. The azopolymer was modeled with $N = 25$ non-intersecting, randomly placed and initially spherical domains, taking up 33% of the simulation area, corresponding to the azopolymer content in the physical samples. To model the irradiation-induced eigenstrain of the azo-domains, which drives the deformation of the composite, a homogeneous deformation gradient was prescribed in the azopolymer phase. For linear and circular polarization, this deformation gradient is denoted by $\mathbf{F}^{\mathbf{lin}}$ and $\mathbf{F}^{\mathbf{circ}}$, and defined as follows:

$$\mathbf{F}^{\mathbf{lin}} = \begin{pmatrix} a & 0 & 0 \\ 0 & 1/\sqrt{a} & 0 \\ 0 & 0 & 1/\sqrt{a} \end{pmatrix}, \mathbf{F}^{\mathbf{circ}} = \begin{pmatrix} b & 0 & 0 \\ 0 & b & 0 \\ 0 & 0 & 1/b^2 \end{pmatrix} \tag{5}$$

where the stretching factors a and b can be adjusted and only the four left top elements corresponding to the x-y subspace are applied explicitly to the finite element model. To model the material behaviour of the SEBS matrix, the hyperelastic Marlow model[64] was fit to the tensile test data given by Kollosche et al[53]. to accurately model the non-linear elastic response. Further, SEBS was considered incompressible[46], with the Poisson ratio reported in the literature being 0.49[65]. The azopolymer inclusions, which exhibit significantly higher stiffness, are modelled hypoelastically (Young's modulus $E = 4$ GPa, Poisson's ratio $\nu = 0.5$). They were considered incompressible, i.e., conserving their volume from one state to another in the simulation, based on previous reports on the photo-deformation of such polymers[10,50]. Their incompressibility was also considered unaffected by the surrounding SEBS matrix whose Young's modulus E ≈ 244 kPa is orders of magnitudes lower[53]. Both phases were assumed to be isotropic. The macroscopic strains were derived from the relative displacement between the reference nodes used in the periodic boundary condition definition to represent the average position of one edge of the simulation domain each. The resulting macroscopic strains are averaged by taking the mean over a set of 9 individual simulations with different randomly initialized azo-domain distributions. Associated error intervals refer to the sample standard deviation of that set. Finally, the scale invariance of the model was verified by varying the number of azo-domains as $N = 15$, $N = 25$ and $N = 35$ at a constant 33% azo-phase for linear stretching with $a = 1.125$. It was observed that the variation of the output is on the order of the sample standard deviation obtained when varying the random azo-domain distributions at $N = 25$.

Data availability

The authors declare that raw data supporting the analysis of thin film deformations is publicly available on figshare repository at https://doi.org/10.6084/m9.figshare.24123156. All other data is available from the authors upon request.

Code availability

MatLab codes for extracting strain parameters from the raw dataset are available on figshare repository at https://doi.org/10.6084/m9.figshare.24123156.

References

1. Stoychev, G., Kirillova, A. & Ionov, L. Light-responsive shape-changing polymers. *Adv. Optical Mater.* **7**, 1900067 (2019).
2. Karageorgiev, P. et al. From anisotropic photo-fluidity towards nanomanipulation in the optical near-field. *Nat. Mater.* **4**, 699–703 (2005).
3. Viswanathan, N. K. et al. Surface relief structures on azo polymer films. *J. Mater. Chem.* **9**, 1941–1955 (1999).
4. Lee, S., Kang, H. S. & Park, J.-K. Directional photofluidization lithography: micro/nanostructural evolution by photofluidic motions of azobenzene materials. *Adv. Mater.* **24**, 2069–2103 (2012).
5. Sekhar Yadavalli, N. et al. A comparative study of photoinduced deformation in azobenzene containing polymer films. *Soft Matter* **12**, 2593–2603 (2016).
6. Labarthet, F. L., Buffeteau, T. & Sourisseau, C. Time dependent analysis of the formation of a half-period surface relief grating on amorphous azopolymer films. *J. Appl. Phys.* **90**, 3149–3158 (2001).

7. Yadavalli, N. S., Saphiannikova, M., Lomadze, N., Goldenberg, L. M. & Santer, S. Structuring of photosensitive material below diffraction limit using far field irradiation. *Appl. Phys. A* **113**, 263–272 (2013).
8. Derouard, M. et al. Polarization-sensitive printing of surface plasmon interferences. *Opt. Express, OE* **15**, 4238–4246 (2007).
9. Li, Y., He, Y., Tong, X. & Wang, X. Photoinduced deformation of amphiphilic azo polymer colloidal spheres. *J. Am. Chem. Soc.* **127**, 2402–2403 (2005).
10. Loebner, S. et al. Light-induced deformation of azobenzene-containing colloidal spheres: calculation and measurement of opto-mechanical stresses. *J. Phys. Chem. B* 9 (2018).
11. Gritsai, Y., Goldenberg, L. M. & Stumpe, J. Efficient single-beam light manipulation of 3D microstructures in azobenzene-containing materials. *Opt. Express, OE* **19**, 18687–18695 (2011).
12. Kong, X. et al. Photomanipulated architecture and patterning of azopolymer array. *ACS Appl. Mater. Interfaces* **9**, 19345–19353 (2017).
13. Jo, W. et al. Programmable fabrication of submicrometer bent pillar structures enabled by a photoreconfigurable azopolymer. *ACS Appl. Mater. Interfaces* **12**, 5058–5064 (2020).
14. Ho, J.-H. et al. Stretching and bending of azopolymer nanorod arrays via laser-induced photo-fluidization. *ACS Appl. Polym. Mater.* https://doi.org/10.1021/acsapm.2c00553 (2022).
15. Puliafito, A. et al. Driving cells with light-controlled topographies. *Adv. Sci.* **6**, 1801826 (2019).
16. Priimagi, A. & Shevchenko, A. Azopolymer-based micro- and nanopatterning for photonic applications. *J. Polym. Sci. Part B: Polym. Phys.* **52**, 163–182 (2014).
17. Kang, H. S., Kim, H.-T., Park, J.-K. & Lee, S. Light-powered healing of a wearable electrical conductor. *Adv. Funct. Mater.* **24**, 7273–7283 (2014).
18. Wang, W. et al. Light-driven shape-memory porous films with precisely controlled dimensions. *Angew. Chem.* **130**, 2161–2165 (2018).
19. Yin, X. et al. Coupling of photoinduced mass immigration with polymer networks to produce nanostructured materials capable of reversibly creating arbitrary deformations. *Macromol. Chem. Phys.* **219**, 1800113 (2018).
20. Jelken, J. & Santer, S. Light induced reversible structuring of photosensitive polymer films. *RSC Adv.* **9**, 20295–20305 (2019).
21. Ryabchun, A. & Bobrovsky, A. Photocontrollable deformations of polymer particles in elastic matrix. *Adv. Optical Mater.* **7**, 1901486 (2019).
22. Rianna, C. et al. Reversible holographic patterns on azopolymers for guiding cell adhesion and orientation. *ACS Appl. Mater. Interfaces* **7**, 16984–16991 (2015).
23. Isomäki, M. et al. Light-responsive bilayer cell culture platform for reversible cell guidance. *Small Sci.* **2**, 2100099 (2022).
24. Takashima, Y. et al. Expansion–contraction of photoresponsive artificial muscle regulated by host–guest interactions. *Nat. Commun.* **3**, 1270 (2012).
25. Wen, H., Zhang, W., Weng, Y. & Hu, Z. Photomechanical bending of linear azobenzene polymer. *RSC Adv.* **4**, 11776–11781 (2014).
26. Wang, D. H. et al. Photomechanical response of glassy azobenzene polyimide networks. *Macromolecules* **44**, 3840–3846 (2011).
27. Jiang, Z.-C., Xiao, Y.-Y. & Zhao, Y. Shining light on liquid crystal polymer networks: preparing, reconfiguring, and driving soft actuators. *Adv. Optical Mater.* **7**, 1900262 (2019).
28. Hines, L., Petersen, K., Lum, G. Z. & Sitti, M. Soft actuators for small-scale robotics. *Adv. Mater.* **29**, 1603483 (2017).
29. White, J. T. et al. A high frequency photodriven polymer oscillator. *Soft Matter* **4**, 1796–1798 (2008).
30. Vantomme, G. et al. Coupled liquid crystalline oscillators in Huygens' synchrony. *Nat. Mater.* 1–5 https://doi.org/10.1038/s41563-021-00931-6 (2021).
31. Zeng, H. et al. Light-fuelled freestyle self-oscillators. *Nat. Commun.* **10**, 5057 (2019).
32. Lee, K. M. et al. Photodriven, flexural–torsional oscillation of glassy azobenzene liquid crystal polymer networks. *Adv. Funct. Mater.* **21**, 2913–2918 (2011).
33. Gelebart, A. H. et al. Making waves in a photoactive polymer film. *Nature* **546**, 632–636 (2017).
34. Camacho-Lopez, M., Finkelmann, H., Palffy-Muhoray, P. & Shelley, M. Fast liquid-crystal elastomer swims into the dark. *Nat. Mater.* **3**, 307–310 (2004).
35. Zeng, H., Wasylczyk, P., Wiersma, D. S. & Priimagi, A. Light robots: bridging the gap between microrobotics and photomechanics in soft materials. *Adv. Mater.* **30**, 1703554 (2018).
36. Palagi, S. et al. Structured light enables biomimetic swimming and versatile locomotion of photoresponsive soft microrobots. *Nat. Mater.* **15**, 647–653 (2016).
37. Ware, T. H., McConney, M. E., Wie, J. J., Tondiglia, V. P. & White, T. J. Voxelated liquid crystal elastomers. *Science* **347**, 982–984 (2015).
38. de Haan, L. T., Sánchez-Somolinos, C., Bastiaansen, C. M. W., Schenning, A. P. H. J. & Broer, D. J. Engineering of complex order and the macroscopic deformation of liquid crystal polymer networks. *Angew. Chem. Int. Ed.* **51**, 12469–12472 (2012).
39. van Oosten, C. L., Bastiaansen, C. W. M. & Broer, D. J. Printed artificial cilia from liquid-crystal network actuators modularly driven by light. *Nat. Mater.* **8**, 677–682 (2009).
40. Wang, M., Lin, B.-P. & Yang, H. A plant tendril mimic soft actuator with phototunable bending and chiral twisting motion modes. *Nat. Commun.* **7**, 13981 (2016).
41. Zuo, B., Wang, M., Lin, B.-P. & Yang, H. Visible and infrared three-wavelength modulated multi-directional actuators. *Nat. Commun.* **10**, 4539 (2019).
42. Li, Y., Liu, Y. & Luo, D. Polarization dependent light-driven liquid crystal elastomer actuators based on photothermal effect. *Adv. Optical Mater*. 2001861 https://doi.org/10.1002/adom.202001861 (2020).
43. Lahikainen, M., Zeng, H. & Priimagi, A. Reconfigurable photo-actuator through synergistic use of photochemical and photo-thermal effects. *Nat. Commun.* **9**, 4148 (2018).
44. Yu, Y., Nakano, M. & Ikeda, T. Directed bending of a polymer film by light. *Nature* **425**, 145–145 (2003).
45. Tabiryan, N., Serak, S., Dai, X.-M. & Bunning, T. Polymer film with optically controlled form and actuation. *Opt. Express, OE* **13**, 7442–7448 (2005).
46. Laflamme, S. et al. Soft elastomeric capacitor network for strain sensing over large surfaces. *IEEE/ASME Trans. Mechatron.* **18**, 1647–1654 (2013).
47. Liu, E. et al. Polarization-dependent ultrasensitive dynamic wrinkling on floating films induced by photo-orientation of azopolymer. *Angew. Chem.* **134**, e202203715 (2022).
48. Ichikawa, R. & Nakano, H. Photoinduced change in the shape of azobenzene-based molecular glass particles fixed in agar gel. *RSC Adv.* **6**, 36761–36765 (2016).
49. Wang, W. et al. Deterministic reshaping of breath figure arrays by directional photomanipulation. *ACS Appl. Mater. Interfaces* **9**, 4223–4230 (2017).
50. Bublitz, D. et al. Photoinduced deformation of azobenzene polyester films. *Appl Phys. B* **70**, 863–865 (2000).
51. Goldenberg, L. M., Kulikovsky, L., Kulikovska, O. & Stumpe, J. Extremely high patterning efficiency in easily made azobenzene-containing polymer films. *J. Mater. Chem.* **19**, 6103–6105 (2009).
52. Salvatore, M., Borbone, F. & Oscurato, S. L. Deterministic Realization of Quasicrystal Surface Relief Gratings on Thin Azopolymer Films. *Adv. Mater. Interfaces* **7**, 1902118 (2020).
53. Kollosche, M., Stoyanov, H., Ragusch, H. & Kofod, G. Dependence on boundary conditions for actuation characteristics of dielectric

elastomer actuators. in (ed. Bar-Cohen, Y.) 76422X https://doi.org/10.1117/12.847515 (2010).
54. Wang, D. H. et al. Flexural-torsional photomechanical responses in azobenzene-containing crosslinked polyimides. *Macromol. Mater. Eng.* **297**, 1167–1174 (2012).
55. Iamsaard, S. et al. Conversion of light into macroscopic helical motion. *Nat. Chem.* **6**, 229–235 (2014).
56. Lahikainen, M., Zeng, H. & Priimagi, A. Design principles for non-reciprocal photomechanical actuation. *Soft Matter* **16**, 5951–5958 (2020).
57. Yadav, B., Domurath, J., Kim, K., Lee, S. & Saphiannikova, M. Orientation approach to directional photodeformations in glassy side-chain azopolymers. *J. Phys. Chem. B* **123**, 3337–3347 (2019).
58. Martella, D., Nocentini, S., Nuzhdin, D., Parmeggiani, C. & Wiersma, D. S. Photonic microhand with autonomous action. *Adv. Mater.* **29**, 1704047 (2017).
59. Chen, Y. et al. Light-driven bimorph soft actuators: design, fabrication, and properties. *Mater. Horiz.* **8**, 728–757 (2021).
60. Yu, Y., Nakano, M. & Ikeda, T. Photoinduced bending and unbending behavior of liquid-crystalline gels and elastomers. *Pure Appl. Chem.* **76**, 1467–1477 (2004).
61. Dunn, M. L. Photomechanics of mono- and polydomain liquid crystal elastomer films. *J. Appl. Phys.* **102**, 013506 (2007).
62. Cheng, F., Yin, R., Zhang, Y., Yen, C.-C. & Yu, Y. Fully plastic microrobots which manipulate objects using only visible light. *Soft Matter* **6**, 3447–3449 (2010).
63. Wani, O. M., Zeng, H. & Priimagi, A. A light-driven artificial flytrap. *Nat. Commun.* **8**, 15546 (2017).
64. Marlow, R. A general first-invariant hyperelastic constitutive model in Constitutive models for rubber III. in 15–17 (2003).
65. Wilkinson, A. N., Clemens, M. L. & Harding, V. M. The effects of SEBS-g-maleic anhydride reaction on the morphology and properties of polypropylene/PA6/SEBS ternary blends. *Polymer* **45**, 5239–5249 (2004).

Acknowledgements

D.U. acknowledges the Norwegian University of Science and Technology for funding the PhD fellowship under project number 989454111 and The Research Council of Norway is acknowledged for the support to the Norwegian Micro- and Nano-Fabrication Facility, NorFab, project number 295864. E.D. and N.M. acknowledge the funding received by Italian Ministero dell'Università e della Ricerca under the Dipartimento di Eccellenza 2018–2022 program. We thank Hexpol A/B for kindly providing a badge of SEBS Mediprene 500120 M free of charge. Further, we acknowledge NTNU's Chemistry Department and in particular Bicheng Gao for their kind assistance in determining the molecular weight of the polymer. The results presented are part of a project that has received funding from the European Research Council (ERC) under the European Union's Horizon 2020 research and innovation programme (Grant agreement No. 949807) with starting date May 2021.

Author contributions

E.D. and D.U. conceived and planned the work. D.U. and N.M. performed sample preparation, measurements, and data analysis for physical samples. C.H.W., J.T. and D.U. developed the mechanical modelling, performed the simulations, and analyzed simulation data. D.R.H contributed to data analysis and provided background laboratory capabilities. All authors contributed to the manuscript writing and revision.

Competing interests

The authors declare no competing interests.

Additional information

Supplementary information The online version contains supplementary material available at https://doi.org/10.1038/s41467-023-42590-y.

Correspondence and requests for materials should be addressed to Emiliano Descrovi.

Peer review information *Nature Communications* thanks Conghua Lu and the other, anonymous, reviewer(s) for their contribution to the peer review of this work. A peer review file is available.

Reprints and permissions information is available at http://www.nature.com/reprints

Supplementary Information

Polarization-driven reversible actuation in a photoresponsive polymer composite

David Urban[1,2], Niccolò Marcucci[2], Christoph Hubertus Wölfle[3], Jan Torgersen[3], Dag Roar Hjelme[1] and Emiliano Descrovi[2]

Corresponding Author
emiliano.descrovi@polito.it

[1] Department of Electronic Systems, Norwegian University of Science and Technology, O.S. Bragstads plass 2b, 7034 Trondheim, Norway

[2] Dipartimento di Scienza Applicata e Tecnologia, Politecnico di Torino, Corso Duca degli Abruzzi 24, 10129, Torino, Italy

[3] Institute of Materials Science, Department of Materials Engineering, TUM School of Engineering and Design, Technical University of Munich, Boltzmannstraße 15, 85748 Garching, Germany

SUPPLEMENTARY FIGURES

Supplementary Figure 1 - Molecular structure, weight, and absorption spectrum of pDR1m-co-mma

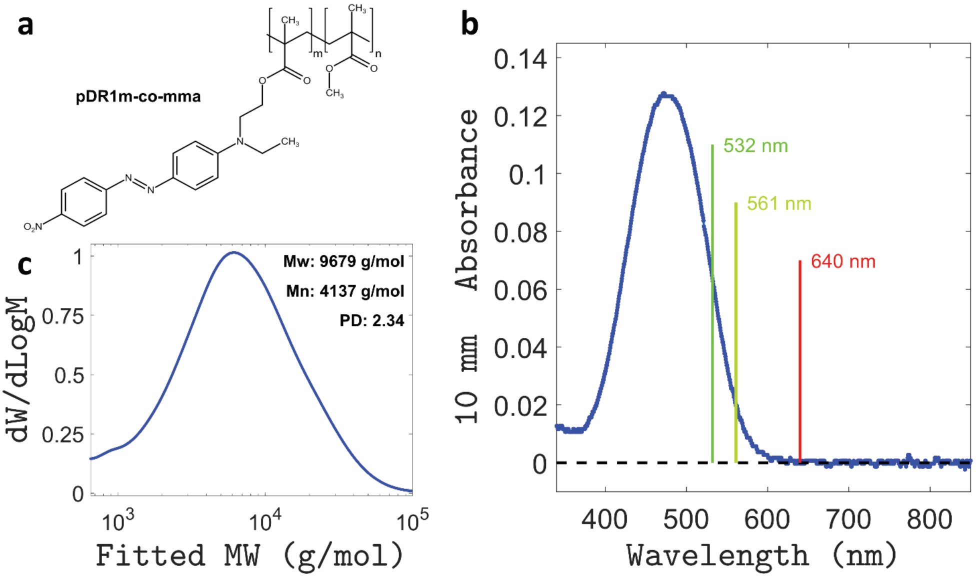

Supplementary Figure 1: (a) Molecular structure of poly [(methyl methacrylate)-co-(Disperse Red 1 methacrylate)] (pDR1m-co-mma). The approximate ratio of DR1 chromophores (m) was indicated as ~15 mol% by the manufacturer. (b) Absorption spectrum of pDR1m-co-mma measured at room temperature and dissolved at 0.0025 mg/mL in acetone. Vertical lines indicate the wavelengths used in this work. 640 nm: planar substrates reading mode. 561 nm planar substrates writing mode. 532 nm: 3D actuators writing mode. The spectrum mainly refers to the absorption by DR1 molecules in the trans isomeric state. (c) Normalized molecular weight distribution obtained by gel permeation chromatography (Agilent Technologies LC 1260) of the polymer dissolved in Tetrahydrofuran (THF) at room temperature, using a polystyrene standard. Inset: Values obtained for weight/number average molecular weight (Mw/Mn) and polydispersity index (PD).

Supplementary Figure 2 - Propagation of displacement outside the illuminated area

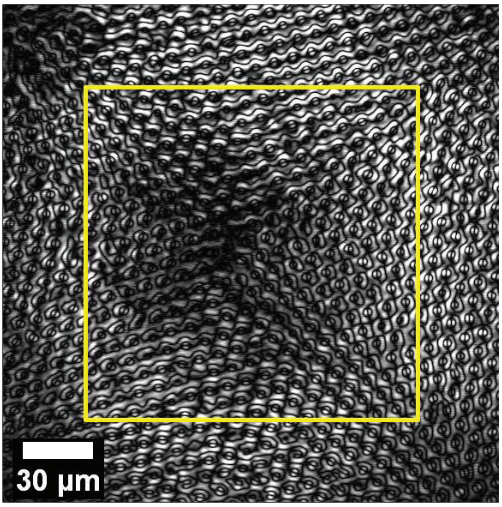

Supplementary Figure 2: Overview differential image of planar substrate before and after irradiation with linear horizontal polarization, qualitatively showing the amplitude of local displacement. Some displacement is seen to extend outside the region of irradiation (yellow frame), accommodating the deformation of the latter. Note that while displacement can be seen to occur in both x- and y directions (and is null in the center indicating absence of translation), the direction of displacement can hardly be discerned on such a plot. For directionality of deformation, see Supplementary Movie 1 (direct space) and/or Figure 2c,d (Fourier space).

Supplementary Figure 3 - Wrinkles on suspended AZO:SEBS film upon irradiation with linear horizontal polarization

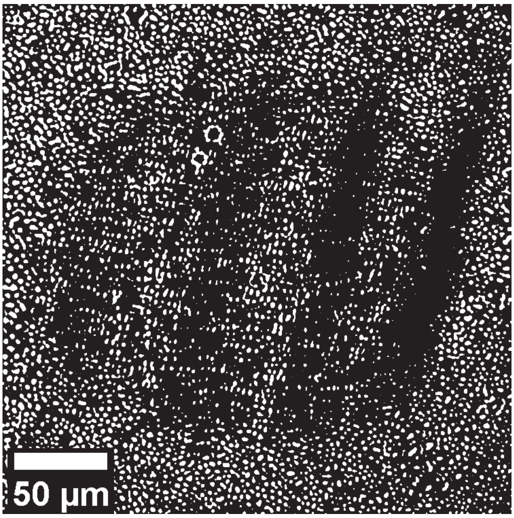

Supplementary Figure 3: Wrinkles upon irradiation with linear horizontal polarization: zoomed-in version of frame 58 of Supplementary Movie 2. Wrinkles have been highlighted through increased contrast and multiple iterations of local background subtraction and Gaussian blurring.

Supplementary Figure 4 – Cumulative sequential deformation of pDR1m micropillars

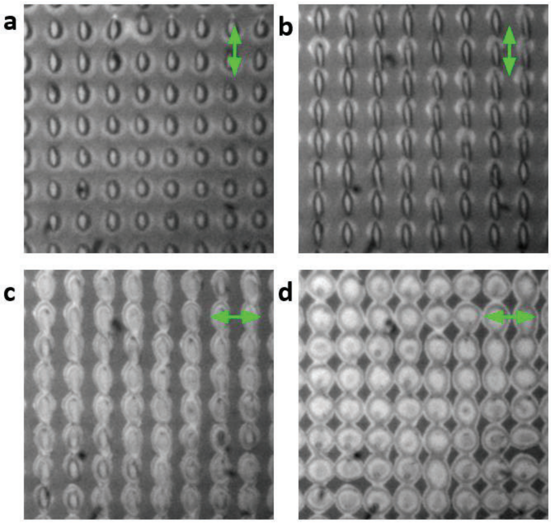

Supplementary Figure 4: (a,b) Early/final state of elongation during irradiation with linearly vertically polarized light. (c,d) Early/final state of deformation when subsequently illuminating the same pillars with perpendicular horizontal polarization. Green Arrow: Direction of polarization.

Supplementary Figure 5 – Light-induced deformation on a pure pDR1m-co-mma film

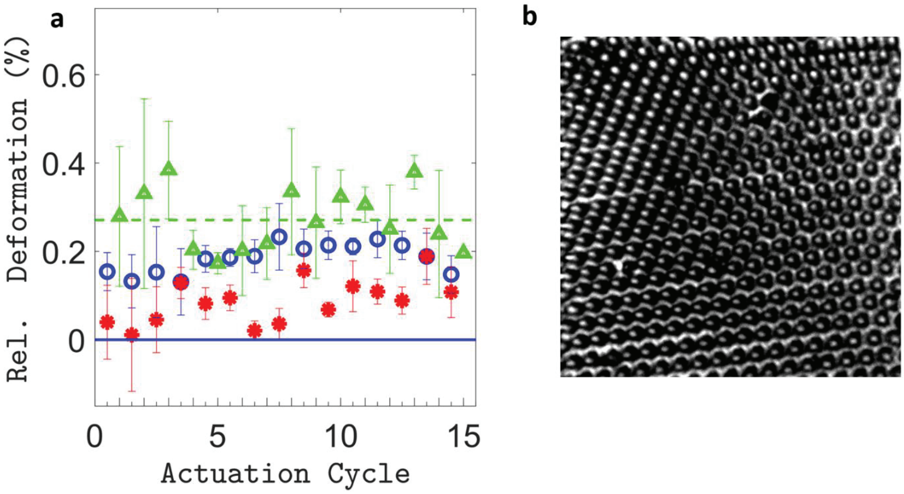

Supplementary Figure 5: Analysis of deformations on a 33.8 x 33.8 μm^2 area of pure azopolymer pDR1m-co-mma patterned with 1 μm spaced, 1 μm wide pillars, illuminated at intensity I = 5.02 W·cm^{-2}. (a) Graph showing relative horizontal elongation strain ε_1 per X-POL step (blue circles), absolute value of relative vertical compression strain $|\varepsilon_2|$ per X-POL step (red asterisks), and relative area expansion δA_{cycle} per full illumination cycle (green triangles). Parameters are shown for the 15 first illumination cycles only, due to gradual degradation of the pillar lattice by cumulative deformations as exemplified in (b), showing the direct space image after 20 illumination cycles (see also Supplementary Movie 3). Error bars: sample standard deviation for 3 acquisitions on different areas.

Supplementary Figure 6 - FE Modelling Details

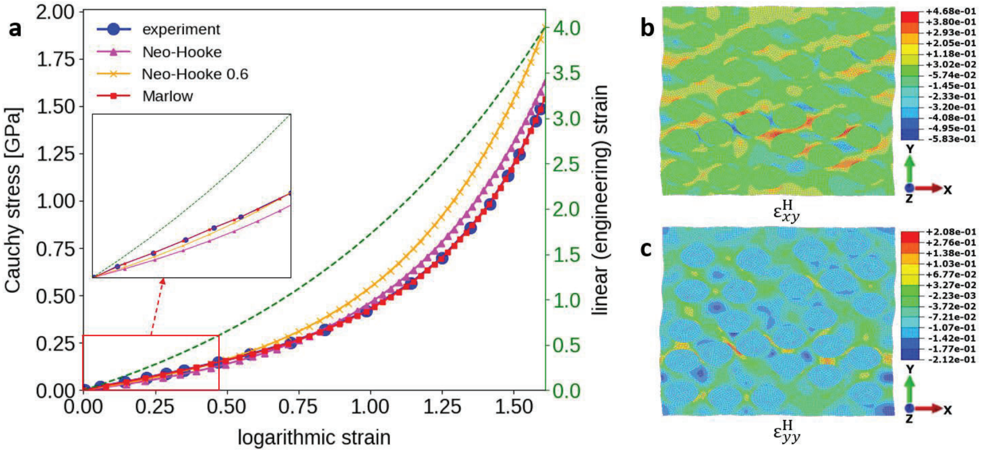

Supplementary Figure 6: (a) Fitting of the tensile testing data from literature (Kollosche et. al, 2010) with three models: Marlow model, Neo-Hookean model and Neo-Hookean model with up to 60% strain input data**.** Green dashed line: help line for transferring logarithmic strain into linear engineering strain (right vertical axis). Inset: Zoom-in on small strain region. (b,c) Simulated strain fields' off-diagonal logarithmic (Hencky) strain ε^{H}_{xy} and logarithmic normal strain ε^{H}_{yy} components around the elliptically deformed azo-domains.

Supplementary Figure 7 - Influence of irradiation parameters on AZO:SEBS film deformation

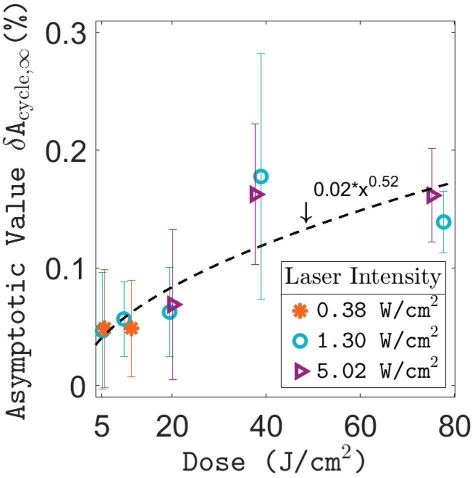

Supplementary Figure 7: Plot showing the asymptotic value of the relative area expansion $\delta A_{\mathrm{cycle},\infty}$ per illumination cycle as a function of applied dose, using the same measurements as in Figure 4. Error bars are three times the standard error of the mean (s.e.m.), as detailed in the Methods section.

Supplementary Figure 8 – Deformation parameters in several illumination conditions

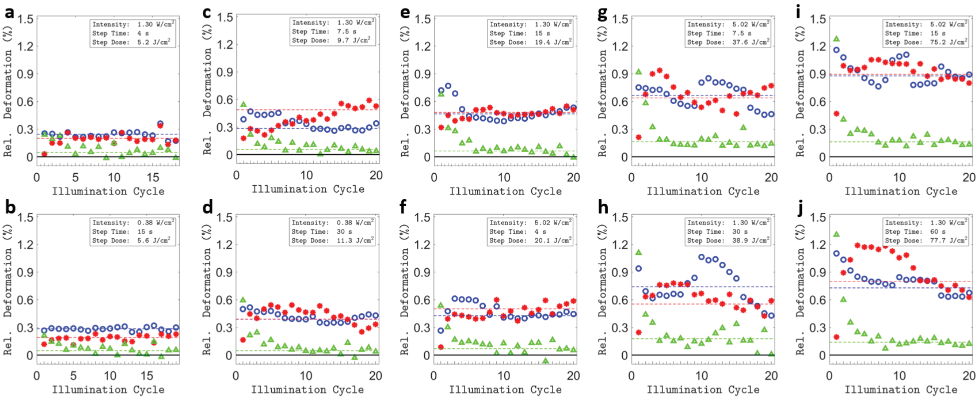

Supplementary Figure 8: 20 illumination cycles on areas of sample 1, using different laser powers and doses. (a-j) Graphs showing relative horizontal elongation strain ε_1 per X-POL step (blue circles), absolute value of relative vertical compression strain $|\varepsilon_2|$ per X-POL step (red asterisks), and relative area expansion per full illumination cycle (green triangles), for increasing value of the dose per illumination step. Helplines visualize the asymptotic values used in Figure 4 and Supplementary Figure 7 and are based on the mean of the last 10 respective datapoints.

Supplementary Figure 9 – Azopolymer domains in samples with different solvent content

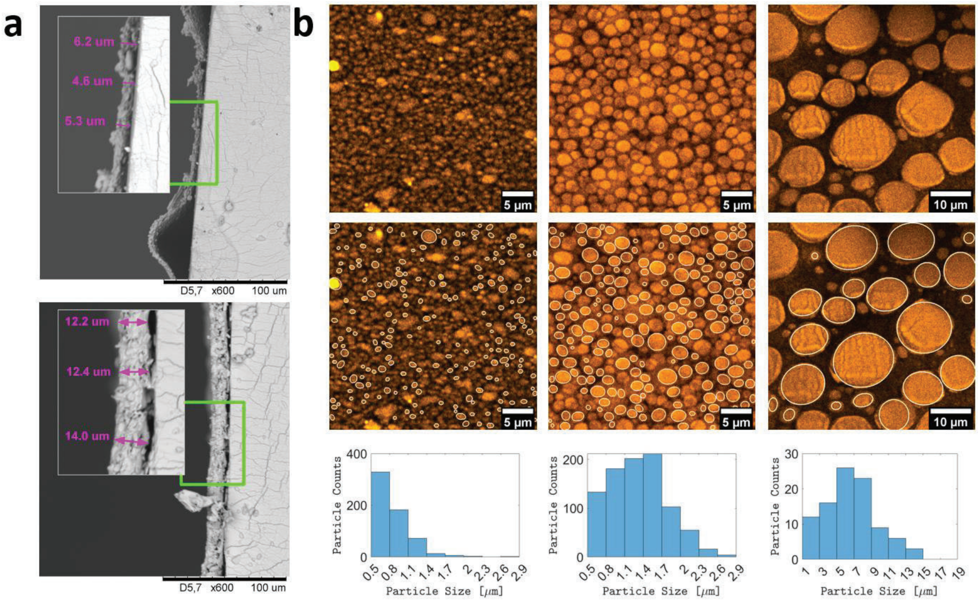

Supplementary Figure 9: (a) Examples of SEM cross-section images of different samples. Top-bottom: sample 2-3, inset: zoom-in on thickness measurement areas. (b) Examples of confocal images used for characterization of the largest aggregate sizes. Left to right: sample 1-3. Histograms show particle sizes summed over 5 similar images from distinct areas for each sample.

Supplementary Figure 10 - Sample 4 fine structure.

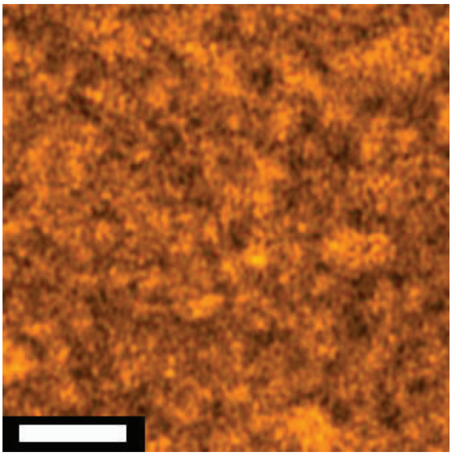

Supplementary Figure 10: Confocal image of interstitial area in-between large aggregates on sample 4. Scale bar: 3 µm.

Supplementary Figure 11 – Deformation of AZO:SEBS film with larger azopolymer domains

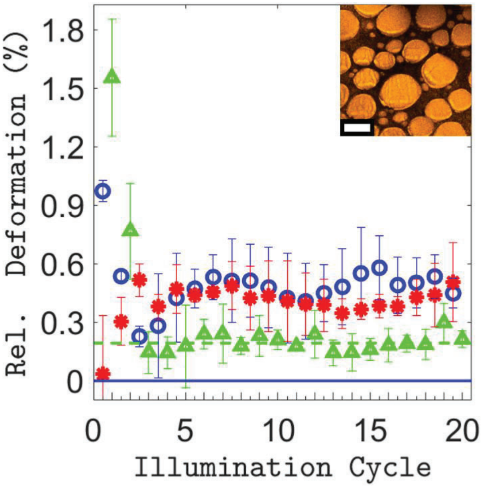

Supplementary Figure 11: Plot of fitted parameters for 20 illumination cycles for Sample 3. The graph shows relative horizontal elongation strain ε_1 per X-POL step (blue circles), absolute value of relative vertical compression strain $|\varepsilon_2|$ per X-POL step (red asterisks), and relative area expansion δA_{cycle} per full illumination cycle (green triangles). Error bars: sample standard deviation for 3 acquisitions on different areas. Inset: confocal image of sample fine structure and aggregate size. Scale bar: 10 µm.

Supplementary Figure 12 - Deformation induced by alternating linear polarizations

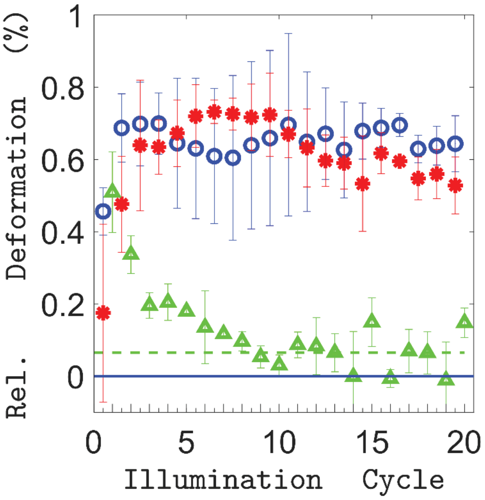

Supplementary Figure 12: Illumination cycles consist of horizontal linear followed by vertical linear polarization (instead of horizontal linear followed by circular polarization). Plot of fitted parameters, i.e., horizontal elongation strain ε_1 per X-POL step (blue circles), absolute value of relative vertical compression strain $|\varepsilon_2|$ per X-POL step (red asterisks) and relative area expansion δA_{cycle} per full illumination cycle (green triangles), for 20 illumination cycles on a sample similar to sample 1. Error bars: sample standard deviation for 3 acquisitions on different areas. Note that the characteristic feature of mostly reversible actuation (δA_{cycle} approaching a low asymptotic value) and area conservation for horizontally polarized illuminations in the switching regime (ε_1 comparable to ε_2) are still observed.

Supplementary Figure 13 - Effect of circularly polarized illumination on membranes

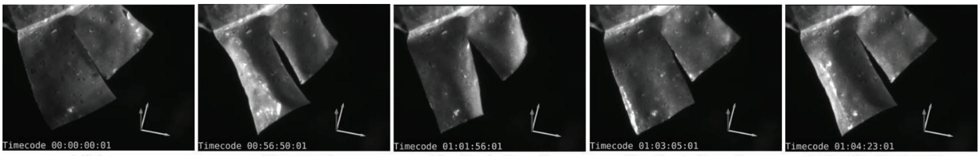

Initial configuration (planar)

After several illumination steps (longitudinal bending)

After illumination with linear polarization (corner bending)

After illumination with circular polarization (planar)

Further illumination with circular polarization (convex)

Supplementary Figure 13: From left to right: two co-planar cantilevers with similar widths and different lengths (initial state) are illuminated with a linear polarization transverse to the cantilever axis (“longitudinal bending” state). Then, the linear polarization is rotated, bringing the cantilevers into a "corner bending” state, similar to Figure 7c,d. The polarization is finally varied to circular. Both cantilevers revert bending, quickly reaching a planar configuration recalling the very initial state. With further illumination, a smooth convexity is observed to appear. This effect is likely to result from the adirectional in-plane expansion of azopolymer domains on top of the membrane.

Supplementary Figure 14 – Temperature on laser-irradiated AZO:SEBS films

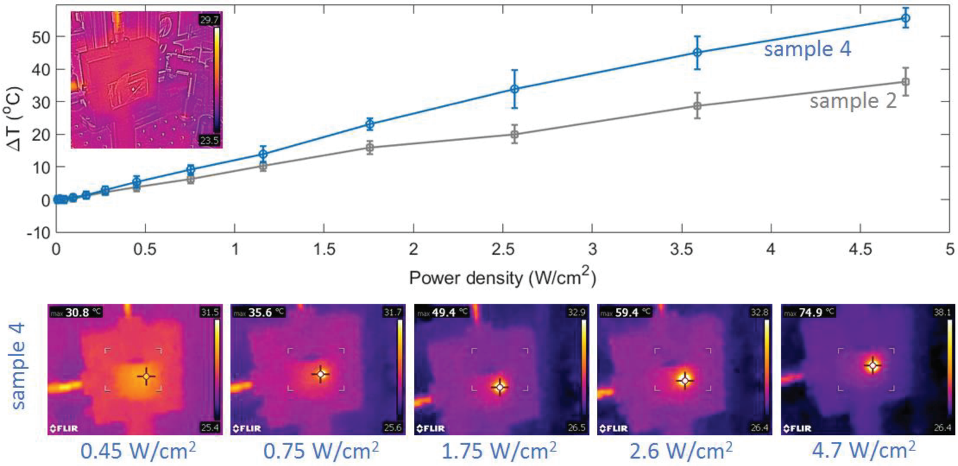

Supplementary Figure 14: Top line: measured temperature excess on azo-SEBS films on PDMS slabs. Sample type 2 and 4 are considered, wherein average azopolymer aggregate size and film thickness are smaller for sample 2 than sample 4. Bottom line: illustrative thermocamera images referred to sample 4 mounted on a 2-axis translational stage and being irradiated with a 532 nm wavelength CW laser at different power densities.

Supplementary Figure 15 – Deformation scheme of a pillar pattern on AZO:SEBS film

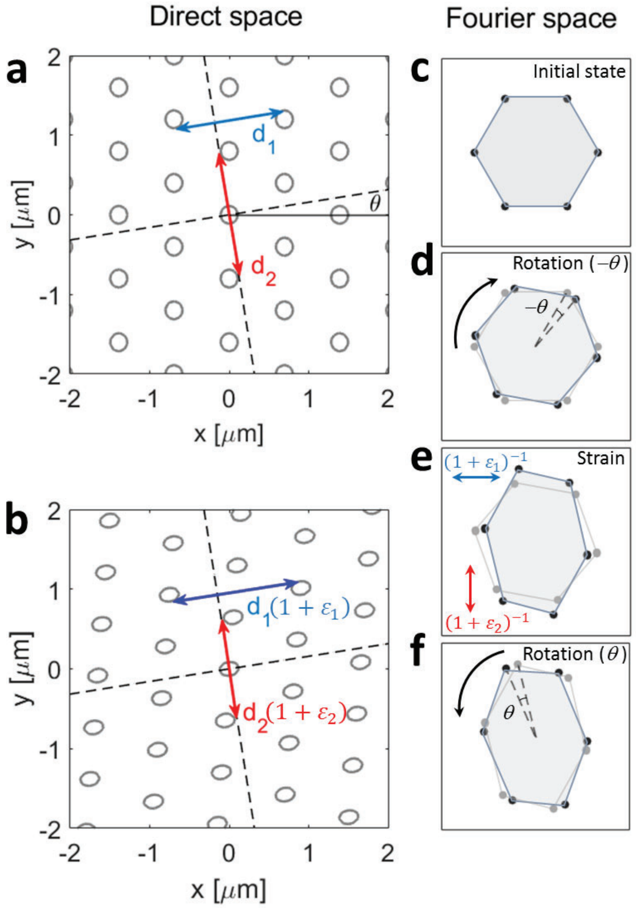

Supplementary Figure 15. (a) Illustrative hexagonal lattice in the direct space. Exemplary lengths d_1 and d_2 are taken along directions parallel and perpendicular to the incident polarization respectively, which is tilted by an angle θ with respect to the x-axis. (b) Photo-responsivity of the composite results into stretching ($\varepsilon_1>0$) and compression ($\varepsilon_2<0$) along said two orthogonal directions. (c) Reciprocal lattice cell in the initial state. (d) Reciprocal lattice cell after the first rotation by an angle $-\theta$. In this representation, the horizontal and vertical axis are aligned to the directions of compression and stretching in the Fourier space, respectively. (e) Lattice cell stretched and compressed along vertical and horizontal directions, respectively. (f) Deformed lattice cell in the final state, after a rotation back by an angle θ.

Supplementary Figure 16 – Impact of a two-dimensional computational model

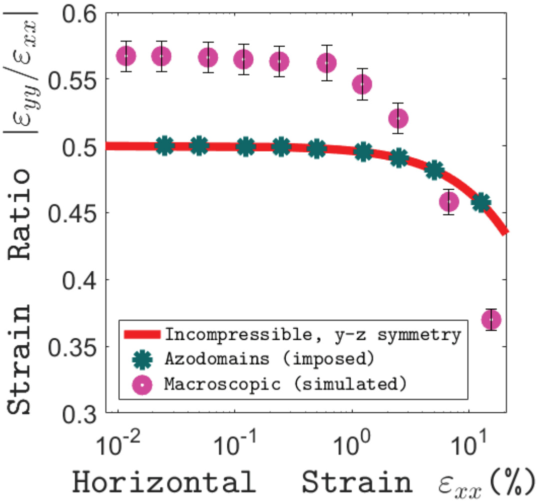

Supplementary Figure 16. Ratio of y-axis compression to x-axis elongation upon ellipsoid deformation, compared to the incompressible case with true axial symmetry around the x-axis (solid red line).

SUPPLEMENTARY NOTE 1 – First order approximations

The explicit computation of the switching tensor $\mathbf{F^3}$ proposed in Equation (3) can be obtained from $\mathbf{F^1}$ and $\mathbf{F^2}$, defined in Equation (2) in the article, via the following computation:

$$
\begin{aligned}
\mathbf{F^3} = \mathbf{F^1}\cdot(\mathbf{F^2})^{-1} &= \begin{pmatrix} 1+\delta & 0 & 0 \\ 0 & 1-\frac{1}{2}\delta & 0 \\ 0 & 0 & 1-\frac{1}{2}\delta \end{pmatrix}\cdot\begin{pmatrix} \dfrac{1}{1+\frac{1}{4}\delta} & 0 & 0 \\ 0 & \dfrac{1}{1+\frac{1}{4}\delta} & 0 \\ 0 & 0 & \dfrac{1}{1-\frac{1}{2}\delta} \end{pmatrix} \\
&= \begin{pmatrix} \dfrac{1+\delta}{1+\frac{1}{4}\delta} & 0 & 0 \\ 0 & \dfrac{1-\frac{1}{2}\delta}{1+\frac{1}{4}\delta} & 0 \\ 0 & 0 & \dfrac{1-\frac{1}{2}\delta}{1-\frac{1}{2}\delta} \end{pmatrix} \\
&= \begin{pmatrix} (1+\delta)(1-\frac{1}{4}\delta+\cdots) & 0 & 0 \\ 0 & (1-\frac{1}{2}\delta)(1-\frac{1}{4}\delta+\cdots) & 0 \\ 0 & 0 & 1 \end{pmatrix} \\
&= \begin{pmatrix} 1+\frac{3}{4}\delta+\cdots & 0 & 0 \\ 0 & 1-\frac{3}{4}\delta+\cdots & 0 \\ 0 & 0 & 1 \end{pmatrix} \approx \begin{pmatrix} 1+\frac{3}{4}\delta & 0 & 0 \\ 0 & 1-\frac{3}{4}\delta & 0 \\ 0 & 0 & 1 \end{pmatrix}
\end{aligned}
\tag{6}
$$

where the first line corresponds to inverting the individual elements to obtain the inverse of the diagonal tensor $\mathbf{F^2}$, the third line to a Taylor expansion writing elements up to the first order of δ and the fourth line to retaining only the first order elements.

Similarly, the tensor $\mathbf{F^{lin}}$ from Equation (5) can be shown to reduce to $\mathbf{F^1}$ from Equation (2), in a first order approximation:

$$\mathbf{F}^{\mathbf{lin}} = \begin{pmatrix} a & 0 & 0 \\ 0 & 1/\sqrt{a} & 0 \\ 0 & 0 & 1/\sqrt{a} \end{pmatrix} = \begin{pmatrix} 1+\delta & 0 & 0 \\ 0 & 1/\sqrt{(1+\delta)} & 0 \\ 0 & 0 & 1/\sqrt{(1+\delta)} \end{pmatrix}$$

$$= \begin{pmatrix} 1+\delta & 0 & 0 \\ 0 & 1-\frac{1}{2}\delta+\cdots & 0 \\ 0 & 0 & 1-\frac{1}{2}\delta+\cdots \end{pmatrix} \approx \begin{pmatrix} 1+\delta & 0 & 0 \\ 0 & 1-\frac{1}{2}\delta & 0 \\ 0 & 0 & 1-\frac{1}{2}\delta \end{pmatrix} \tag{7}$$

$$= \mathbf{F}^{\mathbf{1}}$$

where we have replaced a by $(1+\delta)$ and retained only the first order elements of δ in the Taylor expansion of each matrix element. In this framework δ can be associated to ε_1 (and -1/2 δ to ε_2), hence the Taylor expansion procedure can be seen as small strain approximation. A similar development can be done for $\mathbf{F}^{\mathbf{circ}}$, reducing to $\mathbf{F}^{\mathbf{2}}$ in a first order approximation. In that case, to enforce equal compression along the z-axis, one should set $1/\sqrt{a} = 1/b^2$ and therefore start the Taylor expansion with $b = a^{1/4} = (1+\delta)^{1/4}$, leading to:

$$\mathbf{F}^{\mathbf{circ}} = \begin{pmatrix} b & 0 & 0 \\ 0 & b & 0 \\ 0 & 0 & 1/b^2 \end{pmatrix} = \begin{pmatrix} (1+\delta)^{1/4} & 0 & 0 \\ 0 & (1+\delta)^{1/4} & 0 \\ 0 & 0 & 1/(1+\delta)^{1/2} \end{pmatrix}$$

$$\approx \begin{pmatrix} 1+\frac{1}{4}\delta & 0 & 0 \\ 0 & 1+\frac{1}{4}\delta & 0 \\ 0 & 0 & 1-\frac{1}{2}\delta \end{pmatrix} = \mathbf{F}^{\mathbf{2}} \tag{8}$$

SUPPLEMENTARY NOTE 2 – Accuracy of the 2D modelling approach

To assess the accuracy of the 2D modelling approach, one may compare it to a full 3D simulation of an isotropic representative volume of the azo-SEBS composite. In the 3D case, the axial symmetry around the x-axis, for uniaxial stretching along said axis by a factor *a,* should lead to equal lateral compression values for both perpendicular directions. Given the incompressibility assumption for all constituents of the material, the total simulation volume should be conserved as well, forcing the two lateral compression values to a factor $1/\sqrt{a}$ as apparent from the deformation gradient tensor for the incompressible deformation corresponding to uniaxial tensile loading, $\mathbf{F}^{\mathbf{lin}}$, shown in Equation (5). In a small strain setting, one will then recover the Poisson ratio $-\varepsilon_{yy}/\varepsilon_{xx} = 0.5$, whilst for larger strains, incompressibility will dictate that $-\varepsilon_{yy}/\varepsilon_{xx} = \frac{a^{-0.5}-1}{a-1}$, a line which is plotted in the Supplementary Figure 16 (red line).

Whilst the imposed azo-domain deformations fulfill that condition by definition, the macroscopic average strains computed for the entire simulation domain deviate slightly from that ratio, by about 10 % averaged over the 9 different random geometries we studied. In practice, that means that the simulated y-axis compression of the overall material is slightly stronger than expected, at the expense of the not explicitly computed compression along the z-axis. Roughly speaking, the 2D simulation makes it easier for the composite to get pushed out along the z-axis than what would be expected for an isotropic 3D material.

This effect is reflected in Figure 3c, where the transmission in the simulation using $\mathbf{F}^{\mathbf{lin}}$ is slightly higher along the y-axis (T_{yy}^{lin}) than along the x-axis (T_{xx}^{lin}). Furthermore, the normal transmission factors for the in-plane expansion of azo-domains upon applying $\mathbf{F}^{\mathbf{circ}}$, i.e., T_{xx}^{circ} and T_{yy}^{circ}, are the lowest. This is likely again due to the 2D simulation permitting more material to be pushed out along the z-axis during this in-plane expansion than what would be the case in a 3D isotropic material. Finally, it should be stressed that the actual experimental samples lie somewhere between these 2D and 3D cases, since the largest domain/aggregates are of comparable size to the photo-responsive layer's thickness (see Table 1).

Directional capillary flows induced by photo-deformable colloidal particles

David Urban[1,4], Marcel Rey[2,3], Antonio Ciarlo[3], Emiliano Descrovi[4] and Giovanni Volpe[3]

1. Department of Electronic Systems, Norwegian University of Science and Technology, O.S. Bragstads plass 2b, 7034, Trondheim, Norway
2. Institute of Physical Chemistry, University of Münster, Correnssstr. 28/30, 48149 Münster, Germany
3. Department of Physics, University of Gothenburg, SE-41296, Gothenburg, Sweden
4. Dipartimento di Scienza Applicata e Tecnologia, Politecnico di Torino, Corso Duca degli Abruzzi 24, 10129, Torino, Italy

Corresponding Authors
David Urban: david.urban@ntnu.no
Emiliano Descrovi: emiliano.descrovi@polito.it

Keywords: Optofluidics, optocapillary, polarization-driven flows, azopolymer colloidal particles, water-air interface, anisotropic capillary forces, microparticle self-assembly, light-responsive materials, smart particles.

ABSTRACT

Colloidal particles experience long-ranged capillary attraction at liquid interfaces. The magnitude and directionality of these interactions depend on the particles' shapes. Since these shapes are typically fixed during the fabrication process, the capillary interactions are also fixed, often leading to self-assembly into persistent interfacial structures. Here, we demonstrate an active material composed of polymeric particles at a water-air interface whose shape and, therefore, interactions can be altered by illumination with polarized light. By directionally deforming the particles, we alter their self-assembly at the interface and drive sustained, large-scale interfacial flows with velocities up to 90 μm/s. We tailor the directionality and overall patterns of these flows by controlling and modulating the polarization and intensity of the light. We expect this direct control over the capillary interactions between photo-deformable colloidal particles at interfaces, along with the ensuing interfacial flows, to enable new forms of mixing, manipulation, and assembly of soft matter at liquid interfaces.

INTRODUCTION

Capillary interactions are a fundamental phenomenon at liquid interfaces. In fact, when small objects are adsorbed to an interface, they deform it. These deformations increase the surface tension and are therefore energetically unfavorable. As a consequence, lateral forces between the objects emerge to minimize the surface tension and the surface deformations. This mechanism enables the emergence of intriguing natural phenomena. For example, some insects can climb the slippery curved slopes at a pond edge by adopting quasistatic body postures at the air-water interface[1]. In doing so, they actively create surface deformations that interact with the external edge meniscus so that they are propelled uphill. Biological entities can also use surface deformations to interact directly with each other, for example, by means of anisotropic shapes creating long-ranged, directional capillary attraction forces. Correspondingly, ordered capillary assemblies have been reported on several length scales, including oval beetle bodies[2], ellipsoidal mosquito eggs[3] and boomerang-shaped *ruppia maritima* pollen[4].

Regarding artificial systems, shape-mediated capillary forces were first demonstrated on the mesoscale by guiding the ordered interfacial assembly of millimetric synthetic particles with anisotropic geometries and patterned hydrophilicity into well-defined static patterns[5]. Building upon this concept, tunable systems have recently been reported. Using temperature[6,7], magnetic fields[8] or light[9,10], the mutual interaction and assembly of mesoscale objects was controlled directly at the liquid interface. In all these works, thin, sheet-like rafts were employed, with lateral sizes comprised between 50 µm and several millimeters. The rafts relied on significant contour undulations stemming from well-defined wrinkles, folds or bending to pin the liquid interface to different heights and to induce large, tunable interface deformations.

Downscaling this shape-mediated capillary control to colloidal particles, with sizes between 100 nm and several µm, is of great interest considering the prospect of assembling and manipulating large numbers of particles simultaneously but involves the challenge of controlling the interface deformation geometries at much smaller scales. Thus, researchers have studied the capillary interactions of interface-adsorbed particles with anisotropic shapes such as cylinders[11], curved disks[12], cubes[13], or ellipsoids[14], which can be prepared by methods involving e.g., photolithography[11,12], hematite synthesis[13,15], or mechanical stretching[16,17]. In fact, on the scale of a colloidal particle, a smooth prolate ellipsoidal shape can be sufficient to induce a sizeable near-quadrupolar interface deformation around a particle due to the constant wetting angle[18,19]. Minimizing these quadrupolar deformations, particles were then reported to assemble for example in large-scale tip-to-tip or side-by-side stackings[14,19–22]. However, since these works relied on prefabricating particles with fixed shapes, the assembled particle phases were static. Versatile tunable assembly phase changes have been recently predicted in simulations using an external control mechanisms based on magnetic fields to tilt magnetic ellipsoidal particles at the liquid interface, thereby tuning the induced interface distortions and particle interactions[23,24]. Yet, experimental realizations of tunable colloidal assemblies, based on direct control over shape-mediated capillary forces, have so far remained elusive.

Here, we experimentally introduce a 2D-confined colloidal system that permits us to directly control capillary inter-particle attraction forces and to generate sustained flow patterns. The system consists of colloidal azopolymer particles adsorbed to an air-water interface, whose shape can be altered using polarized visible light. This effect, which can be anisotropic and polarization-dependent[25], has frequently been used in nanofabrication contexts to optically inscribe surface topographies in thin films[26–28] or to reconfigure microscale features and particles bound to solid substrates[29–32], embedded in soft matrices[33–35], or within microporous films[36,37]. Here, we start by extending this phenomenology to the interface-adsorbed, mobile azopolymer particles, inducing both anisotropic and in-plane isotropic deformations depending on the illumination's polarization. We then show how the resulting shape-mediated capillary effects permit local assembly and disassembly of particles. Finally, the continuous deformation of local capillary assemblies in denser particle settings is discovered to enable steady particle flows, whose intriguing properties can be controlled by simple intensity patterns with defined polarization.

RESULTS

Shape-morphing particles at an air-water interface

We start by considering the behavior of single azopolymer particles adsorbed to a liquid interface when subjected to illumination with polarized visible light. Specifically, we show that these particles can be deformed into anisotropic shapes directly at the air-water interface by laser illumination with suitable polarization, complementing the studies that have shown this effect on dry substrates[29,31,32].

The photo-deformable azopolymer particles were prepared by a solvent evaporation method, using the commercial light-responsive polymer poly[(Disperse Red 1 methacrylate)-co-(methyl methacrylate) pDR1m-co-mma (Fig 1a). In brief, a chloroform solution of the polymer was added to a surfactant-containing aqueous solution and emulsified by sonication while the chloroform was continuously evaporated (see Methods for details). This generated a polydisperse set of particles with diameters up to 3 μm (see Supplementary Fig. S1a). These particles were spread at the air-water interface in a sealed sample cell, where their movement was confined to two dimensions. Optical deformation was induced by illuminating the particles with an expanded green laser ($\lambda = 532$ nm) while observing them under an inverted optical microscope with white background illumination (Supplementary Movie M1).

When using a linearly polarized illumination beam, we were able to anisotropically stretch the particle along the polarization direction into a rod-like shape (Fig. 1b). Similar stretching behaviors have already been shown for similar azopolymer particles but on solid substrates[29,31,32]. Some studies also reported this transformation to be close to the uniaxial, isochoric one (i.e., the polymer being incompressible and the deformed particle being symmetric around the axis of polarization and elongation)[32,34].

Next, we observed circular polarization to induce in-plane isotropic flattening of particles, leading to an axially symmetric oblate, disk-like shape (Fig. 1c), again matching with previous studies focusing on immobile microstructures[30,35,39]. In Fig. 1c, note that the particle becomes less visible due to its flattening, reducing the lateral differences in optical path length (i.e., distance times refractive index, integrated along the optical axis), and hence the contrast.

Finally, elliptical polarization can be used to produce an intermediate result, i.e., a flattened ellipsoid with lower in-plane aspect ratio (Fig. 1d). Also this intermediate has been shown previously on solid substrates[30,37] We note that, even in the theoretical case, such an ellipsoid will have three independently adjusted principal axes (no axial symmetry). A similar result can be obtained by using sequential illuminations with different polarization as done in the context of capillary assembly and disassembly in the next section.

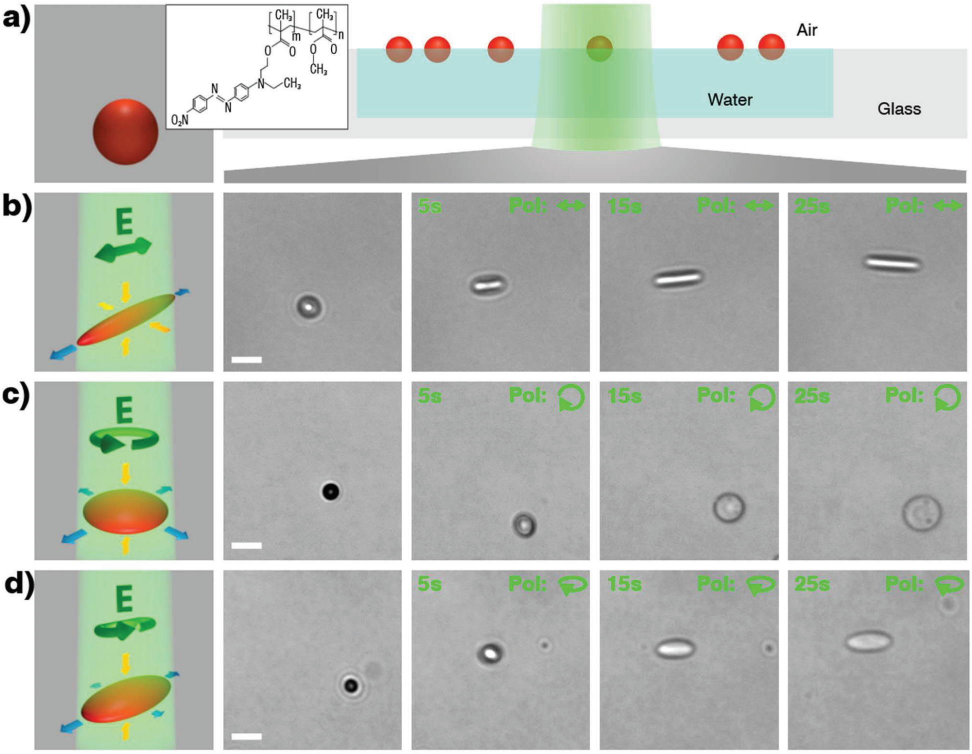

Figure 1. Optical deformation of azopolymer particles at an air-water interface. a) Scheme of a pristine spherical azopolymer particle (red), chemical structure of the polymer and scheme of the optical setup with particles adsorbed to the air-water interface. The laser beam (green) illuminates the sample from below. b-d) Schemes (left) and snapshots from Supplementary Movie M1 (right) showing the in-situ deformation of particles with linearly (b), circularly (c) and elliptically (d) polarized light, leading to rod-like, disk-like and flattened ellipsoidal particle shapes respectively. Illumination intensity: $I = 219$ W/cm^2, Scale bars (white): 5 µm. Blue/orange scheme arrows indicate respective expansion/contraction. Contrast levels in b-d adjusted individually for each row.

Optically controllable capillary interactions and assembly

Next, we illustrate how capillary-driven self-assembly — well known from studies with prefabricated anisotropic particle shapes[11–14,19–22,38] — can be induced *in situ* via light-induced particle deformation directly at the interface. To do so, we study sample regions where several pristine spherical particles are diffusing along the interface in close vicinity. When shining elliptically polarized light on these particles, they deform into ellipsoids, approach each other and bond in a stable side-by-side configuration (Fig 2a, i-iii, Supplementary Movie M2).

This behavior can be attributed to the anisotropic, saddle-like interface deformations which are known to be induced by the constant three-phase contact angle around ellipsoidal particles[18,19], and which have been illustrated in the corresponding schemes shown in Fig. 2b, i-iii. The resulting long-range capillary forces, with quadrupolar symmetry, can significantly exceed the thermal energy k_BT[14,38,40], and lead to directional particle assemblies. Thereby, the observed side-by-side configuration constitutes the minimum energy configuration for two ellipsoidal particles in contact[3,21,41]. The intermediate frames in Supplementary Figure S2 show how the two particles rotate into this configuration upon contact[40,42]. The underlying capillary mechanism is overall surface energy minimization of the liquid interface, which can be achieved by superposing matching deformations, e.g., matching surface elevations or depressions[38].

Interestingly, the stable capillary bond between the particles can be reversed by a subsequent illumination with circular polarization (Fig. 2a, iv-v). This second illumination induces an isotropic flattening of the particles, which is applied on top of the previous deformation since azopolymer deformations are plastic, superposing processes[28,31,34]. Although the particle cross-sections do not become perfectly circular again during this process, the particles consistently disassemble during prolonged exposure.

This is likely due to a combined effect of in-plane ellipse aspect ratio reduction, intrinsically reducing the anisotropic interface deformation, and out-of-plane particle flattening (see schemes in Fig. 2b, iv-v). In fact, since the interface deformation causing the capillary attraction stems from contact line undulations around the physical particle, the maximal deformation height is approximately limited by the (gradually vanishing) particle height[38]. By flattening the particles, the increasingly sharp edge of the flattened particle associated to a diminishing out-of-plane curvature radius, is expected to become the dominant factor and to suppress the capillary attraction.

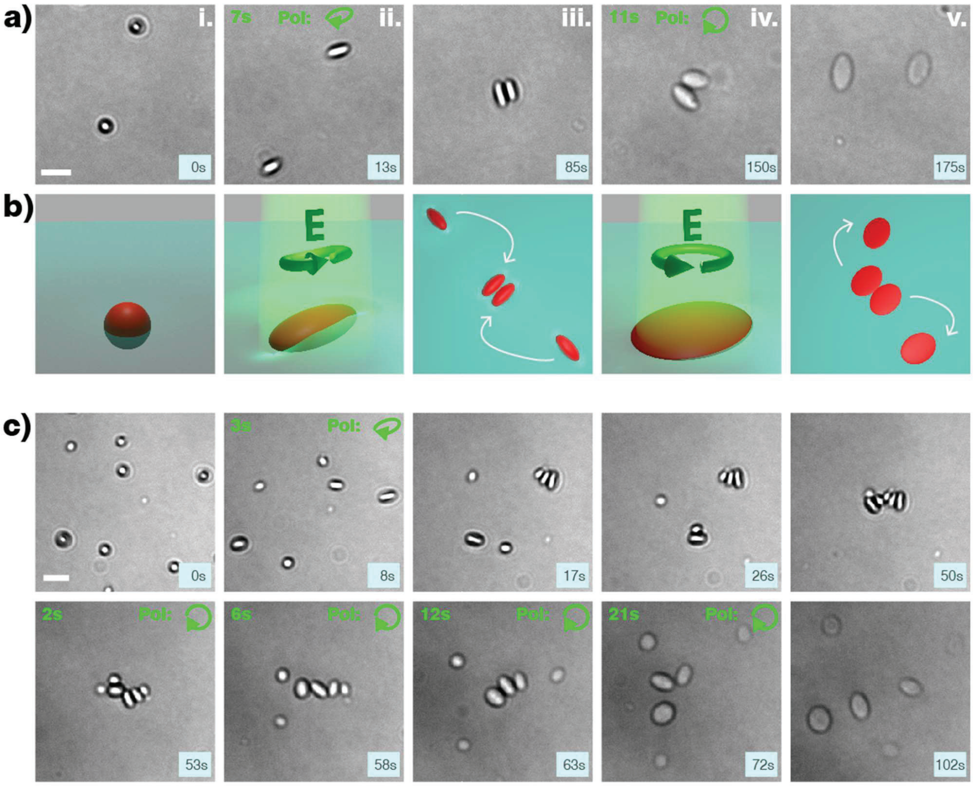

Figure 2 Shape-mediated particle (dis)assembly induced by light. a) Experimental snapshots from Supplementary Movie M2, showing two undeformed, spherical azopolymer particles at the water-air interface (i), which are stretched into ellipsoidal particles upon irradiation with elliptically polarized light (ii) and subsequently bond to minimize the overall interface deformation (capillary effect) (iii). When they are deformed and expanded in the plane with circularly polarized light at a later stage (iv), they de-bond as they become flattened particles (v). b) Schemes depicting the corresponding stages with interface deformations emphasized for illustration purposes. c) Snapshots from Supplementary Movie M3, repeating the sequence in an area containing multiple particles. Note that particles continue to assemble due to their ellipsoidal shape, also after the elliptically polarized illumination has been switched off. They remain rigidly

assembled until their shape is remodeled by illumination with circular polarization. Scale bars (white): 5 μm. Light blue squares in the lower right indicate total acquisition time, green font indicates respective time from illumination onset.

Finally, this tunable capillary assembly and disassembly behavior can be extended to cases involving multiple particles (Fig. 2c; Supplementary Movie M3). It can also be performed using linearly polarized light, which deforms the particles into higher aspect ratio rod-like shapes (Supplementary Fig. S3; Supplementary Movies M4/M5), although the disassembly time with circular polarization tends to increase in this case. Worth to point out that in cases involving pre-assembled structures with many particles, the onset of circular polarization can produce interesting dynamic sequences, where the flattening particles rearrange continuously. With increasing rounding, they typically evolve towards tip-to-tip configurations — the minimum energy configuration of multiple lower-aspect ratio ellipsoids[41] — before eventually disassembling (Fig. S4; Supplementary Movie 6). Although the initial conditions, and hence the exact sequences, differ slightly each time, this nicely illustrates the ongoing remodeling of the surface energy landscape.

Sustained light-induced particle flows

We now report on the emergence of a collective, dynamic flow phenomenon arising from the combination of the previously described particle deformation and capillary assembly processes (Fig 3, Supplementary Movie M7). This intriguing effect was discovered when we increased the density of particles at the interface significantly, from sparsely distributed particles in the previous sections to densely diffusing particles with near homogeneous surface coverage (Fig. 3a-c, i). Upon illumination with light polarized linearly along the y-axis, the particles in the entire illuminated area were stretched and started to self-assemble into aggregates (Fig. 3a-c, ii). These would then further deform in the polarization direction and start pushing onto each other (Fig. 3a/b, iii-iv). The magenta inset magnified in Figure 3c traces the course of such an aggregate which is assembled from pristine particles, deforms further, and is pushed towards the upper border of the field of view by the collective symmetric deformation. Surprisingly, instead of a finite deformation, a continuous flow is generated

(Fig3a/b, v-vi). In fact, the blue inset magnified in Figure 3c displays fresh, peripheric particles at a later stage, which get pulled towards the zone of illumination along the *x*-direction to compensate for aggregates leaving the zone along the *y*-axis. Entering the illumination zone, they assemble into deforming aggregates themselves, further driving the flow and initiating a stationary process.

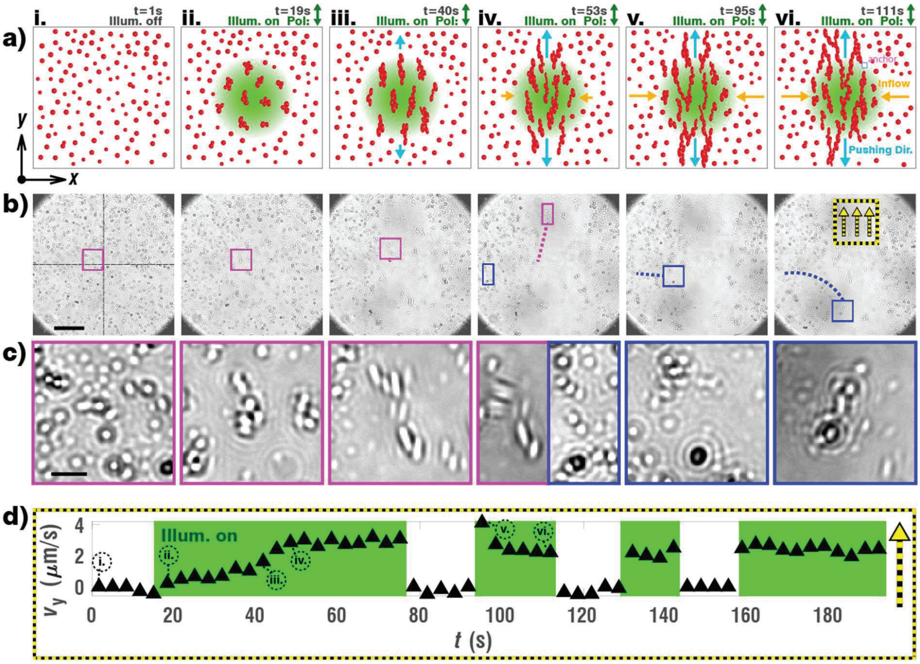

Figure 3. Emergence of sustained symmetric particle flows under constant illumination. a) Sequential schemes showing the unperturbed interface crowded with pristine particles (i), which upon onset of y-axis linearly polarized illumination start capillary assembly (ii), and under prolonged illumination keep deforming (iii), hence exerting a symmetric pushing force along the *y*-direction (light blue arrows) (iv). Expelled aggregates make space for fresh particles to get dragged into the illumination zone orthogonally (orange arrows) (v), fueling a sustained particle displacement flow (vi). Note that aggregates expelled from the illumination zone stay assembled since the particles are permanently deformed. b) Snapshots of Supplementary Movie M7, corresponding to the schematically described steps. Scale bar (black): 30 µm c) Magnified insets from b. Magenta frames follow particles located slightly above the midline in the illumination zone before onset, which assemble, deform, and leave the field of view at the top due to the symmetric *y*-axis deformation. Blue frames, at a later stage, follow pristine peripheric particles which first get pulled in from the lower left below the midline, assemble, deform, and ultimately leave the field of view via the bottom in this case. Scale bar (black): 5 µm d) Graph showing the average y-axis velocity of particles passing the zone highlighted by a black/yellow frame in b, as a function of illumination time. Encircled roman letters indicate the times corresponding to the six frames in a-c. Green background indicates time intervals during which the sample is illuminated.

To quantify this behavior, we measured the *y*-axis velocity of outflowing particle structures in the area contained by the black/yellow square in Figure 3b, vi, using cross-correlation and maximum overlap fitting of subsequent frames (see Methods for details). The resulting velocities were plotted as a function of illumination time in Figure 3d. After an initial phase where the particles are illuminated, but not yet assembled, the outflow velocity slowly rises to a constant value. When the illumination is turned off, the flow almost immediately stops. In contrast, it resumes quickly at full speed when the illumination is switched on again, since the particles are already assembled.

This behavior cannot be explained by photo-deformation alone, which is apparent when comparing the present velocity graph to the well-studied time-dependent deformation effect in fixed azopolymer structures[31–33]. In these works, photo-deformation is shown to start deforming with constant rate immediately when illuminated (at the considered timescales), whilst here the macroscopically transmitted flow displacement arises only after particle assembly, tens of seconds later. On the other hand, the referenced azopolymer deformations consistently saturate during prolonged exposure, upon reaching a maximal deformation. A film made of a single, large azopolymer structure would therefore be expected to cease flowing once the deformation in the illumination zone has saturated. In contrast, we observe that fresh particles are constantly able to reach the center of the illumination zone and efficiently evacuate heavily deformed particles as the capillary assemblies are remodeled.

We note that such a mechanism, which replaces consumed fuel with fresh one in the illumination zone, appears as an essential prerequisite to drive sustained flows from saturating photo-chemical materials under constant illumination conditions. An analogy can be made with interfacial Marangoni flows induced by photo-sensitive azobenzene surfactants, which can saturate upon reaching a photo-stationary equilibrium[43]. Recently, sustained, long-range osmotic flows were elegantly demonstrated using such molecules together with porous particles at solid-liquid interfaces[44,45]. The flows were driven by the porous structure expelling stored surfactant molecules upon photoconversion from the hydrophobic to a more hydrophilic state. However, since the porous particle was able to continuously and preferentially adsorb new hydrophobic state molecules from the bulk solution, a sustained micro-pumping machinery was created along the interface. In our case, there is no simple dichotomy between fully deformed and pristine particles, such as for photo-sensitive surfactants with a hydrophilic and a hydrophobic state. Yet, a conceptually similar pumping mechanism replacing heavily deformed particles with pristine ones is enabling the sustained interface flows as long as fresh particles are available.

Flows with controlled directionality and shear flows

Finally, we demonstrate how the sustained interfacial flows introduced above can be readily tuned by adjusting the illumination pattern and especially the polarization direction (Fig. 4a), which permits us to drive both symmetrical flows with arbitrary direction and pure shear flows. For these experiments, we use azopolymer particles with smaller average size (≤1.5 μm; Fig. S1b), which were observed to result in faster and more homogeneous flows. Instead of solely monitoring outflow velocity, we divide the field of view into regular tiles (Fig. 4b). This approach allows us to compute local velocities and extract entire flow fields through cross-correlation (see Methods). An entire flow field upon Gaussian illumination with y-oriented linear polarization is shown in Figure 4c. If the polarization is x-oriented instead, an orthogonally oriented flow pattern is observed (Fig. 4d), which is a direct consequence of the polarization defining the anisotropic particle deformation direction. The original flows are shown in Supplementary Movie M8. Intriguingly, one can also alter the symmetric outflow axis dynamically during illumination, for example by polarization rotation (Supplementary Movie M9, Supplementary Figure S5).

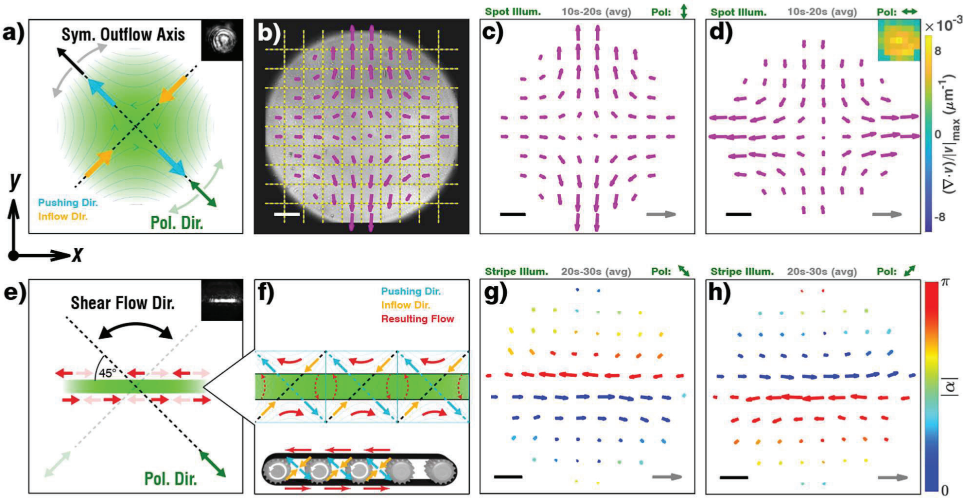

Figure 4. Polarization-controlled rapid flows. a) Scheme of adjustable polarization direction whose rotation will lead to a rotation of the entire flow-field at the water-air interface, including the symmetric outflow axis. Blue arrows: deformation/pushing direction. Orange arrows: inflow. b) Microscope snapshot of Supplementary Movie M8, showing the cutting of the field of view into discrete tiles (black/yellow lines), with one computed flow-field vector (magenta) per tile (and time interval). Scale bar (white): 20 µm. c/d) Flowfields associated to the time interval 10-20 s after illumination onset for *y*- and x-oriented linear polarization respectively. Scale bar (black): 20 µm. Velocity reference arrow (grey): 20 µm/s. Inset: Relative divergence of the flowfield averaged over six consecutive flow fields. e) Scheme of switchable shear flow obtained by tilting the polarization to 45 degrees with respect to a stripe-shaped illumination. f) Explanatory inset showing the origin of a pure shear flow for negligible local divergence (inflow = outflow). Blue arrows: pushing outflow. Orange arrows: compensating inflow. Red arrows: resulting (*x*-oriented) net flows. The conveyor analogy (bottom) shows how the transport movement of such a device may be de-composed into analogous components. g/h) Flowfields computed from data shown in Supplementary Movie M12, demonstrating such shear flows. Arrows are rainbow-colored with respect to the absolute value of their angular deviation from the *x*-axis. Scale bar (black): 20 µm. Velocity reference arrow (grey): 40 µm/s.

It is important to note that smooth and steady flows may not occur at any interfacial particle loading. Although the manual particle dispersion (see Methods) inhibits very precise adjustments, we highlight this by varying the parameter in coarse steps (via pre-dilution/concentration), leading to three extreme situations compared under *y*-oriented linearly polarized illumination (Supplementary Figure S6, Supplementary Movie M10, details in Supplementary Note 1). Crucially, in a fully packed particle monolayer where Brownian motion is severely hindered, the film deformation rate peaks rapidly but decays as the deformation saturates, and no flow is sustained (Supplementary Movie M10, right). This mirrors the immediate onset and saturation behavior of regular azopolymer deformation, as discussed previously. The transient velocity field for this deformation is also highly divergent, due to the lack of particle inflow. Similarly, a net positive divergence (i.e., higher total outflow than inflow) is observed when the starting situation are dense, but still diffusing particles as in Figure 4c/d. This is confirmed by explicit divergence computation (inset, Fig 4d) and may be attributed to the particles increasing surface area as they are stretched. Importantly, using suitable dilution of particles with respect to this case, one can obtain situations where a steady particle flow is still occurring (Supplementary Movie M10, left), but where the contribution of divergence to the flow fields is rendered negligible (Supplementary Note 1). Such situations can be exploited to for example create velocity fields where the particles flow into the illumination zone faster than they exit, using a suitable illumination pattern (Supplementary Figure S7, Supplementary Movie M11). They can also give rise to shear patterns, as detailed below.

Shear flows were created using stripe-shaped illumination, where the linear polarization is oriented at 45 degrees relative to the stripe (Fig. 4e/f). In this configuration, the combined diagonal pushing outflow (light blue arrows) and compensating diagonal inflow of equal magnitude (orange arrows) create parallel flows in opposite directions on either side of the stripe (red arrows). Hence, the result is a pure shear flow with invertible directions for ± 45 degrees offset between the polarization and the stripe axis (Fig. 4g/h; Supplementary Movie M12). At slightly increased densities, occasional turbulence with rotational motion was observed within the stripe region (Supplementary Movie M13). In this case the lateral velocities reached up to 90 µm/s (Supplementary Fig. S8), corresponding to ~100 body sizes per second for the particles.

DISCUSSION

In this work, we studied photo-deformable colloidal azopolymer particles dispersed at a water-air interface. In particular, we used the particles' optical deformation to create strong tunable capillary forces and to control their dynamic interactions directly at the interface. Employing linearly, elliptically and circularly polarized illumination profiles, we induced permanent anisotropic stretching and/or isotropic in-plane expansion of the particles, enabling their shape-mediated assembly and disassembly. Interestingly, continued directional deformation of capillary-assembled particles led to pushing of deformed particles out of, and inflow of fresh particles into, the static zone of illumination. Using this effect, we were able to drive sustained symmetric particle flows across the interface, whose direction we adjusted by changing the illumination's polarization. Furthermore, under appropriate illumination conditions, we could design in plane shear flows with velocities up to 90 μm/s and with controlled directionality.

The first two steps in this cascade of dynamic, deformation-driven effects — photo-deformation of particles at interfaces and ensuing capillary control — may inspire the development of refined material systems for use in colloidal science. Monodisperse particles may be developed, which could be assembled into monolayers before targeted optical deformation, enabling close-packed interface lattices incorporating non-spherical particles[24,40]. Controlled particle sizes may also facilitate the deterministic assembly and modification of more complex particle patterns. In this context, reversible particles may be a benefit (the particles in this work being limited to one assembly cycle, after which they remain flattened). Multi-cycle reversibility could be achieved using light-responsive LCE particles[46] or recently introduced cross-linked amorphous azopolymers[36,47]. We also note the inherent possibility to independently tune the flattening and the in-plane aspect ratio of produced ellipsoidal particles. similar to sophisticated mechanical stretching paradigms[17]. The independent tuneability of the aspect ratio and strength of the capillary forces would expand the current phase diagram of ellipsoidal particles at liquid interfaces[41].

On the other hand, the sustained polarization-steered flows inscribe themselves in a growing context of strategies to control the directionality of individual and collective motion of particles and droplets in various media using the various properties of light.[48]. For example, directional propulsion can be controlled by intensity gradients in one-dimensional capillary tubes[49], or by gradients combined with, e.g., Janus[50] or anisotropically buckling[51] particles in 2D systems. Tilted incidence illumination can make azobenzene microcrystals crawl directionally[52] or induce particle-transporting self-shadowing waves[53]. Sweeping light patterns can guide Marangoni flow traps[54,55] and create propulsive undulating features in particles[56]. Other approaches to directional transport include "light-switch" systems using molecular motors' helicity inversion[57], or spontaneous symmetry breaking for optothermal capillary rafts[10]. Intrinsically polarization-steered particles have also been developed, for example in the case of light-responsive plasmonic microdrones[58,59]. Yet, the ease with which the polarization of the beam, that creates the sustained collective movement, breaks the symmetry of the system and fully controls the fast interface flows in the presented dynamic capillary system seems remarkable. Application-wise, this concept appears highly promising for tasks such as drag-induced displacement and orientation of passive objects floating on liquid interfaces, for mixing in shear flow mode (with built-in transverse velocity components as in efficient microfluidic approaches)[60], or for flows driving the rotation of microgears[61].

METHODS

Particle fabrication

The polymer poly[(Disperse Red 1 methacrylate)-co-(methyl methacrylate) pDR1m-co-mma (Sigma Aldrich, ~15 mol% dye monomer) was dissolved in chloroform at 10|25 mg/mL for samples shown in Supplementary Figure S1a|S1b respectively. 1 mL of solution was then added to 12.5 mL of deionized (DI) water containing 0.5 wt% polyvinyl pyrrolidone (Sigma Aldrich, MW: 360 kD) | polyvinyl alcohol (Sigma Aldrich, MW: 13-23 kD, 87-89%, hydrolyzed) respectively as surfactant. The phase-separated mixtures were sonicated in an ultrasound bath (Elmasonic P30H, 37 kHz, 100 %) for up to five hours interrupted by sporadic manual shaking only, until appearing homogeneously emulsified upon visual inspection. Subsequently, the chloroform solvent was evaporated by transferring the emulsions to an open beaker and sonicating further, whilst slowly raising the bath temperature to the boiling point of chloroform (~0.1 °C/min, from 55 °C upwards). After passing the boiling point, the samples were sonicated for 30 more minutes at 75 °C. Finally, the solutions were filtered with a 10 µm syringe filter and excess surfactant was removed by three times centrifugating the particles and redispersing them in DI water.

Particle characterization

To prepare samples for scanning electron microscopy (SEM), particles from both samples were diluted and dried on regular silicon wafer pieces. They were then sputter-coated with 10 nm of platinum-palladium. Large overview images were obtained using a standard-mode ETD detector (secondary electrons), 5 kV acceleration voltage and 0.1 nA electron current (image size 6144 x 4096 pixels, 33.7 nm/pixel). Particle outlines and sizes were detected in the program imageJ, using the following sequence: *Gaussian Blur (2.5px)* → *Auto Local Threshold v1.11 ("mean", 15px, P1=-15)* → *Convert to Mask* → *Fill Holes* → *Watershed* → *Analyze Particles (Circularity: 0.6-1.0)* using 5|3 images from distinct regions for samples shown in Supplementary Fig S1a|S1b respectively. Finally, the absolute particle counts were reweighted by the particle cross-section in 2D, using the following equation (which leaves the total amount of renormalized particle counts unaltered):

$$h_i = \frac{c_i \cdot n_i}{\sum_j c_j \cdot n_j} \cdot \sum_j n_j \qquad , \qquad c_i = \pi \cdot r_i^2$$

where n_i designs the net particle count in the ith histogram interval, h_i designs its reweighted value used for the histograms in Supplementary Figure S1 e/f (renormalized particle counts), and r_i designs the average radius of the particles in the ith interval which is used to calculate the corresponding cross-section c_i. The distributions were plotted on a logarithmic scale.

Water-air interface

Water-air interfaces were prepared inside dedicated cells, made from two glued microscopy glass sides, where the top slide figures a circular, laser-cut aperture (~5 mm in diameter). The cells were cleaned with a NaOH solution before each use and subsequently filled with 5 μL of DI water. After dilution to a suitable particle density, 10 wt% isopropyl alcohol was added as spreading agent. Then, 0.5 μL of the final mixture were carefully deposited on the interface using a pipette. The sample was left to evaporate in open air for 5 minutes, before it was sealed by a dedicated transparent glass slide fixed with vacuum grease, such as to limit convective and evaporative flows and permit long enough observation times.

Optical setup

The optical setup consisted of a regular inverted microscope, illuminated by a LED (Thorlabs MNWHL4) with a 10x objective as a condenser from the top and with a 40x/0.75 Na objective mounted below the sample for observation. For recordings, a CCD camera from IDS (UI-3060CP-M-GL R2) was used, which permitted reliable acquisition at fixed frame rates of 30 fps and 50 fps. A 532 nm wavelength continuous wave laser diode was employed for the shape-morphing actuation. The beam was introduced from below and focused into the vicinity of the back-focal plane for suitable expansion of the beam width. Intensity was adjusted by means of neutral density filters and polarization was controlled with 0-order waveplates. For assembly experiments, a quarter waveplate's fast axis was oriented at 0, 22, and 45 degrees with respect to the axis of the incoming x-directed polarization, to obtain linear x-axis, elliptical (2.5:1 axis ratio) and circular polarization respectively. To rotate the linear polarization in the flow experiments, a half-wave plate was used instead. Note that in Figure 1d, the images (as well as the underlying movie) are rotated back by 22 degrees for visual alignment with the linear polarization case. Finally, to create the stripe shaped profile in Figure 4e-h, the neat sides of a scribed silicon wafer were mounted on a holder in parallel, facing each other, and inserted in a plane conjugate to the sample plane, leaving a small slit defining the stripe-shaped profile.

Flow analysis algorithm

The analysis code was written in Matlab2021. To analyze the flows, a total number of spatial tiles $n_x \cdot n_y$ and a temporal step length ΔT were defined. The movie stacks were then split into spatiotemporal sub-stacks, each covering the size of one tile in space ($\Delta x \cdot \Delta y = {}^{1}/_{n_x} \cdot {}^{1}/_{n_y}$) and spanning one timestep ΔT in time. The code was optimized for parallel computation of subsequent timesteps to reduce the overall computation time. Eventually, each sub-stack would lead to one velocity arrow, representing the average flow at the given tile position and for the time interval [t_k, $t_k + \Delta T$] where t_k designates the onset time of the *k*th timestep. The procedure to extract this single flow arrow from its corresponding sub-stack is summarized below.

First, after subtraction of - and normalization by – the mean pixel value for each sub-stack image, the correlation between image pairs separated by a given number of frames Δf was computed and averaged. This gives a temporal autocovariance function, which is decaying for increasing Δf, and which is similar to the decay function used in e.g., Dynamic Light Scattering experiments. In the spatiotemporal correlation maps detailed below, these values correspond to the decaying central pixel. Next, all the images of the sub-stack would be shifted by $-i$ pixels in x-direction and $-j$ pixels in y-direction, constructing a second stack. The same correlation would then be computed for image pairs where the first image would be taken from the initial non-shifted stack, whilst the image delayed by Δf frames would be taken from the shifted, second one. Note that this distinction of the delayed image always being the shifted one, is crucial to avoid temporally symmetric results and to be able to extract drift directions as schematically depicted in Supplementary Fig. S9. Finally, for each value of i, j, and Δf the obtained correlation value was plotted as the pixel in position (i,j) with respect to the center on the Δf-th correlation map. Examples of the obtained correlation maps, which depict the full, averaged, spatiotemporal drift-diffusion behavior of the particles pertaining to the sub-stack, are shown in Supplementary Fig. S10.

We note that the 0th correlation map (containing the correlation between image frames with shifted versions of themselves) simply shows the spatial autocovariance, which may be anisotropic, for example if the particles in this part of the field of view and at the given time on average are already anisotropically deformed. The Δf-th correlation map then shows the probability of image features (e.g., particle outlines) moving to new relative positions after Δf frames, on average. This spatiotemporal evolution may be influenced by diffusion, drift (with velocity dispersion), and deformation of features. Here, the only aim was to extract the average drift velocity, which was performed by tracking the average movement of the center of the spatiotemporal probability distribution. Hence, for each correlation map linked to a Δf delay, we started from the pixel with the highest correlation value and attempted to fit the exact peak position within this pixel by a 2D Gaussian fit of the whole map. Finally, the obtained peak positions were plotted against Δf, and the average drift velocity was obtained by a linear fit of motion (see Supplementary Fig. S10), followed by conversion into the final units (from pixel/frame to μm/s). The resulting arrow was then plotted, alongside the arrows from the other tiles, on the flowfield pertaining to the timestep t_k. In Figure 3d, we plot only the y-component of the velocity for the tile of interest.

To calculate divergence maps of entire flowfields, origins were placed in each center between four flow arrows each. The area used to compute an approximation to the local divergence was chosen as a square at an angle of 45 degrees with the velocity vectors' grid (see Supplementary Fig. S11). Then, the total outflow of the four vectors via each side of the square, divided by the total square area, was calculated to obtain the local average divergence. Note that horizontally/vertically adjacent tiles partially overlap (acting as a moving average) and that diagonally adjacent divergence tiles are not independent, since they always share one arrow. Hence, when taking the mean divergence of the whole field, as done in Supplementary Fig. S6f, in practice one computes the outflow only through the total outer boundary of the considered tile region, since internal arrow contributions will cancel out.

ACKNOWLEDGEMENTS

D.U. acknowledges the Norwegian University of Science and Technology for funding the PhD fellowship under project number 989454111 and The Research Council of Norway is acknowledged for the support to the Norwegian Micro- and Nano-Fabrication Facility, NorFab, project number 295864. M.R. acknowledges funding from Sklodowska-Curie Individual Fellowship (Grant No.101064381).

Author contribution:

DU, MR, GV and ED conceived and planned the work jointly. DU prepared the samples. DU, MR and AC performed the experiments, under the supervision of GV and ED. DU performed the data analysis. All authors contributed to discussing and interpreting the results, as well as to the writing and reviewing of the manuscript.

Conflict of interest statement:

The authors declare no competing financial interests.

Data and code availability:

The raw data is made available. In particular, the original flow movies with full framerate and resolution are included, together with the annotated correlation analysis code, and a list of code parameters used for analysis.

REFERENCES

1. Hu, D. L. & Bush, J. W. M. Meniscus-climbing insects. *Nature* **437**, 733–736 (2005).
2. Voise, J., Schindler, M., Casas, J. & Raphaël, E. Capillary-based static self-assembly in higher organisms. *J R Soc Interface* **8**, 1357–1366 (2011).
3. Loudet, J. C. & Pouligny, B. How do mosquito eggs self-assemble on the water surface? *Eur. Phys. J. E* **34**, 76 (2011).
4. Cox, P. A. & Knox, R. B. Two-Dimensional Pollination in Hydrophilous Plants: Convergent Evolution in the Genera Halodule (Cymodoceaceae), Halophila (Hydrocharitaceae), Ruppia (Ruppiaceae), and Lepilaena (Zannichelliaceae). *American Journal of Botany* **76**, 164–175 (1989).
5. Bowden, N., Terfort, A., Carbeck, J. & Whitesides, G. M. Self-Assembly of Mesoscale Objects into Ordered Two-Dimensional Arrays. *Science* **276**, 233–235 (1997).
6. Bae, J. *et al.* Programmable and reversible assembly of soft capillary multipoles. *Mater. Horiz.* **4**, 228–235 (2017).
7. Vandewalle, N. *et al.* Switchable self-assembled capillary structures. *Soft Matter* **16**, 10320–10325 (2020).
8. Wang, W., Giltinan, J., Zakharchenko, S. & Sitti, M. Dynamic and programmable self-assembly of micro-rafts at the air-water interface. *Science Advances* **3**, e1602522 (2017).
9. Hu, Z., Fang, W., Li, Q., Feng, X.-Q. & Lv, J. Optocapillarity-driven assembly and reconfiguration of liquid crystal polymer actuators. *Nat Commun* **11**, 5780 (2020).
10. Kim, H. *et al.* Light-Driven Shape Morphing, Assembly, and Motion of Nanocomposite Gel Surfers. *Advanced Materials* **31**, 1900932 (2019).
11. Lewandowski, E. P. *et al.* Orientation and Self-Assembly of Cylindrical Particles by Anisotropic Capillary Interactions. *Langmuir* **26**, 15142–15154 (2010).
12. Brown, A. B. D., Smith, C. G. & Rennie, A. R. Fabricating colloidal particles with photolithography and their interactions at an air-water interface. *Phys. Rev. E* **62**, 951–960 (2000).

13. Anjali, T. G. & Basavaraj, M. G. Shape-Induced Deformation, Capillary Bridging, and Self-Assembly of Cuboids at the Fluid–Fluid Interface. *Langmuir* **33**, 791–801 (2017).
14. Loudet, J. C., Alsayed, A. M., Zhang, J. & Yodh, A. G. Capillary Interactions Between Anisotropic Colloidal Particles. *Phys. Rev. Lett.* **94**, 018301 (2005).
15. Ozaki, M., Kratohvil, S. & Matijević, E. Formation of monodispersed spindle-type hematite particles. *Journal of Colloid and Interface Science* **102**, 146–151 (1984).
16. Ho, C. C., Keller, A., Odell, J. A. & Ottewill, R. H. Preparation of monodisperse ellipsoidal polystyrene particles. *Colloid Polym Sci* **271**, 469–479 (1993).
17. Champion, J. A., Katare, Y. K. & Mitragotri, S. Making polymeric micro- and nanoparticles of complex shapes. *Proceedings of the National Academy of Sciences* **104**, 11901–11904 (2007).
18. Loudet, J. C., Yodh, A. G. & Pouligny, B. Wetting and Contact Lines of Micrometer-Sized Ellipsoids. *Phys. Rev. Lett.* **97**, 018304 (2006).
19. Madivala, B., Fransaer, J. & Vermant, J. Self-Assembly and Rheology of Ellipsoidal Particles at Interfaces. *Langmuir* **25**, 2718–2728 (2009).
20. Flores-Tandy, L. M. *et al.* Fractal aggregates formed by ellipsoidal colloidal particles at the air/water interface. *Colloids and Surfaces A: Physicochemical and Engineering Aspects* **590**, 124477 (2020).
21. Luo, A. M., Vermant, J., Ilg, P., Zhang, Z. & Sagis, L. M. C. Self-assembly of ellipsoidal particles at fluid-fluid interfaces with an empirical pair potential. *Journal of Colloid and Interface Science* **534**, 205–214 (2019).
22. Honda, K. *et al.* Hydrogel Microellipsoids that Form Robust String-Like Assemblies at the Air/Water Interface. *Angewandte Chemie International Edition* **58**, 7294–7298 (2019).
23. Davies, G. B., Krüger, T., Coveney, P. V., Harting, J. & Bresme, F. Assembling Ellipsoidal Particles at Fluid Interfaces Using Switchable Dipolar Capillary Interactions. *Advanced Materials* **26**, 6715–6719 (2014).
24. Xie, Q. & Harting, J. Controllable Capillary Assembly of Magnetic Ellipsoidal Janus Particles into Tunable Rings, Chains and Hexagonal Lattices. *Advanced Materials* **33**, 2006390 (2021).
25. Saphiannikova, M., Toshchevikov, V. & Tverdokhleb, N. Optical deformations of azobenzene polymers: orientation approach vs. other concepts. *Soft Matter* **20**, 2688–2710 (2024).

26. Viswanathan, N. K. *et al.* Surface relief structures on azo polymer films. *J. Mater. Chem.* **9**, 1941–1955 (1999).
27. Yadavalli, N. S., Saphiannikova, M., Lomadze, N., Goldenberg, L. M. & Santer, S. Structuring of photosensitive material below diffraction limit using far field irradiation. *Appl. Phys. A* **113**, 263–272 (2013).
28. Salvatore, M., Borbone, F. & Oscurato, S. L. Deterministic Realization of Quasicrystal Surface Relief Gratings on Thin Azopolymer Films. *Advanced Materials Interfaces* **7**, 1902118 (2020).
29. Li, Y., He, Y., Tong, X. & Wang, X. Photoinduced Deformation of Amphiphilic Azo Polymer Colloidal Spheres. *J. Am. Chem. Soc.* **127**, 2402–2403 (2005).
30. Lee, S., Kang, H. S., Ambrosio, A., Park, J.-K. & Marrucci, L. Directional Superficial Photofluidization for Deterministic Shaping of Complex 3D Architectures. *ACS Appl. Mater. Interfaces* **7**, 8209–8217 (2015).
31. Li, J. *et al.* Photoguided Shape Deformation of Azobenzene-Containing Polymer Microparticles. *Langmuir* **31**, 13094–13100 (2015).
32. Loebner, S. *et al.* Light-Induced Deformation of Azobenzene-Containing Colloidal Spheres: Calculation and Measurement of Opto-Mechanical Stresses. *J. Phys. Chem. B* 9 (2018).
33. Ryabchun, A. & Bobrovsky, A. Photocontrollable Deformations of Polymer Particles in Elastic Matrix. *Advanced Optical Materials* **7**, 1901486 (2019).
34. Urban, D. *et al.* Polarization-driven reversible actuation in a photo-responsive polymer composite. *Nat Commun* **14**, 6843 (2023).
35. Ichikawa, R. & Nakano, H. Photoinduced change in the shape of azobenzene-based molecular glass particles fixed in agar gel. *RSC Adv.* **6**, 36761–36765 (2016).
36. Wang, W. *et al.* Light-Driven Shape-Memory Porous Films with Precisely Controlled Dimensions. *Angewandte Chemie* **130**, 2161–2165 (2018).
37. Lee, S., Kang, H. S. & Park, J.-K. High-Resolution Patterning of Various Large-Area, Highly Ordered Structural Motifs by Directional Photofluidization Lithography: Sub-30-nm Line, Ellipsoid, Rectangle, and Circle Arrays. *Advanced Functional Materials* **21**, 1770–1778 (2011).

38. Botto, L., P. Lewandowski, E., Cavallaro, M. & J. Stebe, K. Capillary interactions between anisotropic particles. *Soft Matter* **8**, 9957–9971 (2012).
39. Kang, H. S., Kim, H.-T., Park, J.-K. & Lee, S. Light-Powered Healing of a Wearable Electrical Conductor. *Advanced Functional Materials* **24**, 7273–7283 (2014).
40. Trevenen, S. *et al.* Nanoscale Porosity in Microellipsoids Cloaks Interparticle Capillary Attraction at Fluid Interfaces. *ACS Nano* **17**, 11892–11904 (2023).
41. Eatson, J. *et al.* Programmable self-assembly of core-shell ellipsoids at liquid interfaces. Preprint at https://doi.org/10.48550/arXiv.2409.07443 (2024).
42. Loudet, J. C. & Pouligny, B. Self-assembled capillary arrows. *Europhys. Lett.* **85**, 28003 (2009).
43. Kavokine, N. *et al.* Light-Driven Transport of a Liquid Marble with and against Surface Flows. *Angewandte Chemie International Edition* **55**, 11183–11187 (2016).
44. Sharma, A. *et al.* Generation of Local Diffusioosmotic Flow by Light Responsive Microgels. *Langmuir* **38**, 6343–6351 (2022).
45. Feldmann, D. *et al.* Extremely Long-Range Light-Driven Repulsion of Porous Microparticles. *Langmuir* **36**, 6994–7004 (2020).
46. B. Braun, L., Hessberger, T. & Zentel, R. Microfluidic synthesis of micrometer-sized photoresponsive actuators based on liquid crystalline elastomers. *Journal of Materials Chemistry C* **4**, 8670–8678 (2016).
47. Yin, X. *et al.* Coupling of Photoinduced Mass Immigration with Polymer Networks to Produce Nanostructured Materials Capable of Reversibly Creating Arbitrary Deformations. *Macromolecular Chemistry and Physics* **219**, 1800113 (2018).
48. Rey, M., Volpe, G. & Volpe, G. Light, Matter, Action: Shining Light on Active Matter. *ACS Photonics* (2023) doi:10.1021/acsphotonics.3c00140.
49. Lv, J. *et al.* Photocontrol of fluid slugs in liquid crystal polymer microactuators. *Nature* **537**, 179–184 (2016).
50. Lozano, C., ten Hagen, B., Löwen, H. & Bechinger, C. Phototaxis of synthetic microswimmers in optical landscapes. *Nat Commun* **7**, 12828 (2016).

51. Camacho-Lopez, M., Finkelmann, H., Palffy-Muhoray, P. & Shelley, M. Fast liquid-crystal elastomer swims into the dark. *Nature Mater* **3**, 307–310 (2004).
52. Uchida, E., Azumi, R. & Norikane, Y. Light-induced crawling of crystals on a glass surface. *Nat Commun* **6**, 7310 (2015).
53. Gelebart, A. H. *et al.* Making waves in a photoactive polymer film. *Nature* **546**, 632–636 (2017).
54. Lv, C., Varanakkottu, S. N., Baier, T. & Hardt, S. Controlling the Trajectories of Nano/Micro Particles Using Light-Actuated Marangoni Flow. *Nano Lett.* **18**, 6924–6930 (2018).
55. Piñan Basualdo, F. N., Bolopion, A., Gauthier, M. & Lambert, P. A microrobotic platform actuated by thermocapillary flows for manipulation at the air-water interface. *Science Robotics* **6**, eabd3557 (2021).
56. Palagi, S. *et al.* Structured light enables biomimetic swimming and versatile locomotion of photoresponsive soft microrobots. *Nature Mater* **15**, 647–653 (2016).
57. Lancia, F. *et al.* Reorientation behavior in the helical motility of light-responsive spiral droplets. *Nat Commun* **10**, 5238 (2019).
58. Tanaka, Y. Y. *et al.* Plasmonic linear nanomotor using lateral optical forces. *Science Advances* **6**, eabc3726 (2020).
59. Wu, X. *et al.* Light-driven microdrones. *Nat. Nanotechnol.* **17**, 477–484 (2022).
60. Battat, S., Weitz, D. A. & Whitesides, G. M. Nonlinear Phenomena in Microfluidics. *Chem. Rev.* **122**, 6921–6937 (2022).
61. Maggi, C., Saglimbeni, F., Dipalo, M., De Angelis, F. & Di Leonardo, R. Micromotors with asymmetric shape that efficiently convert light into work by thermocapillary effects. *Nat Commun* **6**, 7855 (2015).

Supplementary Materials

Directional capillary flows induced by photo-deformable colloidal particles

David Urban[1,4], Marcel Rey[2,3], Antonio Ciarlo[3], Emiliano Descrovi[4] and Giovanni Volpe[3]

1. Department of Electronic Systems, Norwegian University of Science and Technology, O.S. Bragstads plass 2b, 7034, Trondheim, Norway

2. Institute of Physical Chemistry, University of Münster, Corrensstr. 28/30, 48149 Münster, Germany

3. Department of Physics, University of Gothenburg, SE-41296, Gothenburg, Sweden

4. Dipartimento di Scienza Applicata e Tecnologia, Politecnico di Torino, Corso Duca degli Abruzzi 24, 10129, Torino, Italy

Corresponding Authors
David Urban: david.urban@ntnu.no
Emiliano Descrovi: emiliano.descrovi@polito.it

SUPPLEMENTARY MOVIE LEGENDS

Supplementary Movie M1

Movie showing the smooth deformation of azopolymer particles adsorbed to an air-water interface under illumination with linear (left), circular (middle), and elliptical (right) polarization at a wavelength of $\lambda = 532$ nm and an intensity of $I = 219$ W·cm^{-2}. Real time acquisition speed (non-accelerated).

Supplementary Movie M2

Movie showing the assembly of two azopolymer particles, initially freely diffusing while adsorbed to an air-water interface, upon deformation into ellipsoidal particles with elliptically polarized light ($\lambda = 532$ nm, $I = 219$ W·cm^{-2}). At a later stage, the particles are disassembled upon prolonged exposure to circularly polarized light, with otherwise identical illumination parameters. 5x accelerated.

Supplementary Movie M3

Movie showing the assembly of several azopolymer particles, initially freely diffusing while adsorbed to an air-water interface, upon deformation into ellipsoidal particles with elliptically polarized light ($\lambda = 532$ nm, $I = 219$ W·cm^{-2}). At a later stage, the particles are disassembled upon prolonged exposure to circularly polarized light, with otherwise identical illumination parameters. 5x accelerated.

Supplementary Movie M4

Movie showing the assembly of two azopolymer particles, initially freely diffusing while adsorbed to an air-water interface, upon deformation into rod-like particles with linearly polarized light ($\lambda = 532$ nm, $I = 339$ W·cm^{-2}). At a later stage, the particles are disassembled upon prolonged exposure to circularly polarized light, with otherwise identical illumination parameters. 5x accelerated.

Supplementary Movie M5

Movie showing the assembly of several azopolymer particles, initially freely diffusing while adsorbed to an air-water interface, upon deformation into rod-like particles with linearly polarized light ($\lambda = 532$ nm, $I = 171$ W·cm^{-2}). At a later stage, the particles are disassembled upon prolonged exposure to circularly polarized light, with otherwise identical illumination parameters. 5x accelerated.

Supplementary Movie M6

Two acquisitions added sequentially which show the assembly of multiple particles with linearly|elliptically polarized light, and subsequent disassembly using circularly polarized light ($\lambda = 532$ nm, $I = 171|219$ W·cm^{-2}). During disassembly multiple out-of-equilibrium configuration pathways can be seen. 5x accelerated.

Supplementary Movie M7

Movie showing larger particles (Supplementary Figure S1a) at high density under illumination with linear polarization along the y-axis (frame vertical). Upon exposure, the particles are seen to deform, assemble, and initiate a flow. When illumination is interrupted, the flow stops, and the particles appear rigidly assembled. Illumination parameters: λ = 532 nm, I = 100 W·cm^{-2}, Gaussian beam. 5x accelerated.

Supplementary Movie M8

Movie showing the sustained flow of smaller particles (Supplementary Figure S1b) under illumination with linear polarization along the *y*-axis (frame vertical) on the left and along the *x*-axis (frame horizontal) on the right. Computed flow-field arrows (magenta) are overlayed over the original microscope movie images. Illumination parameters: λ = 532 nm, I = 56 W·cm^{-2}, Gaussian beam. 4x accelerated.

Supplementary Movie M9

Movie showing the rotating flow direction of smaller particles (Supplementary Figure S1b) under illumination with linear polarization whose axis is rotated stepwise for a total of 180 degrees. Computed flow-field arrows (magenta) are shown besides the original microscope movie images. Illumination parameters: λ = 532 nm, I = 26 W·cm^{-2}, Gaussian beam 3x accelerated.

Supplementary Movie M10

Movie showing the flow of smaller particles (Supplementary Figure S1b) under illumination with linearly polarized light. Left to right: particles initially filling the interface with very low density, intermediate density, and fully filled packed layer. In the top graphs, the mean absolute velocity over all arrows for the different situations is tracked. Illumination parameters: λ = 532 nm, I = 56|56|32 W·cm^{-2}, Gaussian beam. 2x accelerated.

.

Supplementary Movie M11

Movie showing the flow of smaller particles (Supplementary Figure S1b) under a stripe-shaped illumination with linear polarization along the *x*-axis (parallel to stripe) on the left and along the *y*-axis (perpendicular to stripe) on the right. Illumination parameters: λ = 532 nm, I = 645 W·cm^{-2}, stripe-shaped pattern. 2x accelerated.

Supplementary Movie M12

Movie showing the flow of smaller particles (Supplementary Figure S1b) under a stripe-shaped illumination with linear polarization offset by +45 degrees (counterclockwise, with respect to stripe axis) on the left and by -45 degrees (clockwise, with respect to stripe axis) on the right. Illumination parameters: λ = 532 nm, I = 645 W·cm^{-2}, stripe-shaped pattern. 4x accelerated.

Supplementary Movie M13

Movie showing the flow of smaller particles (Supplementary Figure S1b) under a stripe-shaped illumination with linear polarization offset by +45 degrees (counterclockwise, with respect to stripe axis) and density slightly increased with respect to Supplementary Movie M12, giving rise to faster flows and slight rotational turbulences. Illumination parameters: λ = 532 nm, I = 645 W·cm^{-2}, stripe-shaped pattern. Real time acquisition speed (non-accelerated).

SUPPLEMENTARY FIGURES

Supplementary Figure S1 – SEM Particle Size Distributions

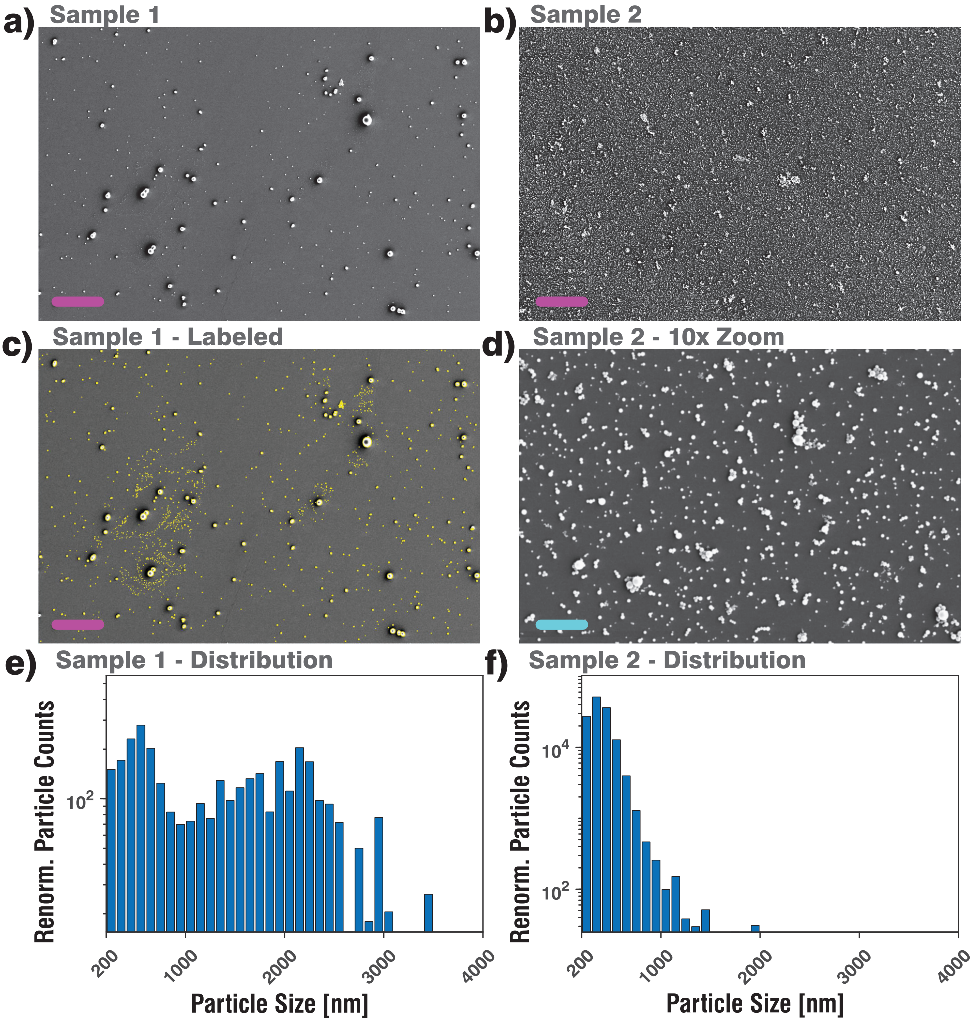

Supplementary Figure S1: SEM images of dilute, dried particles on a silicon substrate and particle counts. a/b Raw SEM images of Sample 1/Sample 2 respectively, with similar absolute content of azopolymer before drying. Note that sample 1 was employed in result sections 1-3, whilst Sample 2 was employed in result section 4. c) Example image of detected particle outlines (yellow) superimposed on raw image for Sample 1. Scale bars (magenta): 20 µm d) 10x larger zoom-in on Sample 1 particles, highlighting the presence of small particles. Scale bar (cyan): 2 µm. e/f) Particle counts based on 5 large area images, as in (a), for Sample1 and 3 large area images, as in (b), for Sample 2. Particle absolute counts were renormalized to the occupied cross-section in 2D at the interface.

Supplementary Figure S2 – Fast dynamics of tip-to-tip approach and rotation.

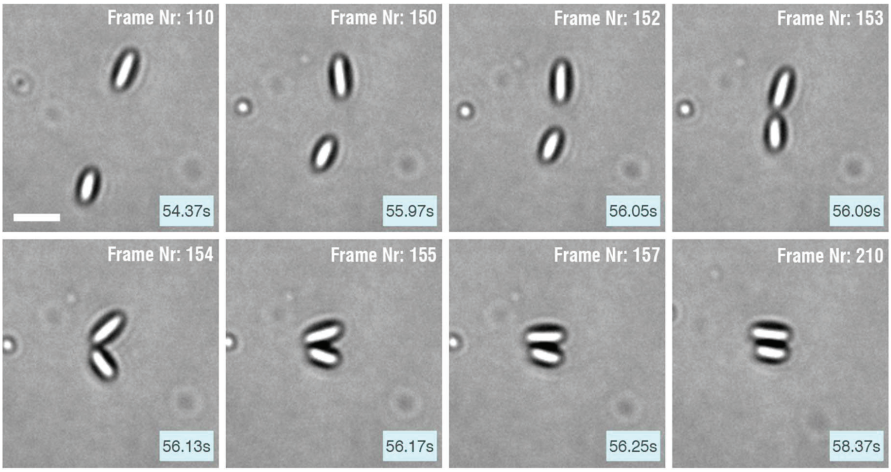

Supplementary Figure S3: Frames from Supplementary Movie M2 around the bonding event (no illumination). The elliptical particles are seen to approach in a tip-to-tip configuration. Upon apparent contact, they rotate about the bonding point within a fraction of a second. Scale bar (white): 5 µm. Light blue squares in the lower right indicate total time.

Supplementary Figure S3 – Linear → Circular Deformation Sequence

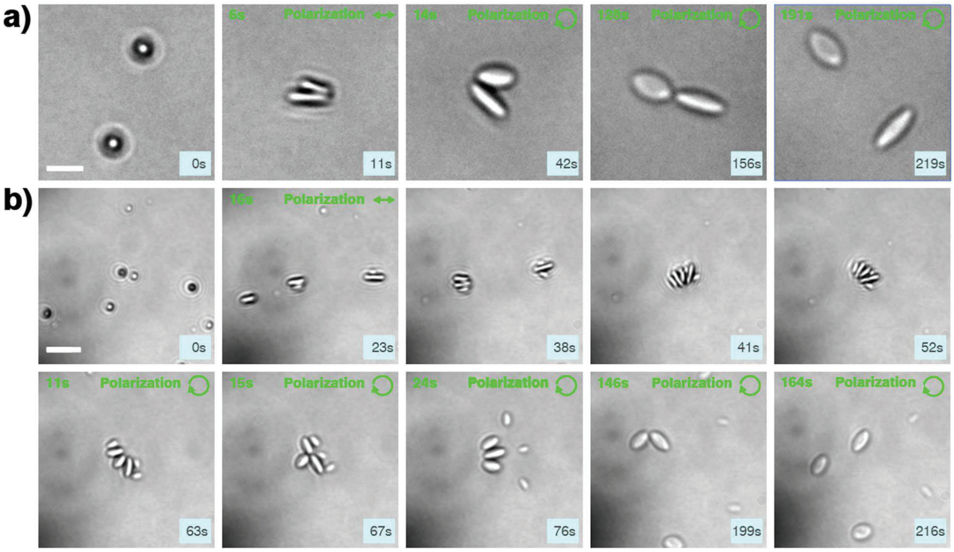

Supplementary Figure S2: a) Snapshots from Supplementary Movie M4, showing left-to-right: Deformation with linear polarization leading to rod-like shapes and consequential assembly, followed by prolonged illumination with circular polarization leading to increasing roundness and flattening and eventually to disassembly. b) Similar sequence involving multiple particles. Note that particles continue to assemble due to their rod-like shape, also after linear polarization has been switched off. They stay rigidly assembled until illumination with circular polarization remodels their shape. Full sequence is shown in Supplementary Movie M5. Scale bars (white): 5 µm. Light blue squares in the lower right indicate total acquisition time, green font indicates respective time from illumination onset.

Supplementary Figure S4 – Dynamic remodeling behavior during particle flattening.

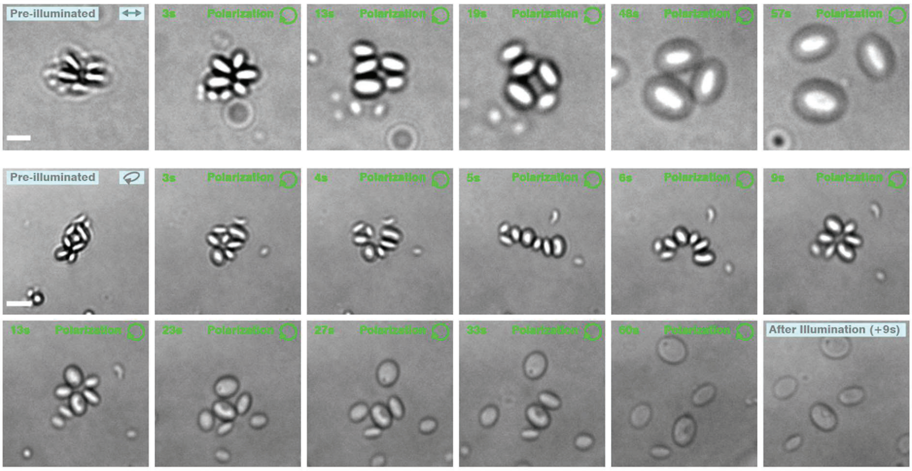

Supplementary Figure S4: a) Prolonged illumination of an optically pre-assembled particle structure with circularly polarized light. During the flattening of the particles the structure is continuously re-configurating itself, passing through symmetric flower-like, rectangular and finally triangular shapes before final disassembly. Scale bar (white): 3 µm. b) Example of another optically pre-assembled particle structure during prolonged illumination with circularly polarized light. The structure passes from tightly assembled through chain-like, ring-like, flower-shaped and dog-shaped stages before final disassembly. Scale bar (white): 5 µm. Green font indicates respective times from circularly polarized illumination onset. Note that, although some of these structural motives were repeatedly observed during the experiments, no deterministic control was obtained over such transformation sequences, in part certainly due to the varying particle sizes and initial assembly conditions. Full movies are shown in Supplementary Movie M6.

Supplementary Figure S5 – In situ rotation of the polarization/flow direction.

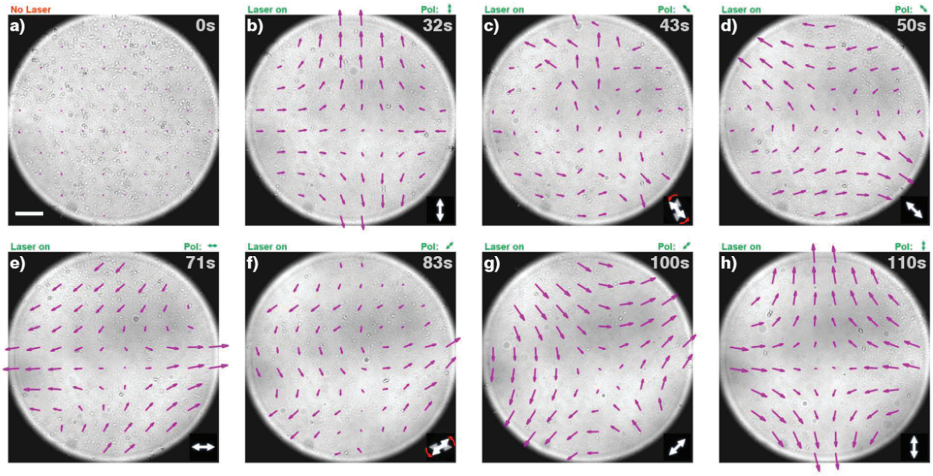

Supplementary Figure S5: a-h) Selected snapshots from Supplementary Movie M9 with overlaid flow-fields (magenta), showing how the flow direction follows the varying polarization direction during the same flow event. The time intervals of c and f include a discrete step of the illumination polarization by 45 degrees, giving rise to transient features. The time intervals used for flow-field computation and averaging are 3s. Scale bar (white): 20 µm.

Supplementary Figure S6 – Flows with varying particle density

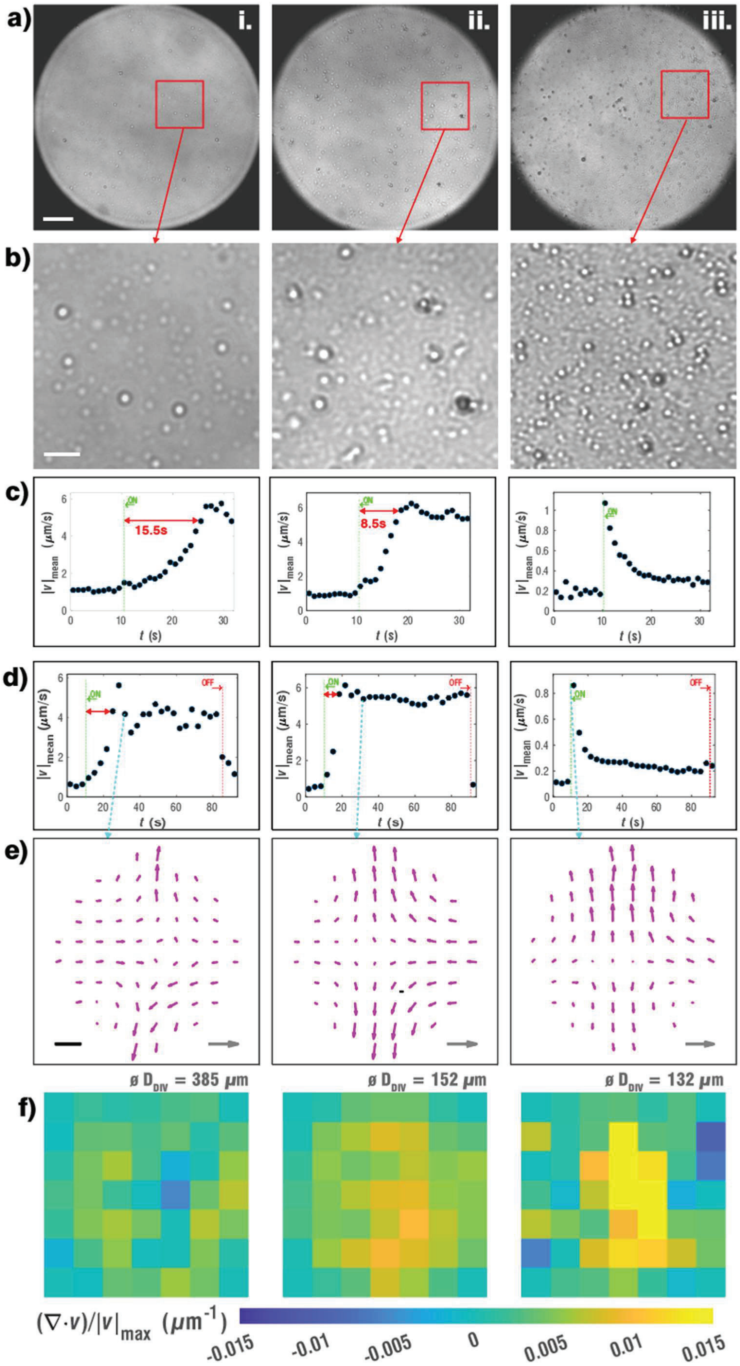

Supplementary Figure S6: a) Frames from flow movies (Supplementary Movie M10) with different particle densities increasing from left to right (i-iii, 5x concentration steps for the precursor solution). Note that in the highest density case (iii), particle diffusion was severely hampered, as the particles formed a densely packed carpet. Scale bar (white): 20 µm. b) Insets for better visualization of the particle density differences. Scale bar (white): 5 µm. c) Temporal evolution of the mean of the individual absolute velocities in the flowfield during the first 20s of illumination (1s steps). A slightly slower rise is observed for the dilute sample (i), whilst the carpet-like sample (iii) deforms with maximal velocity immediately. d) Full length velocity graphs (3s steps), showing constant plateaus for the sustained flows, whilst the carpet's velocities rapidly decay (iii), owing to the saturating deformation. e) Selected flowfields, corresponding to the respective datapoint indicated by the cyan dotted arrow. Scale bar (black): 20 µm, reference arrows (gray): 20 µm/s (i), 20 µm/s (ii), 3 µm/s (iii). The outflow/inflow ratio seems to increase for higher concentrations (indicating more flow divergence). f) Relative divergence calculations over the field of view, averaged over 20 timesteps (3s) in each case, and displayed on the same color scale, confirming higher relative divergence for higher concentrations. The inverse of the average relative divergence (D_{Div}) is calculated omitting the outermost boarder values (non-illuminated) and indicated above each plot. This value estimates the characteristic distance over which divergence alone would build up to the maximal velocity present on the flowfield. Finally, note that both intensity and illumination spot size were slightly decreased for the most concentrated case (iii), to limit heavy absorption by the dense particles. Raw data from iii. was also rotated by 90 degrees to fit the flow direction of the other movies.

Supplementary Figure S7 – Stripe illumination with orthogonal/parallel polarization.

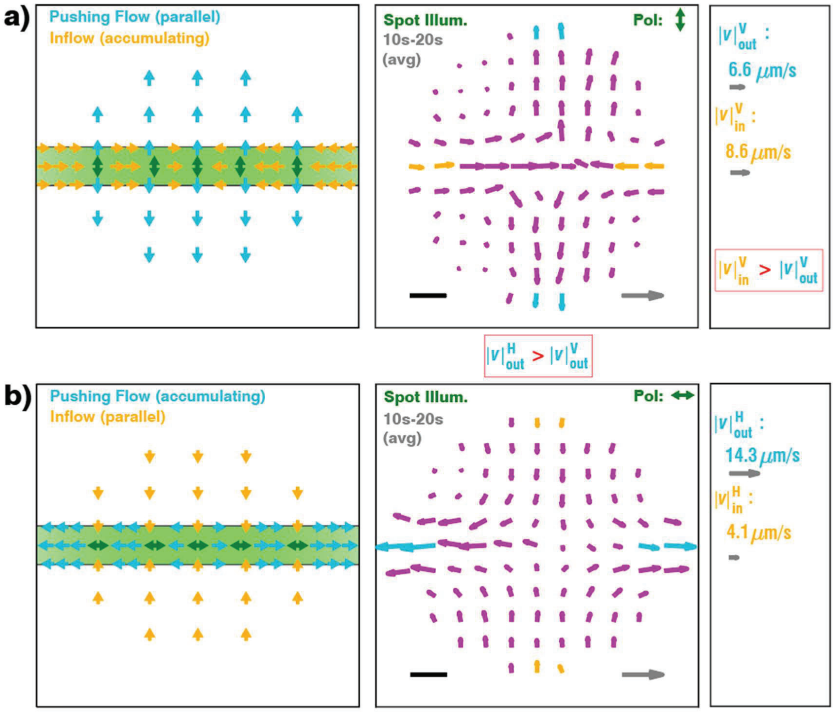

Supplementary Figure S7: a) Scheme (left) and flowfield (right) for a stripe illumination experiment with polarization oriented orthogonally to the stripe pattern, at low particle density (computed based on the data shown in Supplementary Movie M11). As schematically illustrated, the outflow perpendicular to the stripe illumination acts only over a short pushing distance (short axis of the stripe). The compensating inflow on the other hand accumulates along the stripe. In addition, the compensating inflow should be locally similar in size to the outflow everywhere, due to the low divergence condition. As a result, the average extremal inflow velocity (8.6 µm/s) surpasses the average outflow velocity (6.6 µm/s) in this configuration. b) Scheme (left) and flowfield (right) for the same illumination pattern, but with polarization oriented parallel to the long axis of the stripe. In this case, it is the outflow velocity that accumulates, which leads to a higher outflow velocity in this case (14.3 µm/s), consistent with a pushing effect acting over a much longer distance. All velocity averages are taken as the mean of the individual absolute velocities of the arrows marked in the corresponding colors on the respective plot. Scale bars (black): 20 µm. Reference arrows (gray): 20 µm/s.

Supplementary Figure S8 – Manual measurement of turbulent shear velocity.

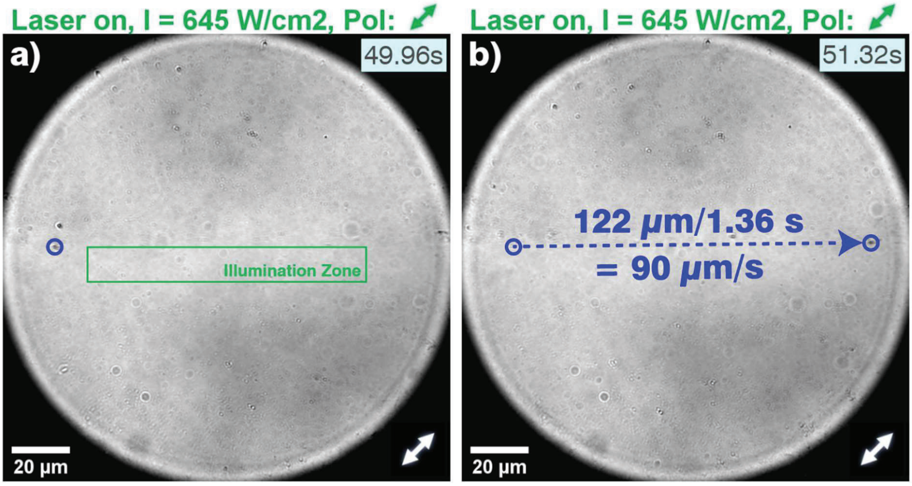

Supplementary Figure S8: Manual measurement to estimate the maximal translational velocities involved in the slightly turbulent shear flow of Supplementary Movie M13. The correlation-based algorithm, relying on spatiotemporal averaging (over a whole tile and a timestep), would perform poorer at this task. a) Movie snapshot showing a particle (inside blue circle) entering the field of view on the left. b) After traversing the field of view close to the upper boarder of the stripe-shaped illumination zone (green square), where the velocities are highest, the particle is again highlighted by a blue circle. From the distance travelled and the total time necessitated, the velocity for traversing the field of view can be estimated to 90 µm/s.

Supplementary Figure S9 – Scheme of algorithm steps for correlative velocity measurements.

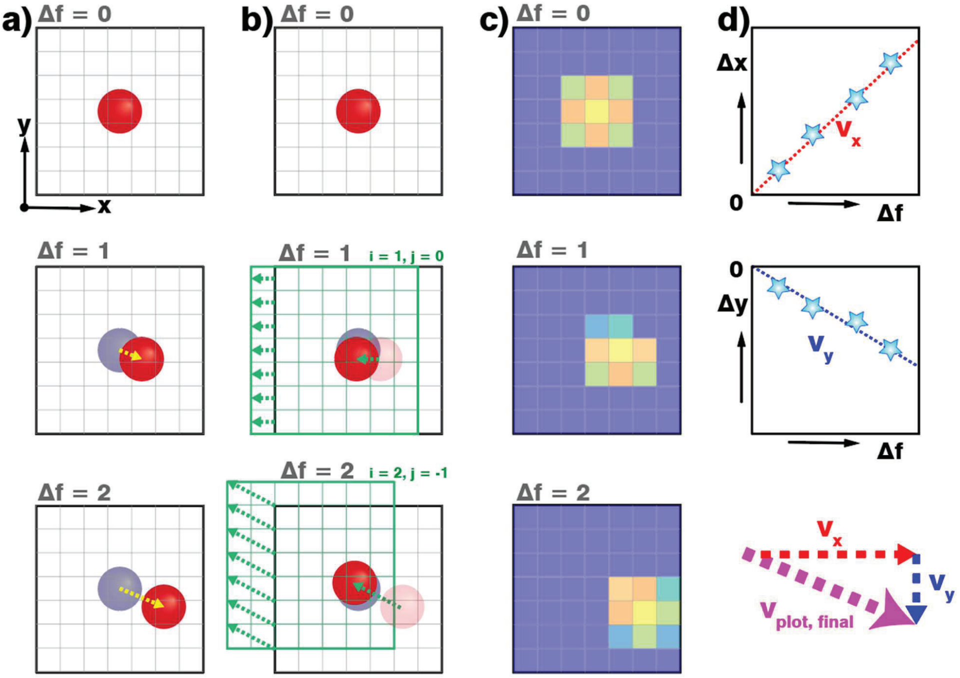

Supplementary Figure S9: Schematic representation of computation steps undertaken by the algorithm to extract the average drift velocity pertaining to a single tile and a single timestep. a) Sequence of consecutive movie frames showing the drift of a single particle (red) over three frames (top to bottom) and indicating its initial position ($\Delta f = 0$) as reference on the two later frames (gray). b) Spatially shifting the later images (bottom) by the right number of pixels, the drifting particle (red) can be almost exactly superposed with its initial position (gray). This will lead to the highest overlap on the correlative maps in c. c) Schematic correlative map examples where the maximum overlap shift displayed in b is naturally the brightest (yellow) pixel. However, the procedure is performed for all possible pixel shifts (up to a user-defined maximal shift value), in order to obtain full correlation maps. Further, the maps are taken as average, where any movie frame within the considered timestep is taken as reference frame exactly once, provided it is followed by at least Δf_{max} frames. The sequence of correlation maps for increasing Δf hence shows the averaged spatio-temporal drift-diffusion of features/particles. d) Schematic graph example plotting the *x*- and *y* positions of the correlation peak, which are obtained by Gaussian fitting of the maps shown in c. Finally, a linear fit of these positions will lead the average velocity along each axis (in pixel/frame units), permitting the construction of the final flow arrow after unit conversion.

Supplementary Figure S10 – Algorithm correlative velocity example on real data.

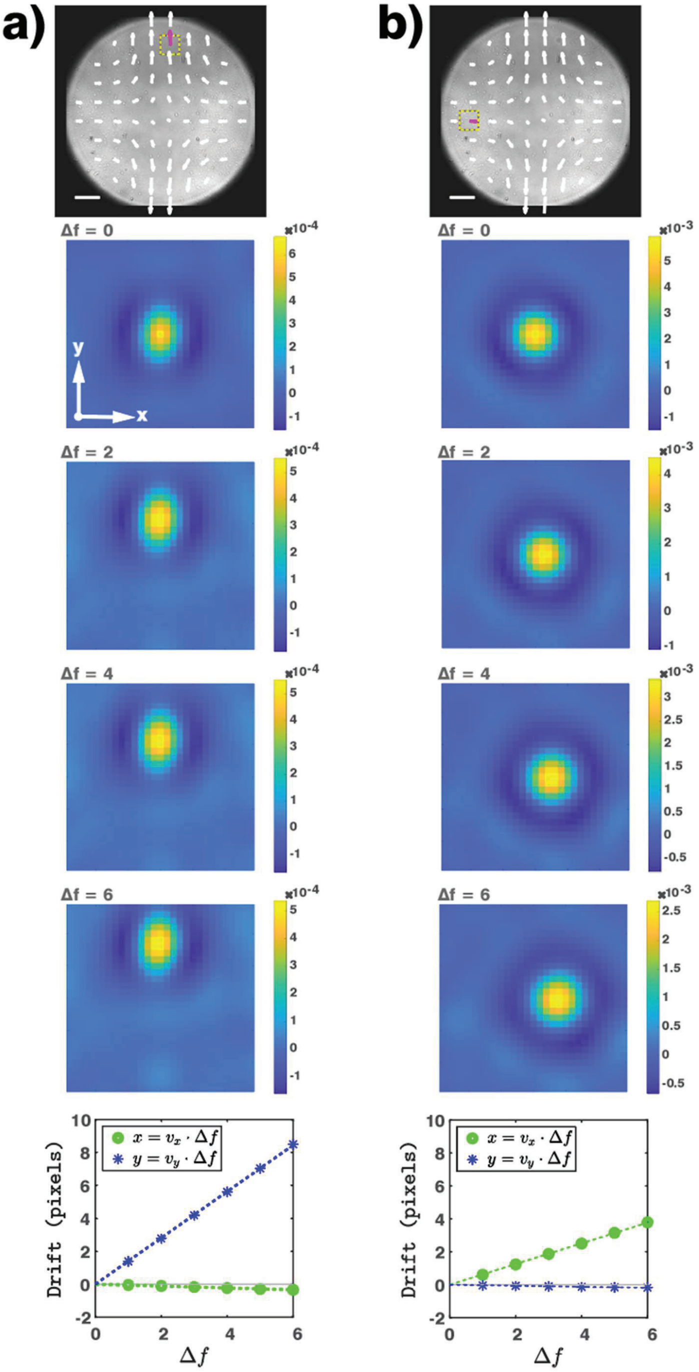

Supplementary Figure S10: Example of the computation of two flow vectors pertaining to the velocity field shown in Figure 4c (*y*-directed polarization flow). a) Computation of an arrow belonging to a tile where deformed particles are flowing out of the field of view at the upper boarder. b) Computation of an arrow in a tile where pristine, undeformed particles flow towards the zone of illumination. In each column, the images show (top to bottom): Flow field from Figure 4c with arrow to be computed marked in magenta and tile of interest marked by a yellow/black dotted frame. The four computed correlation maps, corresponding to $\Delta f = 0, 2, 4$, and 6 respectively, which may be interpretated as the average motion of virtual particles initially located at the center (i.e., autocovariance at $\Delta f = 0$). Finally, a graph showing the (Gaussian fitted) *x*- and *y*-positions of the correlation peaks in $\Delta f = 1$-6, with linear fit of motion (dotted lines) used to extract the average drift velocity along each axis. Note that, whilst the correlation peak is perfectly isotropic in (b), and merely expanding due to the diffusion of pristine particles, the peaks in a can be seen to be slightly elongated in the *y*-direction. Although not used in this work, such information may be useful in other contexts. For example, the *y*-axis elongation of the spatial autocovariance function ($\Delta f = 0$) in (a) reflects the anisotropic shape of the *y*-axis deformed particles themselves. Another factor, apart from Fickian diffusion, which can influence the width and shape of the spatiotemporally evolving correlation peaks is velocity dispersion (i.e. non uniform velocity) either spatially within a tile, or temporally within a timestep (due to flow fluctuations).

Supplementary Figure S11 – Flowfield local divergence computations.

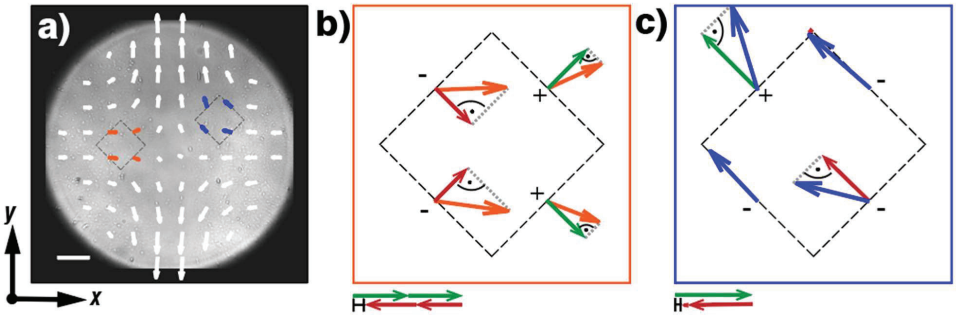

Supplementary Figure S11: Example of the computation of local divergence tiles such as shown in Supplementary Figure S6. a) Flowfield from Figure 4c (*y*-directed linear polarization flow). Two local divergence tiles are marked with black dotted squares (tilted at 45 degrees with respect to the flow vector grid), and the arrows corresponding to the tiles are colored (orange/blue). b) Computation of the local divergence averaged over the tile spanned by the orange vectors. Only contributions orthogonal to the tile boundary should be considered. Arrows representing negative contributions (net inflow) across the tile boundary are colored in red and marked with a minus sign, whilst positive contributions to the divergence (net outflow) are colored in green and labeled with a plus sign. At the bottom of the subplot, the length of the green and red arrows is compared. The difference between their total lengths is the measured (small) divergence, after correction by the factor (circumference/area). c) Same procedure applied to the tile spanned by the blue vectors.

SUPPLEMENTARY NOTE 1 – Coarse density variations and flow behavior.

Protocol Adaptation

Using the method of simple pipette-aided dispersion of particles at the water-air interface (see methods), precise control over the density is difficult, and inter-sample (between different manual particle dispersions) as well as intra-sample (different areas of the same sample interface) variations are usually observed. Therefore, the density was varied in very coarse steps, by means of 1:4 sample pre-dilution, no dilution, and 5-fold sample pre-concentration prior to using the same interface deposition protocol. The three cases were compared side-by-side in Supplementary Movie M10 (Flow movies and live velocity graphs) and in Supplementary Figure S6 (Sample images, velocity graphs, flowfield examples, divergence comparison). In case of the 5-fold, heavy, pre-concentration, a static film with no visible diffusion was observed on the interface. In both other case, diffusing particles are observed prior to illumination, with visually appreciable lower density for the strongly diluted sample.

Flow Rise and Persistence Comparison

In the two cases where the particles are not forming a static film, the upon illumination onset with linear y-axis polarization, a delay is observed, after which the polarization-driven flow emerges. We have attributed this delay to the necessity of first deforming particles and creating capillary particle assemblies, before the pushing mechanism can become effective at large scale (see section *Sustained Light-Induced Flows*). In fact, as shown in Supplementary Figure S6 c/d and apparent in Supplementary Movie M10, the non-diluted sample starts flowing after a shorter delay, possibly due to faster aggregation with more particles available. This picture is consistent with the case of the heavily pre-concentrated sample, where the particles form a static film. In fact, in this case the particles are already aggregated when the illumination starts, and hence can start transmitting the symmetric deformation-caused pushing force immediately. Consequently, the deformation rate is maximal at the illumination onset, and then follows the saturation-related decay that would be expected from the known deformation vs. illumination time behavior for azopolymer structures in fixed settings. Since the particles assume fixed positions with respect to each other in such a solid film, the movement ultimately stops, when the particles have been maximally deformed and no fresh particles can enter the illumination zone. This contrasts with the case of the two initially diffusing, lower density samples, where the sustained flow regime is obtained, and a constant flow velocity plateau is reached after the initial rise. We also note that in the dilute case, the flow is seen to be slightly more turbulent (and the plateau velocity less stable), possibly due to larger local particle density variations.

Divergence Comparison

Another parameter that can be computed from the flow fields and compared in these different situations is the two-dimensional flow divergence. Mathematically, the flow divergence is defined as the infinitesimal difference between local outflow and inflow in each spatial point. Although defined locally, the quantity may be integrated over an area, the result of which will quantify the total outflow/inflow difference across the boundary delimiting the integration area (divergence theorem). Hence, the average flow divergence may be estimated by simply comparing the total flow out of to the perpendicular flow into the illumination zone. A quick look onto the exemplary flow fields in Supplementary Figure S6e shows that this difference seems to increase for higher particle densities (from left to right). This observation is in confirmed by explicit computation of the divergence as shown in Supplementary Figure S6f. Here, the local average of the sustained, relative flow divergence in each zone between 4 adjacent flow-field arrows is mapped and displayed on identical color scales for all three situations (temporally averaging over the last 20 timesteps). The divergence is seen to roughly map the illuminating laser spot and increases for higher densities.

Assuming the water-air interface itself to be incompressible, one may hypothesize this difference in sustained divergence to stem from the average in-plane expansion - and hence from the deformation - of the particles themselves. In fact, also for a uniaxial, isochoric transformation associated with linear polarization, a net in-plane expansion results from the compression along the out-of-plane axis (optical axis), which is apparent from considering deformation tensor describing such a transformation in the small strain approximation[34]:

$$\boldsymbol{F}^{\text{uniaxial,isochoric}} = \begin{pmatrix} 1+\varepsilon_1 & 0 & 0 \\ 0 & 1+\varepsilon_2 & 0 \\ 0 & 0 & 1+\varepsilon_3 \end{pmatrix} = \begin{pmatrix} 1+\delta & 0 & 0 \\ 0 & 1-\frac{1}{2}\delta & 0 \\ 0 & 0 & 1-\frac{1}{2}\delta \end{pmatrix}$$

where the net in-plane area expansion is given by $\Delta A \approx \varepsilon_1 + \varepsilon_2 = \delta - \frac{1}{2}\delta = \frac{1}{2}\delta$. Hence, if divergence is caused by this deformation-related in plane expansion of the particles themselves, it will naturally follow the local illumination intensity (i.e., the shape of the Gaussian illumination) and may increase for higher particle densities, as experimentally observed.

Finally, note that in the above, we have consistently compared the relative divergence $\nabla\cdot\mathrm{v}/|\mathrm{v}|_{\max}$, i.e. the divergence normalized by the maximum velocity present in the flow field. Given that the absolute divergence would linearly scale with the multiplication of all velocity vectors, this normalized divergence is a more appropriate comparison tool between different flow situations with different speeds. In fact, its units (μm^{-1}) indicate that it describes a spatial frequency, which is the frequency with which a flow field with the given divergence and maximal velocity would spatially vary. Conversely, its inverse can be seen as the characteristic distance D_{Div} over which the measured divergence would (unidirectionally) cause velocity fields with the maximal amplitude in question. If this characteristic distance is much larger than the illumination zone (Gaussian spot size) in which the flow field is created, one may then conclude that divergence contributes in a negligible manner to the total flow field. The spatially averaged values for D_{Div}, computed over the illumination zone (25 innermost tiles), are indicated on Supplementary Figure S6f. One can see that in the lowest divergence case (left), this distance amounts to 385 μm, which is much larger than the illumination spot radius (~50 μm), and thereby indicates that the divergence contribution to the flow field of such diluted samples can indeed be considered negligible. This opens for the obtention of a pure shear flow, which mathematically consists of curl contributions only, as shown in Figure 4 e-h.

IX. Appendix C: Reversibility Measure

The reversibility measure mentioned in section 1.3.2 was defined as $R = 1 - {}^{\delta A}/_{\varepsilon}$, and is meaningful for repeated two-step cycles where each of the alternating illumination steps has a specified polarization (one of the polarizations being linear), in passive reversibility azopolymer systems. Here, ε designates the relative expansive strain created by (one of) the illumination step(s) with linear polarization along the direction parallel with the latter. δA on the other hand is the relative area expansion measured after both sequential illumination steps of the cycle have been applied. To highlight the usefulness of this measure in a more general azopolymer context, we write down the tensors related to x-polarized ($\mathbf{F^x}$), y-polarized $\mathbf{F^y}$ and circularly polarized ($\mathbf{F^c}$) illumination for azopolymer deformations, each of which are expressed as a function of the small strain parameter δ.

$$\mathbf{F^x} = \begin{pmatrix} 1+\delta & 0 & 0 \\ 0 & 1-\frac{1}{2}\delta & 0 \\ 0 & 0 & 1-\frac{1}{2}\delta \end{pmatrix}, \quad \mathbf{F^y} = \begin{pmatrix} 1-\frac{1}{2}\delta & 0 & 0 \\ 0 & 1+\delta & 0 \\ 0 & 0 & 1-\frac{1}{2}\delta \end{pmatrix}, \mathbf{F^c} = \begin{pmatrix} 1+\frac{1}{4}\delta & 0 & 0 \\ 0 & 1+\frac{1}{4}\delta & 0 \\ 0 & 0 & 1-\frac{1}{2}\delta \end{pmatrix}$$

Note that these tensors can be constructed from the assumption of uniaxial/biaxial stretching for linear/circular polarizations respectively and are defined by the symmetries of the problems as well as by the assumption of the material being incompressible under photo-deformation (see Article 3). The amplitudes in $\mathbf{F^c}$ relative to the linear tensors are based on the phenomenological observation we made, that, at least in our case, the z-axis compression was equal for any polarization given the same exposure dose.

We first proceed to calculate the combined deformation tensor for an illumination cycle if the photo-deformations are purely irreversible and superimposed (cumulatively for small strains) onto each other. In this case, assuming $\delta << 1$ (and making first order approximations), for a sequence of linear x-polarization followed by circular polarization we get:

$$\mathbf{F}^{\mathbf{cycle,irr}} = \mathbf{F}^{\mathbf{x}} \cdot \mathbf{F}^{\mathbf{c}} = \begin{pmatrix} 1+\delta & 0 & 0 \\ 0 & 1-\frac{1}{2}\delta & 0 \\ 0 & 0 & 1-\frac{1}{2}\delta \end{pmatrix} \cdot \begin{pmatrix} 1+\frac{1}{4}\delta & 0 & 0 \\ 0 & 1+\frac{1}{4}\delta & 0 \\ 0 & 0 & 1-\frac{1}{2}\delta \end{pmatrix}$$

$$= \begin{pmatrix} (1+\delta)(1+\frac{1}{4}\delta) & 0 & 0 \\ 0 & (1-\frac{1}{2}\delta)(1+\frac{1}{4}\delta) & 0 \\ 0 & 0 & (1-\frac{1}{2}\delta)(1-\frac{1}{2}\delta) \end{pmatrix}$$

$$= \begin{pmatrix} 1+\frac{5}{4}\delta+\cdots & 0 & 0 \\ 0 & 1-\frac{1}{4}\delta+\cdots & 0 \\ 0 & 0 & 1-\delta+\cdots \end{pmatrix} \approx \begin{pmatrix} 1+\frac{5}{4}\delta & 0 & 0 \\ 0 & 1-\frac{1}{4}\delta & 0 \\ 0 & 0 & 1-\delta \end{pmatrix}$$

In this case, the relative expansion strain parameter associated to the linear step is $\varepsilon = \delta$ (taken directly from tensor $\mathbf{F}^{\mathbf{x}}$), and the relative area expansion of the whole cycle is $\delta A \approx \varepsilon_1 + \varepsilon_2 = \frac{5}{4}\delta - \frac{1}{4}\delta = \delta$, where the strain parameters ε_1 and ε_2 are taking from the tensor for the irreversible cycle $\mathbf{F}^{\mathbf{cycle,irr}}$. Hence the reversibility measure in this case is $R = 1 - {}^{\delta A}/_{\varepsilon} = 1 - {}^{\delta}/_{\delta} = 0$. The exact same calculation, leading the same relative area expansion and the same value for the reversibility measure, can be done if the second illumination is not circularly, but orthogonally linearly polarized.

If the system is reversibly switching between different shapes however, then as outlined in the Supplementary Information of Article 3, the transformation produced by the linear polarization step considered to define ε is simultaneously erasing (i.e., applying the inverse transformation of) any previous deformation. Hence, if the previous illumination was circularly polarized (a case denoted for the relevant quantities using a single apostrophe hereafter, whilst double apostrophes will denote situations with alternating orthogonal linear polarizations), the linear step will in practice be:

$$\mathbf{F}^{\mathbf{Lin,x'}} = \mathbf{F}^{\mathbf{x}} \cdot (\mathbf{F}^{\mathbf{c}})^{-1} = \begin{pmatrix} 1+\delta & 0 & 0 \\ 0 & 1-\frac{1}{2}\delta & 0 \\ 0 & 0 & 1-\frac{1}{2}\delta \end{pmatrix} \cdot \begin{pmatrix} \dfrac{1}{1+\frac{1}{4}\delta} & 0 & 0 \\ 0 & \dfrac{1}{1+\frac{1}{4}\delta} & 0 \\ 0 & 0 & \dfrac{1}{1-\frac{1}{2}\delta} \end{pmatrix}$$

$$= \begin{pmatrix} (1+\delta)(1-\frac{1}{4}\delta+\cdots) & 0 & 0 \\ 0 & (1-\frac{1}{2}\delta)(1-\frac{1}{4}\delta+\cdots) & 0 \\ 0 & 0 & (1-\frac{1}{2}\delta)(1+\frac{1}{2}\delta+\cdots) \end{pmatrix}$$

$$= \begin{pmatrix} 1+\frac{3}{4}\delta+\cdots & 0 & 0 \\ 0 & 1-\frac{3}{4}\delta+\cdots & 0 \\ 0 & 0 & 1+\cdots \end{pmatrix} \approx \begin{pmatrix} 1+\frac{3}{4}\delta & 0 & 0 \\ 0 & 1-\frac{3}{4}\delta & 0 \\ 0 & 0 & 1 \end{pmatrix}$$

Thus, the relative elongation strain along the *x*-axis induced by the linear polarization step (here $\mathbf{F}^{\mathbf{Lin,x'}}$) amounts to $\varepsilon = \frac{3}{4}\delta$. On the other hand, the circularly polarized step is defined correspondingly as $\mathbf{F}^{\mathbf{Circ}} = \mathbf{F}^{\mathbf{c}} \cdot (\mathbf{F}^{\mathbf{x}})^{-1}$. Thus the full cycle tensor in the switching case is given by $\mathbf{F}^{\mathbf{Cycle,Switch}} = \mathbf{F}^{\mathbf{Lin,x'}} \cdot \mathbf{F}^{\mathbf{Circ}} = \mathbf{F}^{\mathbf{x}} \cdot (\mathbf{F}^{\mathbf{c}})^{-1} \cdot \mathbf{F}^{\mathbf{c}} \cdot (\mathbf{F}^{\mathbf{x}})^{-1} = \mathbf{I}$, non-surprisingly stating that the full cycle transformation in the shape switching case is simply the identity. Therefore, $\delta A = 0$ for the cycle and the introduced reversibility measure returns $R = 1 - {}^{0}\!/_{\frac{3}{4}\delta} = 1$.

The same reasoning applies in the switching case if alternating orthogonal polarizations are used and the result will again be the identity for a full cycle. However, the relative expansive strain parameter will be larger in this case, since for the linear *x*-polarized step we get:

$$\mathbf{F}^{\mathbf{Lin,x''}} = \mathbf{F}^{\mathbf{x}} \cdot (\mathbf{F}^{\mathbf{y}})^{-1} = \begin{pmatrix} 1+\delta & 0 & 0 \\ 0 & 1-\frac{1}{2}\delta & 0 \\ 0 & 0 & 1-\frac{1}{2}\delta \end{pmatrix} \cdot \begin{pmatrix} \dfrac{1}{1-\frac{1}{2}\delta} & 0 & 0 \\ 0 & \dfrac{1}{1+\delta} & 0 \\ 0 & 0 & \dfrac{1}{1-\frac{1}{2}\delta} \end{pmatrix}$$

$$= \begin{pmatrix} (1+\delta)(1+\frac{1}{2}\delta+\cdots) & 0 & 0 \\ 0 & (1-\frac{1}{2}\delta)(1-\delta+\cdots) & 0 \\ 0 & 0 & (1-\frac{1}{2}\delta)(1+\frac{1}{2}\delta+\cdots) \end{pmatrix}$$

$$= \begin{pmatrix} 1+\frac{3}{2}\delta+\cdots & 0 & 0 \\ 0 & 1-\frac{3}{2}\delta+\cdots & 0 \\ 0 & 0 & 1+\cdots \end{pmatrix} \approx \begin{pmatrix} 1+\frac{3}{2}\delta & 0 & 0 \\ 0 & 1-\frac{3}{2}\delta & 0 \\ 0 & 0 & 1 \end{pmatrix}$$

In this case $\varepsilon = \frac{3}{2}\delta$ for the relative expansive strain along the *x*-axis for *x*-polarized illumination. This reflects the fact that higher transformation strain along the *x*-axis is needed to go from a pre-deformed *y*-axis stretched shape to an *x*-axis stretched shape than if the starting situation would be the in-plane expanded shape associated with circular polarization, which is already expanded along the *x*-axis. Of course, this does not affect the reversibility measure in the perfect switching case, since $\delta A = 0$ is still valid for the full cycle and thus $R = 1 - {}^{0}\!/_{\frac{3}{2}\delta} = 1$.

However, if the switching process is imperfect, one may imagine an irreversible cycle transformation superimposed onto the reversible switching one. Using the same approximations as above, the total transformation then becomes $\mathbf{F}^{\mathbf{cycle,tot}} = \mathbf{F}^{\mathbf{cycle,irr}} \cdot \mathbf{F}^{\mathbf{Cycle,Switch}} = \mathbf{F}^{\mathbf{cycle,irr}} \cdot \mathbf{I} = \mathbf{F}^{\mathbf{cycle,irr}}$, for any of the two polarization sequences. Hence, $\delta A = \delta_{\mathrm{irr}}$ in either case, using the result computed for the purely irreversible situation (first calculation) and denoting the small strain parameter relating to the irreversible component of the deformations as δ_{irr}. However, the *x*-polarized linear step for orthogonal polarizations would become:

$$\mathbf{F}^{\mathbf{Lin,x'',mixed}} = \mathbf{F}^{\mathbf{x,irr}} \cdot \mathbf{F}^{\mathbf{Lin,x''}} = \begin{pmatrix} 1+\delta_{\mathrm{irr}} & 0 & 0 \\ 0 & 1-\frac{1}{2}\delta_{\mathrm{irr}} & 0 \\ 0 & 0 & 1-\frac{1}{2}\delta_{\mathrm{irr}} \end{pmatrix} \cdot \begin{pmatrix} 1+\frac{3}{2}\delta_{\mathrm{rev}} & 0 & 0 \\ 0 & 1-\frac{3}{2}\delta_{\mathrm{rev}} & 0 \\ 0 & 0 & 1 \end{pmatrix}$$

$$= \begin{pmatrix} (1+\delta_{\mathrm{irr}})(1+\frac{3}{2}\delta_{\mathrm{rev}}+\cdots) & 0 & 0 \\ 0 & (1-\frac{1}{2}\delta_{\mathrm{irr}})(1-\frac{3}{2}\delta_{\mathrm{rev}}+\cdots) & 0 \\ 0 & 0 & 1-\frac{1}{2}\delta_{\mathrm{irr}} \end{pmatrix}$$

$$\approx \begin{pmatrix} 1+\delta_{\mathrm{irr}}+\frac{3}{2}\delta_{\mathrm{rev}} & 0 & 0 \\ 0 & 1-\frac{1}{2}\delta_{\mathrm{irr}}-\frac{3}{2}\delta_{\mathrm{rev}} & 0 \\ 0 & 0 & 1-\frac{1}{2}\delta_{\mathrm{irr}} \end{pmatrix}$$

Here we further assumed that the small strain parameter can be written as $\delta = \delta_{\mathrm{irr}} + \delta_{\mathrm{rev}}$. In this case, the relative expansive strain along the *x*-axis becomes $\varepsilon = \delta_{irr} + \frac{3}{2}\delta_{\mathrm{rev}}$ and the total reversibility strain measure becomes

$$R'' = 1 - \delta_{irr} / \left(\delta_{irr} + \frac{3}{2}\delta_{\mathrm{rev}}\right) = 1 - 1 / \left(1 + \frac{3}{2} \cdot \frac{\delta_{\mathrm{rev}}}{\delta_{irr}}\right)$$

Conversely, if considering the case where switching is induced with *x*-polarized linear and circular polarization respectively, then the transformation associated with linear *x*-polarization becomes:

$$\mathbf{F}^{\mathbf{Lin,x',mixed}} = \mathbf{F}^{\mathbf{x,irr}} \cdot \mathbf{F}^{\mathbf{Lin,x'}} = \begin{pmatrix} 1 + \delta_{\mathrm{irr}} & 0 & 0 \\ 0 & 1 - \frac{1}{2}\delta_{\mathrm{irr}} & 0 \\ 0 & 0 & 1 - \frac{1}{2}\delta_{\mathrm{irr}} \end{pmatrix} \cdot \begin{pmatrix} 1 + \frac{3}{4}\delta_{\mathrm{rev}} & 0 & 0 \\ 0 & 1 - \frac{3}{4}\delta_{\mathrm{rev}} & 0 \\ 0 & 0 & 1 \end{pmatrix}$$

$$\approx \begin{pmatrix} 1 + \delta_{\mathrm{irr}} + \frac{3}{4}\delta_{\mathrm{rev}} & 0 & 0 \\ 0 & 1 - \frac{1}{2}\delta_{\mathrm{irr}} - \frac{3}{4}\delta_{\mathrm{rev}} & 0 \\ 0 & 0 & 1 - \frac{1}{2}\delta_{\mathrm{irr}} \end{pmatrix}$$

Thus, similarly to the previous case we can compute $\varepsilon = \delta_{irr} + \frac{3}{4}\delta_{\mathrm{rev}}$ and, finally,

$$R' = 1 - \delta_{irr} / \left(\delta_{irr} + \frac{3}{4}\delta_{\mathrm{rev}}\right) = 1 - 1 / \left(1 + \frac{3}{4} \cdot \frac{\delta_{\mathrm{rev}}}{\delta_{irr}}\right) < R''$$

We therefore note, that for the same ratio between irreversible and reversible strain, reversibility in the mixed case may appear higher, and care should be taken to specify the polarization sequence when using this quantification of partial reversibility, as mentioned in section 1.3.2.

ISBN 978-82-326-8946-0 (printed ver.)
ISBN 978-82-326-8945-3 (electronic ver.)
ISSN 1503-8181 (printed ver.)
ISSN 2703-8084 (online ver.)

NTNU
Norwegian University of
Science and Technology